2009

# Sulfur adsorption, structure, and effects on coarsening on Ag(111) and Ag(100)

Mingmin Shen
*Iowa State University*

**Sulfur adsorption, structure, and effects on coarsening on Ag(111) and Ag(100)**

by

**Mingmin Shen**

A dissertation submitted to the graduate faculty

in partial fulfillment of the requirements for the degree of

DOCTOR OF PHILOSOPHY

Major: Chemistry

Program of Study Committee:
Patricia A. Thiel, Major Professor
James W. Evans
Mark S. Gordon
Klaus Schmidt-Rohr
Sriram Sundararajan

Iowa State University

Ames, Iowa

2009

# TABLE OF CONTENTS

# CHAPTER 1. GENERAL INTRODUCTION

## 1. Adsorbates on metal surfaces

The interactions among adsorbed species on metal surfaces have been studied for many years to understand their effects on adsorbate structures and chemical reactions on catalyst surfaces, on surfaces during microelectronics fabrication, on chemical sensors and electrodes, and on surfaces undergoing corrosion.[1] The study of these interactions continues to attract attention, as the industrial need for control over these surfaces increases. For example, environmental protection demands new catalysts with good selectivity. In this field, one of the objectives is to establish an atomic-scale description of the interactions between adsorbates to help guide the design of functional surface properties.

Adsorbate structures have been analyzed previously with a variety of methods.[2] Even the adsorption of a single component frequently yields many different surface structures, depending on its coverage and the substrate temperature (which influences the adsorbate's mobility and leads to its ability to produce more-or-less ordered structures and complete surface homogeneity). Different adsorption structures were found on metal surfaces with techniques such as low-energy electron diffraction (LEED), photoemission electron microscopy, and later scanning tunneling microscopy (STM).

Sulfur adsorption on metal surfaces has been studied extensively. Molecular sulfur undergoes rapid dissociative chemisorption on Ag(111) at and forms two different LEED patterns [$\sqrt{39}$R16.1°×$\sqrt{39}$R16.1° and ($\sqrt{7}$×$\sqrt{7}$) R10.9°] at different S coverages.[3] Using $H_2S$ as a precursor to produce S on the Ag low index surfaces also leads to the formation of different structures with different S coverages at different temperatures.[4,5] The S/Cu(111) surface was also studied in detail by exposing to $H_2S$,[6-11] and a ($\sqrt{7}$×$\sqrt{7}$) R19.1° structure is

generally assigned to a surface completely saturated by sulfur. The same kind of structure is found on S/Pd(111),[12] S/Ru(0001),[13] S/Ag(111)[14], $SCH_3$/Ag(111).[15,16] An ordered ($\sqrt{3}\times\sqrt{3}$) R30° sulfur adlayer forms on S/Au(111),[17-19] S/Pt(111)[20], S/Rh(111).[21]

**2. Adsorbates in metal thin film growth**

The deposition, growth, and equilibration of thin films and nanostructures hold considerable technological importance, and have been a subject of much interest.[22] For example, significant advancements in the field of thin films have driven the transistor size on integrated circuits down to the 100-nm regime. Fabrication of promising structures such as nanowires,[23,24] quantum dots,[25] and novel nanoelectromechanical devices[26] has also benefited from advancements in thin film growth techniques. However, consistency in the control and reproduction of nanostructures with very small size has proven to be difficult. To compound this problem, the interactions between these nanostructures with the surface, deposited atoms, and other structures are not fully understood and attract much attention.

As the size of thin films and nanostructures continues to become smaller, manipulation and control over these structures depends on understanding the fundamental interactions between the substrate and deposited materials. Ultimately, this means understanding the growth process at the atomic level. To achieve this goal, experiments must be conducted in ultra-clean environments, free from interference from unwanted elements. Ultrahigh vacuum conditions are chosen to ensure the highest level of cleanliness so the interactions of interest proceed unimpeded. However, even in the cleanest environments, contamination from foreign species can never be entirely eliminated. Consequently, contaminants, adsorbates, may adversely affect film growth and surface interactions. Conversely, it is also possible for the presence of a foreign species to enhance the growth and

properties of the film, such as adsorbate assisted layer-by-layer growth. Therefore, to understand the applicable characteristics of these films and structures, it is of the utmost importance to also understand the possible effects of adsorbed foreign species.

The specific use of adsorbed species, or surfactants, to aid in the growth of metal thin films and structures is well known. The addition of an Sb monolayer prior to deposition of Ag on Ag(111) is one of numerous examples in the use of metal surfactants to induce smooth layer-by-layer growth.[27-32] As other examples, the use of fluorine on the Fe/Cu(100)[33] and oxygen on the Cu/Ru(0001)[34] heteroepitaxial systems, both promote smooth film growth. Oxygen has also been found to act as a surfactant in the homoepitaxial growth of Pt/Pt(111)[35] and Cu/Cu(100).[36]

While surfactants are purposely chosen for their properties in affecting film growth, it has long been known that spontaneously adsorbed species from residual gas can also influence film morphology during growth.[37] Many studies have shown that film growth on an adsorbate-precovered surface can be altered as compared to the growth on the respective clean surface.[38-44] Adsorbate effects on nanostructure growth and equilibration have also been of considerable interest. For example, Au nanostructures on Au(111), which are stable in vacuum, decay rapidly when exposed to air.[45,46] The presence of minute amounts of CO affect the size, shape, and density of the resultant islands during the deposition of Pt/Pt(111).[47] A final example is the rotation and elongation of Ni islands deposited on an oxygen precovered Ni(100) surface.[48] Adsorbate effects on step structures on low-index metal surfaces can also be pronounced, and have been studied extensively.[49-54]

**3. Chalcogen elements on coinage metal surfaces**

The interactions between chalcogen elements (O, S, Se …) and the surfaces of coinage metals (Cu, Ag, Au) is of strong interest for a variety of reasons. One is the role of Ag in heterogeneous catalysis for the synthesis of epoxides from alkenes,[55-58] wherein the state and properties of adsorbed oxygen are crucial. Another is the prevalence of Au as a substrate for self-assembled monolayers of alkanethiols. In these systems, the Au-S interaction plays a key role, hold promise for a wide variety of applications, such as combinatorial screening, organic transistors, sensors, and drug delivery.[59-61] Another reason is the use of Cu films in microelectronics, which arises in part from their resistance to attack by $O_2$ and other oxidizing agents. The adsorption of S on metals such as Cu is also important in electrochemistry.[62]

The ability of two chalcogens, O and S, to facilitate mass transfer on these metal surfaces, i.e. to facilitate restructuring, is of special interest. As early as 1967, Perdereau and Rhead[63] noted that the presence of adsorbed S increases the surface diffusion coefficient of Ag by a factor of up to $10^4$. More than 25 years later, scanning tunneling microscopy (STM) studies began to reveal similar effects. For instance, such studies showed that adsorbed O can dramatically accelerate restructuring kinetics on Ag surfaces, e.g. the faceting of vicinal Ag(110),[64] and the ripening of deposited Ag islands on Ag(100).[65-67] At about the same time, researchers reported that adsorbed alkanethiols are associated with Au mass transport,[68-70] and that S accelerates coarsening on Cu(111).[71,72]

This accelerated mass transport of the metal may affect any or all of the applications mentioned above, particularly when the metal is in the form of nanoparticles that are subject to coarsening, e.g. the supported metal particles used in heterogeneous catalysis.[73,74] Furthermore, the chemical similarity between these systems—they are all Group VIA

elements adsorbed on Group IB metal surfaces—leads naturally to the idea that a common principle or set of principles may be in operation.

**4. Ag(111) and Ag(100) surfaces**

The Ag(111) and Ag(100) homoepitaxial systems have several features which make them good surfaces for these studies. First, Ag(111) and Ag(100) do not have reconstruction upon annealing at high temperature; hence, they are bulk-terminated, except for slight relaxations for the first three layers.[75-80] Second, the Ag(111) and Ag(100) surfaces are relatively unreactive and remain contaminant free during sample preparation and observation. This is particularly important in studying adsorbate/surface interactions.

Ag is a face-centered cubic (fcc) metal. The (111) face consist of a hexagonal close packed array in which the crystal directions within the plane are oriented at 60° to each other (see Figure 1). These are [$\bar{1}$10], [$\bar{1}$01], and [01$\bar{1}$]-type crystallographic directions. These close packed <$\bar{1}$10> type directions are more common than the <1$\bar{2}$1>-type orientations. "Jogs" or irregularities in a <$\bar{1}$10> type step form sites are known as kinks. A step that is parallel to the <1$\bar{2}$1> direction is a linear chain of kink sites.

The terraces on Ag(111) surface offers various adsorption sites which have different local symmetries and lead to different coordination geometries - specifically there are:

- On-top sites
- Bridging sites, between two Ag atoms
- Three-fold (3f) hollow sites (fcc and hcp )

Depending upon the site occupied, an adsorbate species (with a single point of attachment to the surface) is therefore likely to be bonded to either one, two, or three metal atoms (Figure 1). Deposition of Ag adatoms onto the Ag(111) surface produces surface structures, such as submonolayer islands, with hexagonal equilibrium geometry and surface steps oriented in the $<\bar{1}\,10>$ type directions. The steps alternate between so-called A- and B-type steps (see Figure 1). These differ in the local atom geometry. The A-type step has (100) microfacet, and the B-type step has (111) microfacet.

The Ag(100) surface orientation exhibits four-fold (4f) symmetry with rows of Ag atoms separated by rows of four-fold hollow sites (see Figure 2). Two common step orientations exist: the close packed <110>-type step {[011] and $[0\,\bar{1}\,1]$} and the metastable <001> step. The <110> step is the more stable orientation and dominates the step structure on the clean Ag(100) surface. The open nature of the <001> step can also be described as a step comprised of a linear chain of kink sites. Deposition of Ag onto the Ag(100) surface produces square islands with steps oriented in four <110>-type directions. Different adsorption sites are show in Figure 2.

**5. Instrumental methods**

Our primary experimental technique is STM. It has several strengths in studying surfaces. First, STM provides real-space images, therefore surface structures and surface features can be observed directly. Because the principle goal is to observe the surface structure, it is important that our imaging technique does not interfere with the surface. STM is a logical choice for our studies in that there is no contact between the tip and surface. If correctly adjusted, imaging can occur without surface/tip interference or perturbations.

Second, the resolution in STM is high allowing images of surface structures down to the nanometer level. This is very important in our experiments where surface islands may only be a few nanometers in size. Lastly, STM provides sequential real-time imaging with a time scale of only minutes between images. Therefore, evolution and dynamics of surface structures can be observed in some cases. The microscope itself is easily adapted to ultra high vacuum conditions, which are necessary for our experiments. Additionally, our microscope is fitted with variable temperature capabilities, which allows us to explore the surface anywhere from 50 to 750 K. A good summary of STM operation and applications can be found in C. J. Chen's book,[81] "Introduction to scanning tunneling microscopy."

Auger electron Spectroscopy (AES) is used as a supplemental technique for checking adsorbate coverage.

**6. Dissertation organization**

This dissertation includes three published papers and one to be submitted for publication, and one more chapter about sample preparation. Chapter 2, "Novel Self-Organized Structure of a Ag-S Complex on the Ag(111) Surface below Room Temperature," appears in volume 112 of *The Journal of Physical Chemistry C* on pages 4281-4290, 2008. Chapter 3, "Accelerated coarsening of Ag adatom islands on Ag(111) due to trace amounts of S: Mass-transport mediated by Ag–S complexes," appears in volume 130 of *The Journal of Chemical Physics* on pages 094701-1 to -13, 2009. Chapter 4, "The effect of chalcogens (O, S) on coarsening of nanoislands on metal surfaces," appears in volume 603 of *Surface Science* on pages 1486-1491, 2009. Chapter 5, "S effects on Ag/Ag(100) coarsening" will be submitted. Chapter 6, "Preparation of Ag(111) single crystal surfaces," talk about sample preparation. General conclusion will be presented in chapter 7. Appendix I, "Ripening of

monolayer vacancy pits on metal surfaces: Pathways, energetics, and size-scaling for Ag(111) versus Ag(100),” appears in volume 75 of Physical Review B on pages 245409-1 to -10, 2007. The remaining appendices present additional material concerning vacancy decay on Ag(111), electrochemical sulfur evaporator, and a database of the STM experiments.

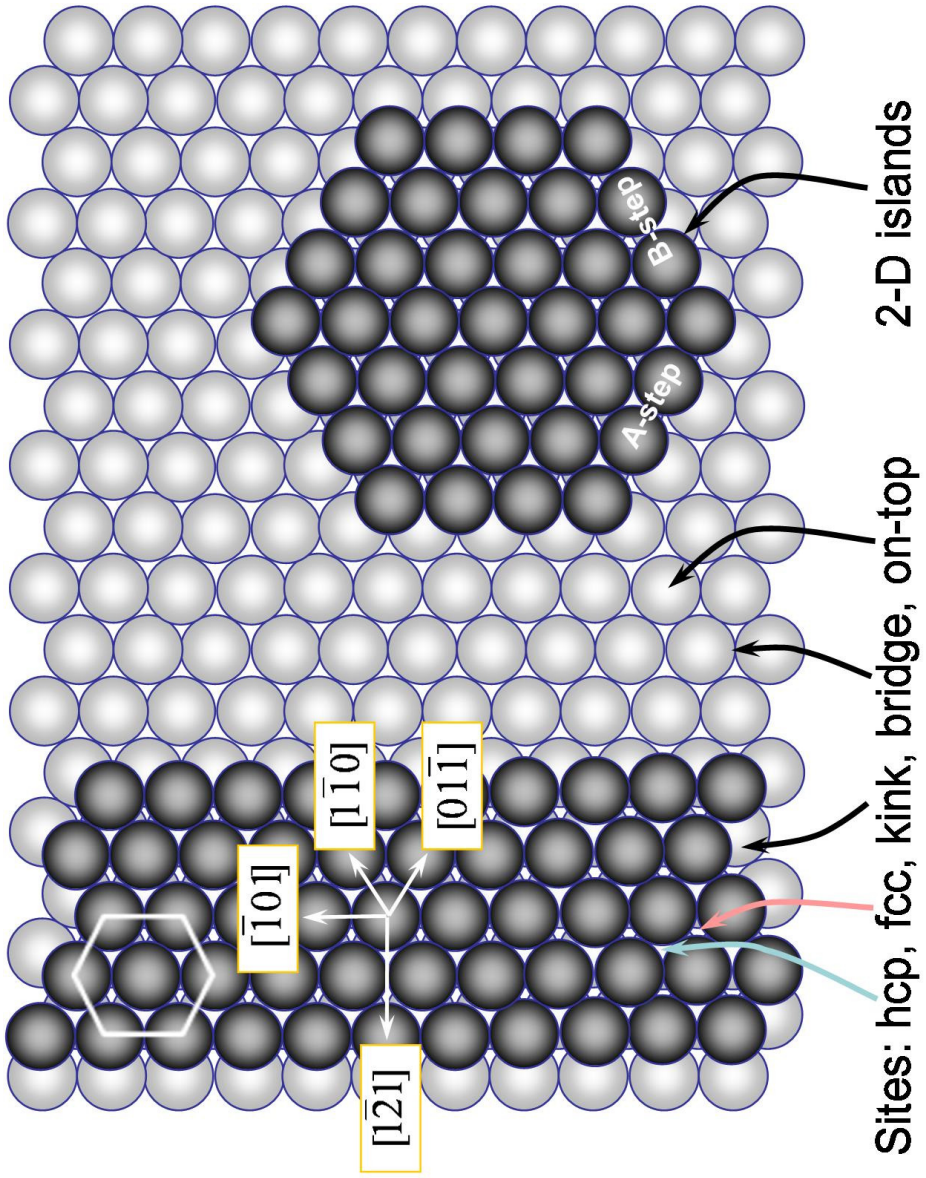


Figure 1. Top view of the Ag(111) surface. Darker spheres signify atoms occupying higher layers. The straight arrows show various crystallographic directions.

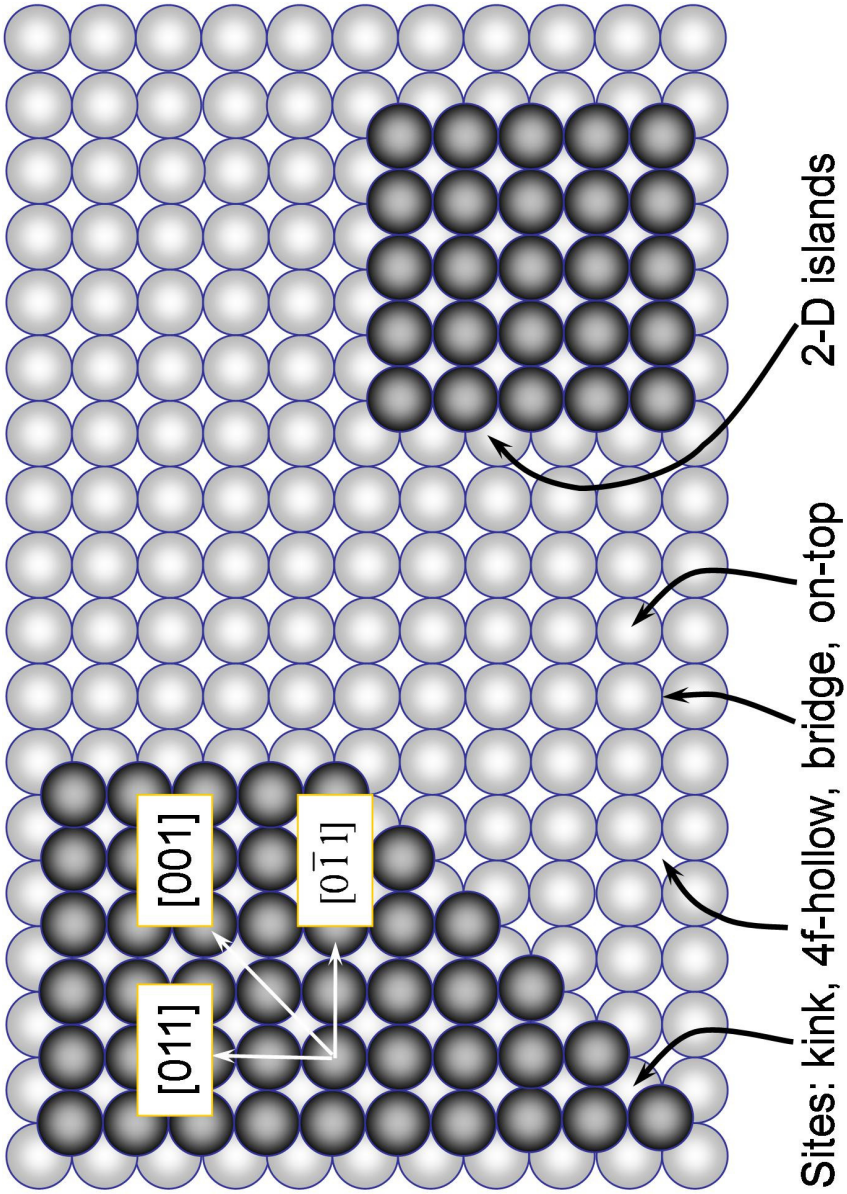


Figure 2. Top view of the Ag(100) surface. Darker spheres signify atoms occupying higher layers.

**References**

(1) Matsushima, T. *Surface Science* **2004**, *558*, 1.

(2) Ertl, G.; Küppers, J. *Low energy electrons and surface chemistry*; VCH: Weinheim, 1985.

(3) Schwaha, K.; Spencer, N. D.; Lambert, R. M. *Surface Science* **1979**, *81*, 273.

(4) Rovida, G.; Pratesi, F. *Surface Science* **1981**, *104*, 609.

(5) Oudar, J.; Huber, M. *Journal of Crystal Growth* **1975**, *31*, 345.

(6) Wahlström, E.; Ekvall, I.; Olin, H.; Lindgren, S.-Å.; Walldén, L. *Physical Review B* **1999**, *60*, 10699.

(7) Wahlström, E.; Ekvall, I.; Kihlgren, T.; Olin, H.; Lindgren, S.-Å.; Walldén, L. *Physical Review B* **2001**, *64*, 155406.

(8) Wahlström, E.; Ekvall, I.; Olin, H.; Walldén, L. *Applied Physics A* **1998**, *66*, S1107.

(9) Saidy, M.; Mitchell, K. A. R. *Surface Science* **1999**, *441*, 425.

(10) Wiame, F.; Maurice, V.; Marcus, P. *Surface Science* **2006**, *600*, 3540.

(11) Jackson, G. J.; Driver, S. M.; Woodruff, D. P.; Cowie, B. C. C.; Jones, R. G. *Surface Science* **2000**, *453*, 183.

(12) Alfonso, D. R. *Surface Science* **2007**, *601*, 4899.

(13) Sklarek, W.; Schwennicke, C.; Jurgens, D.; Pfnur, H. *Surface Science* **1995**, *330*, 11.

(14) Yu, M.; Woodruff, D. P.; Satterley, C. J.; Jones, R. G.; Dhanak, V. R. *Journal of Physical Chemistry C* **2007**, *111*, 3152.

(15) Yu, M.; Woodruff, D. P.; Bovet, N.; Satterley, C. J.; Lovelock, K.; Jones, R. G.; Dhanak, V. *Journal of Physical Chemistry B* **2006**, *110*, 2164.

(16) Yu, M.; Driver, S. M.; Woodruff, D. P. *Langmuir* **2005**, *21*, 7285.

(17) Biener, M. M.; Biener, J.; Friend, C. M. *Surface Science* **2007**, *601*, 1659.

(18) Min, B. K.; Alemozafar, A. R.; Biener, M. M.; Biener, J.; Friend, C. M. *Topics in Catalysis* **2005**, *36*, 77.

(19) Yu, M.; Ascolani, H.; Zampieri, G.; Woodruff, D. P.; Satterley, C. J.; Jones, R. G.; Dhanak, V. R. *Journal of Physical Chemistry C* **2007**, *111*, 10904.

(20) Yoon, H. A.; Materer, N.; Salmeron, M.; Van Hove, M. A.; Somorjai, G. A. *Surface Science* **1997**, *376*, 254.

(21) Yoon, H. A.; Salmeron, M.; Somorjai, G. A. *Surface Science* **1998**, *395*, 268.

(22) Brauman, J. I.; Szuromi, P. *Science* **1996**, *273*, 855.

(23) *MRS bulletin* **1999**, *24*.

(24) HU, J.; Odom, T. W.; Lieber, C. M. *Accounts of Chemical Research* **1999**, *32*, 435.

(25) *MRS bulletin* **1998**, *23*.

(26) *Science* **2000**, *290*.

(27) Vrijmoeth, J.; van der Vegt, H. A.; Meyer, J. A.; Vlieg, E.; Behm, R. J. *PHYSICAL REVIEW LETTERS* **1994**, *72*, 3843.

(28) Fiorentini, V.; Oppo, S.; Scheffler, M. *Applied Physics A: Materials Science & Processing* **1995**, *60*, 399.

(29) van der Vegt, H. A.; van Pinxteren, H. M.; Lohmeier, M.; Vlieg, E.; Thornton, J. M. C. *PHYSICAL REVIEW LETTERS* **1992**, *68*, 3335.

(30) Fukutani, K. *Surface Science* **1993**, *281*, 285.

(31) van der Vegt, H. A.; Vrijmoeth, J.; Behm, R. J.; Vlieg, E. *Physical Review B* **1998**, *57*.

(32) van der Vegt, H. A.; Huuisman, W. J.; Howes, P. B.; Turner, T. S.; Vlieg, E. *Surface Science* **1996**, *365*, 205.

(33) Egelhoff, W. F. *Surface Science* **1998**, *404*, 32.

(34) Wolter, H.; Schmidt, M.; Wandelt, K. *Surface Science* **1993**, *298*, 173.

(35) Esch, S.; Hohage, M.; Michely, T.; Comsa, G. *Physical Review Letters* **1994**, *72*, 518.

(36) Yata, M.; Rouch, H.; Nakamura, K. *Physical Review B* **1997**, *56*, 10579.

(37) Bauer, E.; Poppa, H. *Thin Solid Films* **1972**, *12*, 167.

(38) Egelhoff, W. F.; Steigerwald, D. A. *Journal of Vacuum Science & Technology a-Vacuum Surfaces and Films* **1989**, *7*, 2167.

(39) Schröder, J.; Günther, C.; Hwang, R. Q.; Behm, R. J. *Ultramicroscopy* **1992**, *42*, 475.

(40) Hwang, R. Q.; Günther, C.; Schröder, J.; Günther, S.; Kopatzki, E.; Behm, R. J. *Journal of Vacuum Science & Technology a-Vacuum Surfaces and Films* **1992**, *10*, 1970.

(41) Layson, A. R.; Evans, J. W.; Fournée, V.; Thiel, P. A. *JOURNAL OF CHEMICAL PHYSICS* **2003**, *118*, 6467.

(42) Layson, A. R.; Thiel, P. A. *Surface Science* **2001**, *472*, L151.

(43) Layson, A. R.; Evans, J. W.; Thiel, P. A. *Physical Review B* **2002**, *65*, 193409.

(44) Ling, W. L.; Bartelt, N. C.; Pohl, K.; de la Figuera, J.; Hwang, R. Q.; McCarty, K. F. *Physical Review Letters* **2004**, *93*, 166101.

(45) Cooper, B. H.; Peale, D. R.; McLean, J. G.; Phillips, R.; Chason, E. Mass flow and stability of nanoscale features on Au(111). In *Evolution of Surface and Thin Film Microstructure:MRS Symposium Proceedings*; Atwater, H. A., Chason, E., Grabow, M. H., Eds. Warrendale, PA, 1993; pp 37.

(46) Peale, D. R.; Cooper, B. H. *Journal of vacuum science and technology A* **1992**, *10*, 2210.

(47) Kalff, M.; Comsa, G.; Michely, T. *Physical Review Letters* **1998**, *81*, 1255.

(48) Kopatzki, E.; Günther, S.; Nichtl-pecher, W.; Behm, R. J. *Surface Science* **1993**, *284*, 154.

(49) Nakakura, C. Y.; Altman, E. I. *Surface Science* **1999**, *424*, 244.

(50) Frank, E. R.; Hamers, R. J. *Journal of Catalysis* **1997**, *172*, 406.

(51) Nakakura, C. Y.; Altman, E. I. *Surface Science* **1998**, *416*, 488.

(52) Nakakura, C. Y.; Zheng, G.; Altman, E. I. *Surface Science* **1998**, *401*, 173.

(53) Nakakura, C. Y.; Altman, E. I. *Surface Science* **1998**, *398*, 281.

(54) Matsumoto, T.; Bennett, R. A.; Stone, P.; Yamada, T.; Domen, K.; Bowker, M. *Surface Science* **2001**, *471*, 225.

(55) Verykios, X. E.; Stein, F. P.; Coughlin, R. W. *Catalysis Reviews-Science and Engineering* **1980**, *22*, 197.

(56) Sajkowski, D. J.; Boudart, M. *Catalysis Reviews-Science and Engineering* **1987**, *29*, 325.

(57) Van Santen, R. A.; Kuipers, H. P. C. E. *Advances in Catalysis* **1987**, *35*, 265.

(58) Serafin, J. G.; Liu, A. C.; Seyedmonir, S. R. *Journal of Molecular Catalysis A-Chemical* **1998**, *131*, 157.

(59) Schreiber, F. *J. Phys.: Cond. Matter* **2004**, *16*, R881.

(60) Ulman, A. *Self-Assembled Monolayers of Thiols (Thin Films)*; Academic Press: New York, 1998.

(61) Dimitrakopoulos, C. D.; Mascaro, D. J. *IBM J. Res. Dev.* **2001**.

(62) Tansel, T.; Magnussen, O. M. *Phys. Rev. Lett* **2006**, *96*, 026101.

(63) Perdereau, J.; Rhead, G. E. *Surf. Sci* **1967**, *7*, 175.

(64) Ozcomert, J. S.; Pai, W. W.; Bartelt, N. C.; Reutt-Robey, J. E. *Phys. Rev. Lett.* **1994**, *72*, 258.

(65) Layson, A. R.; Thiel, P. A. *Surf. Sci.* **2001**, *472*, L151.

(66) Layson, A. R.; Evans, J. W.; P.A.Thiel. *Phys. Rev. B* **2002**, *65*, 193409 (4 pages).

(67) Layson, A. R.; Evans, J. W.; Thiel, P. A. *J. Chem. Phys.* **2003**, *118*, 6467.

(68) Edinger, K.; Gölzhäuser, A.; Demota, K.; Wöll, C.; Grunze, M. *Langmuir* **1993**, *90*, 4.

(69) McCarley, R. L.; Dunaway, D. J.; Willicut, R. J. *Langmuir* **1993**, *9*, 2775.

(70) Stranick, S. J.; Parikh, A. N.; Allara, D. L.; Weiss, P. S. *J. Phys. Chem.* **1994**, *98*, 11136.

(71) Feibelman, P. J. *Phys. Rev. Lett.* **2000**, *85*, 606.

(72) Ling, W. L.; Bartelt, N. C.; Pohl, K.; de la Figuera, J.; Hwang, R. Q.; McCarty, K. F. *Phys. Rev. Lett.* **2004**, *93*, 166101.

(73) Ruckenstein, E.; Lee, S. H. *J. Catal.* **1988**, *109*, 100.

(74) Wodiunig, S.; Keel, J. M.; Wilson, T. S. E.; Zemichael, F. W.; Lambert, R. M. *Cat. Lett.* **2003**, *87*, 1.

(75) Xie, J.; de Gironcoli, S.; Baroni, S.; Scheffler, M. *Physical Review B* **1999**, *59*, 970.

(76) Statiris, P.; Lu, H. C.; Gustafsson, T. *PHYSICAL REVIEW LETTERS* **1994**, *72*, 3574.

(77) Lewis, L. J. *Physical Review B* **1994**, *50*, 17693.

(78) Li, H.; Quinn, J.; Li, Y. S.; Tian, D.; Jona, F.; Marcus, P. M. *Physical Review B* **1991**, *43*, 7305.

(79) Gupta, R. P. *Physical Review B* **1981**, *23*, 6265.

(80) Wan, J.; Fan, Y. L.; Gong, D. W.; Shen, S. G.; Fan, X. Q. *Modelling and Simulation in Materials Science and Engineering* **1999**, *7*, 189.

(81) Chen, C. J. *Introduction to Scanning Tunneling Microscopy*; Oxford University Press: New York, 1993.

# CHAPTER 2. NOVEL SELF-ORGANIZED STRUCTURE OF A Ag-S COMPLEX ON THE Ag(111) SURFACE BELOW ROOM TEMPERATURE

A paper published in *Journal of Physical Chemistry C*

Mingmin Shen, Da-Jiang Liu, Cynthia J. Jenks, and Patricia A. Thiel

**Abstract**

A well-ordered, self-organized dot-row structure appears after adsorption of S on Ag(111) at 200 K. This dot-row motif, which exhibits fixed spacing between dots within rows, is present over a wide range of coverage. The dots are probably $Ag_3S_3$ clusters with adsorbed S in the spaces between dots. Dynamic rearrangements are observed. Small domains of aligned dot-rows form during adsorption and grow quickly after adsorption ends. The domains also exhibit large equilibrium fluctuations after adsorption. The dot-row structure disappears reversibly upon heating above 200 K, and transforms reversibly to an 'elongated island' structure upon cooling below 200 K. DFT supports the assignment of the dots as $Ag_3S_3$ trimers, and also lends insight into the possible origins of other structures observed in this complex system.

## 1. Introduction

The interaction of chalcogens (O, S, …) with surfaces of the coinage metals (Ag, Au, Cu) is of strong interest for a variety of reasons. One is the role of Ag in heterogeneous catalysis. Ag is used in a major industrial reaction, synthesis of epoxides from alkenes,[1-4] wherein the state and properties of adsorbed oxygen are crucial. Another is the prevalence of Au as a substrate for self-assembled monolayers of alkanethiols. These systems, in which the Au-S interaction plays a key role, hold promise for a wide variety of applications, such as

combinatorial screening, organic transistors, sensors, and drug delivery.[5-7] Yet another reason is the use of Cu films in microelectronics, which arises in part from their resistance to attack by $O_2$ and other oxidizing agents. The adsorption of S on metals such as Cu is also important in electrochemistry.[8]

Of particular interest to us is the ability of two chalcogens, O and S, to facilitate mass transfer on these metal surfaces, i.e. to facilitate restructuring. As early as 1967, Perdereau and Rhead[9] noted that the presence of adsorbed S increases the surface diffusion coefficient of Ag by a factor of $10^4$. More than 25 years later, scanning tunneling microscopy (STM) studies began to reveal similar effects. For instance, such studies showed that adsorbed O can dramatically accelerate restructuring kinetics on Ag surfaces, e.g. the faceting of vicinal Ag(110),[10] and the ripening of deposited Ag islands on Ag(100).[11-13] At about the same time, researchers reported that adsorbed alkanethiols are associated with Au mass transport,[14-16] and that S accelerates coarsening on Cu(111).[17,18]

This accelerated mass transport of the metal may affect any or all of the applications mentioned above, particularly when the metal is in the form of nanoparticles that are subject to coarsening, e.g. the supported metal particles used in heterogeneous catalysis.[19,20] Furthermore, the chemical similarity between these systems—they are all Group VIA elements adsorbed on Group IB metal surfaces—leads us to speculate that a common principle or set of principles may be in operation.

In this paper, we describe a basic STM study of the structures formed by S adsorbed on Ag(111). We find a rich variety of phases below room temperature. This system, S/Ag(111), has been studied previously with low-energy electron diffraction (LEED) and with STM, but only at room temperature.[21-23] These studies revealed two structures for S on

Ag(111) that develop with increasing coverage. First, a structure that was originally identified as a $(\sqrt{39}R16^{o}x\sqrt{39}\overline{R}16^{o})$ phase[21] appears. The detailed structure of this phase has not been resolved, even with the help of STM.[23] At higher coverage, a ($\sqrt{7}$ x $\sqrt{7}$)R19$^{o}$ phase (abbreviated $\sqrt{7}$) develops. This phase has been assigned as a reconstruction in which the top layer resembles $Ag_2S(111)$.[21,23]

Sulfur adsorption on the (111) surfaces of the other two coinage metals, Au and Cu, has also been studied with STM.[24-30] On Cu, a complex series of apparently-static structures evolve with coverage below room temperature. Similar to the $\sqrt{7}$ on Ag(111), they were interpreted as surface reconstructions that mimic aspects of $Cu_2S(111)$.[25,26] At the same temperature, however, other research indicated the presence of a mobile $Cu_3S_3$ species, at least at very low coverage,[17,18] and arguments have also been made for structures based on $Cu_4S$ tetramers.[31] On Au(111), one recent set of experiments indicated the formation of a very mobile Au-S complex at room temperature and above.[27-30] However, another study of the same system indicated that the most important species are molecular and polymeric $S_n$, at least for coverages greater than 0.4 monolayers.[32] Clearly, a variety of different structural models and mobile species have been proposed for these systems, and many of them involve metal surface reconstructions or metal-S clusters.

The present contribution is different, because it focuses on a temperature range that has not been investigated previously for S/Ag(111). We find that under the conditions of our experiments, the most distinctive feature in STM is a dot-like protrusion that tends to form linear chains, appears to be mobile, and is most likely $Ag_3S_3$. Furthermore, DFT provides insight into the relationship between this structure, an $Ag_2S$-like phase, and other possible

low-temperature phases. The result is a set of insights that are new, but complementary to previous work.

**2. Details of Experiments and Calculations.**

The Ag(111) sample used in these studies was grown by the Ames Laboratory Materials Preparation Center.[33] The surface was oriented perpendicular to the <111> direction within 0.25°. The sample was polished to a mirror finish using 6, 1, and 0.25 μm diamond paste.

All experiments were carried out in a stainless steel ultrahigh vacuum (UHV) chamber with base pressure of $1 \times 10^{-10}$ Torr, equipped with an ion gun and with a retarding field analyzer (RFA) for Auger electron spectroscopy (AES). In one part of the chamber, the sample was cleaned by repeated cycles of $Ar^+$ sputtering (15 min, 20 mA, 1.0 -1.5 kV, T = 300 K) followed by annealing. This was carried out until no impurities could be detected by AES, and until STM showed large terraces on the order of at least 100 nm in width, together with a very low density of apparent impurities, especially pinning sites at steps.

The other part of the chamber contained an Omicron variable-temperature STM. In addition, this part contained a solid-state electrochemical Ag|AgI|$Ag_2S$|Pt cell following the design of Wagner.[34] The sample could be exposed to $S_2$ generated by the electrochemical cell. Only Ag and S were detected by AES on the surface after S deposition—not iodine or oxygen.

Sulfur coverage was determined after each run using the S(LMM)/Ag(MNN) AES intensity ratio. We adopted a calibration that was published by Schwaha, Spencer and Lambert (SSL) in 1979,[21] derived largely from LEED but corroborated by temperature-programmed desorption and work function measurements. The experiments of SSL were

similar to ours in several key respects. SSL studied chemisorbed sulfur produced by an electrochemical $S_2$ source, and they measured S coverage using a RFA for AES. Because of these similarities, their calibration should be applicable. Furthermore, a very similar proportionality between S/Ag Auger intensity and S coverage was reported later by Rovida and Pratesi[22], for a p(2x2) structure on Ag(100) and also for the √7 structure on Ag(111), under similar conditions (cf. Table 1 of Ref. 22).

We report the S coverage, $\theta_S$, as the ratio of S atoms to Ag atoms, also expressed as monolayers (ML). Note that some other authors have chosen a different definition of coverage when reporting studies of S adsorption (e.g. SSL in Ref. 21). With the electrochemical doser, S flux was in the range of 0.005 to 0.05 ML/minute.

During S adsorption and STM imaging, the sample was usually cooled with liquid nitrogen. Sample temperature, $T_s$, was measured by means of a silicon diode at the cooling stage, which surrounded the sample holder on all sides but one. There was a temperature offset between the cooling stage and the sample. We took $T_s = T_{diode} + A(T_{diode})$, where $A(T_{diode})$ was provided by the manufacturer (Omicron).

All STM images were acquired at the stated temperature, which was most commonly 135, 200, or 300 K. Heating from 135 to 200 K, or from 200 to 300 K, required 25-30 minutes in order to reach a stable endpoint. Cooling between these same temperatures required 45-50 minutes. Unless stated otherwise, all images were acquired at least 10 minutes after $S_2$ exposure ended.

All STM images were collected using electrochemically-etched W tips.[35] Typical tunneling conditions were -2.0 V and 1.0 nA. Qualitatively, the images of the dot-rows were invariant over the range +2 to -5 V.

Density-functional theory (DFT) calculations were performed using the VASP[36-38] total energy code, with Perdew-Burke-Ernzerhof (PBE)[39] generalized gradient approximation (GGA) and the projected augmented-wave (PAW)[40] method. Results were obtained using five-layer Ag slabs (unless otherwise noted), fixing the lower two layers of atoms to their bulk positions. Adsorbates were attached to one side of the slab. The lattice constant was set to 0.417 nm, the bulk PBE value (versus the experimental value of 0.409 nm). Methfessel-Paxton smearing[41] of the occupancy function (with $N = 1$ and $\sigma = 0.2$ eV) was used for efficiency. The energy cutoff was 280 eV for all calculations. The vacuum spacing between slabs was 1.2 nm.

**3. Experimental Results.**

**3.1 Coverage-dependence of structures at 200 K.**

Figure 1 shows a progression of STM images after deposition of varying amounts of S at 200 K. The surface in Fig. 1a is clean. Atomically-resolved images at higher magnification allow unambiguous assignment of the crystallographic directions in the surface plane, as shown in the inset. The surface shown in Fig. 1b has $\theta_S = 0.007$. There is no detectable difference between the surfaces in Figs. 1a and 1b. As S coverage increases to $\theta_S = 0.02$ (Fig. 1c), the steps facet, i.e. they break up into linear segments. The faceted steps are decorated with dots, as shown in the high-magnification inset. Further increasing $\theta_S$ causes dots to appear on the Ag(111) terraces as well, as seen in Figure 1d at $\theta_S = 0.1$. The dots are arranged in linear rows, which we call a "dot-row" motif. The rows form domains separated by angles of 60° or 120°. The dot-rows lie parallel to the close-packed Ag rows in the substrate, which are the <110>-type directions. Figure 1e shows a surface with $\theta_S = 0.4$. At

this high coverage, the dot-rows are much denser and they coexist with irregularly-shaped pits. Also, a few small worm-like protrusions exist.

Figure 2 allows closer examination of the coverage regime wherein the dot-row structure builds and pits eventually appear. When $\theta_S = 0.030$ (Fig. 2a, a'), the density of dot-rows on the terraces is low. The rows mainly orient in one direction over large length scales (ca. 100 nm in Fig. 2a). In Fig. 2a, there are three domains of parallel rows. Within each domain, the inter-row separation is 1.5-2.7 nm. It is apparent that the rows cluster together due to (net) attractive interactions, drawing the rows to within distances below 3 nm. In addition to the dot-rows, the terraces contain some disordered material. When $\theta_S$ increases to 0.14 (Fig. 2b, b'), the range of inter-row separations broadens to 1.3-5 nm. Separations toward the upper end of this range may simply be considered as gaps between adjacent domains. When $\theta_S$ increases further to $\theta_S = 0.3$ (Fig. 2c, c') pits are visible, and they are static over observation periods of at least several hours at 200 K. The range of row separations here is 1.1 to 3.4, with a peak in the distribution at about 1.6 nm. Finally, at $\theta_S \geq 0.4$, the dots form a hexagonal honeycomb array, as in Fig. 1e. In the honeycomb, the dots are all separated by 1.6 nm, the same as their intra-row separation at lower coverage.

Whereas the inter-row separation changes with coverage, the separation between dots in a given row is constant at $1.6 \pm 0.1$ nm (range = 1.42 to 1.77 nm, $n > 100$). This is between 5 and 6 times the lattice constant of the Ag(111) unit cell. The diameter of individual dots, based on their full-width at half-maximum, is $0.70 \pm 0.06$ nm. At a bias voltage of -2 V and at $\theta_S = 0.03$, the dots are only $0.13 \pm 0.01$ nm higher than surrounding regions that must be mainly clean Ag(111), i.e. large terrace areas devoid of dot-rows.

In Section 4, we will argue that the dots are $Ag_3S_3$ clusters. However, they can account for only a fraction of the adsorbed S. For instance, from the STM images at $\theta_S = 0.1$, the dot density is 0.10-0.15 $nm^{-2}$. Assuming three S atoms per dot, this corresponds to 0.02-0.03 ML, i.e. 20-30% of the total S. The majority of S must be in the interstices between dots. Evidence for this interstitial S can be seen in the different heights of the areas between rows in Fig. 1d, particularly at the shorter row separations. In some cases, substructures between the dot-rows can be imaged. Figure 3a shows two different dot-row orientations on a single terrace. The substructure is shown for each orientation in Fig. 3b and 3c. It consists of smaller bumps that define the corners of rhombi with dimensions, shapes, and orientations that are characteristic of a $(\sqrt{3} \times \sqrt{3})R30^\circ$ lattice (abbreviated $\sqrt{3}$ henceforth).

The $\sqrt{3}$ structure is observed in the range $0.05 \leq \theta_S \leq 0.3$, and between rows separated by 2.3 to 3.4 nm. If the dot-row separation is larger than 3.4 nm, there is evidence of adsorbed material, but in a disordered and probably mobile state (as will be discussed further in section 3.2). If the dot-row separation is smaller than 2.3 nm, different ordered structures exist between the rows that cannot be assigned at present. The two arrows in Fig. 3a point to one such unassigned structure. Another appears between dots in the honeycomb array at $\theta_S \geq 0.4$ (Fig. 3d). The main features of the latter substructure are dark depressions, one of which is accentuated by the arrow in Fig. 3d.

To summarize this section, the dot-row is a robust structural motif at 200 K. It first forms at step edges, at a coverage as low as 0.02 ML, and emerges on terraces shortly thereafter at 0.03 ML. The separation between dots within a row is fixed at $1.6 \pm 0.1$ nm, but the separation between rows is variable. When rows are farther than 3.4 nm apart, the intervening substrate contains some material in a disordered and probably mobile state.

When rows are separated by 3.4 nm and less, the substrate is typically covered by ordered substructures, one of which can be identified as a ($\sqrt{3}$ x $\sqrt{3}$)R30$^o$ lattice. The rows become so compressed at $\theta_S$ = 0.4 that the dot-rows form a honeycomb lattice. Static pits develop on the terraces at $\theta_S$ > 0.2, showing that Ag is consumed in the adsorbate lattice. (Ag is probably consumed at lower $\theta_S$ as well, but preferentially from step edges.) This observation and interpretation of S-induced pitting are both reminiscent of ones reported for Au(111) at 300 K and above,[29,30] and also of ones reported for Ag(111) at 300 K.[23] However, nothing analogous to the dot-row structure was found in those studies.

**3.2. Temperature dependence of S structures: 135, 200, and 300 K.**

Figure 4 illustrates the temperature-dependence of the S structures on Ag(111) at $\theta_S$ = 0.09. After deposition at 135 K, irregularly-shaped islands exist both on the terrace and at the step edge, as seen in Fig. 4a. After being heated to 200 K, Fig. 4b shows that the dot-row structure emerges, appearing similar to Fig. 1d and 2b/b'.

When the same surface is cooled back to 135 K, as shown in Fig. 4c, the dot-rows disappear, but the original irregular islands are not restored. Instead, compact elongated islands form. The long axes of these islands parallel the three orientations of the dot-rows. The features of Fig. 4b and 4c can be reproduced by cycling between 135 K and 200 K at this coverage. This reversibility indicates that the dot-row and elongated-island structures are equilibrium phases.

Figure 4d shows the surface with $\theta_S$ = 0.09 after heating from 200 to 300 K. Here, the surface is similar to clean Ag(111): steps are smooth, rather than faceted, and no dot-row structure can be imaged. When the surface is cooled back to 200 K, as in Fig. 4e, the dot-row structure returns reversibly.

The schematic of Fig. 5 summarizes our observations in the form of a partial phase diagram. This representation excludes the irregular islands of Fig. 4a, because they are not an equilibrated structure. Figure 5 suggests a range of temperature at which the dot-row structure disappears, as a function of $\theta_S$, at least through 0.09 ML. For instance, the dot-row phase disappears below 200 K for $\theta_S < 0.03$, and above 200 K for higher $\theta_S$.

**3.3. Evolution and fluctuations in structure during and after adsorption.**

The surface structures change and evolve on the time scale of experimental observation. One illustration is given in Fig. 6a-b. Here, the surface is imaged continuously during adsorption at 200 K, and immediately after, on a timescale of 120 s/image. Fig. 6a is an image taken toward the end of adsorption, where the final coverage is $\theta_S = 0.1$, and Fig. 6b is an image taken 10 minutes later. Clearly, the dot-rows form much smaller domains during adsorption than after adsorption stops, indicating that considerable domain growth takes place in a period of a few minutes.

Another example is given in Fig. 6c-e ($\theta_S = 0.09$), where a surface is imaged continuously, starting several hours after adsorption ends, and (more importantly) after heating to 300 K and re-cooling to 200 K. Both the temporal and thermal histories indicate that the surface is initially at or close to an equilibrium structure. Yet during the course of imaging, without a change in temperature or coverage, the positions of numerous rows change. This is particularly clear in the lower half of the images, where a large group of rows rotate by $60^o$ between Fig. 6c to 6d, then flip back again in Fig. 6e. Therefore, the surface is continuously sampling an ensemble of configurations, which can only be true if there is a dynamic equilibrium between a mobile S-containing species and those fixed in the observable structures. Immediately after adsorption, the mobile species mediates an evolution

toward larger dot-row domains, and at longer times it facilitates seemingly-random fluctuations in domain orientations.

The STM tip may play a role in assisting diffusion of the S-containing species. It is unlikely, however, that it can be solely responsible for the observed changes in the dot-row domains because these changes require concerted, long-range displacements. Furthermore, we observe the domains to be significantly more stable at 175 K than at 200 K, indicating that rearrangements are thermally activated, at least in part.

The streaks evident in some STM images may be related to the above rearrangements. For instance, see Fig. 1c. There, streaks are evident but only in the largest gaps between rows. In Fig. 2a', the streaks take a shape suggestive of partial dots, in the largest gap between rows. Thus, the streaks may be caused by dots diffusing rapidly on clean, or relatively-clean, regions of the Ag(111) surface.

**4. DFT results.**

**4.1 Basic insights into Ag-S interactions.**

Using the Monkhorst-Pack (MP) method[42] with a (2x2) supercell and (6x6x1) grids of *k*-points, we find that the fcc site is the most favorable adsorption site for a S adatom (at 0.25 ML). The hcp, bridge, and top sites are 0.06, 0.19 and 1.16 eV per S atom less favorable, respectively, consistent with DFT results reported earlier.[43] With 1 ML of S adatoms, all on fcc sites, the adsorption energy per S is 1.1 eV less favorable than at 0.25 ML. Consequently, we can deduce that there is a n.n. repulsion between S of about 0.37 eV (neglecting longer-range and many-body interactions).

Using a (3x3) supercell and (4x4x1) MP *k*-points grid, we find that Ag-S adatom pairs have a weak attractive interaction of 0.05 eV. Significant relaxation occurs with both

adatoms initially occupying n.n. fcc sites but moving closer to a bridge site, indicating that the bond between Ag and the substrate is significantly weakened by a nearby S atom.

Much stronger attraction between S and Ag adatoms can be achieved when they form a larger complex. A prime candidate for such a complex is $Ag_3S_3$, analogous to the $Cu_3S_3$ whose existence was inferred on the basis of kinetic measurements[18] and DFT calculations[17] for the S/Cu(111) system. Using a (5x5) supercell and (4x4x1) MP *k*-point grid, we find the most stable structure for this stoichiometry to be that shown in Fig. 7. It is a S-decorated Ag trimer with Ag at fcc sites forming a triangle with a surface Ag atom beneath its center. The S atoms are located near bridge sites adjacent to the Ag trimer on (100)-microfacets. The total adsorption energy is nearly 2 eV more favorable than that of three isolated Ag and three isolated S adatoms. The Ag and S atoms are nearly co-planar. The Ag nuclei in this trimer are 0.236 nm above the Ag(111) plane, and the S nuclei are only slightly lower, 0.224 nm. A closely related structure is obtained wherein Ag forms a triangle with a hollow site beneath the center of the triangle, and S decorates the three bridge-sites adjacent to the Ag trimer on (111)-microfacets (corresponding to B-type steps). This structure is 0.29 eV less favorable than the previous one. The difference mainly reflects stronger binding of S to (100)- rather than (111)-microfacets, i.e. stronger binding to (pseudo)fourfold sites than to (pseudo)threefold sites. Stronger binding of S at fourfold hollow-like sites has also been noted in a proposed model for the reconstruction of the S/Cu(111) system.[17]

The adsorption sites for Ag in the above discussions are all fcc sites. However, most of the results also apply if the Ag adsorption sites are hcp. In particular, two types of $Ag_3S_3$ clusters can also be formed by decorating Ag trimers with Ag atoms on hcp sites. As in the case of fcc-trimers, the one having a Ag atom beneath the center of the Ag trimer and

forming (100)-microfacets is more stable than the one having a hollow site beneath the center and forming (111)-microfacets.

We have calculated the adsorption energy for the above-mentioned $Ag_3S_3$ with supercells ranging from (3x3) to (6x6). Results are relatively insensitive to the size of the supercell. The calculation for $Ag_3S_3$ shows that the adsorption energy with a (3x3) supercell is about 0.06 eV weaker than in larger supercells, thus indicating some repulsion between the S-decorated Ag clusters. However, we caution that comparisons between results with different supercells are difficult and convergence has not yet been achieved even with a large number of *k*-points. Here we used up to bulk equivalent of 24x24x24 *k*-points. Given the experimental data indicating the presence of sulfur in some form between dots, we have also investigated some mixtures of $Ag_3S_3$ trimers and adsorbed S atoms, with total $\theta_S < 0.4$. We have not found any that are as stable as the pure cluster structures according to DFT, indicating that the S structure between row-dots is probably more complicated than simple motifs involving small supercells.

We have used DFT to simulate STM images of the $Ag_3S_3$ cluster via the Tersoff-Hamann method.[44] The predicted image, shown in the inset to Fig. 7, is a rounded triangle, with maximum dimension of 0.8 nm at the FWHM, and a height of 0.14 nm, assuming a tunneling gap of 0.4 nm. These calculated dimensions are in very good agreement with the measured values, 0.70 ± 0.06 nm and 0.13 ± 0.01 nm, respectively. This agreement lends credence to the assignment of the bright dots as $Ag_3S_3$ clusters. The height of 0.13-0.14 nm is surprisingly low, given that the ion cores in the cluster are 0.22-0.23 nm higher than those in the Ag(111) surface. This makes the agreement between calculated and measured heights especially significant. By contrast, for pure Ag islands on Ag(111), the height is 0.24 nm, and

for a $Ag_3S$ trimer discussed below, the simulated height is 0.30 nm.

General insights into other possible types of Ag-S clusters on Ag(111) can be obtained by applying a simplified analysis. First, interactions between Ag adatoms can be well described by a n.n. pair-wise attraction of about 0.2 eV. Second, compared with adsorption at the (most favorable) fcc hollow site on a flat Ag(111) surface, S binds more strongly to a step edge that is a (111)-microfacet (by 0.3 eV) and even more strongly to a step edge that is a (100)-microfacet (by 0.4 eV). The total energy of many types of clusters can be deduced from these simple rules. For example, the binding energy (defined as the energy gain relative to isolated adatoms at their most favorable adsorption site on a smooth (111) terrace) of $Ag_2S_2$ should be 0.9 eV, and that of the S-decorated trimer should be 1.8 eV. These values are close to the DFT results of 0.88 and 1.93 eV, respectively.

One other type of cluster that we have considered on Ag(111) is the planar $Ag_3S$ cluster, with a S atom in the middle of three Ag atoms. Starting from a configuration wherein S is at an fcc site, with three Ag at the three nearest hcp sites, no stable planar cluster has been found with relaxation. Instead, a stable configuration with the S atom on top of a Ag3 trimer is found. The resultant height of the cluster is predicted to be 0.30 nm in STM, which is incompatible with the experimental result of 0.13 nm. The binding energy of 0.86 eV is also unfavorable, since it is essentially the same as a bare Ag ad-trimer.

**4.2 Ordering of $Ag_3S_3$ clusters.**

Strain-induced self-organization is a much studied and proposed mechanism for nanoscale patterning (e.g. Ref. 45). Thus, it is appropriate to investigate whether strain introduces a significant driving force for self-organization of the row-dot structure in this system. According to DFT calculations, substantial local strain is induced in the Ag(111)

substrate by a $Ag_3S_3$ cluster. Again, using a (5x5) supercell, we find that the Ag atom beneath the center of the Ag trimer is depressed by about 0.01 nm, while the six Ag atoms surrounding it move outwards by about 0.009 nm. First-principles calculations however are impractical for assessing the associated longer-range strain field, which could impact ordering.

Instead, we study a simple system in which particles are coupled by Lennard-Jones (LJ) potentials with parameters chosen to reproduce the lattice constant and cohesive energy of Ag. In order to mimic the strain introduced by the adsorbed cluster, we change the $\sigma$ parameter of the six particles underneath the ad-cluster to a slightly larger value. We find a six-fold symmetry in the strain field about the $Ag_3S_3$ cluster, and also in the binding energy of LJ atoms or clusters. However, for this LJ system, the energy differences are very small—on the order of a few meV—so it is not expected that these would impact ordering.

Another mechanism for stabilization of the dot-row structure is through interactions between dots and additional S adatoms. Calculations show that a primitive $\sqrt{3}$ structure of chemisorbed S, with $\theta_S = 1/3$, has only small energy penalty (within 30 meV) in chemisorption energy compared with isolated S adatoms. This could lead to arrangements such as that shown in Fig. 8e, an arrangement of four S adatoms plus a $Ag_3S_3$ complex in a (5x5) supercell. However, this does not have a $\sqrt{3}$ lattice that is as quite as extensive as the one seen in experiment (Fig. 3b-c). We speculate that a more extended arrangement with wider separation of rows could lead to stabilization of the dot-rows, but at present we do not have the capability to perform calculations on much larger supercells.

**4.3 Stabilities of possible structures.**

As shown by the present experiments and those reported in the literature, there are a

wide variety of structures observed with different temperature and coverage conditions. Here we explore other possible structures using DFT.

In order to compare relative stabilities of various Ag-S complexes with different compositions, we calculate the chemical potential of a sulfur atom in a $Ag_mS_n$ complex as

$$\mu_S=[E_{ad}(Ag_mS_n, L)-E_0(L)-m\mu_{Ag}]/n,$$

where $E_{ad}(Ag_mS_n, L)$ is the total energy of a system of $L$ layers of Ag(111) slabs with a $Ag_mS_n$ adsorbate complex, and $E_0(L)$ is the energy of the clean Ag substrate. We assume there is an efficient exchange of Ag adatoms with a reservoir so that $\mu_{Ag}$, the chemical potential of a Ag adatom, is constant and can be calculated as $\mu_{Ag}=[E_0(L)- E_0(L\text{-}1)]/N$, where $N$ is the number of atoms in each layer.

Figure 8 shows some of the structures considered, and Fig. 9 shows $\mu_S$ vs. $\theta_S$ for various structures from DFT. In Fig. 9, there are three main families of structures. Structures with S adatoms occupying fcc sites of unreconstructed Ag(111) substrates (denoted by pluses) have the highest $\mu_S$ and are therefore least stable. In the middle, denoted by asterisks, are $Ag_3S_3$ clusters like those shown in Fig. 7, with no additional adsorbed S atoms. The most stable type of structure involves Ag-Ag chains. The energy differences are around 50 meV per S atom between different families, and within each family $\mu_S$ increases slightly with increasing S coverage.

The Ag-Ag chain structures deserve further comment. The most stable chain is a single row of Ag atoms with S decorating both sides, but at alternating positions (see Fig. 8c). A less-stable variation of this is a double Ag chain, with S decorating both sides of the islands, and also residing on top of islands in (pseudo)fourfold hollow sites (Fig. 8d). These

chains resemble aspects of models proposed for S on Cu(111),[24,31] where the driving force was postulated to be the favorable adsorption of S at fourfold hollow-like sites atop the Cu reconstruction. The importance of the fourfold hollow site has been noted already in Section 4.1 for the $Ag_3S_3$ clusters, where S is located at (100)-type microfacets.

We also investigated two different ($\sqrt{7}$ x $\sqrt{7}$)R19$^o$ structures, denoted $\sqrt{7}$-a and $\sqrt{7}$-b in Fig. 9. The first, $\sqrt{7}$-a (Fig. 8a), is obtained by relaxation from an initial structure that is an overlay of a single layer of an fcc-bulk $Ag_2S$(111)-like structure atop the Ag(111) surface. The initial structure is one of two proposed for S on Ag(111) at room temperature by Yu et al.[23] (cf. their Fig. 2). It has 3 S atoms in a ($\sqrt{7}$ x $\sqrt{7}$)R19$^o$ supercell (corresponding to $\theta_S$ = 3/7 = 0.43), one occupying the top site, and two occupying hollow sites. Our second structure, $\sqrt{7}$-b (Fig. 8b), is a variation of the $Ag_3S_3$ cluster structure. It has a slightly lower energy according to DFT than the $Ag_2S$-like $\sqrt{7}$-a structure. It can be seen that the two $\sqrt{7}$ structures are related by atomic displacements.

Finally, we considered the possibility of molecular $S_2$ structures on the unreconstructed Ag(111) substrate, following the work by Rodriguez et al which suggested that this adsorbate may be present on Au(111) at room temperature.[32] Using a (2×2) supercell we find that $S_2$ is more stable than 2 S adatoms occupying n.n. fcc sites. The bond length is 0.21 nm with S atoms residing close to adjacent fcc and hcp sites. However, $\mu_S$ is around -4.3 eV, much higher than the cluster- or adatom-based structures shown in Fig. 9. Therefore molecular $S_2$ is unlikely to be significant for equilibrated structures, at least in the range of coverages investigated here ($\theta_S < 0.4$). It is still possible, however, for adsorbed $S_2$ to be present in a metastable state at low temperature. This may be the origin of the irregular islands that form directly upon adsorption at 135 K, as in Fig. 4a, since they are obviously

metastable. (They transform irreversibly into the dot-rows upon heating).

**5. Discussion**

The dot-row motif is the dominant feature of the present study. It is remarkably robust, prevailing over a wide range of coverage (0.03 to 0.5 ML), and a variety of inter-row milieus. It is characterized by a spacing of 1.6 ± 0.1 nm between dots. To our knowledge it is quite different than anything reported previously for S on Group IB metals (with one possible exception noted below.)

The dots are probably $Ag_3S_3$ clusters. This assignment is supported by several factors. First, the DFT calculations show these clusters to be among the most favorable adsorbed species. Second, there is good agreement between the calculated and observed dimensions of the dots in STM. The agreement between the heights is particularly important, given that this quantity is unusually low. Third is the observation of pitting which shows that formation of the dot-row structure at 200K consumes Ag. The assignment is also reasonable by analogy with Cu(111), where a mobile $Cu_3S_3$ species at 300 K was suggested both from theory and experiment. Our data suggest that isolated dots are quite mobile on Ag(111) even at 200 K, and are sometimes "caught" in STM images between hops (e.g. Fig. 2a'), which reinforces their assignment as $Ag_3S_3$.

However, the dots account for only 20-30% of the total S coverage at 200 K. The majority of S exists outside of the dots, but evidence for its existence is also observable with STM. Some of it is in a disordered form on terraces at low coverage, i.e. in the large gaps between domains. Evidence for this disordered S can be seen in STM images at very low coverage, as in Fig. 2a. Some of it also exists between dots within domains of dot-rows, where it produces at least three discernible signatures in STM images (cf. Fig. 3). One of

those three corresponds to a √3 structure. This simple structure has not been reported previously for S adsorbed on Ag(111) in UHV, although it forms in an electrochemical cell[45] and it is adopted by S on close-packed planes of several other transition metals in UHV.[46] It is possible that this and the other (unidentified) structures help stabilize the linear alignment of the $Ag_3S_3$ clusters, as suggested by Fig. 8e. We estimate that strain fields alone are not large enough to produce this effect.

DFT indicates that a variety of structures are energetically close—within a span of about 100 meV per S atom at a given coverage—based upon their chemical potentials as defined in Section 4.3. Of these, each may prevail in a different temperature range due to entropic contributions. The most reasonable candidate for the equilibrium phase we call elongated islands, which is stable at 135 K and $\theta_S = 0.09$, is a structure involving single or double Ag-Ag chains, based on the compact but anisotropic shape of the islands. Furthermore, DFT shows that the chains lie parallel to the close-packed rows, consistent with the orientations of the elongated islands.

About 50 meV less favorable is the family of $Ag_3S_3$ trimer structures, which we postulate can account for the dot-rows that prevail at 200 K (at all but the lowest coverage, $\theta_S < 0.03$). The dot-rows must be stabilized by net attractive interactions, based upon their existence at very low coverage (Fig. 5). Furthermore, these interactions must encompass attractions between rows, given their aggregation into domains at very low coverages as shown in Fig. 2a.

At 300 K, the √7 is a well-known phase, for which a $Ag_2S$-like model has been proposed.[23] However, an alternative model (√7-b in Fig. 9) can be built from $Ag_3S_3$ trimers and it is slightly more stable than the relaxed $Ag_2S$-like structure (√7-a in Fig. 9). The √7-a

and √7-b structures have identical Ag-S stoichiometries and are related by small atomic displacements, so they can be considered variants of one another. The $Ag_3S_3$ trimer-based structure should be considered as a candidate for the room-temperature √7 phase. Indeed, if one examines the STM images of Yu et al., one sees that the √7 consists of dot-like features under certain tunneling conditions (Fig. 6 of Ref. 23).

Finally, $S_2$ is not energetically viable, relative to the cluster-based structures, at least for $\theta_S < 0.4$. We postulate that it is observed, however, in the metastable irregularly-shaped islands that follow adsorption directly at 135 K (0.09 ML, Fig. 4a).

There is a wealth of dynamics exhibited by this system at 200 K. During adsorption, dot-rows form and align on a time scale comparable with imaging. Rearrangements, both local and long-range, continue after equilibration. In the latter case, large domains of dot-rows flip orientation, seemingly at random. Other authors have inferred the existence of mobile S-metal complexes on Ag, Au, and Cu surfaces.[17,18,23,27,29,30,32] In our case, we assert that we are directly imaging those mobile species in the form of $Ag_3S_3$ clusters. A temperature of 200 K is particularly advantageous for observing these species in a semi-static state and also for observing some dynamics on a time scale compatible with typical STM imaging.

**Conclusions.**

At 200 K, adsorbed S self-organizes into a distinctive dot-row structure and into other forms of adsorbed S. The dot-row structure exists over a coverage range that spans an order of magnitude (0.03 to 0.5 ML). A strong case, based partly on energy calculations and the height of the dots in STM, can be made for assigning the dots as $Ag_3S_3$ clusters in a matrix of adsorbed S. The dot-row structure undergoes two reversible transitions, one of which may be transformation to a Ag-Ag chain structure. Dynamics of ordering during adsorption, and

equilibrium fluctuations, can be observed. DFT lends insight into the viability of other structures in this rich system, including a new candidate for the well-known ($\sqrt{7}$ x $\sqrt{7}$)R19$^o$ phase.

**Acknowledgments.**

This work was supported primarily by NSF Grant CHE-0414378. DJL was supported by the Division of Chemical Sciences, Basic Energy Sciences, US Department of Energy (USDOE). The work was performed at the Ames Laboratory which is operated for the USDOE by Iowa State University under Contract No. DE-AC02-07CH11358.

**References**

(1) Verykios, X. E.; Stein, F. P.; Coughlin, R. W. *Catalysis Rev.* **1980**, *22*, 197.

(2) Sajkowski, D. J.; Boudart, M. *Catal. Rev.* **1987**, *29*, 325.

(3) van Santen, R. A.; Kuipers, H. *Adv. Catal.* **1987**, *35*, 265.

(4) Serafin, J. G.; Liu, A. C.; Seyedmonir, S. R. *J. Mol. Cat. A: Chemical* **1998**, *131*, 157.

(5) Schreiber, F. *J. Phys.: Cond. Matter* **2004**, *16*, R881.

(6) Ulman, A. *Self-Assembled Monolayers of Thiols (Thin Films)*; Academic Press: New York, 1998.

(7) Dimitrakopoulos, C. D.; Mascaro, D. J. *IBM J. Res. Dev.* **2001**.

(8) Tansel, T.; Magnussen, O. M. *Phys. Rev. Lett.* **2006**, *96*, 026101.

(9) Perdereau, J.; Rhead, G. E. *Surf. Sci* **1967**, *7*, 175.

(10) Ozcomert, J. S.; Pai, W. W.; Bartelt, N. C.; Reutt-Robey, J. E. *Phys. Rev. Lett.* **1994**, *72*, 258.

(11) Layson, A. R.; Thiel, P. A. *Surf. Sci.* **2001**, *472*, L151.

(12) Layson, A. R.; Evans, J. W.; P.A.Thiel. *Phys. Rev. B* **2002**, *65*, 193409 (4 pages).

(13) Layson, A. R.; Evans, J. W.; Thiel, P. A. *J. Chem. Phys.* **2003**, *118*, 6467.

(14) Edinger, K.; Gölzhäuser, A.; Demota, K.; Wöll, C.; Grunze, M. *Langmuir* **1993**, *90*, 4.

(15) McCarley, R. L.; Dunaway, D. J.; Willicut, R. J. *Langmuir* **1993**, *9*, 2775.

(16) Stranick, S. J.; Parikh, A. N.; Allara, D. L.; Weiss, P. S. *J. Phys. Chem.* **1994**, *98*, 11136.

(17) Feibelman, P. J. *Phys. Rev. Lett.* **2000**, *85*, 606.

(18) Ling, W. L.; Bartelt, N. C.; Pohl, K.; de la Figuera, J.; Hwang, R. Q.; McCarty, K. F. *Phys. Rev. Lett.* **2004**, *93*, 166101.

(19) Ruckenstein, E.; Lee, S. H. *J. Catal.* **1988**, *109*, 100.

(20) Wodiunig, S.; Keel, J. M.; Wilson, T. S. E.; Zemichael, F. W.; Lambert, R. M. *Cat. Lett.* **2003**, *87*, 1.

(21) Schwaha, K.; Spencer, N. D.; Lambert, R. M. *Surf. Sci* **1979**, *81*, 273.

(22) Rovida, G.; Pratesi, F. *Surf. Sci* **1981**, *104*, 609.

(23) Yu, M.; Woodruff, D. P.; Satterley, C. J.; Jones, R. G.; Dhanak, V. R. *J. Phys. Chem.* **2007**, *111*, 3152.

(24) Driver, S. M.; Woodruff, D. P. *Surf. Sci* **1997**, *497*, 1.

(25) Wahlström, E.; Ekvall, I.; Olin, H.; Lindgren, S. A.; Wallden, L. *Phys. Rev. B* **1999**, *60*, 10699.

(26) Wahlström, E.; Ekvall, I.; Kihlgren, T.; Olin, H.; Lindgren, S. A.; Wallden, L. *Phys. Rev. B* **2001**, *64*, 155406.

(27) Min, B. K.; Alemozafar, A. R.; Biener, M. M.; Biener, J.; Friend, C. M. *Topics in Catalysis* **2005**, *36*, 77.

(28) Biener, M. M.; Biener, J.; Friend, C. M. *Langmuir* **2005**, *21*, 1668.

(29) Friend, C. M. *J. Phys. Chem.* **2006**, *110*, 15663.

(30) Biener, M. M.; Biener, J.; Friend, C. M. *Surf. Sci* **2007**, *601*, 1659.

(31) Foss, M.; Feidenhans'l, R.; Nielsen, M.; Findeisen, E.; Buslaps, T.; Johnson, R. L.; Besenbacher, F. *Surf. Sci.* **1997**, *388*, 5.

(32) Rodriguez, J. A.; Dvorak, J.; Jirsak, T.; Liu, G.; Hrbek, J.; Aray, Y.; Gonzalez, C. *J. Am. Chem. Soc.* **2003**, *125*, 276.

(33) Single crystals were synthesized at the Materials Preparation Center, Ames Laboratory USDOE, Ames, IA, USA. See: www.mpc.ameslab.gov.

(34) Wagner, C. *J. Chem. Phys.* **1953**, *21*, 1819.

(35) Chen, C. J. *Introduction to Scanning Tunneling Microscopy*; Oxford University Press: New York/Oxford, 1993.

(36) Kresse, G.; Hafner, J. *Phys. Rev. B* **1993**, *47*, 558.

(37) Kresse, G.; Hafner, J. *Phys. Rev. B* **1994**, *49*, 14251.

(38) Kresse, G.; Furthmuller, J. *Phys. Rev. B* **1996**, *54*, 11169.

(39) Perdew, J. P.; Burke, K.; Ernzerhof, M. *Phys. Rev. Lett.* **1996**, *77*, 3865.

(40) Kresse, G.; Joubert, J. *Phys. Rev. B* **1999**, *59*, 1758.

(41) Methfessel, M.; Paxton, A. T. *Phys. Rev. B* **1989**, *40*, 3616.

(42) Monkhorst, H. J.; Pack, J. D. *Phys. Rev. B* **1976**, *13*, 5188.

(43) Alfonso, D. R.; Cugini, A. V.; Sholl, D. S. *Surf. Sci* **2003**, *546*, 12.

(44) Tersoff, J.; Hamann, D. R. *Phys. Rev. B* **1985**, *32*, 805.

(45) Aloisi, G. D.; Cavallini, M.; Innocenti, M.; Foresti, M. L.; Pezzatini, G.; Guidelli, R. *J. Phys. Chem.* **1997**, *101*, 4774.

(46) Somorjai, G. A. *Introduction to Surface Chemistry and Catalysis*; John Wiley and Sons: New York, 1994.

**Figure Captions.**

**Figure 1.** STM images of Ag(111) after S adsorption at 200 K, showing the major effects of S adsorption. (a) Clean surface, 60 x 60 $nm^2$. Inset is 1.5 x 1.5 $nm^2$. (b) $\theta_S = 0.007$, 60 x 60 $nm^2$. (c) $\theta_S = 0.02$, 40 x 40 $nm^2$. Inset is 8 x 8 $nm^2$, and shows dots decorating a step edge. (d) $\theta_S = 0.1$, 60 x 60 $nm^2$. (e) $\theta_S = 0.4$, 50 x 50 $nm^2$.

**Figure 2.** STM images of Ag(111) after S adsorption at 200 K, showing the evolution of dot-rows and pits with increasing coverage. In the left column (a-c), each image is 100 x 100 $nm^2$, and in the right column (a'-c') each is 25 x 25 $nm^2$. Values of $\theta_S$ are (a,a') 0.03; (b,b') 0.1; (c,c') 0.3.

**Figure 3.** STM images of Ag(111) after S adsorption at 200 K, showing ordered structures between some dot-rows. (a) 30 x 30 $nm^2$ image at $\theta_S = 0.1$. Arrows point to an unidentified substructure found between rows separated by 2.1-2.2 nm. (b, c) 6 x 6 $nm^2$ images showing the $\sqrt{3}$ substructure. (d) 10 x 10 $nm^2$ image at $\theta_S = 0.4$. Arrow points to a depression that distinguishes this unidentified substructure.

**Figure 4.** STM images of Ag(111) at $\theta_S = 0.09$, showing the effect of heating and cooling to various temperatures. (a) After adsorption at 135 K, 120 x 120 $nm^2$; (b) after heating to 200 K, 60 x 60 $nm^2$; (c) after cooling back to 135 K, 120 x 120 $nm^2$; (d) after heating to 300 K, 120 x 120 $nm^2$; and (e) after cooling back to 200 K, 60 x 60 $nm^2$.

**Figure 5.** Temperature-coverage diagram illustrating the three main types of structure observed with STM in this study. The triangle represents the elongated-island

phase; squares are dot-rows; and diamonds mean no dot-row structure is observed with STM.

**Figure 6.** STM images of Ag(111), showing temporal changes in dot-row domains at 200 K, in two different experiments. In (a) and (b), image size is 30 x 30 $nm^2$ and acquisition time is 35 s/image. $\theta_S$ changes from 0.083 to 0.088 during imaging in (a), then $S_2$ exposure stops and ten minutes elapse before image (b) is acquired. In (c-e), image size is 60 x 60 $nm^2$, acquisition time is 200 s/image, and $\theta_S = 0.09$. There is no time lapse between images.

**Figure 7.** $Ag_3S_3$ cluster configuration from DFT calculations. Results are obtained using a 5x5 supercell denoted by the dashed line. Inset shows the STM image simulated from the DFT charge density as described in the text.

**Figure 8.** (a) √7-a structure. (b) √7-b structure. (c) Ag-S single-chain structure. (d) Ag-S double-chain structure. (e) $Ag_3S_3 + 4S$ structure.

**Figure 9.** Sulfur chemical potential, $\mu_S$, vs. $\theta_S$ for different structures obtained from DFT. A family of unreconstructed S adatom structures is shown by plus signs, a group of $Ag_3S_3$ clusters without additional S is shown by asterisks, and a set of single-chain Ag-S structures is shown by diamonds. Also shown and labeled are some other structures mentioned in the text.

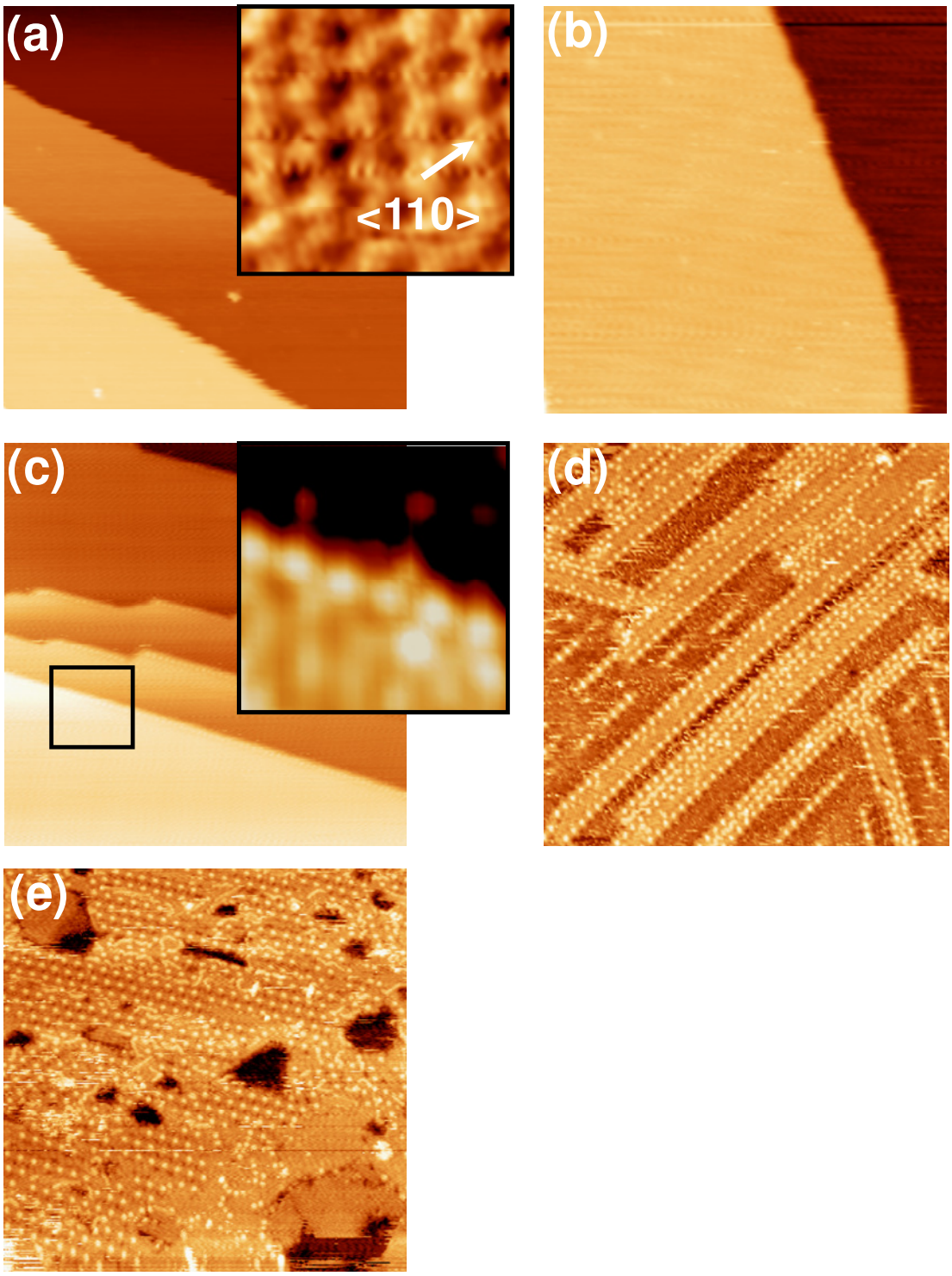


Figure 1

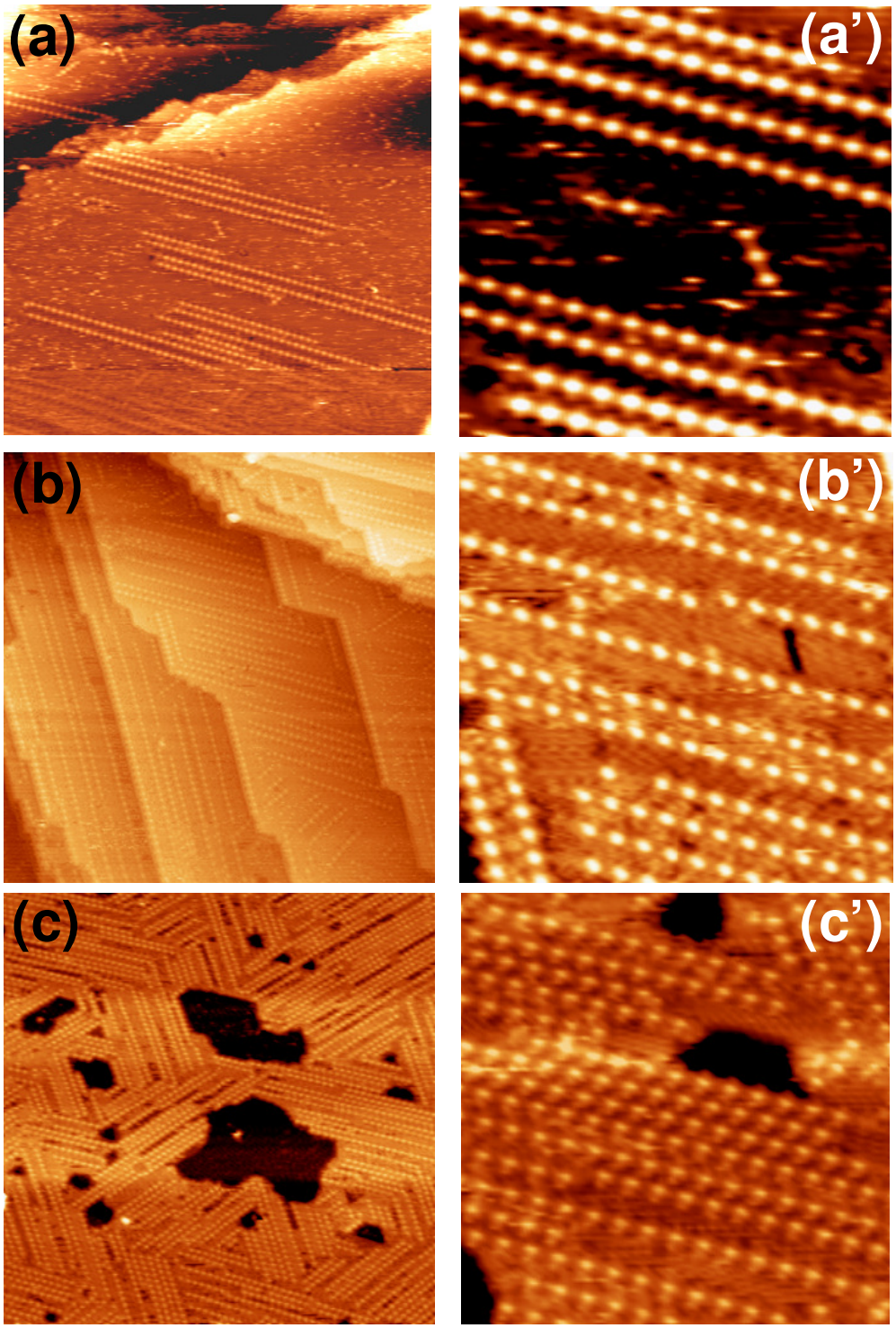


Figure 2

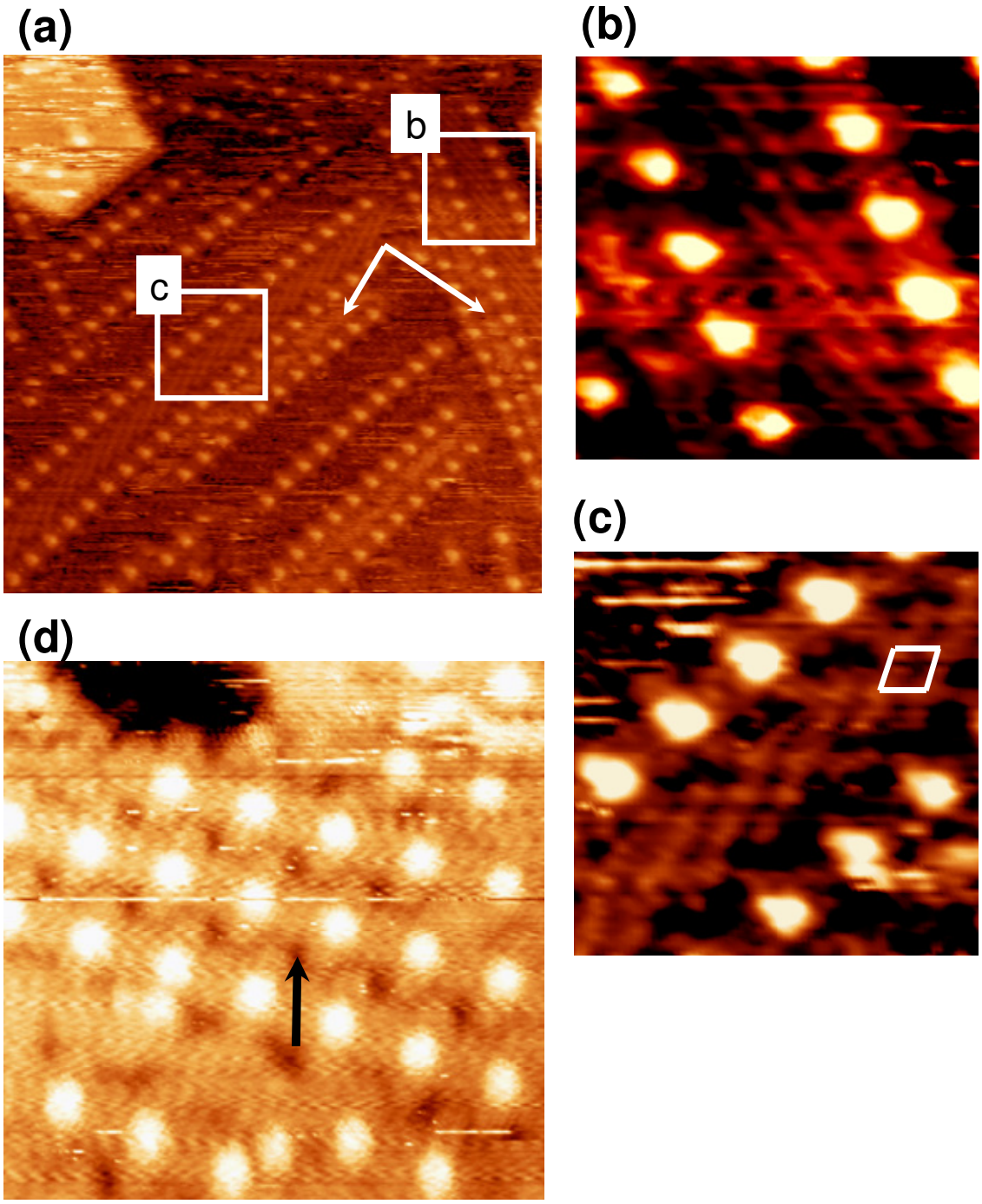


Figure 3

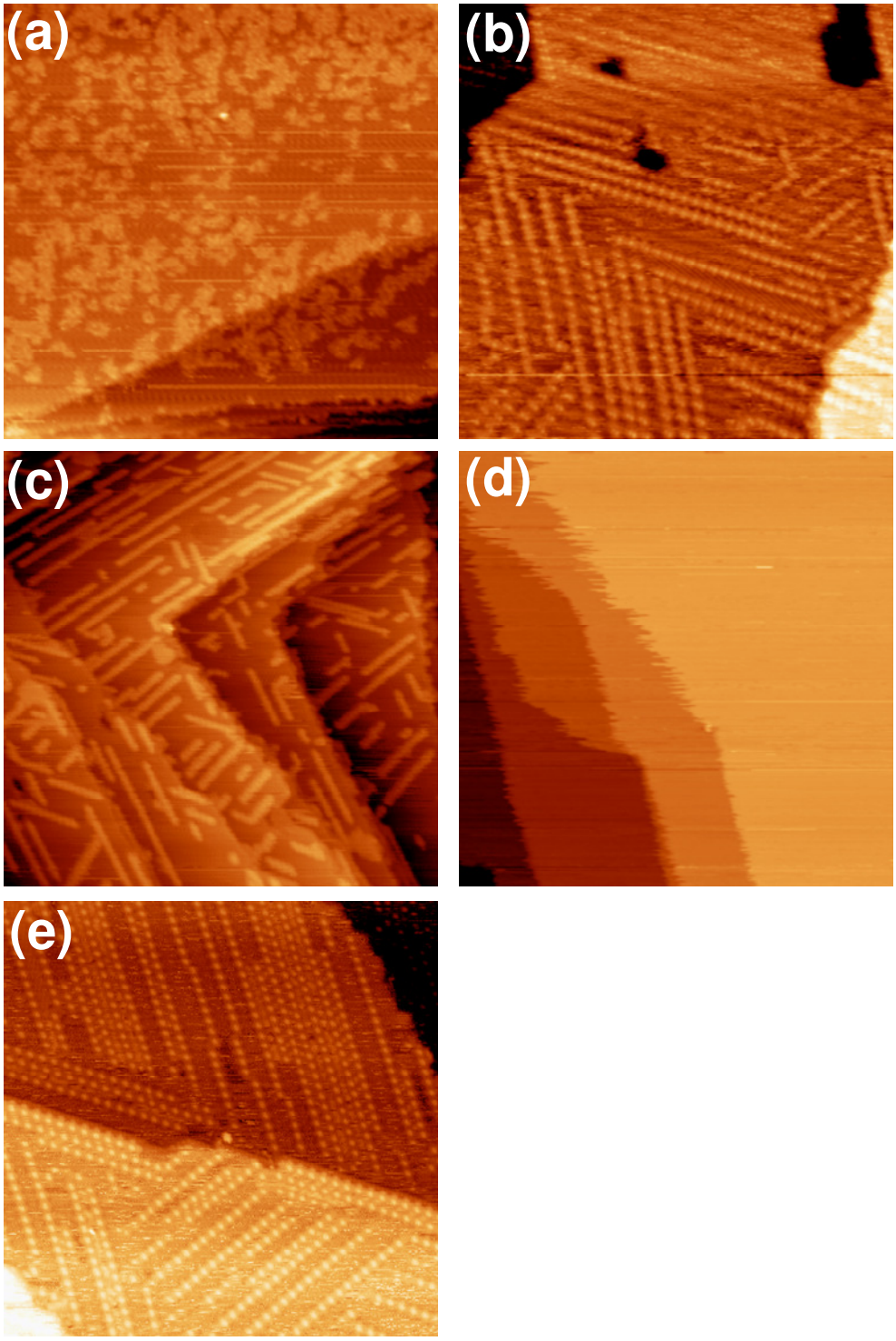


Figure 4

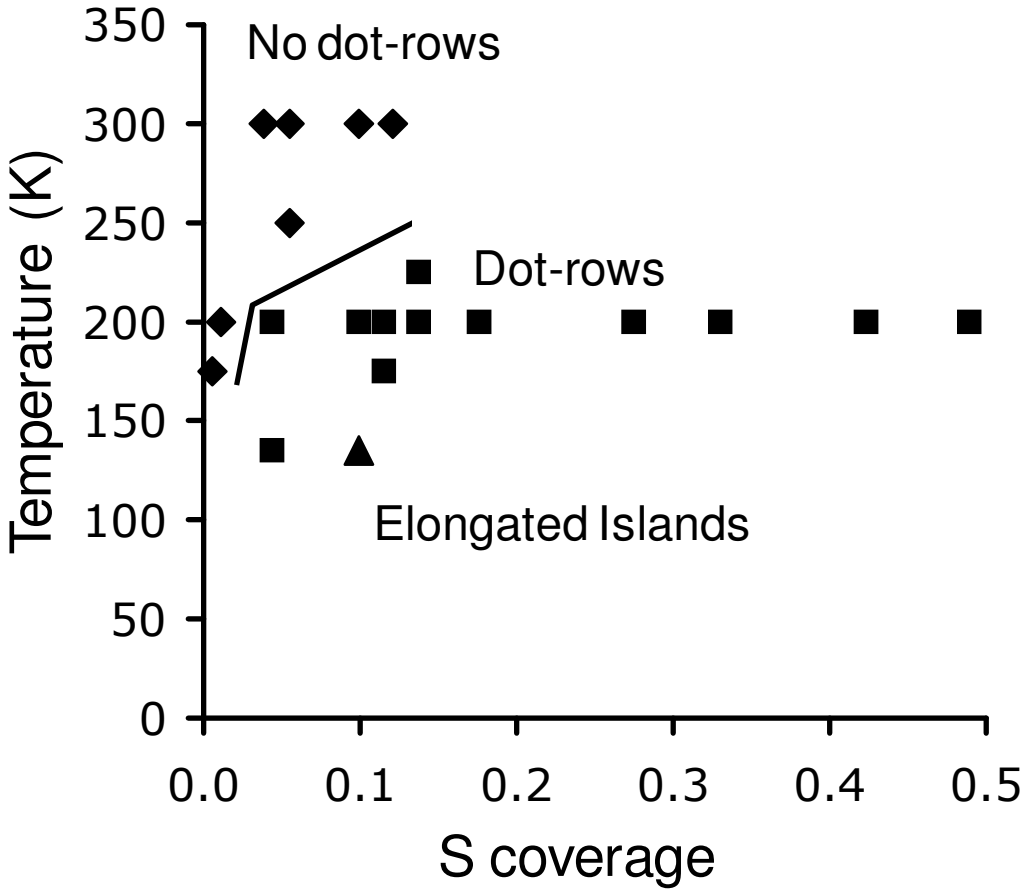


Figure 5

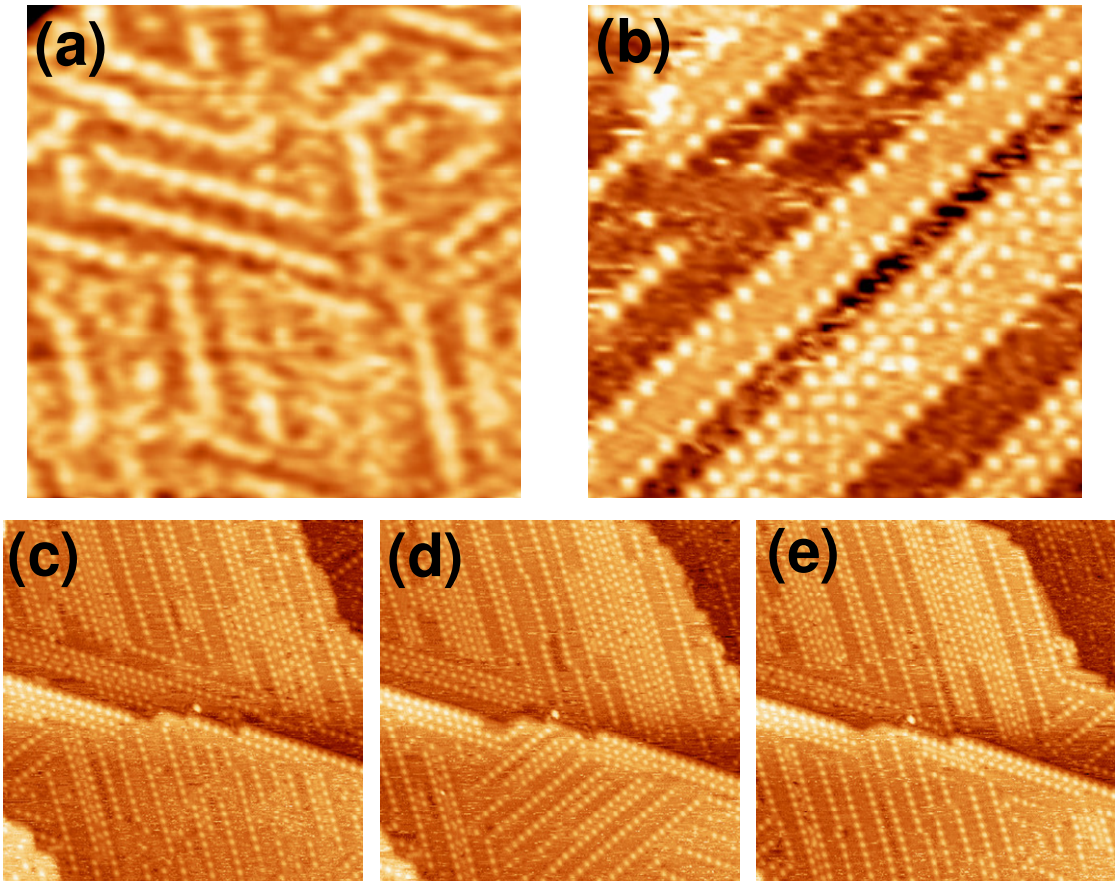


Figure 6

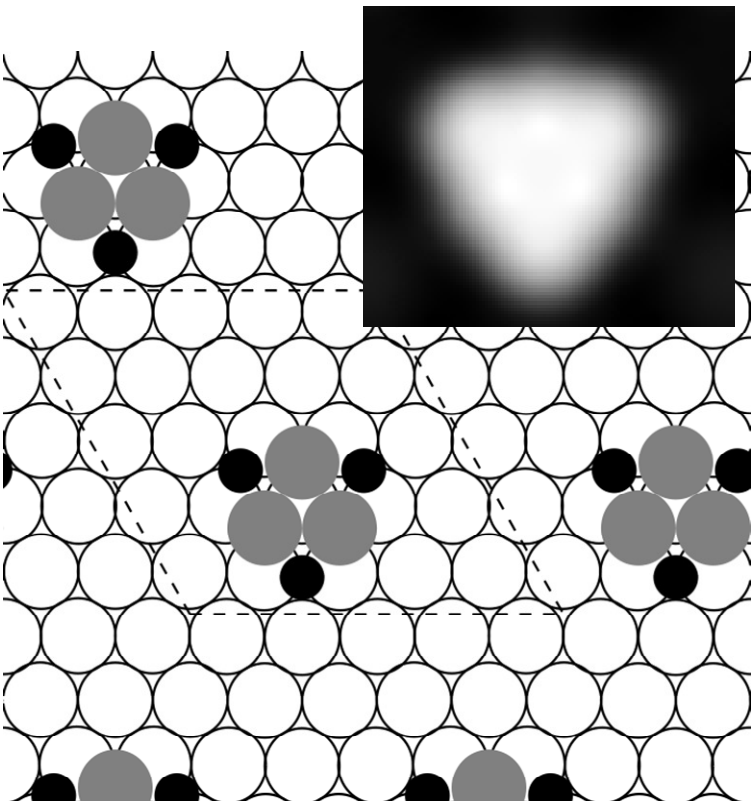

Figure 7

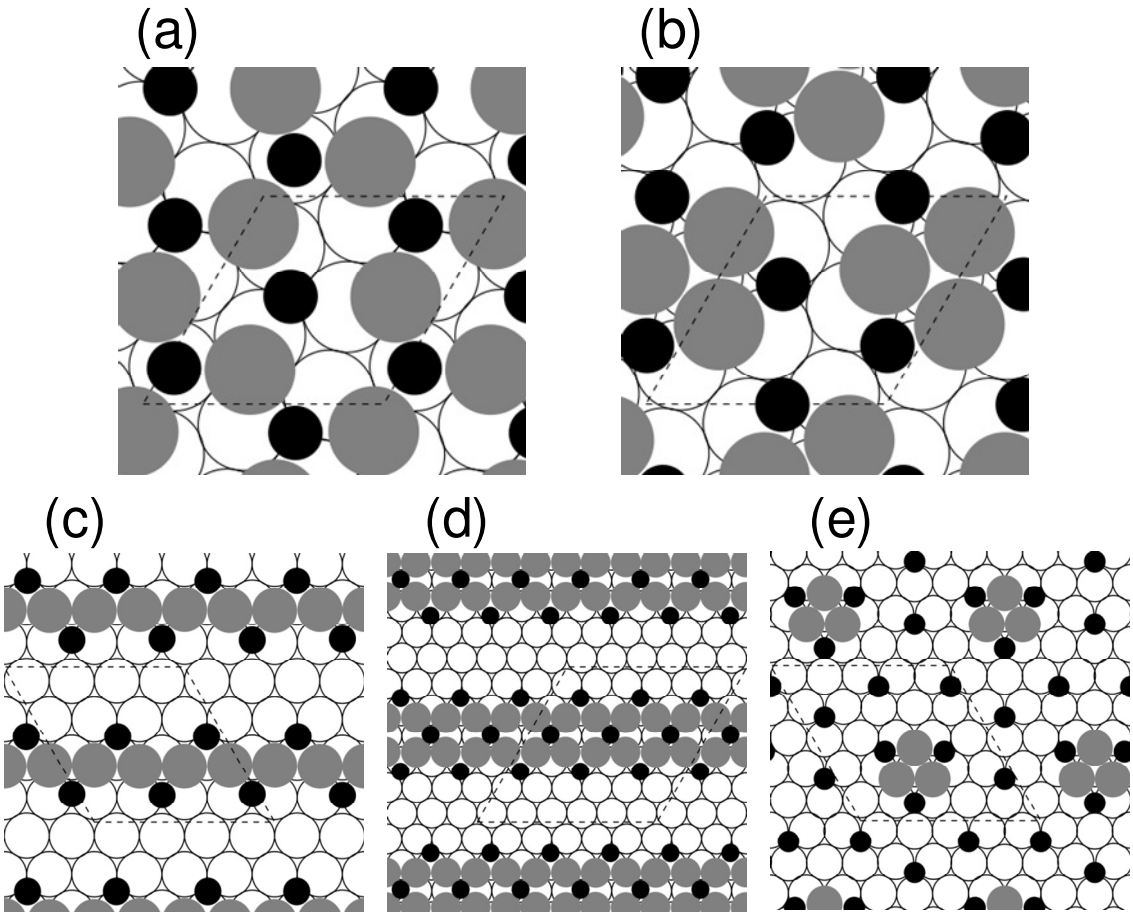


Figure 8

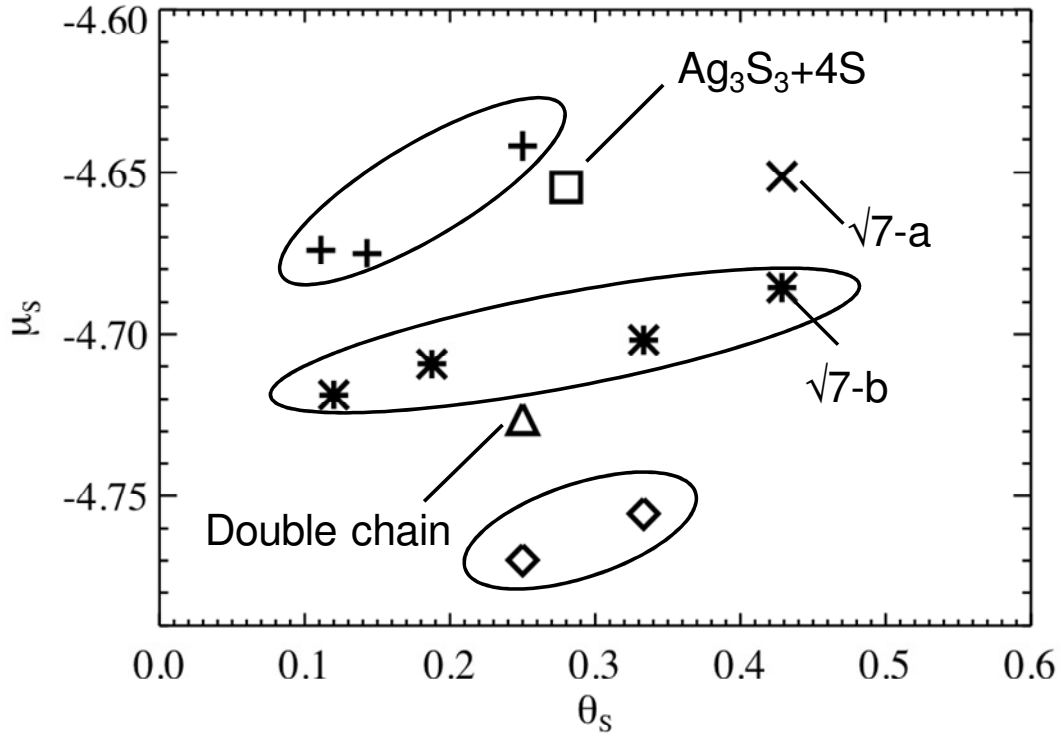


Figure 9

**Appendix**

Data presented in this chapter thus far, have shown the structure of S on Ag(111) with S coverage lower than 0.4 ML at 200 K. Here we present additional data for S on Ag(111) with higher S coverage, and some *in situ* S deposition data.

1. S on Ag(111) at $\theta_S$ = 0.46 ML, 300 K

After S deposition at 300 K to a S coverage of 0.46 ML, two different types of structures form on the surface. The first is based upon pairs of dots. The most common manifestation at this coverage is a rope-like structure with three different orientations, lying parallel to the three different orientations of the "dot-row" structure, corresponding to the close packed <110> crystallographic directions. This is shown in Fig. A1a. Fig. A1a' is an image of the rope-like structure at higher magnification. It reveals that the structure is actually formed by pairs of dots. Within each pair, the separation of the two dots (A) is A ≈ 0.79 ± 0.04 nm. The separation between pairs (B) is B ≈ 1.27 ± 0.07 nm. The separation between the "ropes" (C) is C ≈ 2.02 ± 0.10 nm. A schematic diagram is shown in Fig. A1a". In other areas, pair fragments are seen on the surface as shown in Fig. A1b. Here, note that the dot separation is very close to the √7 structure lattice constant, 0.76 nm.

The distances in these structures, and in the dot-row structures, are compared in Table A.

The other structure that forms on this surface (visible in parts of Fig. A1a) is a dense structure which exists close to step edges. Fig. A1c shows such a region near a step edge at high magnification. This reveals a hexagonally close-packed arrangement of dots. From STM, the lattice constant of this dense structure is 0.78 ±0.04 nm, and the unit cell makes an angle of ~ 19 ° with the close packed <110> crystallographic direction. So the structure is

very similar to the one identified by Yu et al[1] as Ag(111)(√7x√7)R19º-S, with an ideal coverage of 0.43 ML. Here we don't see the √7 structure cover the whole surface even though the S coverage is higher than the ideal coverage, and this is consistent with Yu's report that rather modest increase in S coverage above the √7 ideal coverage to ~ 0.5 ML were needed to form a surface dominated by the √7 structure. We must note that this close-packet √7 structure is significantly different from the close-packet dot-row structure shown in Fig. 1e of Ch. 2. This √7 structure has a lattice constant of ~ 0.78 nm, and the close-packet dot-row structure has a one-dimensional lattice constant of about 1.6 nm.

2. Temperature-dependence of S structures at $\theta_S$ = 0.51 ML: 132, 200, and 300 K

Fig. A2 illustrates the temperature-dependence of the S structures on Ag(111) at $\theta_S$ = 0.51 ML. After S deposition at 132 K, layers of irregularly-shaped islands exist both on the terrace and at the step edge, as shown in Fig. A2a. After being heated to 200 K, the surface morphology changes to an etched pit structure (Fig. A2b). The higher magnification image in Fig. A2b' gives a closer view of the surface structure and one can see a close-packed arrangement of dots, similar to that in Fig. A1c, in the bottom of the pits, and an ill-defined structure on top. In the close-packed arrangement, we find that the alignment of the dots is again at an angle of ~ 19 º to the close packed <110> crystallographic direction. The separation between dots is constant at 0.78 ± 0.07 nm ($n_{dot\text{-}pairs}$ > 120). This is very close to the lattice constant of the √7 structure, and henceforth we name this as the √7.

When the same surface is cooled back to 132 K and heated again to 200 K, as shown in Fig. A2c and A2d, the same structure is obtained as after the first heating to 200 K in Fig. A2b. Thus, the cooling-heating process does not destroy the structure.

Fig. A2e shows the surface with $\theta_S$ = 0.51 ML after heating from 200 to 300 K, and imaged at 300 K. Here, the surface has different domains of the √7 structure, as also seen by Yu and co-workers.[1] No pits are seen on the surface. The ill-defined structure at the top of the pits has also disappeared. Cooling the same surface back again to 200 K gives the same structure as at 300 K, with "fragments" of different domains, as seen in Fig. A2f. All of the heating-cooling experiments together indicate that the √7 dot structure is the equilibrium phase at 200-300 K, at this coverage. Starting from adsorption of $S_2$ at 130 K, the surface is partially converted to the √7 structure at 200 K, and fully converted at 300 K.

Fig. A2g shows the √7 dot structure at higher magnification. Some parts of the image may have become somewhat distorted due to the heating and cooling process. The diameter of individual dots, based on their full-width at half-maximum, is 0.52 ± 0.06 nm ($n_{dots}$ >130). This is much smaller than the dot size of ~ 0.70 nm in the dot-row structure that forms at 200 K and at lower S coverage, which has been discussed in the main part of this chapter. The dot height here has a large variation, from 0.03 to 0.08 nm, with an average of 0.053 ±0.02 nm (n > 130) relative to the surrounding lower regions.

It must be noted that the √7 structure we observed in these STM data is consistent with the structure we proposed in Fig. 8b, wherein the √7 consists of a simple unit cell with a $Ag_3S_3$ cluster at each corner.

3. In situ STM with final $\theta_S$ = 0.11 ML, 200 K

Fig. A3 shows a series of STM images taken continuously during S deposition at 200 K, and immediately after, on a time scale of 120 s/image. The clean Ag(111) surface right before S deposition is shown here in Fig. A3a, and the inset gives the higher magnification view of the step edge. Assuming S flux is constant, the sulfur coverages of the images in Fig.

A3b, c, d, and e are 0.00 to 0.027, 0.027 to 0.055, 0.055 to 0.082, and 0.082 to 0.11, respectively. The different surface features here are similar to the one shown in Figure 1. No obvious difference is detected with low S coverage (< 0.02 ML, see Fig. A3b), and then the step edge facets when the S coverage increases above 0.03 ML (Fig. A3c). With further S deposition, dots appear on the Ag(111) terraces and are arranged in short linear rows (Fig. A3d). The surface structure also changes on the time scale of experimental observation. Fig. A3e is an image taken toward the end of adsorption, where the final coverage is $\theta_S = 0.11$, and Fig. A3f is an image taken 10 minutes later. Clearly, the dot-rows form much smaller domains during adsorption than after adsorption stops, indicating that considerable domain growth takes place in a period of a few minutes.

References to the Appendix.

(1) Yu, M.; Woodruff, D. P.; Satterley, C. J.; Jones, R. G.; Dhanak, V. R. *Journal of Physical Chemistry C* **2007**, *111*, 3152.

Table A: Comparison of different structures on Ag(111) surface

| Structure | Dot separation | Row separation | Dot size (FWHM) | Dot height | Number analyzed |
|---|---|---|---|---|---|
| Rope-like | A ≈ 0.79 ± 0.04 nm | C ≈ 2.02 ± 0.10 nm | 0.55 ± 0.10 nm | 0.06 ± 0.02 nm | > 30 |
| | B ≈ 1.27 ± 0.07 nm | | | | > 30 |
| Dot-row | 1.60 ± 0.10 nm | 1.1 to 3.4 nm | 0.70 ± 0.06 nm | 0.13 ± 0.01 nm | > 100 |
| √7 | 0.78 ± 0.07 nm | | 0.52 ± 0.06 nm | 0.053 ± 0.02 nm | > 130 |

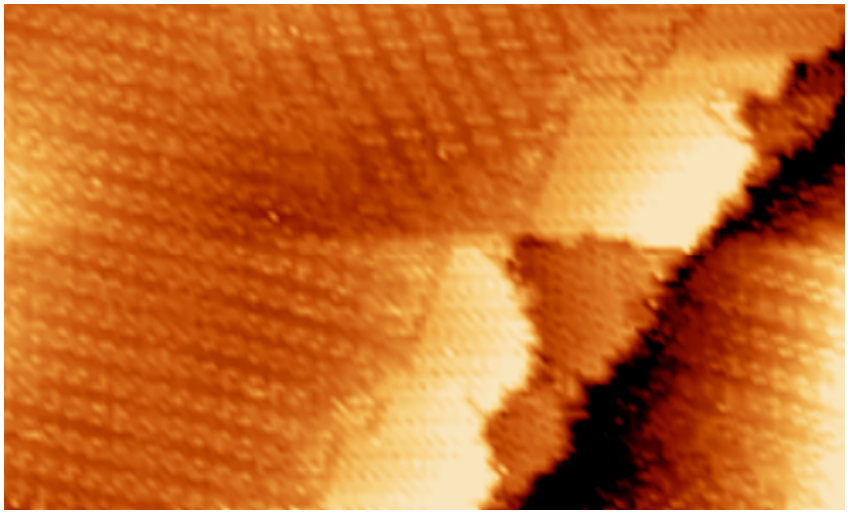

Fig. A1a. 12-11-2006, # 31, 50 nm x 30 nm, 0.46 ML S

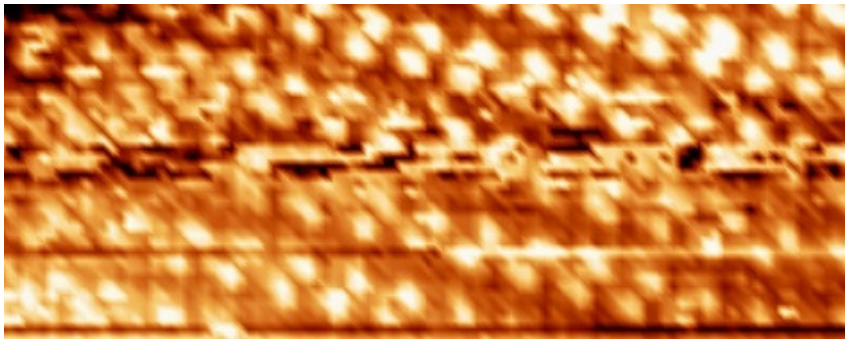

Fig. A1a'. 12-11-2006, # 45, 20 nm x 8 nm, 0.46 ML S

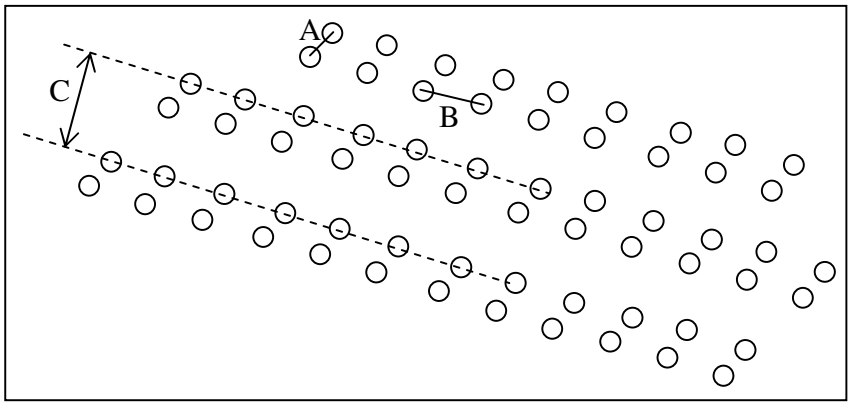


Fig. A1a''. Schematic diagram of the rope-like structure

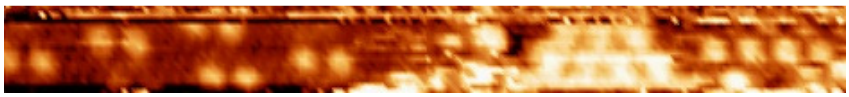

Fig. A1b. 12-11-2006, # 48, 20 nm x 1.8 nm, 0.46 ML S

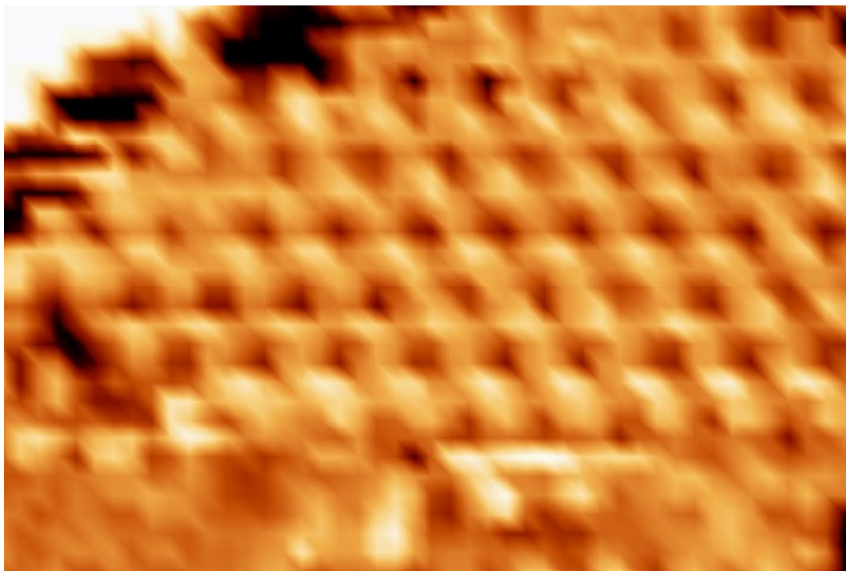

Fig. A1c. 12-11-2006, # 45, 9.2 nm x 6.2 nm, 0.46 ML S

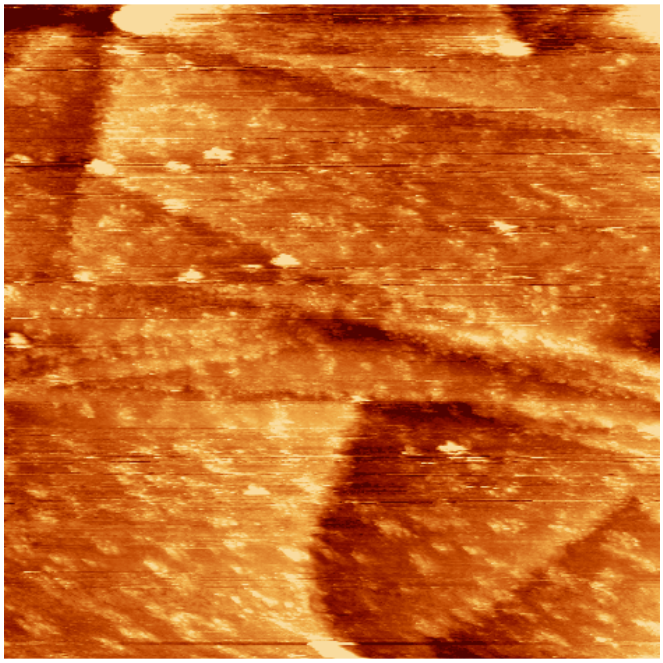

Fig. A2a. 04-24-2008, # 17, 200 nm x 200 nm, 132 K, 0.515 ML S

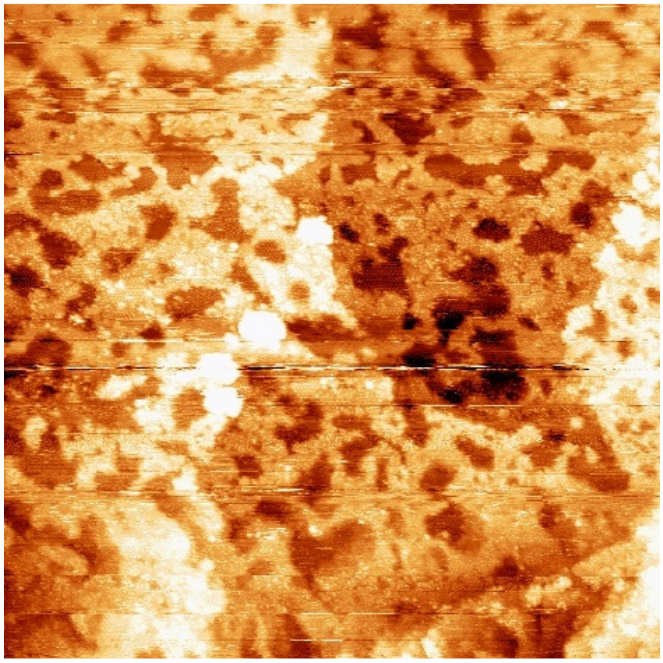

Fig. A2b. 04-24-2008, # 47, 150 nm x 150 nm, 200 K, 0.515 ML S

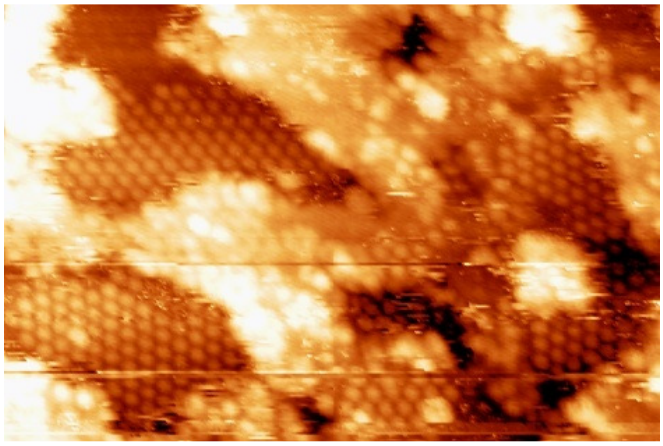

Fig. A2b'. 04-24-2008, # 52, 30 nm x 20 nm, 200 K, 0.515 ML S

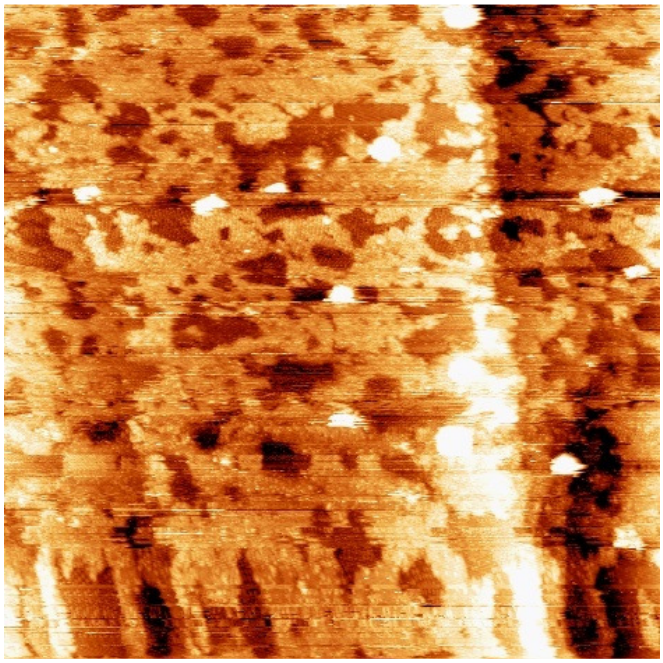

Fig. A2c. 04-24-2008, # 54, 150 nm x 150 nm, 132 K, 0.515 ML S

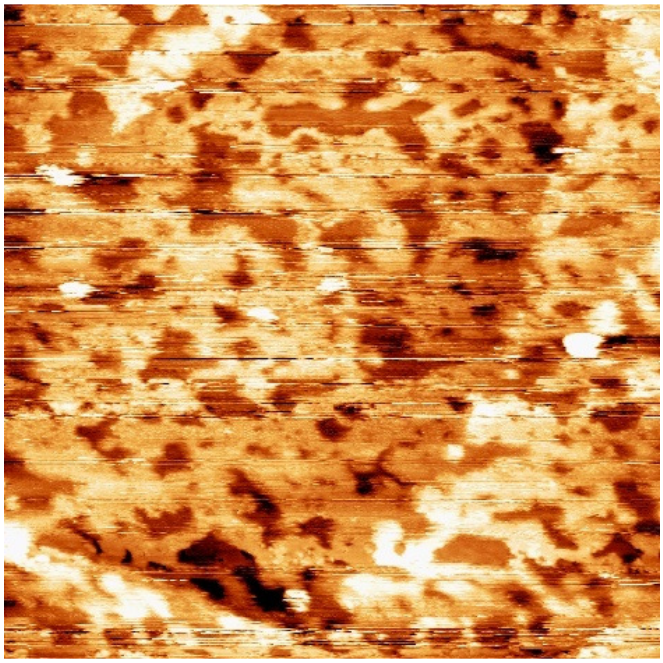

Fig. A2d. 04-24-2008, # 71, 150 nm x 150 nm, 200 K, 0.515 ML S

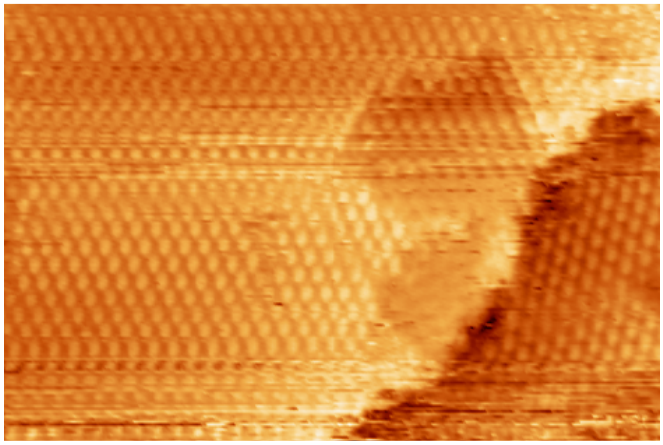

Fig. A2e. 04-24-2008, # 132, 30 nm x 20 nm, 300 K, 0.515 ML S, -1.12 V, 1.06 A

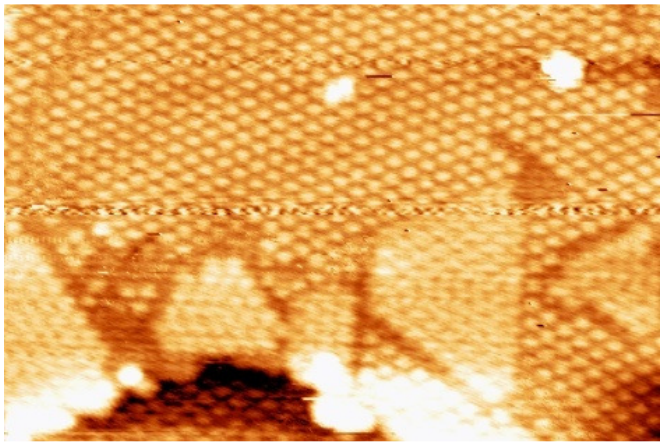

Fig. A2f. 04-24-2008, # 153, 30 nm x 20 nm, 200 K, 0.515 ML S, -2.0 V, 1.0 A

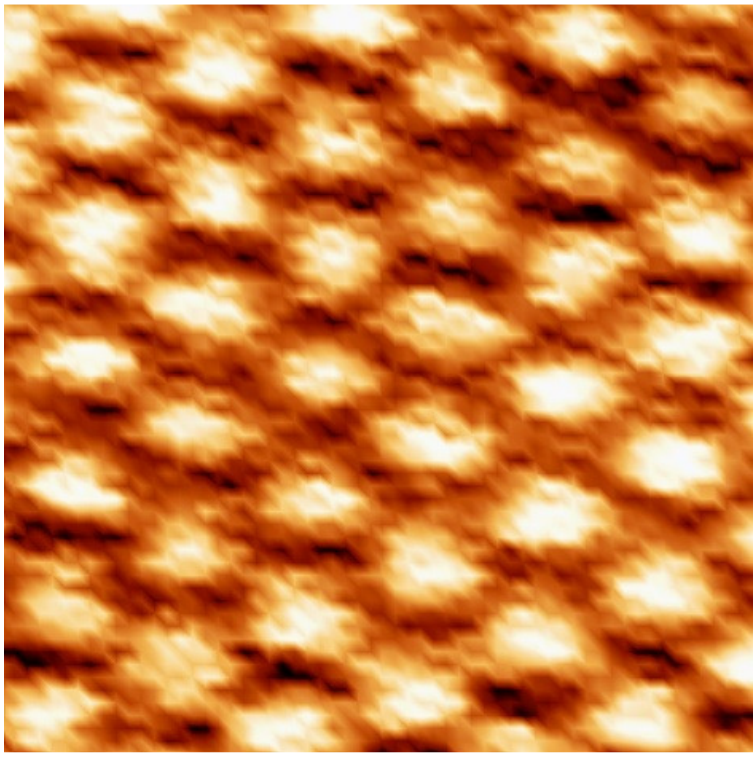

Fig. A2g. 04-24-2008, # 153, 5 nm x 5 nm, 200 K, 0.515 ML S

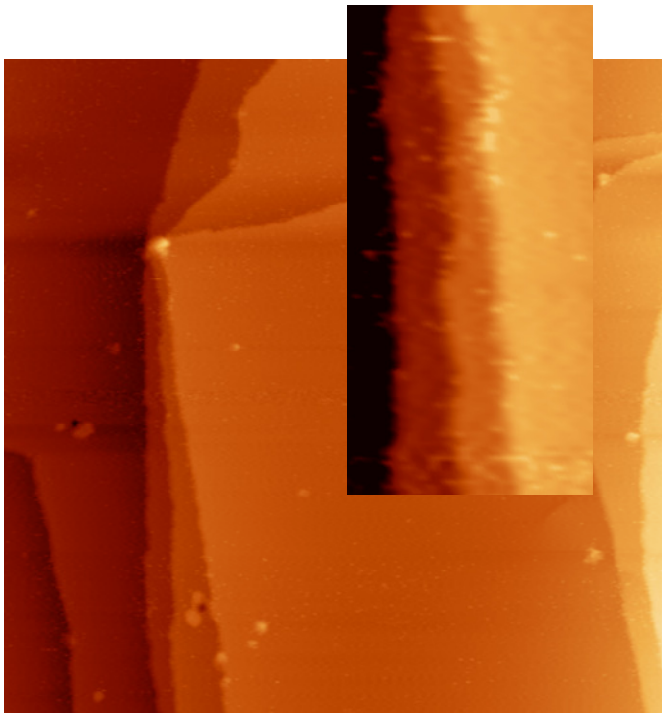

Fig. A3a. 02-14-2007, # 13, 140 nm x 140 nm, clean surface, 200 K, right before S deposition, inset: 15 nm x 30 nm

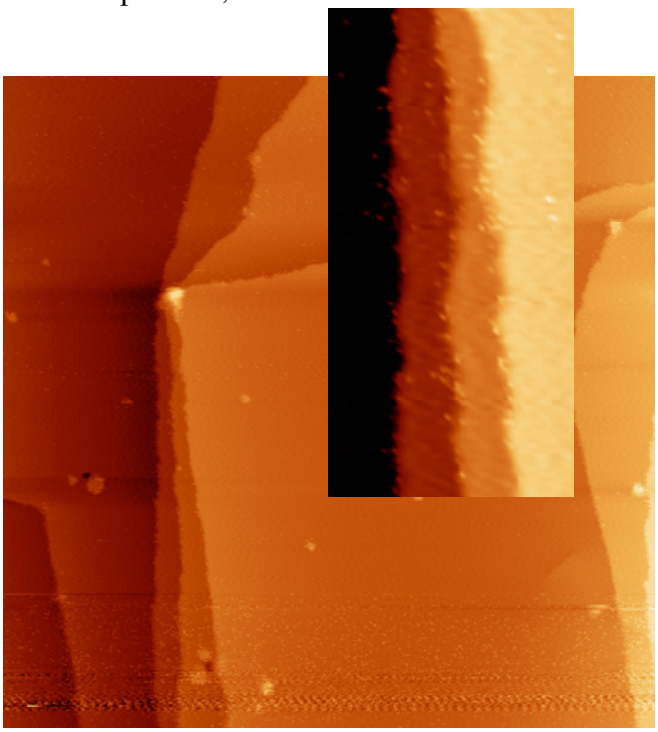

Fig. A3b. 02-14-2007, # 14, 140 nm x 140 nm, during S deposition, 0-2 min, 200 K

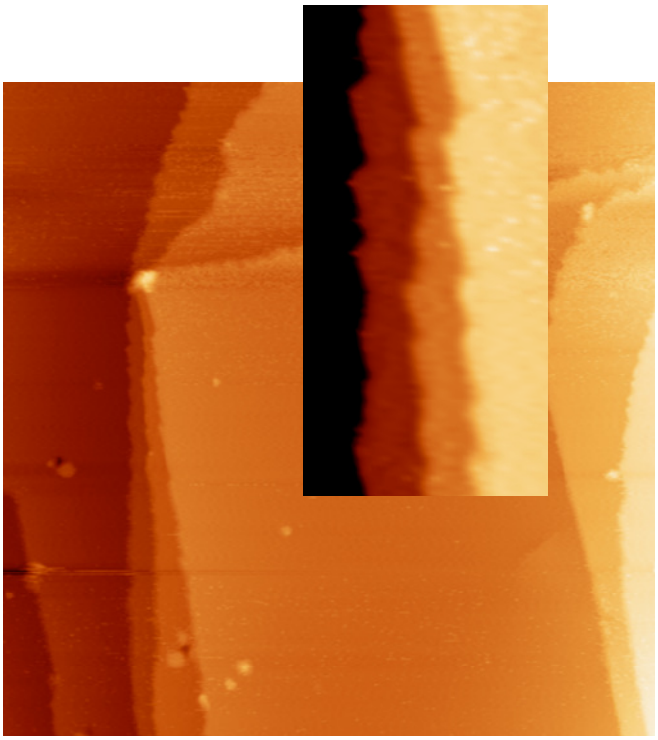

Fig. A3c. 02-14-2007, # 15, 140 nm x 140 nm, during S deposition, 2-4 min, 200 K

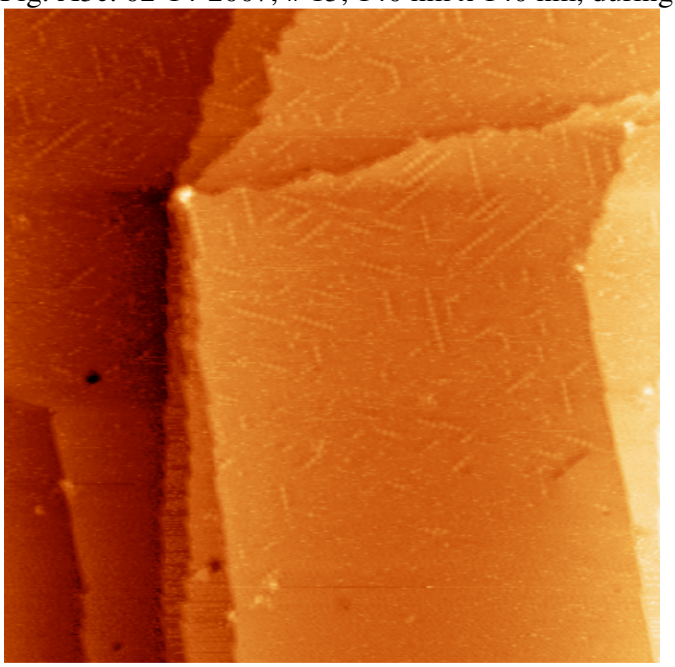

Fig. A3d. 02-14-2007, # 16, 140 nm x 140 nm, during S deposition, 4-6 min, 200 K

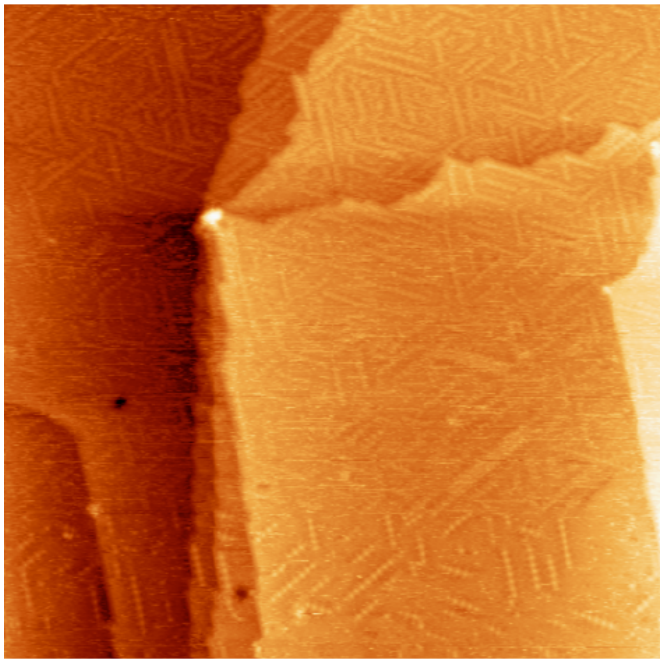

Fig. A3e. 02-14-2007, # 17, 140 nm x 140 nm, during S deposition, 6-8 min, 200 K

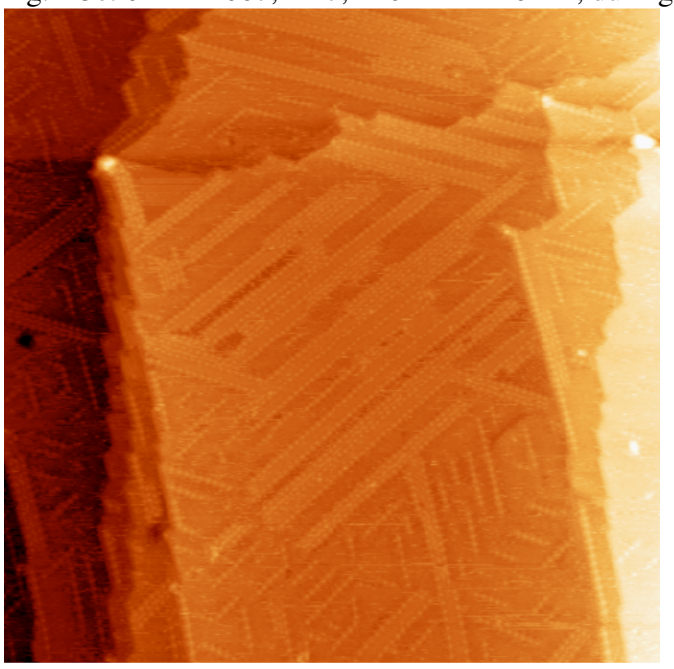

Fig. A3f. 02-14-2007, # 23, 140 nm x 140 nm, 10 min after S deposition, 200 K

# CHAPTER 3. ACCELERATED COARSENING OF Ag ADATOM ISLANDS ON Ag(111) DUE TO TRACE AMOUNTS OF S: MASS-TRANSPORT MEDIATED BY Ag-S COMPLEXES

A paper published in *Journal of Chemical Physics*

Mingmin Shen, Da-Jiang Liu, C.J. Jenks, P.A. Thiel, and J.W. Evans

## ABSTRACT

Scanning Tunneling Microscopy studies reveal that trace amounts of adsorbed S below a critical coverage on the order of 10 millimonolayers have little effect on the coarsening and decay of monolayer Ag adatom islands on Ag(111) at 300K. In contrast, above this critical coverage, coarsening is greatly accelerated. This critical value appears to be determined by whether all S can be accommodated at step edges. Accelerated coarsening derives from the feature that the excess S residing on the terraces produces significant populations of metal-sulfur complexes which are stabilized by strong Ag-S bonding. These include AgS2, Ag2S2, Ag2S3, and Ag3S3. Such complexes are sufficiently populous and mobile that they can potentially lead to greatly enhanced metal mass transport across the surface. This picture is supported by Density Functional Theory analysis of the relevant energetics, as well as by reaction-diffusion equation modeling to assess the mechanism and degree of enhanced coarsening.

## I. INTRODUCTION

Coarsening phenomena (also referred to as ripening or sintering) are ubiquitous in materials science and chemical physics for two-phase materials ranging from solid alloys to surface deposits to liquid droplets [1]. Such processes frequently involve the evolution of distributions of clusters (or islands or droplets) of one phase embedded within another

wherein the number of clusters decreases and their mean size increases. The driving force for such evolution is reduction of the excess free energy associated with the interface region between phases. The underlying mechanism is often Ostwald ripening [1] which involves transfer of material between smaller and larger clusters, so that the latter grow at the expense of the former.

Coarsening of surface deposits is of particular interest in the context of nanofabrication processes which typically utilize deposition techniques. Here, a key challenge and goal is to assure stability of the surface nanostructures thus created. Extensive investigations have been performed of the coarsening of three-dimensional (3D) island distributions in heteroepitaxial systems [2], but also of two-dimensional (2D) islands distributions in homoepitaxial systems [3-6]. For the latter, which will be considered in this paper, a particularly detailed level of analysis and understanding has been possible. Most of these studies have been performed for pristine impurity-free systems under ultra-high-vacuum (UHV) conditions. However, operation of nanoscale devices may involve non-UHV conditions where the presence of chemical additives in the environment could impact stability and coarsening. Thus, it is appropriate to perform systematic studies of the influence of different additives on nanostructure evolution.

In fact, observations exist for a variety of systems indicating that the presence of even minute amounts of a chemisorbed additive can have a significant impact on mass transport on metal surfaces. Examples where the additive is a chalcogen (e.g., sulfur, S, or oxygen, O) either by design or by default include:

(i) Accelerated metal mass transport by exposure of Ag surfaces to S [7].

(ii) Enhanced sintering of supported Pt nanoparticles[8] presumed due to formation of $PtO_2$.

(iii) Accelerated decay of nanostructures on Au(111) surface after expose air, and likely specifically to a component, oxygen, in air [9].

(iv) Extensive chemisorption-induced restructuring of Au(111) surfaces following chemisorption of organothiols [10], of S [11-13], and of O [14]. Here, mass transport of Au can be induced by lifting of the surface reconstruction and associated density change in surface layer, and by formation of surface sulphide for case of S adsorption.

(v) Enhanced release of Au adatoms from edge of small Au islands, and thus enhancing sintering of such nanoclusters, proposed in the presence of S or O [15], and

(vi) Massive S-induced transformation of arrays of Co nanoparticles on Au(111) into a cobalt sulfide phase mediated by formation of $Co_3S_4$ complexes [16], as well as the transformation of Co nanoparticles at step edges on Ag(111) into various sulfide structures[17].

Systematic studies also exist for chalcogen-enhanced coarsening and decay of 2D adatom island distributions prepared by deposition both for Ag/Ag(100) exposed to O [18-20], and for Cu/Cu(111) exposed to S [21-23]. The common proposal in these studies is that facile formation of a mobile metal-chalcogen complex or cluster enhances mass transport relative to that by metal adatoms. A basic requirement for such enhanced transport is that the sum of the formation energy and the diffusion barrier for the complex should be lower than that for metal adatoms [20, 22]. The latter sum determines the maximum attainable rate of coarsening, at least assuming that there is no additional barrier for attachment of the mass-transporting adspecies.

It is appropriate to also mention that a different additive, hydrogen, has been observed to both enhance [24] and inhibit [25] mass transport on metal surfaces, and also to enhance mass transport on Si surfaces [26]. In addition, there is a vast body of literature on the effect

of additives on the thermodynamic properties of surfaces [27,28], and on their impact as surfactants in modifying film growth modes [29].

The current study explores the coarsening and decay of Ag adatom islands on Ag(111) at 300 K after exposure to S. The key observation is enhanced decay of these islands, but only above a critical coverage of S. This critical coverage corresponds to complete saturation of step edges with S. We propose that this accelerated coarsening is mediated by facile formation of metal-S complexes or clusters incorporating excess S which cannot be accommodated at step edges. This picture is supported by density functional theory (DFT) analysis of the relevant energetics, as well as by reaction-diffusion equation modeling. Section II provides background information on our experimental and computational procedures. The key experimental observations on island coarsening and decay are then described in Sec. III. Then, in Sec. IV, we present our DFT results for relevant energies in the S+Ag/Ag(111) system, and provide in Sec. V a basic analysis of the kinetics and energetic driving force and kinetics for coarsening. Next, in Sec. VI, we describe a reaction-diffusion equation formulation for coarsening kinetics, and provide in Sec. VII the associated detailed analysis. Finally, Sec. VIII presents a discussion of related behavior in other systems, and provides concluding remarks.

## II. EXPERIMENTAL AND COMPUTATIONAL PROCEDURES

The Ag(111) sample used in these studies was grown at the Ames Laboratory - USDOE Materials Preparation Center [30]. The surface was oriented perpendicular to the <111> direction to within 0.25°. The sample was polished to a mirror finish using 6, 1, and 0.25 μm diamond paste. All experiments were carried out in a stainless steel ultrahigh vacuum (UHV) chamber with base pressure of $1 \times 10^{-10}$ Torr, equipped with an ion gun and

with a retarding field analyzer (RFA) for Auger electron spectroscopy (AES). One part of the chamber contained an Omicron variable-temperature Scanning Tunneling Microscope (STM). All STM images were acquired using electrochemically-etched W tips [31] at the stated temperature, 300 K. Typical tunneling conditions were -2.0 V and 1.0 nA. In the other part of the chamber, the sample was cleaned by repeated cycles of $Ar^+$ sputtering (15 min, 20 mA, 1.0 -1.5 kV, T = 300 K) followed by annealing. This procedure was carried out until no impurities could be detected by AES, and until images acquired with the STM showed large terraces on the order of at least 100 nm in width, together with a very low density of apparent impurities as evidenced by a lack of pinning sites of steps.

For our study of adatom island coarsening and decay, deposition of Ag on the Ag(111) single-crystal surface was performed using an Omicron EFM3 UHV evaporator containing Ag (99.99% pure) as the deposition source. The Ag flux was held fixed at 0.014-0.018 monolayers (ML)/sec. in all experiments. Sulfur deposition was then performed by exposing the sample to $S_2$ generated by a solid-state electrochemical Ag|AgI|$Ag_2S$|Pt cell following the design of Wagner [32]. With the electrochemical doser, the S flux was in the range of 5 to 50 mML/minute. Our recent work [33] used this electrochemical cell to deposit S on Ag(111) surface, and then to study in detail the structure of S-adlayers at 200K.

Only Ag and S were detected by AES on the surface after S deposition—not iodine or oxygen. Sulfur coverage was determined after each run using the S(LMM)/Ag(MNN) AES intensity ratio, where the letters in parenthesis denote electronic levels, and combination indicates the electronic energy transitions involved. We adopted a calibration that was published in Ref.[34] in 1979 derived largely from Low Energy Electron Diffraction (LEED)

but corroborated by temperature-programmed desorption and work function measurements by another group[35].

Density-functional Theory (DFT) calculations were performed using the VASP total energy code [36-38]. We used the Perdue-Burke-Ernzerhof form of the generalized gradient approximation (GGA) [39]. The ion-electron interactions were treated by the projector augmented-wave method [40]. The energy cutoff was 280 eV for all calculations. The lattice constant was set to 0.417 nm, the theoretical value for the PBE-GGA functional (versus the experimental value of 0.409 nm). We used a slab of thickness of five or six layers, fixing the lower two layers of atom to their bulk positions. Adsorbates were attached only to the top side of the slab. Methfessel-Paxton smearing [41] with a width of 0.2 eV was used for efficiency. The vacuum spacing between slabs was 1.2 nm. Most of the results were obtained using a (3×3) supercell, with the surface BZ sampled with a 4×4 grid of k-points, using the Monkhorst-Pack method [42]. For consistency, we use the same number of irreducible k-points for the clean surface for all calculations, even though the presence of adsorbates can break symmetries.

We should emphasize that there is some dependence of DFT predictions for energetics on parameter choices (which we have examined), and also intrinsic inaccuracy in the theory. For example, results below indicate a dependence of quantities such as binding or interaction energies on slab thickness. Some quantum size effects are of course expected for thin slabs typically used in calculations. However, even basic quantities such as the Ag nearest-neighbor pair interactions can vary quite strongly. Some of this variation may be due to the relatively coarse k-point grid used, although using a finer (6×6) grid shows more or less the same dependence on slab thickness. Comparing results for different thickness, etc.,

we believe that results such as those in Table III below should be accurate within ~0.1 eV. Despite this uncertainty, these results are still valuable in identifying basic trends in relevant energies.

## III. ISLAND DECAY KINETICS: EXPERIMENTAL ANALYSIS

A common approach in analyzing coarsening kinetics is to quantify the decrease with time, t, in the island number or density for large arrays of islands. Ideally, this analysis is performed on broad terraces where evolution is not significantly impacted by preexisting extended steps on the surface. This approach can be applied either for Ostwald Ripening (OR), i.e., simultaneous dissolution of smaller islands and growth of larger islands mediated by mass transport across terraces between them, or for Smoluchowski ripening (SR), i.e., diffusion and coalescence of islands [3-6,43]. However, such an analysis of the coarsening kinetics is sensitive to the presence of narrow terraces. Thus, here we utilize a more robust alternative for OR. Specifically, we characterize the decay with t of the area, A(t), of individual small adatom islands [3]. In analysis of either the evolution of large island arrays or of individual island decay for OR, the key energetic parameters are the diffusion barrier, $E_d$, and the formation energy, $E_{form}$, for the species transporting mass across the surface [2,3].

Often analyses of island area evolution exploit generic features of decay for small islands [3]. For terrace diffusion (TD)-limited decay, one has that $A(t)^{3/2} \sim A_0^{3/2} - R_{TD}\, t$ for islands that are significantly smaller than their neighbors, so their chemical potential is correspondingly higher. The decay rate, $R_{TD}$, has an Arrhenius energy of $E_{act} = E_d + E_{form}$. For the S-free surface, non-linear decay of A(t), with t of this form, is apparent in our data, as it was in previous data [44,45]. For attachment-detachment (AD) limited decay, one has that $A(t) \sim A_0 - R_{AD}\, t$ for islands far smaller than the average size. Now the decay rate, $R_{AD}$, has

an Arrhenius energy of $E_{act} = E_d + E_{form} + \delta$, where $\delta$ denotes the (additional) attachment barrier.

However, one complication for our system with nonzero S coverages, $\theta_S>0$, is that we do not know a priori whether decay is TD or AD limited, or in an intermediate transition regime, or described by a different mechanism. Thus, application of the above expressions is problematic, and we adopt a simpler versatile alternative (see Ref. 23). For adatom island distributions on Ag(111) surfaces with various S-coverages, $\theta_S$, we compare the decay times, $\tau$, for "small" islands with a specific selected initial size or area, $A_0$, which are in similar environments. In our case, we will select $A_0 = 300$ nm$^2$, sometimes interpolating or extrapolating $\tau$-data for other sizes, and choose islands which are always close to an ascending step. Such a step provides a strong sink driving island decay which is common to all cases. Islands further removed from such a step may decay more slowly depending on the details of their local environment [2,3].

Examples of the STM data used for this analysis of island coarsening and decay at 300 K are shown in Fig. 1and 2. For our "benchmark" studies of the S-free surface where $\theta_S=0$, Fig. 1a and 1b reveals coarsening with smaller islands shrinking and larger islands growing (at least initially). A very similar behavior is observed for $\theta_S=7$ mML in Fig. 1c and 1d for an array of islands on a terrace, which is similar in size to that in Fig.1a. In contrast, much faster decay of substantially larger islands is observed for $\theta_S = 11$ mML in Fig. 2. Here, it should be noted that in all experiments with S coverages below 11 mML, STM images were acquired prior to S exposure and then again no earlier than 10 min after exposure. However, for experiments with $\theta_S = 11$ mML and higher (the latter described

below), STM scanning was performed *in situ* during S deposition given the faster decay of islands. Thus, for example, in the experiment with $\theta_S$ = 11 mML, the first image prior to exposure of S was taken only 1 min. after completion of S deposition.

In Fig. 3, we present data for decay of island areas for various initial island sizes at $\theta_S$ = 0, 7, and 11 mML. For $\theta_S$ = 0 and 7 mML, the non-linear variation of A(t) with t is indicative of TD-limited decay, as established previously for the S-free surface [44,45]. For $\theta_S$ = 11 mML, A(t) appears to decrease linearly with t, a behavior normally associated with AD-limited decay. However, other origins for such behavior are possible in systems including additives, as discussed below and in Ref. [23]. From analysis of island decay data of this type for various $\theta_S$, we extract a decay rate, R, based on the decay time, $\tau$ (in minute, say), for islands of initial size $A_0$ = 300 $nm^2$ as R=300/$\tau$ (in $nm^2$/min.). The results reported in Table I indicate no systematic dependence of $\tau$ or R on $\theta_S$ between $\theta_S$=0 and $\theta_S$=7 mML. However, there is a dramatic increase in R by a factor of ~200 as $\theta_S$ increases from 7 to 11 mML. For the latter, we have extrapolated decay times for larger islands down to $A_0$ = 300 $nm^2$. This prompts us to define a critical coverage, $\theta_S$(crit) ≈ 8-10 mML, only above which coarsening or decay is enhanced.

Island decay for $\theta_S$ significantly above 11 mML is so rapid that quantitative analysis of $\tau$ or R is difficult. A major complication is that significant decay occurs on the time scale of S deposition, i.e., as $\theta_S$ increases towards its final value. Also, decay can occur within a fraction of the time required to obtain a complete STM image of 100-200 s.

We now describe observations for a final $\theta_S$ = 35 mML where is S deposited relatively quickly in ~45 s. Fig.4 shows a distribution of islands on an S-free surface (left

frame), and then the same area scanned during exposure of S (right frame). Acquisition of a complete image here takes 200 s. S deposition commences at the bottom of the right frame and thus was complete 20-25% through image acquisition. A few islands are still visible in this initial phase of scanning, but all have disappeared by the end of S exposure. For example, a 613 $nm^2$ island on the lower right has disappeared when imaged ~ 45 s after exposure to S [i.e., ~30 sec. after reaching $\theta_S(crit)$]. From this observation, we make a strict upper estimate that $\tau<0.25$ min. as indicated in Table I.

Next, we describe an additional experiment designed to explore island decay behavior in the regime of enhanced coarsening. Here, S was deposited relatively slowly at a rate of 0.2 mML/sec up to a final coverage of $\theta_S$ = 25 mML which takes a total time of 125 sec. allowing us to monitor the decay of islands during the buildup of the sulfur coverage. Below, we use $\theta_S(crit) \approx 8$ mML which is achieved after 40 sec. of deposition, and let $\delta t$ denote the time elapsed since $\theta_S$ has reached $\theta_S(crit)$ and $\delta A$ the corresponding observed mean decrease in island area (effective over a time interval $\delta t$). In the regime above the critical S coverage, the average island decay rate during buildup of S are given by $R_{av} = \delta A/\delta t$ = 32, 40, 157, and 425 $nm^2$/min for $\delta t \approx$ 30, 42, 65, and 80 s, where the final $\theta_S \approx$ 14, 16.5, 21, and 24 mML, respectively. Behavior is consistent with that reported above. Another significant observation is that for the large array of islands observed during the enhanced coarsening phase of this experiment, one does not observe growth of larger than average islands. Rather, the areas of islands of all sizes decay in time.

It is also appropriate to compare our observations with previous data for Ag adatom island decay on S-free clean Ag(111) surfaces: **(a)** Previous analysis of decay of a small

isolated adatom island of initial area $A_0 = 300$ nm$^2$ inside a larger monolayer vacancy pit revealed a decay time of $\tau \approx 80$ min [44]. This decay is slightly slower than but reasonably consistent with behavior observed here for $\theta_S \leq 7$ mML. **(b)** Previous analysis of decay of smaller islands within a large array of islands on broad terraces far from extended steps indicates decay times strongly dependent on the local environment of the island, as expected for TD-limited decay. Selected examples reveal decay times of $\tau \approx 70$ min when $A_0 \approx 450$ nm$^2$ (with a favorable local environment for decay) and $\tau \approx 140$ min for $A_0 \approx 300$ nm$^2$ and 350 nm$^2$ (with a less favorable environment) [45]. Again, this behavior is reasonably consistent with our observations for $\theta_S \leq 7$ mML given the weaker driving force for decay within such island arrays. **(c)** Analysis of decay of a large isolated adatom island of initial area $A_0 \approx 2600$ nm$^2$ inside a large monolayer vacancy pit indicates a decay time of $\tau \approx 12$ h [44]. This should be compared with our observation of accelerated decay with $\tau \approx 6$ min. for $A_0 \approx 2500$ nm$^2$ when $\theta_S = 11$ mML, illustrating again the dramatic enhancement of mass transport at this S coverage.

Next, to elucidate the above behavior, it is instructive to compare the S coverage with total step edge population on the surface (i.e., the number of step edge sites available to accommodate S). This step edge population varies somewhat between experiments. However, for the surface prior to deposition of Ag islands, the step density is typically around 4-5 nm per 100 nm$^2$ of surface area, or $1.1\times10^{-2}$ edge atoms per surface atom or per fcc adsorption site. The step density increases to ~8 nm per 100 nm$^2$ of surface area, or $2.0\times10^{-2}$ edge atoms/site after Ag island formation. We have assessed step density on roughly 20 regions of size of 300 x 300 nm2 and fond variations of about ±20%. Thus, we believe

that a step density of $2.0\times10^{-2}$ edge atoms per site represents behavior on the region of the surface accessible to S in our coarsening study. Since steps can accommodate one S adatom for every two step edge sites (see Sec.5), it follows that steps are not saturated for $\theta_S \leq 7$ mML, but excess S is available for $\theta_S = 11$ mML. Thus, the critical coverage, $\theta_S(crit) \sim 8$-10mML, introduced above, corresponds to the maximum $\theta_S$ where all S can be accommodated at step edges.

Finally, we mention that in Appendix A, we present an analysis of the fluctuations in position of the Ag(111) surface exposed to S. This analysis reveals behavior consistent with the existence of a critical coverage of S as introduced above.

## IV. ADSPECIES INTERACTIONS, CLUSTER STABILITIES, AND DIFFUSION BARRIERS: DFT ANALYSIS

Below, for convenience, we denote Ag metal adatoms by M, and sulfur adatoms by S. Our analysis of relevant energetics utilizes DFT as described in Sec.II. First, we characterize a few basic interactions between these adspecies which significantly impact overall coarsening behavior: **(i)** S binds at extended step edges on Ag(111) with strength of $\phi_S^e > 0$ from 0.12-0.25 eV per S adatom. These results are obtained from calculating the adsorption energy of a S adatom on slabs representing the Ag(221) and Ag(332) surfaces, which mimic Ag(111) vicinal surfaces with (111)-microfaceted Bsteps and (100)-microfaceted A steps, respectively. In contrast, for M trimers decorated with three S adatoms, one finds a stronger binding per S adatom of $\phi_S^t \approx 0.4$ eV at edges corresponding to (100)-microfacets, i.e., A-steps, and $\phi_S^t \approx 0.3$ eV at (111)-microfacets, i.e., B-steps [33]. We emphasize here that a simple short-range pairwise additive picture of M-S interactions is not adequate for this

system. Energetics often reflects the unusual stability of linear S-M-S chains described below. **(ii)** The effective saturation population of step edges is one S atom per two M adatoms, as there are significant effective repulsions between S on adjacent step sites. **(iii)** Metal adatom interactions are described reasonably by effective nearest-neighbor (NN) M-M attractions of strength $\phi_M \approx 0.2$ eV [43,46]. These interactions imply an equilibrium state for Ag adlayers on Ag(111) corresponding to a two-dimensional (2D) condensed island phase coexisting with a dilute 2D gas phase on clean and S-exposed Ag(111) surfaces. They also drive island formation during deposition of Ag [46]. **(iv)** There are also short-range repulsions between S adatoms on terraces, so there is no tendency for excess S (above the amount required to saturate step edges) to aggregate into islands on terraces.

In Appendix B, we provide a brief discussion of the eauilibrium shape of decorated islands based on the above picture for energetics.

Next, we discuss the stability of various metal-sulfur complexes, $C=M_nS_m$, which could potentially lead to enhanced coarsening. In Table II, we report: **(a)** the total adsorption energy, $E_{ads}(C) > 0$, relative to the separated constituents in the gas phase, which includes both adspecies-substrate bonding as well as adspecies interactions; **(b)** the total internal binding energy or interaction energy, $E_{bind}(C=M_nS_m) = E_{ads}(C) - nE_{ads}(M) - mE_{ads}(S) > 0$, which gives the difference in adsorption energy between the cluster and its separated constituent adspecies; **(c)** the chemical potential of each S adatom within the complex C, $\mu_S(C) = [-E_{ads}(C) - n\mu(M)]/m$, where $\mu(M)$ is the chemical potential of each M atom in a complete surface layer. This quality was introduced in a previous study [33], where lower chemical potentials reflect more effective ways to incorporate excess S into clysters in order to lower the free energy of the system. Within a NN interaction model, one has $\mu(M) = -$

$E_{ads}(M) - 3\phi_M = -2.84$ eV, the second term reflecting the feature that each M adatom has six shared bonds to NN M adatoms.

Our primary interest here is in determining particularly stable clusters (see Table II) and their configurations (see Fig. 5). Our DFT results shown in Table II were obtained using a five-layer Ag slab and revealed that MS clusters ($E_{bind}$=0.03 eV) are not very stable compared to linear $MS_2$ clusters ($E_{bind}$=0.64 eV). The "symmetric" $M_2S_2$ cluster with M on adjacent fcc sites decorated by S bonded at a (100) and (111) microfacets on both sides is quite stable ($E_{bind}$=0.38 eV), as is an analogous cluster with M on hcp sites. However, a distinct "bent" $M_2S_2$ configuration, which is essentially a linear $MS_2$ with an M attached in one corner ($E_{bind}$=0.71 eV), and also an $M_2S_3$ cluster ($E_{bind}$=1.10 eV) are significantly more stable. The enhanced stability of these clusters derives from the feature that they both incorporate linear with $MS_2$ subconfigurations.

Finally, we note that certain $M_3S_3$ clusters are even more stable. One of these consists of an $M_3$-trimer with M on fcc sites and its center of mass above a top site (fcc-top), decorated by 3 S on (100) microfacets ($E_{bind}$=1.88 eV). Another which is almost as stable consists of an "inverted" $M_3$ trimer with M on hcp sites and its center of mass also above a top site (hcp-top), decorated by 3 S again on (100) microfacets ($E_{bind}$=1.87 eV). Both $M_3S_3$ configurations incorporate three linear $MS_2$ subconfigurations. Estimates for these binding energies using a six-layer Ag slab tend to be somewhat higher [47].

Of key importance for coarsening is the formation energy $E_{form}(C)$, for creating various metal-containing clusters, $C=M_nS_m$ with $n>0$. $E_{form}(C)$ will control the equilibrium population of these species, which can potentially facilitate mass transportation. Creation of an isolated metal (M=Ag) adatom by removal from kink or corner sites requires breaking of

three Ag-Ag bonds, so $E_{form}(M) \approx 3\phi_M = 0.6$ eV [43]. For other clusters containing S, one can consider two separate scenarios:

(i) Cluster creation by extracting both M and S from the step edge for $\theta_S < \theta_S(crit)$. Here, formation energy is determined from the difference between the total cost of extracting M and S from step edges and the gain in binding energy for the cluster, i.e., $E_{form}(C=M_nS_m) = nE_{form}(M)+mE_{form}(S)-E_{bind}(C)$. This process is essentially costly given the need to break multiple M-M bonds and lack of a major gain in M-S bonding. Thus, e.g., one finds that $E_{form}(M_3S_3) \approx 0.67$ eV is prohibitively high for there to be a significant terrace population of $M_3S_3$. This feature underlies the absence of enhanced coarsening in the regime where $\theta_S < \theta_S(crit)$.

(ii) Cluster creation utilizing "excess" S already on terrace for $\theta_S > \theta_S(crit)$. Now, the formation energy is determined by $E_{form}(C=M_nS_m) = nE_{form}(M)-E_{bind}(C)$, which is lower than the above since there is no cost to extract S from step edges and a major gain in M-S bonding upon incorporating S into M-S clusters. Thus, e.g., one finds a slightly negative formation energy $E_{form}(M_nS_m) \approx -0.08$eV. Note also that $E_{form}(C)$ is simply related to the S chemical potential, $\mu_S(C)$, defined in Ref. 33 and above by $E_{form}(C)=m[\mu_S(C)+E_{ads}(S)]$. Table II shows that several clusters have lower formation energies than M adatoms in this regime. Not just $E_{form}(M_3S_3)$ but also $E_{form}(MS_2)$ may even be slightly negative, in which case such clusters would form spontaneously in the presence of excess S on terraces.

Finally, Table II also reports DFT results for the diffusion barrier, $E_d(C)$, for various clusters, C. Previous DFT and experimental analyses consistently indicate that $E_d(M) = 0.10$ eV [46]. We now also briefly comment on the diffusion of $M_3S_3$ which has two particularly stable configurations, fcc-top and hcp-top, described above. Two less stable configurations,

hcp-3fh and fcc-3fh, exist with the center of mass of the $M_3$ trimer now above a threefold hollow site (3fh), in both cases decorated by three S on (111) micofacets. One expects that a dominant diffusion path for $M_3S_3$ clusters involves a quasi-rigid translation between fcc-top and hcp-3fh configurations. A simple estimate for $E_d(M_3S_3)$ comes from the energy difference between these configurations of ~0.3 eV, which is mainly due to the difference in binding strength for S at the different types of microfacets [33]. We have confirmed the validity of this picture for the diffusion path and associated energy barrier with a DFT-nudged elastic band analysis (see Fig. 6). Such a diffusion path has also been proposed for undecorated $M_3$ clusters on M(111) surfaces [48,49], and for $Cu_3S_3$ clusters on Cu(111) [22].

## V. COARSENING OF Ag ISLANDS: ANALYSIS OF KEY ENERGETICS

Here, we first analyze the energetic driving force for coarsening both with and without S. In general, coarsening is driven by the reduction in the total free energy associated with steps due to a decrease in the overall perimeter length of islands [1-4]. This energy decrease is determined from the step energy, $\gamma$, where a reduction in perimeter length of L M atoms produces a decrease in energy of $\Delta E_L = -L\gamma$. For the S-free fcc(111) surface, one has $\gamma \approx \phi_M$ per atom, as two shared bonds are broken for each step atom in creating a step. We now present a modified analysis to obtain the relevant energy decrease, and thus effective step energy, for steps which are saturated with S. In this case, S is ejected to the terrace due to perimeter length reduction during coarsening.

First, we consider the scenario where step length reduction of S-saturated step edges during coarsening ejects S onto the terraces, and that S is not incorporated into metal-sulfur clusters. In this case, for a reduction of L atoms in step length, there is an energy reduction due to the gain in M-M bonding of $-L\phi_M$ within islands (just as for the S-free surface), but

also an increase in energy due to the loss of bonding of ½L sulfur adatoms to the step edge of $+½L\phi_S^e$. Thus, the total energy change, $\Delta E_L = -(\phi_M - ½\phi_S^e)L$ (so $\Delta E_L < 0$ for $\phi_S^e < 2\phi_M \approx 0.4$eV) is relatively small compared to the S-free system. Second, consider length reduction of S-saturated step edges where the ejected S is incorporated into $M_3S_3$ clusters created by net dissolution of M atoms from the islands. For a reduction of L M atoms in perimeter length, again ½L sulfur atoms are ejected from the step edge, now requiring dissolution of ½L M atoms to create L/6 $M_3S_3$ clusters. Detailed analysis reveals no net change in the amount of M-M bonding, but a net increase in M-S bonding since S is bound more strongly at (100) microfacets in small clusters than at extended step edges. Thus, one has an overall decrease in energy of $\Delta E_L = -½(\phi_S^e - \phi_S^t)L < 0$. In either case, the effective step energy as determined from $|\Delta E_L|/L$ is relatively small compared to the S-free system. This reduced energy is consistent with enhanced step fluctuations described in Appendix A, at least if there is sufficient excess S to saturate the extended length of the wandering steps.

Next, we consider the rate of coarsening, which must include both a thermodynamic component (reflecting the energetic driving force for coarsening) and a kinetic component (reflecting the efficiency for mass transport). Consequently, one anticipates that the maximum possible rate of coarsening, $R_C(\max)$, where mass transport is mediated by an M-containing species or cluster, $C=M_nS_m$, can be estimated from the product

$$R_C(\max) \sim D_C \, \theta_C^{eq}, \qquad (5.1)$$

where $D_C = D_0 \exp[-\beta E_d(C)]$ is the diffusion coefficient for C with invert temperature $\beta = 1/(k_BT)$ and $\theta_C^{eq}$ is the equilibrium concentration or coverage for C. When all cluster formation energies, $E_{form}(C)$ are non-negative, i.e., taking $E_{form}(M_3S_3) \approx 0$ and $E_{form}(MS_2) \approx 0$,

one can write $\theta_C^{eq} \approx \exp[-\beta E_{form}(C)](\Delta\theta_S)^n$ where $\Delta\theta_S = \theta_S - \theta_S(crit)$ is roughly the coverage of excess S free to participate in cluster formation. For a significantly negative $E_{form}(M_3S_3)$, the equilibrium population of $M_3S_3$ is controlled by the amount of excess S, i.e., $\theta_{M3S3}^{eq} \sim \Delta\theta_S/3$; i.e., most excess S is incorporated in $M_3S_3$ clusters. The populations of smaller clusters are now determined by the difference in their binding or formation energy relative to $M_3S_3$. Finally, we emphasize that the above maximum possible rate might not be achieved even if coarsening is dominated by mass transport of C [23], a subtlety analyzed in the following sections.

Using the above rate estimates, we consider coarsening behavior in two distinct regimes:

(i) Low S-coverages $\theta_S < \theta_S(crit)$: Since all S can be incorporated at step edges, the populations of M-containing clusters on the terraces are very low, and coarsening must be mediated by M adatom transport. Thus, the rate for coarsening scales like $R_M = R_M(max) \sim \exp[-\beta E_{eff}(M)]$, where $E_{eff}(M)=E_d(M)+E_{form}(M)=0.7$ eV, just as for the S-free surface. Indeed, experimental data in Sec. II indicates that coarsening occurs at a rate similar to that for S-free surface for $\theta_S < \theta_S(crit)$.

(ii) Higher S-coverages $\theta_S > \theta_S(crit)$: Now step edges are saturated with S, and extra S populates terraces as adatoms and as part of various clusters $C = M_nS_m$. This allows for the possibility of enhanced coarsening with rate potentially as high as $R_C(max) \sim \exp[-\beta E_{eff}(C)]$, where $E_{eff}(C) = E_d(C)+E_{form}(C)$ is below $E_{eff}(M)=0.7$eV for various C including $MS_2$, $M_2S_3$, or $M_3S_3$. However, such enhanced coarsening also requires sufficiently strong coupling

between spatial gradients in the diffusion field for M adatoms and those for C (see Sec. VI and VII and Ref. [23]).

## VI. COARSENING OF Ag ISLANDS: REACTION-DIFFUSION EQUATIONS

Ling *et al.* [23] have argued that even if metal-sulfur clusters cannot directly attach and detach from step edges, sufficiently strong coupling of the spatial gradients in the diffusion field for metal adatoms, M, to those for certain clusters could enhance coarsening. They analyzed a simplified coupled pair of linear reaction-diffusion equations for $\theta_M$ and $\theta_{M3S3}$ in the steady-state regime, but did not specify the basis of the linearization or the details of the coupling mechanism. (Here, $\theta_C$ denotes the coverage of clusters, C, in units of ML). However, elaboration of these issues is important for full validation of the theoretical model. For example, one cannot regard $M_3S_3$ as being directly created from simultaneous collision of 3 M and 3 S adatoms, as the associated coupling would be too weak. Instead, one should explore possibilities for coupling mediated though "reactions" involving smaller clusters, e.g., $M + M_2S_3 \rightarrow M_3S_3$. In fact, various reaction pathways should also be considered which couple the diffusion field for M adatoms to those for $M_3S_3$ and other clusters capable of enhancing coarsening.

In order to assess these various mechanisms for enhanced coarsening, we develop a coupled set of non-linear reaction-diffusion equations for the spatially-varying coverages of relevant metal-containing clusters, C. The non-linearity derives from the form of the rates of various cluster formation and decay processes. Let K(C+C′) denote the rate for formation or creation of the cluster CC′ via $C+C' \rightarrow CC$, and F(C+C′) denote the rate for the reverse fragmentation process. The reaction-diffusion equations must account for gain and loss in

local adspecies populations due to all relevant "reaction" processes (i.e., cluster formation and fragmentation), as well as due to diffusion for spatially non-uniform systems. Leaving implicit the terms for many reaction processes and focusing on the reaction $M + M_2S_3 \rightarrow M_3S_3$, these equations in the relevant steady-state regime have the form

$$\partial/\partial t\ \theta_M = D_M \nabla^2\theta_M - K(M+M_2S_3) + F(M+M_2S_3) + \ldots \approx 0, \qquad (6.1a)$$

:

$$\partial/\partial t\ \theta_{M2S3} = D_{M2S3} \nabla^2\theta_{M2S3} - K(M+M_2S_3) + F(M+M_2S_3) + \ldots \approx 0, \qquad (6.1b)$$

$$\partial/\partial t\ \theta_{M3S3} = D_{M3S3} \nabla^2\theta_{M3S3} + K(M+M_2S_3) - F(M+M_2S_3) + \ldots \approx 0, \qquad (6.1c)$$

The total diffusion flux for metal across the surface either as adatoms or in clusters,

$$J_{MTOT} = \sum_{n\geq 0} n \sum_{m\geq 0} D_{MnSm} \nabla\theta_{MnSm}, \qquad (6.2)$$

naturally satisfies $\nabla \cdot J_{MTOT} = 0$ in the steady-state regime.

Given that spatial variations in coverages during coarsening are small, it is natural to linearize the above equations by expanding coverages about their equilibrium values, i.e., $\theta_C = \theta_C^{eq} + \delta\theta_C$ (where 'eq' will be used to denote equilibrium values of various quantities). An analogous expansion of the relevant rates then yields

$$K(C+C') = (D_C+D_{C'})\theta_C\theta_{C'} \approx K^{eq}(C+C') + \alpha_C(C')\delta\theta_C + \alpha_{C'}(C)\delta\theta_{C'}, \qquad (6.3a)$$

$$F(C+C') = (D_C+D_{C'})\exp[-\beta\Delta E(C+C')]\theta_{CC'} = F^{eq}(C+C') + \beta(C+C')\delta\theta_{CC'}, \qquad (6.3b)$$

where $\alpha_C(C') = (D_C+D_{C'})\theta_{C'}^{eq}$, $\beta(C+C') = (D_C+D_{C'})\exp[-\beta\Delta E(C+C')]$, and $\Delta E(C+C')$ is the binding energy difference between the separated C+C′configuration and the CC′ configuration. Our notation (specifically, the use of $\alpha$ and $\beta$) is chosen to mimic that of Ref.[23]. Note the identities $K^{eq}(C+C') = F^{eq}(C+C')$, and $\beta(C+C')\theta_{CC'}^{eq} = \alpha_C(C')\theta_C^{eq} =$

$\alpha_{C'}(C)\theta_{C'}^{eq}$. It also is instructive to introduce diffusion lengths and modified equilibrium constants as [50]

$$L_C(C') = [D_C/\alpha_C(C')]^{1/2} \text{ and } R_{C/CC'} = (D_C\theta_C^{eq})/(D_{CC'}\theta_{CC'}^{eq}) \qquad (6.4)$$

Here $L_C(C')$ denotes the diffusion length for C before reaction with C′ to form CC′. The magnitude of these lengths relative to the typical island separation, $L_{isl}$ ~ 100-300 lattice constants, will be key in determining the strength of coupling between different diffusion fields. In the case of high populations of clusters on the terraces, one should replace the "bare" value of diffusion coefficient $D_C$ for isolated clusters, C, with an effective value for the populated terrace. This would likely reduce $D_C$ and perhaps also $L_C(C')$.

Our goal in obtaining linearized steady-state reaction-diffusion equations is to cast them in a form which highlights the key factors controlling coarsening behavior. To this end, we rescale the spatially varying component of the coverages introducing $\rho_C = D_C\,\delta\theta_C/D_M$, and also utilize the above characteristic lengths and equilibrium constants. One then obtains the equations

$$0 \approx \nabla^2\rho_M - \rho_M/L_M(M_2S_3)^2 - \rho_{M2S3}/L_{M2S3}(M)^2 + \rho_{M3S3}\,R_{M/M3S3}/L_M(M_2S_3)^2 + \ldots \qquad (6.5a)$$

:

$$0 \approx \nabla^2\rho_{M2S3} - \rho_M/L_M(M_2S_3)^2 - \rho_{M2S3}/L_{M2S3}(M)^2 + \rho_{M3S3}\,R_{M/M3S3}/L_M(M_2S_3)^2 + \ldots \qquad (6.5b)$$

$$0 \approx \nabla^2\rho_{M3S3} + \rho_M/L_M(M_2S_3)^2 + \rho_{M2S3}/L_{M2S3}(M)^2 - \rho_{M3S3}\,R_{M/M3S3}/L_M(M_2S_3)^2 + \ldots \qquad (6.5c)$$

again leaving implicit terms describing the rates for many processes. Note that

$$\rho_{MTOT} = \sum_{n\geq 1} n\sum_{m\geq 0} \rho_{MnSm} \text{ satisfies } \nabla^2\rho_{MTOT} \approx 0. \qquad (6.6)$$

We must also impose appropriate boundary conditions for these equations. Suppose that only adatoms attach and detach from islands with no attachment barrier (see Ref. [23]).

Then, $\rho_M$ equals the excess equilibrium adatom density at the island edge, which from the Gibbs-Thompson condition satisfies $\rho_M^{eq} \propto (1/r - 1/r_{av})$ for an island of radius r [2,3]. Here $r_{av}$ is the average island radius. The $\rho_C$ for other clusters C satisfy zero-flux boundary conditions. One cannot discount the possibility of complex processes involving direct detachment from the step edge, e.g., of a MS perhaps facilitated by S on the terrace. If such processes are competitive, then one must modify the boundary condition for the detaching cluster at the island edge.

**VII. COARSENING OF Ag ISLANDS AT 300K: ANALYSIS OF KINETICS**

Here, we first consider the scenario where only M adatoms attach and detach from step edges. Lengths are reported in dimensionless units of surface lattice constants. Below, we let $\rho_M^*$ denote a typical magnitude of $|\rho_M|$ at edges of smaller or larger islands and r denotes the distance across terraces measured from the edge of an island where r =0. One could potentially assess the impact of various clusters on coarsening from complete solution of Eq. (6.5a), (6.5b), and (6.5c). See Appendix C. However, below we adopt a simpler but quite instructive approach.

Our simplified analysis will first focus on the reaction pathway $M + M_2S_3 \rightarrow M_3S_3$ to illustrate the potential coupling the diffusion field $\rho_M$ to $\rho_{M3S3}$. Thus, we initially ignore the many terms implicit in Eq. (6.1a), (6.1b), (6.1c), (6.5a), (6.5b), and (6.5c). A detailed analysis in Appendix D indicates that

$$L_M(M_2S_3) \approx (\Delta\theta_S)^{-1/2}, \; L_{M2S3}(M) >> L_{isl}, \; R_{M/M3S3} << 1 \text{ at 300 K}, \qquad (7.1)$$

Expect that the latter breaks down for extremely small $\Delta\theta_S = \theta_S - \theta_S(crit)$. Accounting for these inequalities, Eq. (6.5a) adopts the particularly instructive approximate form

$$0 \approx \nabla^2 \rho_M - \rho_M / L_M(M_2S_3)^2. \qquad (7.2)$$

For small $\Delta\theta_S \leq 0.025$ mML, we have that $L_M(M_2S_3) \geq L_{isl} \approx 200$ from (7.1). Then, (7.2) effectively becomes $\nabla^2 \rho_M \approx 0$, which implies negligible coupling of $\rho_M$ to all other cluster diffusion fields. Consequently, one has TD-mediated coarsening dominated by diffusion of metal adatoms with a quasilinear variation of $\rho_M$ across terrace, so that

$$\delta\theta_M(r) = \rho_M(r) \sim \rho_M^* r/L_{isl} + \text{const and } J_{MTOT} \sim D_M \rho_M^*/L_{isl} \qquad (7.3)$$

with suitable adjustment of the constant to match the boundary conditions.

For larger $\Delta\theta_S \geq 3$ mML, say, one now has that $L_M(M_2S_3) \leq 18$ from Eq. (7.1) which is well below $L_{isl} \approx 200$. Analysis of Eq. (7.2) in this regime implies that

$$\delta\theta_M(r) = \rho_M(r) \sim \rho_M^* \exp[-r/L_M(M_2S_3)] \text{ and } J_{MTOT} \sim D_M \rho_M^*/L_M(M_2S_3) \qquad (7.4)$$

for r below ~ $1/2L_{isl}$ in the first result. The result [Eq. (7.4)] for $J_{MTOT}$ follows from two observations. First, the flux is essentially constant across terraces. Second, since there is no contribution to this flux from S-containing clusters at island edge, it must correspond to the flux of M adatoms at the island edge. Another consequence of Eq. (7.4) is that $\rho_M$ is very small (and spatially uniform) in the middle of terraces, i.e., for distances greater than ~$L_M(M_2S_3)$ from island edges. Thus, again since $J_{MTOT}$ is essentially constant, there must be a quasilinear variation in $\rho_{M3S3}(r) \sim \rho_M^* r/L_M(M_2S_3)$ across the middle of terraces. The result [Eq. (7.4)] for $J_{MTOT}$ continues a significant enhancement over Eq. (7.3) since $L_M(M_2S_3) << L_{isl}$. Finally, since the mass flux this regime of $M_3S_3$-dominated transport is independent on the distance $L_{isl}$ between islands, one expects coarsening kinetics similar to AD-limited behavior, including linear decay of island areas.

Fig. 7 provides a schematic of the behavior of $\rho_M$ and $\rho_{M3S3}$ in two distinct regimes described above. Note that gradients are possibly induced in other diffusion fields. Significantly, the above analysis indicates that the key diffusion length, $L_M(M_2S_3)$, will decrease below $L_{isl}$ when $\Delta\theta_S$ increases to a few millimonolayer. This is qualitatively consistent with the observed enhanced coarsening and linear island decay for $\theta_S \approx 11$ mML. The above identification of distinct regimes for coarsening kinetics corresponds to the scenarios for the simpler model in Ref. [23]. The analysis in Ref. 23 also identified another possible regime where $L_M(M_2S_3)/L_{isl} < R_{M/M3S3}$ promoting local equilibration, i.e., $\rho_M \approx R_{M/M3S3}\, \rho_{M3S3}$. Here, both densities would vary quasi-linearly across terraces and $J_{TOT}$ would be further enhanced. However, this regime may not be realized for our system [51].

We emphasize that the above analysis does not treat all reaction pathways which might couple $\rho_M$ to $\rho_{M3S3}$. Furthermore, it does not treat reaction pathways coupling $\rho_M$ to other $\rho_C$ for which $R_C(\max) >> R_M(\max)$, which could also potentially enhance or dorminate mass transport. One such possibility is $M+S \rightarrow MS$ and $MS + S \rightarrow MS_2$, noting the unusual stability of $MS_2$. Detailed analysis in Appendix D indicates that the relevant diffusion lengths satisfy $L_M(S) \approx L_{MS}(S) \approx (\theta_S^{eq})^{-1/2} \approx 2(\Delta\theta_S)^{-1/6}$. Typically, one has $L_M(S)/L_{isl} << R_{M/MS}$, so it follows that $\theta_M$ and $\theta_{MS}$ are well-equilibrated (see Ref. [23]). Also, the key diffusion length, $L_{MS}(S) \approx 5$, for MS to react with S to form $MS_2$ is well below $L_{isl} \approx 200$ for $\Delta\theta_S \approx 3$ mML. This feature, together with the inequalities $R_{MS/MS2} << L_{MS}(S)/L_{isl} << 1$, implies a particularly strong enhancement of coarsening with linear decay of island areas associated with mass transport via $MS_2$ (see analysis above and Ref. [23]).

Another possibility, mentioned at the end of Sec.VI, is that certain clusters are formed by direct detachment from step edges. Indeed, detachment of MS aided by S on the terrace would seem most likely to have a relatively low energetic cost. However, under this scenario, one would expect standard TD-limited behavior, i.e., non-linear decay of island areas, unless diffusion fields for these clusters are suitably coupled to other clusters such as $M_3S_3$.

**VIII. DISCUSSION AND SUMMARY**

As noted in Sec. I, additive-enhanced mass transport and coarsening appear to be general phenomena. Accelerated coarsening in the S+Cu/Cu(111) system [21-23] was proposed to derive from the low formation energy and significant mobility of $Cu_3S_3$ clusters. Specifically, it was shown that [22] $E_{eff}(Cu_3S_3) \approx 0.63$ eV for $Cu_3S_3$-mediated mass transport, versus $E_{eff}(Cu) \approx 0.84$ eV for mass transport mediated by Cu adatoms [52]. Experimental observations of coarsening at 215 C indicated TD-limited coarsening similar to the S-free system for $\theta_S \leq 2$ mML, enhanced AD-like coarsening for 2 mML $< \theta_S \leq 6.5$ mML[similar to that observed for S+Ag/Ag(111) at 11 mML], and enhanced TD-like coarsening for $\theta_S > 6.5$ mML. No critical coverage of S was identified, i.e., $\theta_S(crit) \approx 0$, although it is possible that a low $\theta_S(crit) > 0$ may exist. The coarsening rate was proposed to scale like $(\theta_S)^3$, although this should only apply for additive-enhanced coarsening. Furthermore, our DFT analysis reveals a particularly stable $CuS_2$species, which could contribute to enhanced coarsening. A detailed analysis will be presented elsewhere.

For the O+Ag(100) system, we proposed that enhanced coarsening via OR (versus SR for the O-free surface) was due to facile mass transport by a $C=Ag_mO_n$, where $E_{eff}(C) < E_{eff}(Ag)$ [19]. The O coverage is very low in this system, and presumably most O is strongly

bonded at kink sites on island edges. Our kinetic picture involved detachment of C from step edges, thereby transporting Ag to other islands. However, C could perhaps form spontaneously on terraces incorporating Ag detaching from step edges, at least when kinks are saturated by O. However, an alternative scenario proposed recently for enhanced coarsening in this system is that the presence of O at kink sites along the island edges reduces the barrier for interlayer vacancy attachment and thus catalyzes OR via TD of vacancies [6].

This current study provides another example of additive-enhanced mass transport involving formation of metal-additive complexes. Trace amounts of S were shown to greatly enhance coarsening of Ag adatom islands on Ag(111), but only above a critical coverage where all step edges are saturated with S. This picture is consistent with our DFT results demonstrating the stability and mobility of various metal-S clusters, together with our analysis of coarsening kinetics based on non-linear reaction-diffusion equations incorporating appropriate mechanisms and rates for cluster formation. In contrast to the other systems mentioned above, one of the stable clusters, $Ag_3S_3$, which can contribute to enhanced coarsening has been observed directly by STM as a component of S adlayer structures on Ag(111) at around 200 K [33] (Again, we note that other clusters such as $AgS_2$ could provide even greater enhancement). Interestingly, another recent STM study [53] revealed formation of aggregates, likely $Ni_3S_3$ clusters with a structure analogous to that of $Ag_3S_3$ clusters, on Ni(111) surface exposed to S.

**ACKNOWLEDGEMENTS**

We thank Karina Morgenstern for information on previous studies of Ag adatom island decay on Ag(111). This work was supported by NSF Grants CHE-0414376 and CHE-

0809472. DJL was supported by the Division of Chemical Sciences, BES, US Department of Energy (USDOE). The work was performed at Ames Laboratory which is operated for the USDOE by Iowa State University under Contract No. DE-AC02-07CH11358.

**APPENDIX A: FLUCTUATIONS AT S-DECORATED STEPS**

Our STM images of the Ag(111) surface exposed to various amounts of S suggest an increase in the amplitude of the fluctuations of step edges as is $\theta_S$ increased at least above 20 mML. To quantify such behavior, one could consider the spatial correlation function, G(y), which gives the mean-square difference in positions in the direction orthogonal to the step for two points on the step edge separated by a distance y (in the direction of the step edge) [54]. For smaller separations, G(y) increases linearly with y with a coefficient proportional to the step diffusivity, $b^2$, which is inversely proportional to step stiffness. Instead, one can consider the mean-square roughness of the step, $\sigma^2(L)$, simply measured as the variance of the distribution of step positions in the direction orthogonal to the step for a segment of the step of length L. This quantity will also reflect the step diffusivity.

One complication for analysis of step fluctuations on non-vicinal surfaces (where step orientations can vary) is that step stiffness or diffusivity depends on orientation. For a model of a fcc(111) surface with nearest-neighbor interactions of strength $\phi_M$, variation of diffusivity with step orientation has been determined for various T below the critical temperature for phase separation, $T_c$, where $kT_c = ½\ \phi_M/\ln(\sqrt{3})$ [55]. We apply these results for S-free Ag(111) surfaces at 300K where $\phi_M \approx 0.2$eV [43,46], and T = 300 K $\approx T_c/7$ (and where the stiffness of close-packed steps has been measured previously [56]). One finds that $b^2$ increases by a factor of ~4 (~9) as the step orientation varies from the close-packed

direction to a 10° (30°) mis-orientation. Note that the maximum is achieved at 30°, mid-way between close-packed directions. Thus, in our comparative analysis of step fluctuations for different $\theta_S$, we attempt to choose step segments with similar orientations.

Illustrative results for distributions of step positions in the direction orthogonal to the step are shown in Fig. 8 for L=48 nm. The behavior of variance, $\sigma^2$, of these distributions for various $\theta_S$ is shown in Table III. Results show that the diffusivity is essentially constant for $\theta_S \leq 10$mML, but exhibits a significant increase for $\theta_S \geq 25$mML. We conclude that for $\theta_S \leq \theta_S(\text{crit})$, where steps are not saturated with S, fluctuation behavior is similar to that for the S-free surface. However, sufficiently above the critical coverage, fluctuations are enhanced. At such higher $\theta_S$, there should be sufficient excess S to cover the greater length of the fluctuating steps in which case the effective step energy is much lower than for the S-free surfaces (see Sec. V). Finally, we remark that detailed experimental and statistical mechanical analysis of the fluctuations of decorated steps is a developing area [57].

**APPENDIX B: EQUILIBRIUM SHAPES OF DECORATED ISLANDS**

Energies of (100) and (111) steps on the S-free M(111) surface, for M = Ag or Cu, are almost equal resulting near-perfect hexagonal equilibrium island shapes [3]. The presence of S could modify these equilibrium shapes. For a shape analysis, some results from geometry are relevant. A distorted hexagonal island with sides of alternating length $L_{\pm} = (1\pm\delta)L$ and perimeter length of P=6L has an area satisfying $A = (\sqrt{3}/4)[(1+\delta)(9-6\delta+\delta^2)^{1/2} + (1-\delta)(9+6\delta+\delta^2)^{1/2}]L^2 \sim (3\sqrt{3}/2)(1-\delta^2/3)L^2$, as $\delta \to 0$. Special cases are $A = (3\sqrt{3}/2)L^2$ for a perfect hexagon of side length L ($\delta$=0), and $A = \sqrt{3}\,L^2$ for an equilateral triangle of side length 2L ($\delta$=1).

We now present some observations on zero-temperature equilibrium shapes of decorated islands where S-bonding is assumed stronger at (100) than (111) steps by an amount $\Delta\phi_S \geq 0$:

**(i)** S-coverage low enough that less than half the island perimeter is covered. All S should decorate the (100) steps. The island remains hexagonal since this minimizes perimeter length.

**(ii)** S-coverage slightly above that needed to completely cover the (100) steps. The hexagonal island should distort to acquire longer (100) step edges allowing accommodation of this extra S with stronger bonding. Introducing a small first-order difference in the lengths of (100) and (111) step edges produces only a second-order increase in perimeter length (see above), so there is minimal additional energy cost associated with this perimeter length increase.

**(iii)** S-coverage high enough to completely cover a perfect hexagon of side length $L_h$. Consider area-conserving conversion to a distorted hexagon with (100) sides of length $2L_h$ fully covered by S, and uncovered (111) sides of length $0.1414L_h$ (see above). This produces an energy decrease of $3L_h\Delta\phi_S^e$ from enhanced S-bonding, and an energy increase of $3\times0.1414L_h\phi_M$ from increased perimeter length. Thus, the energy is lowered relative to the decorated perfect hexagon and this distortion is preferred if $\Delta\phi_S^e > 0.14\phi_M$. For smaller $\Delta\phi_S^e$, the minimum energy shape is less distorted.

Finally, we comment on experimentally observed shapes. There appear to be no substantial deviation from hexagonal shape in the presence of S up to $\theta_S$ =7mML (although we cannot be certain that these shapes are fully equilibrated). This suggests that $\Delta\phi_S^e$ is small.

## APPENDIX C: ANALYSIS OF 1D LINEARIZED REACTION-DIFFUSION EQUATIONS

One could potentially assess the impact of various clusters on coarsening from complete solution of the linearized equations [Eq. (6.5a), (6.5b), and (6.5c)] for the $N_C$ distinct cluster densities, $\rho_C$. This approach would most readily be explored in a one-dimensional setting solving Eq. (6.5a), (6.5b), and (6.5c) in an interval $0<r<L_{isl}$ imposing different $\rho_M$-values and zero gradients for $\rho_{C\neq M}$ at the end points (see Ref. [23]). In this case, one seeks linearly independent solutions of the form $\rho_C \propto a_C \exp(\lambda r)$, setting $a_M=1$. Eliminating $a_C$ yields a secular equation of the form $\lambda^2[A_0 + A_1\lambda^2 + \ldots + A_{NC-1}\lambda^{2(NC-1)}] = 0$. Physical symmetry demands that both $\pm\lambda$ are solutions producing a polynomial in $\lambda^2$. The degenerate case $\lambda=0$ incorporates both the spatially uniform (equilibrium) solution, and a solution where all $\rho_C$ vary linearly. Complete solution to the boundary value problem can be obtained from a suitable linear combination of all these solutions.

**APPENDIX D: ANALYSIS OF DIFFUSION LENGTHS AND EQUILIBRIUM CONSTANTS**

For the reaction $M + M_2S_3 \rightarrow M_3S_3$, the diffusion length satisfies $L_M(M_2S_3) \approx (\theta_{M2S3}^{eq})^{-1/2}$, noting that $D_M >> D_{M2S3}$. We use the result $\theta_{M3S3}^{eq} \approx \Delta\theta_S/3$, where $\Delta\theta_S = \theta_S - \theta_S(crit)$ (see Sec. V) together with the identity $\theta_{M3S3}^{eq} \approx \exp(\beta\Delta E)\theta_M^{eq}\theta_{M2S3}^{eq}$ to determine $\theta_{M3S3}^{eq}$. Here $\Delta E \approx 0.6$-$0.8$ eV is the difference in binding energies for $M_3S_3$ and $M_2S_3$, accounting for uncertainty in DFT estimates. This analysis, together with the result that $\theta_M^{eq} \approx \exp(-\beta 0.6)$, implies that at 300 K

$L_M(M_2S_3) \approx (\Delta\theta_S)^{-1/2}$ (a lower estimate),

$L_{M2S3}(M) \approx (D_{M2S3}/D_M)^{1/2} (\theta_M^{eq})^{-1/2} \approx 10^5 (D_{M2S3}/D_M)^{1/2} >> L_{isl}$,

$R_{M/M3S3} = (D_M/D_{M3S3})(\theta_M^{eq}/\theta_{M3S3}^{eq}) \approx 10^{-7}(\theta_{M3S3}^{eq})^{-1} << 1$ (except for $\theta_S <<< 1$).

For the pathway $M + S \rightarrow MS$ and $MS + S \rightarrow MS_2$, the relevant diffusion lengths satisfy $L_M(S) \approx L_{MS}(S) \approx (\theta_S^{eq})^{-1/2}$ since $D_M >> D_S$ and $D_{MS} >> D_S$. To evaluate these quantities, we determine the population, $\theta_S^{eq}$, of S on terraces which is free to participate in such reactions from the identity $\theta_{M3S3}^{eq} \approx \exp(\beta 1.9eV)(\theta_M^{eq})^3(\theta_S^{eq})^3$ using the above expression for $\theta_{M3S3}^{eq}$. We conclude that $\theta_S^{eq} \approx \exp(-\beta 0.03)(\Delta\theta_S/3)^{1/3} \approx ¼ (\Delta\theta_S)^{1/3}$ at 300 K, which implies that

$$L_M(S) \approx L_{MS}(S) \approx 2(\Delta\theta_S)^{-1/6}.$$

Relevant equilibrium constants satisfy

$$R_{M/MS} = (D_M/D_{MS})(\theta_M^{eq}/\theta_{MS}^{eq}) \text{ and } R_{MS/MS2} = (D_{MS}/D_{MS2})(\theta_{MS}^{eq}/\theta_{MS2}^{eq}).$$

To evaluate $\theta_{MS}^{eq}$ and thus $R_{M/MS}$, we use the identity $\theta_{M3S3}^{eq} \approx \exp(\beta\Delta E)(\theta_{MS}^{eq})^3$ where $\Delta E \approx 1.79$ eV is the relevant binding energy difference. It follows that $\theta_{MS}^{eq} \approx \exp(-\beta 0.56)(\Delta\theta_S/3)^{1/3}$ and $R_{M/MS} \sim (\Delta\theta_S)^{-1/3} >> 1$. The inequality $L_M(S)/L_{isl} << R_{M/MS}$ implies that $\theta_M$ and $\theta_{MS}$ are well-equilibrated based on the analysis of Ref. [23]. To evaluate $\theta_{MS2}^{eq}$ and thus $R_{MS/MS2}$, we use the identity $\theta_{MS2}^{eq} \approx \exp(\beta\Delta E)\theta_M^{eq}(\theta_S^{eq})^2$ where $\Delta E \approx 0.64$ eV is the binding energy of $MS_2$. Thus, one obtains $\theta_{MS2}^{eq} \approx \exp(-\beta 0.02)(\Delta\theta_S/3)^{2/3}$ which implies that $R_{MS/MS2} << 1$. Consequently, one has that at 300K.

**REFERENCES**

[1] L. Ratke and P.W. Voorhees, *Coarsening and Growth: Ostwald Ripening in Materials Processes* (Springer, Berlin, 2001).

[2] M. Zinke-Allmang, L.C. Feldman, and M.H. Grabow, Surf. Sci. Rep. **16**, 377 (1992).

[3] K. Morgenstern, Phys. Stat. Sol. (b) **242**, 773 (2005) (Feature Article).

[4] M. Giessen, Rep. Prog. Phys. **68**, 1 (2001).

[5] P.A. Thiel and J.W. Evans, J. Phys. Chem. B **104**, 1663 (2000) (Feature Article).

[6] P.A. Thiel, M. Shen, D.-J. Liu, and J.W. Evans, J. Phys. Chem. C, 2009,(Centennial Feature Article, in press).

[7] J. Perdereau and G.E. Rheed, Surf. Sci. **7**, 175 (1967).

[8] P.J.F. Harris, Int. Mat. Rev. **40**, 97 (1995).

[9] D.R. Peale and B.H. Cooper, J. Vac. Sci. Technol. A **10**, 2210 (1992).

[10] G. Yang and G.-Y. Liu, J. Phys. Chem. B **107**, 8746 (2003).

[11] M.M. Biener, J. Biener, and C.M. Friend, Langmuir **21**, 1668 (2005).

[12] S.Y. Quek, M.M. Biener, J. Biener, J. Bhattacharjee, C.M. Friend, U.V. Waghmare, and E. Kaxiras, J. Phys. Chem. B Lett. **110**, 15663 (2006).

[13] M.M. Biener, J. Biener, and C.M. Friend, Surf. Sci. **601**, 1659 (2007).

[14] B.K. Min, X. Ding, D. Pinnaduwage, and C.M. Friend, Phys. Rev. B **72**, 121410 (2005).

[15] B.K. Min, A.R. Alemozafar, M.M. Biener, J. Biener, and C.M. Friend Top. in Catal. **36**, 77 (2005).

[16] J. Kibsgaard, K. Morgenstern, E. Laegsgaard, J.V. Lauritsen, and F. Besenbacher, Phys. Rev. Lett. **100**, 116104 (2008).

[17] K. Morgenstern, E. Laegsgaard, and F. Besenbacher, Surf. Sci. **602**, 661 (2008).

[18] A.R. Layson and P.A. Thiel, Surf. Sci. **472**, L151 (2001).

[19] A.R. Layson, J.W. Evans, and P.A. Thiel, Phys. Rev. B **65**, 193409 (2002).

[20] A.R. Layson, J.W. Evans, and P.A. Thiel, J. Chem. Phys. **118**, 6467 (2003).

[21] K. Pohl, J. de la Figuera, M.C. Bartelt, N.C. Bartelt, P.J. Feibelman, and R.Q. Hwang, Bulletin American Physical Society **44**, 1716 (1999).

[22] P.J. Feibelman, Phys. Rev. Lett. **85**, 606 (2000).

[23] W.L. Ling, N.C. Bartelt, K. Pohl, J. de la Figuera, R.Q. Hwang, and K.F. McCarty, Phys. Rev. Lett. **93**, 166101 (2004). Note that the diffusion length appearing in this analysis should be defined as $L_D = \sqrt{(D_1/\alpha)}\ (1+R)^{-1/2}$ where $R=(c_1^{eq}D_1)/(c_2^{eq}D_2)$.

[24] S. Horch, H.T. Lorensen, S. Helveg, E. Laegsgaard, I. Stensgaard, K.W. Jacobsen, J.K. Norskov, and F. Besenbacher, Nature **398**, 398 (1999).

[25] G.L. Kellogg, Phys. Rev. Lett. **79**, 4417 (1997).

[26] J. Nara, T. Sasaki, and T. Ohno, Phys. Rev. Lett. **79**, 4421 (1999).

[27] Q. Chen and N.V. Richardson, Prog. Surf. Sci. **73**, 59 (2003).

[28] See, e.g., M. Kalff, G. Comsa, and T. Michely, Phys. Rev. Lett. **81**, 1255 (1998).

[29] W.F. Egelhoff et al. J. Appl. Phys. **79**, 2491 (1996).

[30] For the Materials Preparation Center, see: www.mpc.ameslab.gov.

[31] C.J. Chen, *Introduction to Scanning Tunneling Microscopy* (Oxford University Press, New York/Oxford, 1993).

[32] C. Wagner, J. Chem. Phys. **21**, 1819 (1953).

[33] M. Shen, D.-J. Liu, C.J. Jenks, and P.A. Thiel, J. Phys. Chem. C **112**, 4281 (2008).

[34] K. Schwaha, N.D. Spencer, and R.M. Lambert, Surf. Sci. **81**, 273 (1979).

[35] G. Rovida and F. Pratesi, Surf. Sci. **104**, 609 (1981).

[36] G. Kresse and J. Hafner, Phys. Rev. B **47**, 558 (1993).

[37] G. Kresse and J. Hafner, Phys. Rev. B, **49**, 14251 (1994).

[38] G. Kresse and J. Furtmuller, Phys. Rev. B **54**, 11169 (1996).

[39] J. P. Perdew, K. Burke, and M. Ernzerhof, Phys. Rev. Lett. **77**, 3865 (1996).

[40] G. Kresse and D. Joubert, Phys. Rev. B **59**, 1758 (1999).

[41] M. Methfessel and A. T. Paxton, Phys. Rev. B **40**, 3616 (1989).

[42] H. J. Monkhorst and J. D. Pack, Phys. Rev. B **13**, 5188 (1976).

[43] M. Shen, J.M. Wen, C.J. Jenks, P.A. Thiel, D.-J. Liu, and J.W. Evans, Phys. Rev. B **75**, 245409 (2007).

[44] K. Morgenstern, G. Rosenfeld, E. Laegsgaard, F. Besenbacher, and G. Comsa, Phys. Rev. Lett. **80**, 556 (1998).

[45] K. Morgenstern, G. Rosenfeld, and G. Comsa, Surf. Sci. **441**, 289 (1999).

[46] J.W. Evans, P.A. Thiel, and M.C. Bartelt, Surf. Sci. Rep. **61**, 1 (2006).

[47] DFT analysis for a 6-layer Ag slab yields $E_{ads}$ ($E_{bind}$) ≈ 2.22 (-), 4.63 (-), 6.92 (0.07), 12.19 (0.71), 14.54 (0.84), 19.50 (1.17), and 11.57 (2.02) eV for Ag, S, AgS, $AgS_2$ (linear), $Ag_2S_2$ (bent), $Ag_2S_3$, and $Ag_3S_3$ (fcc-t).

[48] C.M. Chang, C.M. Wei, and S.P. Chen, Phys. Rev. Lett. **85**, 1044 (2000).

[49] C. Busse, C. Polop, M. Mueller, K. Albe, U. Linke, and T. Michely, Phys. Rev. Lett. **91**, 056103 (2003).

[50] Note also the identity $R_{C/CC'}/L_C(C')^2 = R_{C'/CC'}/L_{C'}(C)^2 = \theta_C^{eq}\theta_{C'}^{eq}/\theta_{CC'}^{eq}$.

[51] Here, one has $J_{MTOT} \sim (D_{M3S3}\ \theta_{M3S3}|_{equil}\ \rho_M^{max})/(\theta_M|_{equil}\ L_{isl})$, but this regime may not be realized for increasing $\theta_S$ given that both $L_M(M_2S_3)/L_{isl}$ and $R_{M/M3S3}$ decrease.

[52] $E_{eff}(Cu_3S_3)$is the sum of $E_{form}(Cu_3S_3)$ ≈ 0.28eV and $E_d(Cu_3S_3)$ ≈ 0.35 eV. $E_{eff}(Cu)$ is the sum of $E_{form}(Cu)$ = 0.79 eV and $E_d(Cu)$ = 0.05 eV.

[53] M. Yamada, H. Hirashima, A. Kitada, K. Izumi, and J. Nakamura, Surf. Sci. **602**, 1659 (2008).

[54] H.C. Jeong and E.D. Williams, Surf. Sci. Rep. **34**, 171 (1999).

[55] .J. Stasevich, and T.L. Einstein, SIAM Multiscale Mod. Sim. **6**, 90 (2007).

[56] T.J. Stasevich, H. Gebremariam, T.L. Einstein, M. Giesen, C. Steimer, and H. Ibach, Phys. Rev. B **71**, 245414 (2005).

[57] C.G. Tao, T.J. Stasevich, W.G. Cullen, T.L. Einstein, and E.D. Williams, Nano. Lett. **7**, 1495 (2007).

TABLE I. Decay time, $\tau$, and decay rate, $R$ (in units of $nm^2/min$), for islands of initial size $A_0=300$ $nm^2$ and for various amounts of S as indicated.

| $\theta_s$ | 0 ML | <1 mML | 2 mML | 7 mML | 11 mML | 35 mML |
|---|---|---|---|---|---|---|
| $\tau$ (decay) (min) | 50 | 60 | 40 | 65 | 0.6 | <0.25 |
| $R$ (decay) | 6.0 | 5.0 | 7.5 | 4.6 | $1.0\times10^3$ | $>2.4\times10^3$ |

TABLE II. DFT values using a five-layer Ag slab for adsorption energy, $E_{ads}(C)$; internal binding energy, $E_{bind}(C)$; chemical potential, $\mu_s(C)$, for S within, $C$; formation energy, $E_{form}(C)$, incorporating terrace S; and diffusion barrier, $E_d(C)$, for various clusters, $C=Ag_nS_m$. Note that fcc sites are preferred for both isolated M and S.

| $C=Ag_mS_n$ | $E_{ads}$ (eV) | $E_{bind}$ (eV) | $\mu_s$ (eV) | $E_{form}$ (eV) | $E_d$ (eV) |
|---|---|---|---|---|---|
| Ag | 2.24 | 0 | ··· | 0.60 | 0.10 |
| S | 4.68 | 0 | −4.68 | 0 | 0.19 |
| AgS | 6.95 | 0.03 | −4.11 | 0.57 | ~0.15 |
| $AgS_2$ (linear) | 12.24 | 0.64 | −4.70 | −0.04 | ~0.1−0.2 |
| $Ag_2S_2$ (symm) | 14.22 | 0.38 | −4.27 | 0.81 | 0.11 |
| $Ag_2S_2$ (bent) | 14.54 | 0.71 | −4.43 | 0.49 | ··· |
| $Ag_2S_3$ | 19.62 | 1.10 | −4.65 | 0.10 | ··· |
| $Ag_3S_3$ (hcp-t) | 22.63 | 1.87 | −4.70 | −0.07 | ~0.3 |
| $Ag_3S_3$ (fcc-t) | 22.64 | 1.88 | −4.71 | −0.08 | 0.30 |

TABLE III. Variance of step position distribution (orthogonal to step direction) for $L=48$ nm in unit of Å$^2$. Orientations are given relative to the closest close-packed step (A or B type). For $\theta_s=16.5$ mML, we observed that $\sigma^2=3.8$ for an orientation 0°-B, the smaller value perhaps reflecting perfect alignment with a close-packed step direction.

| $\theta_s$ (mML) | 0 | 2.4 | 11 | 25 | 30 | 35 | 50 | 95 |
|---|---|---|---|---|---|---|---|---|
| $\sigma^2$ (var) | 6.7 | 5.8 | 5.3 | 53 | 132 | 155 | 235 | 302 |
| Orientation | 10°-A | 6°-B | 16°-B | 13°-A | 9°-B | 6°-A | 10°-B | 10°-A |

**FIGURE CAPTIONS**

**Fig. 1** STM images of coarsening of arrays of Ag adatom islands on Ag(111). Top (150 nm × 220 nm): Benchmark behavior for S-free surface at (a) 0 min and (b) 121 min. Bottom (160 nm × 220 nm): behavior for $\theta_S$ = 7 mML at (c) 0 min and (d) 132 min after S exposure.

**Fig. 2** Sequence of STM images (190×300 $nm^2$) showing Ag adatom island decay for $\theta_S$ = 11 mML (a) 0 min; (b) 1 min; (c) 2 min; (d) 9 min. Islands are labeled consistent with Fig. 3(c).

**Fig. 3** Decay with time of the area of selected small islands near ascending steps for (a) $\theta_S$ = 0 mML, (b) $\theta_S$ = 7 mML, and (c) $\theta_S$ = 11 mML.

**Fig. 4** STM images (300×300 $nm^2$) showing rapid decay of adatom islands while $\theta_S$ increases to 35 mML: (a) island distribution before exposure to S, (b) imaging during S exposure, which starts at bottom as indicated by a lower arrow and which is completed at top arrow. We also indicate the change in size (in $nm^2$) of two selected islands near the bottom of the images.

**Fig. 5** Configurations of various clusters $C=M_mS_n$. Top left to right: AgS, $Ag_2S$, $Ag_2S_2$ (bent). Bottom left to right: $Ag_2S_3$, $Ag_3S_3$ (hcp-top), $Ag_3S_3$ (fcc-top).

**Fig. 6** DFT-Nudged Elastic band analysis of diffusion pathway for the $M_3S_3$ complex.

**Fig. 7** Schematic of behavior of key (rescaled) densities in different regimes. Left: very small $\Delta\theta_S$ where $L_M(M_2S_3)>>L_{isl}$ and coarsening is similar to the S-free surface. Right: larger $\Delta\theta_S$ where $L_M(M_2S_3)<L_{isl}$ and coarsening is characterized by linear decay of island areas.

**Fig. 8** Histograms of step positions in a direction orthogonal to the step orientation. Positions are measured relative to the average location for a step segment of length L=48 nm. Results

are shown for: (a) $\theta_S$ = 0 mML (10° from A); (b) 2.5 mML (6° from B); (c) 11 mML (11° from B); (d) 25 mML (13° from A); and (e) 95 mML (10° from A).

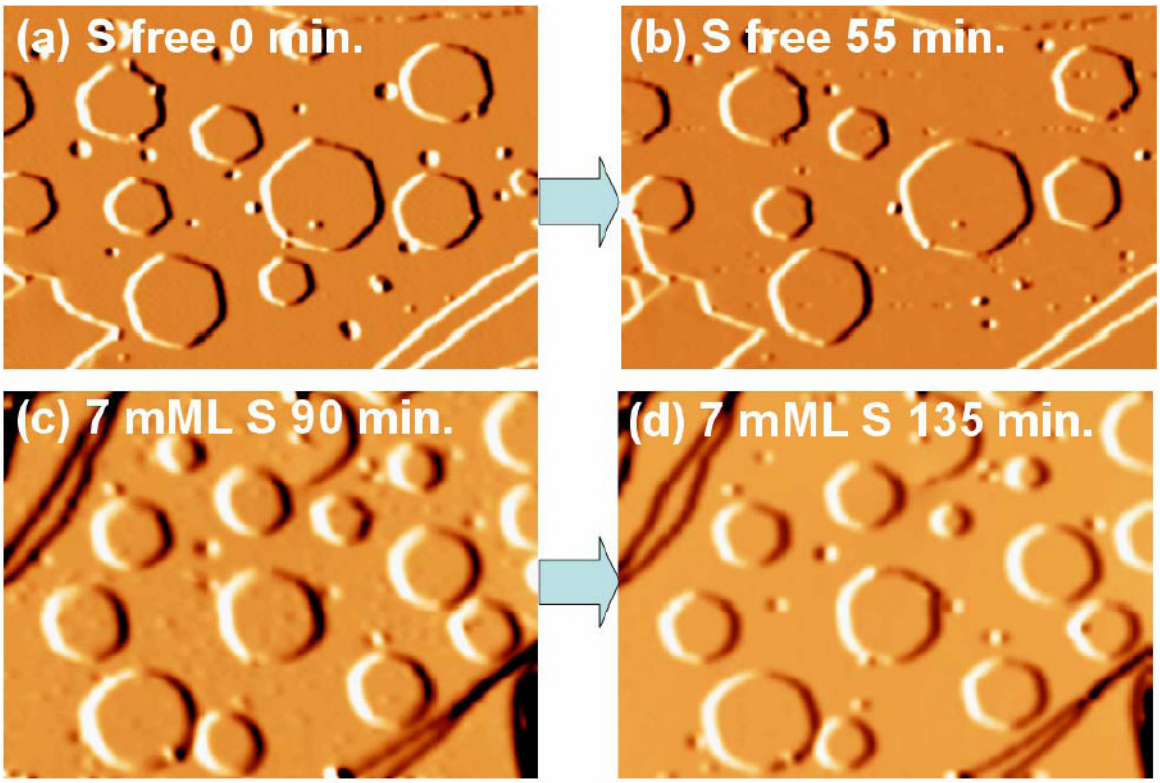


Figure 1

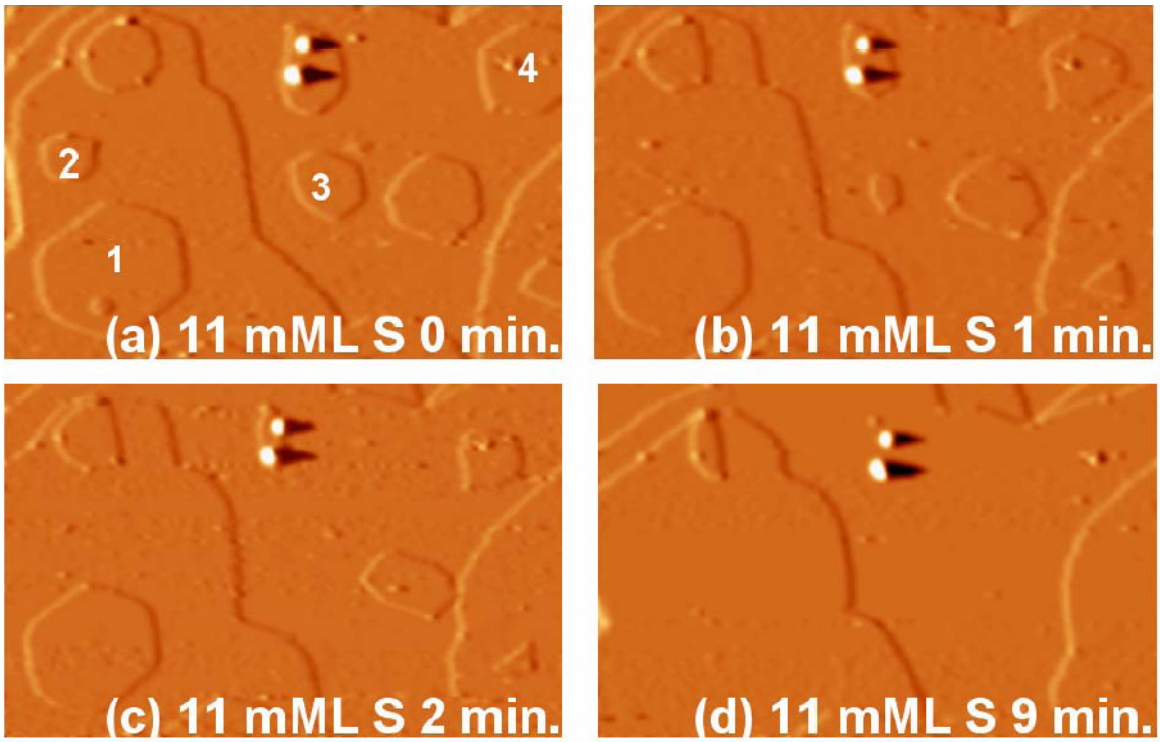


Figure 2

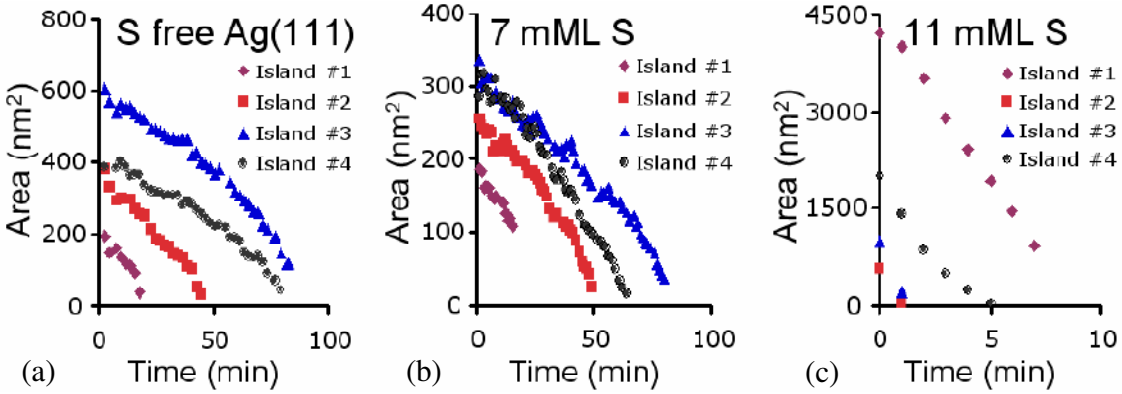


Figure 3

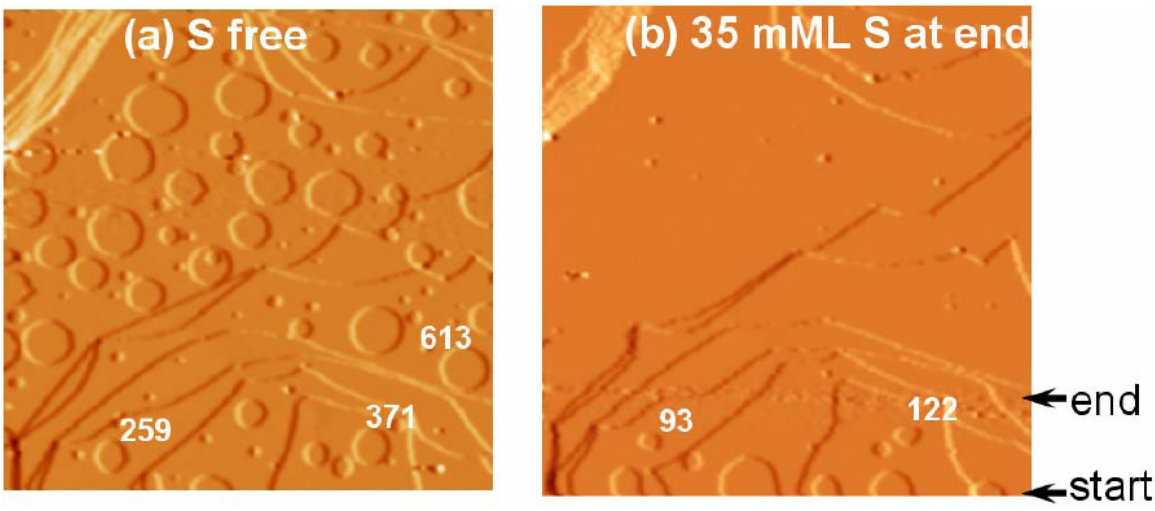


Figure 4

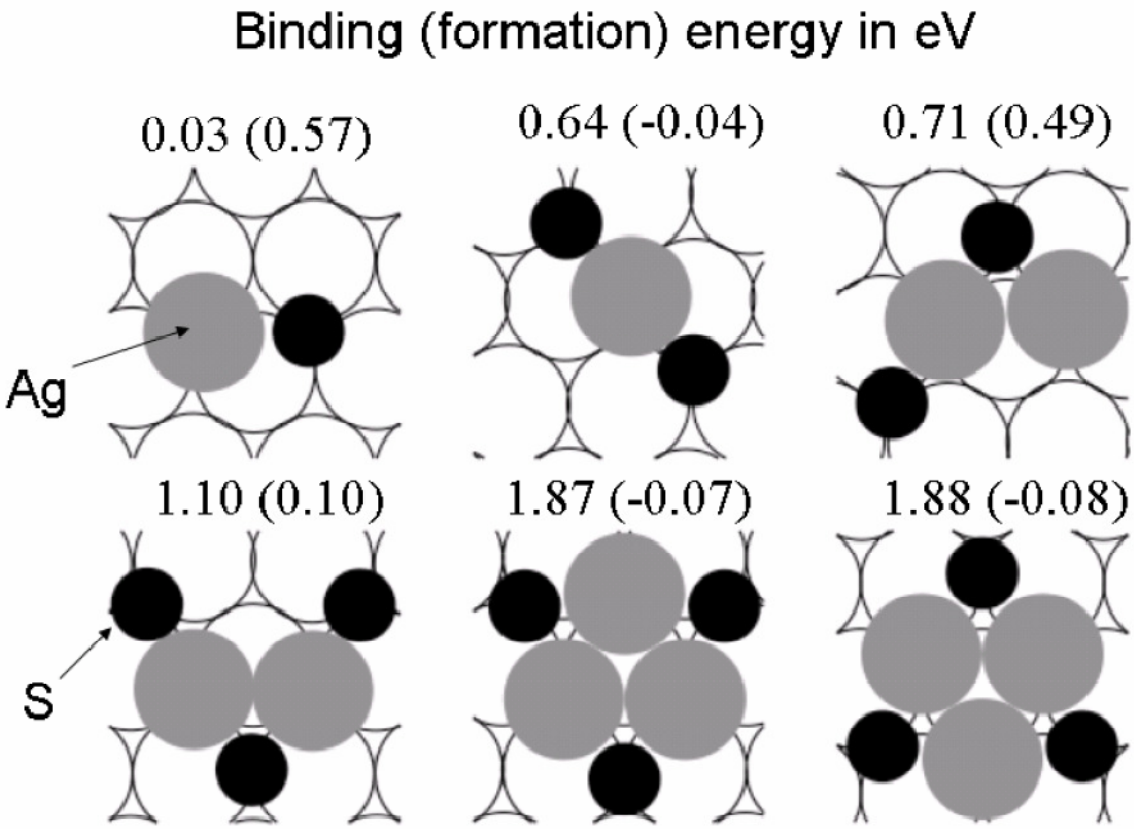


Figure 5

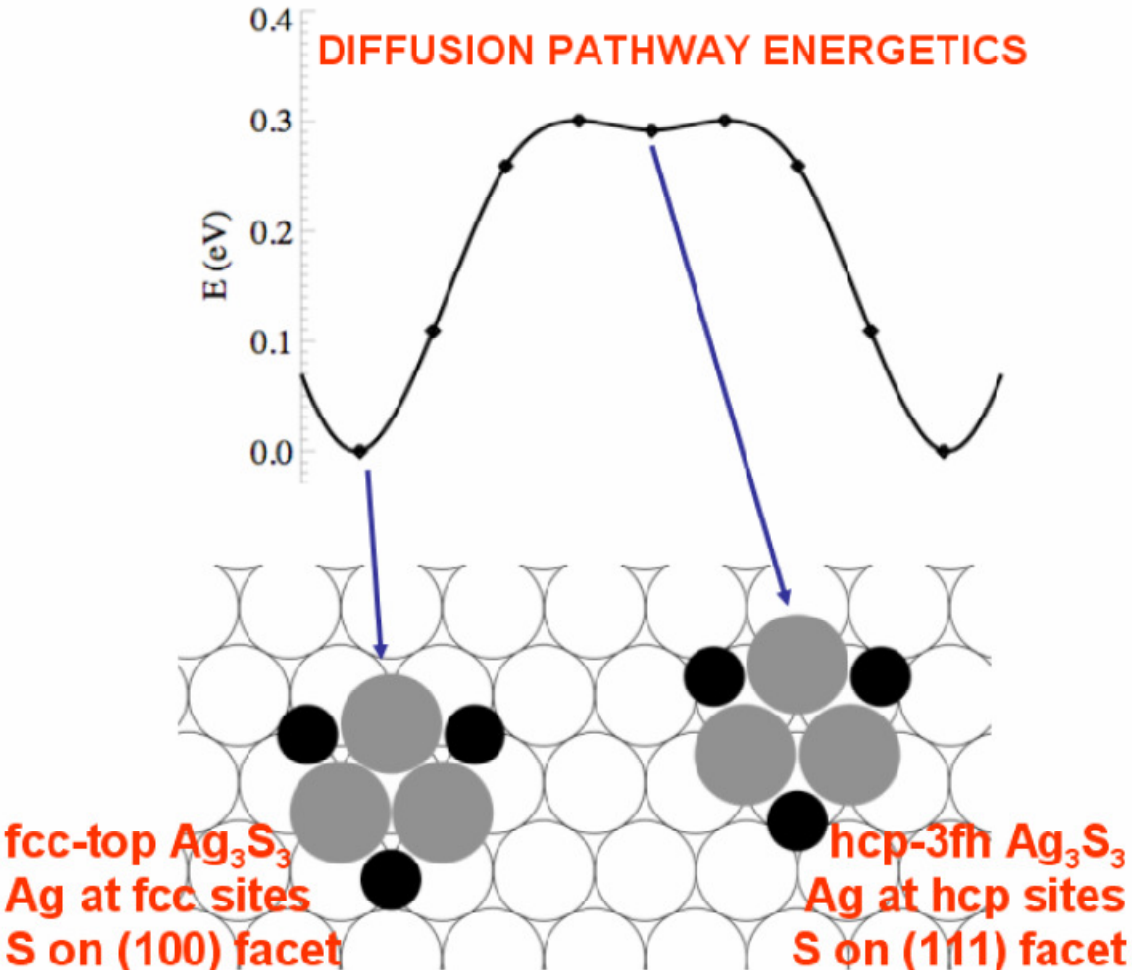


Figure 6

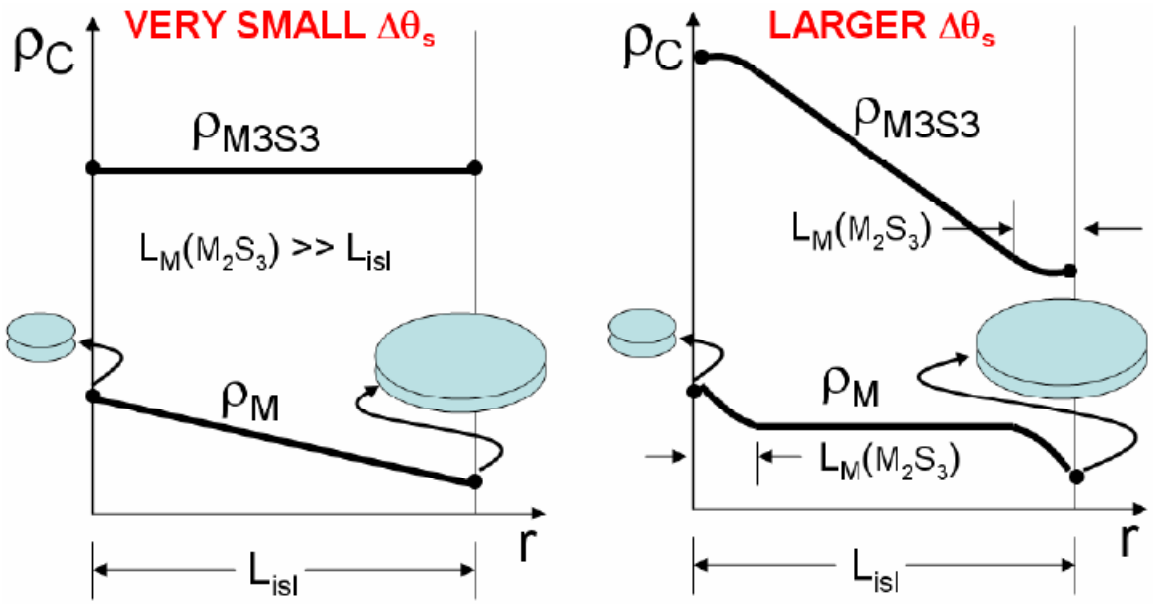


Figure 7

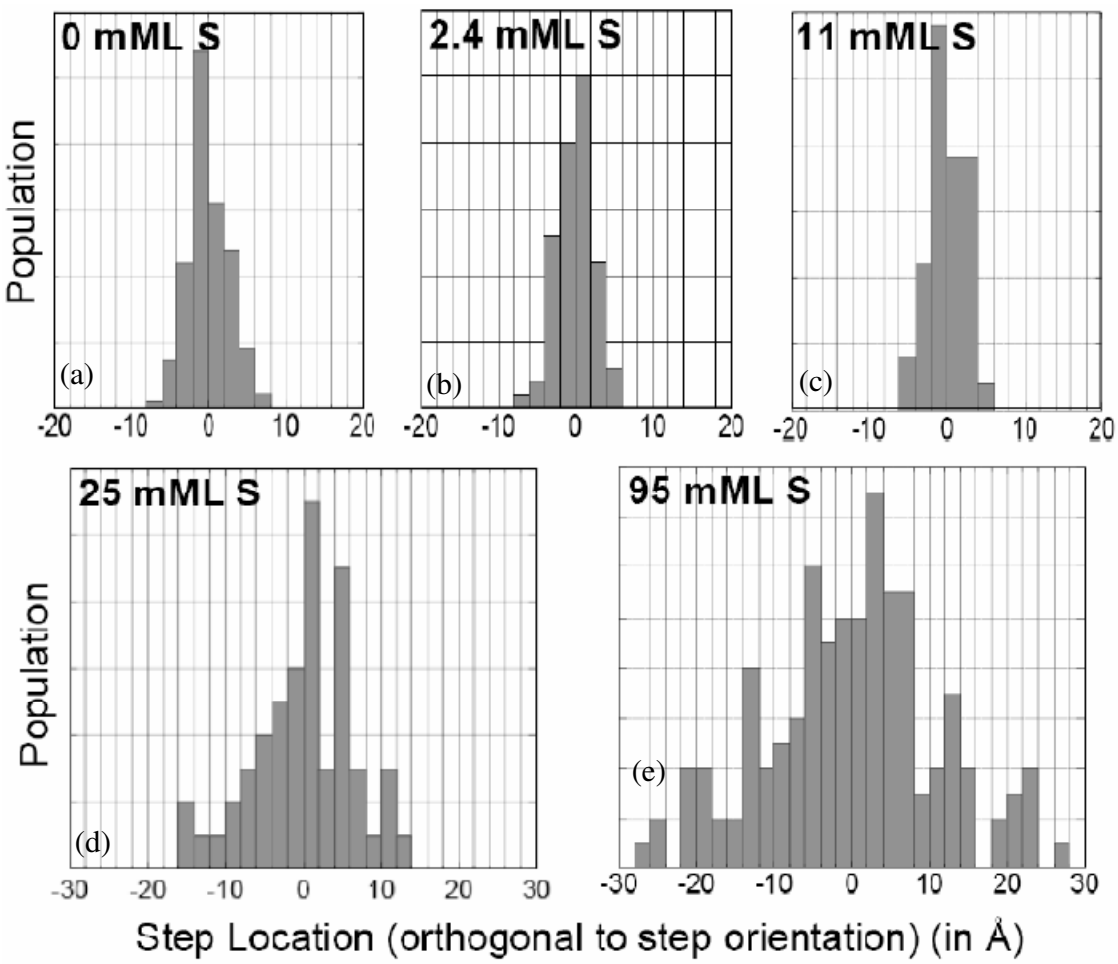


Figure 8

**Appendix E: Supplemental Data at Room Temperature.**

Here we present additional, relevant data concerning the effect of S on coarsening of Ag islands on Ag(111). The data span different S coverages, both before and after Ag deposition. The coverage of deposited Ag ranges from about 0.3 to 0.4 ML, and this variation appears to be insignificant. Coarsening is studied at room temperature (RT). The first two sections describe experiments in which S was deposited first, then Ag. The next four sections describe experiments in which the deposition sequence was reversed, and the last section presents data for step edge fluctuations.

1. S deposition (0.002 ML) followed by Ag deposition (~ 0.3 ML), RT

Fig. E1 shows snapshots from a sequence of STM images of the Ag(111) surface, taken 32 min and 118 min after ~ 0.3 ML Ag was deposited at RT on a surface pre-covered with 0.002 ML S. The coarsening of Ag islands is similar to that forcthe clean Ag(111) surface and also to the situation with lower S coverage (0.001 ML, Part 1). Fig. E1c presents the Ag island decay vs. time. The non-linear behavior is the same as for the clean Ag(111) surface.

2. S deposition (0.032 ML) followed by Ag deposition (~ 0.3 ML), RT

Figure E2 shows STM images before and after Ag deposition on the 0.032 ML S/Ag(111) surface. We are able to scan the same area before and after S deposition. It is clear that extended step edges form as marked by dashed lines and the step edges have roughened as a result of S adsorption. Furthermore, no Ag islands exist on the S adsorbed surface. This stands in contrast to the data previously discussed, shown in Fig. E1a, wherein Ag islands can form on a S-precovered surface when the S coverage is much lower (0.002 ML). Together, these two experiments reinforce the conclusion that when the S coverage is higher

than a critical value of about 0,010 ML. S leads to fast Ag island decay, but when it is below this critical value, S has no effect except to adsorb at the step edges. In the main part of Ch. 3, we showed that this was true when Ag was deposited first, followed by S. In these experiments, we have shown that this is true also when S is deposited first, followed by Ag. In other words, the conclusion is valid regardless of the sequence of deposition.

1. Ag deposition (~ 0.4 ML) followed by S deposition (~ 0.001 ML), RT

Fig. E3a and E3b show snapshots from a sequence of STM images of the Ag(111) surface, taken 5 min and 128 min, respectively, after S deposition at RT on top of pre-deposited Ag islands. The STM movie reveals Ostwald ripening, with small Ag islands shrinking and large Ag islands growing (at least initially). This behavior is very similar to that of the clean Ag/Ag(111) surface shown in Fig. 1a and 1b. Fig. E3c shows the time-dependent decay of island areas for various initial island sizes. The non-linear variation of island area with time indicates that the kinetics are limited by terrace-diffusion, which is the same as for the clean Ag(111) surface.

4. Ag deposition (~ 0.3 ML) followed by S deposition (0.003 ML), RT

Fig. E4 shows snapshots from a sequence of STM images of a Ag(111) surface at RT, taken 2 min and 138 min after S deposition on a surface with pre-covered Ag islands (~ 0.3 ML). The coarsening of the Ag islands here is again similar to what would be expected in the absence of S. Fig. E4c presents the Ag island decay vs. time. The non-linear behavior is the same as would be seen in the absence of S.

5. Ag deposition (~ 0.3 ML) followed by in situ S deposition (0.024 ML), RT

Fig. E5 shows a series of continuous STM images of Ag islands before, during, and immediately following S deposition, with the final S coverage being 0.024 ML. Acquisition

of a complete image here takes 100 s. S deposition commences at the bottom of Fig. E5b and is ~ 15 % complete at the end of the image in Fig. E5c. Most islands are still visible in the initial phase of scanning, but all have disappeared a few seconds after the end of S deposition. For example, a 660 $nm^2$ island in the right middle of the image in Fig. E5a has disappeared when imaged ~ 135 s after starting S exposure, i.e. ~ 70 s after reaching the critical S coverage, assuming constant S flux. From this observation, we can estimate that the decay time, $\tau$, for an initial island size of $A_0 = 300$ $nm^2$, has an upper limit of 0.5 min.

6. Ag deposition (~ 0.3 ML) followed by S deposition (0.048 ML, 0.095 ML), RT

Figures E6a and b show STM images before and after deposition of 0.048 ML S at RT. The surface after S deposition is scanned at least 10 min after S deposition ends, and no Ag islands are seen. Furthermore, the step edge is rough after S adsorption. The same thing happens to the surface with a S coverage of 0.095 ML (Fig. E6c and d). All these data are consistent with our earlier observation that even with a S coverage of only 0.024 ML, all the Ag islands disappear within a few seconds after S deposition, as in Fig. E5.

7. STM images showing fluctuations of S-decorated steps

Figure E7 shows the STM images used for the analysis of the histograms of step positions in Appendix A. As can be seen from the STM images, the step edge fluctuation is essentially similar for $\theta_S \leq 11$ mML, but has a significant increase for $\theta_S \geq 25$ mML.

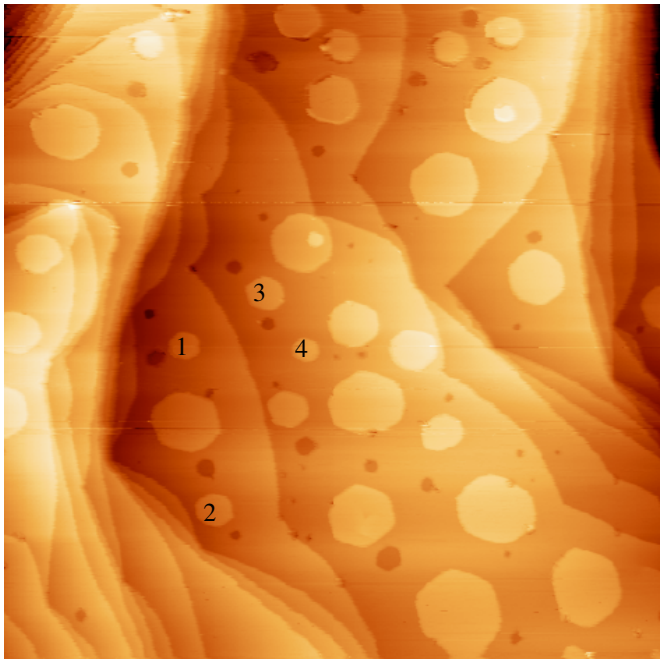


Fig. E1a. 03-14-2007, # 28, 300 nm x 300 nm, after Ag deposition, 19:27 pm

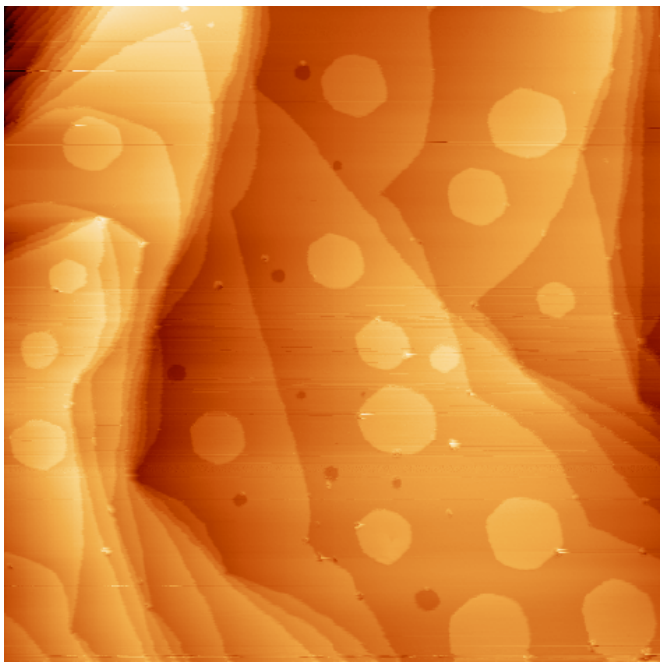

Fig. E1b. 03-14-2007, # 68, 300 nm x 300 nm, after Ag deposition, 20:53 pm

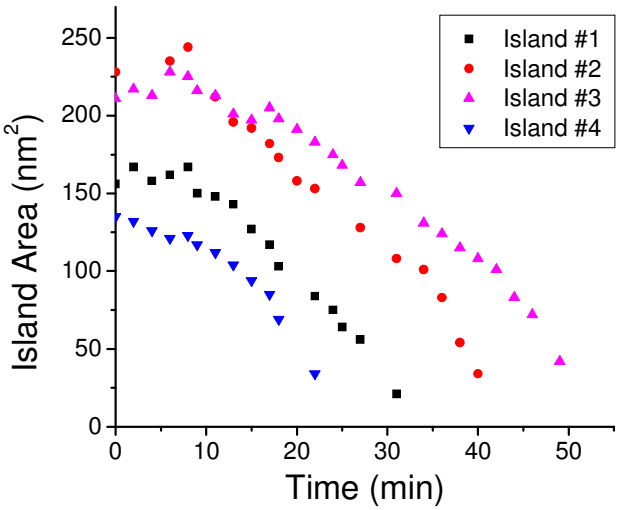


Fig. E1c. Decay with time of the area of selected small islands

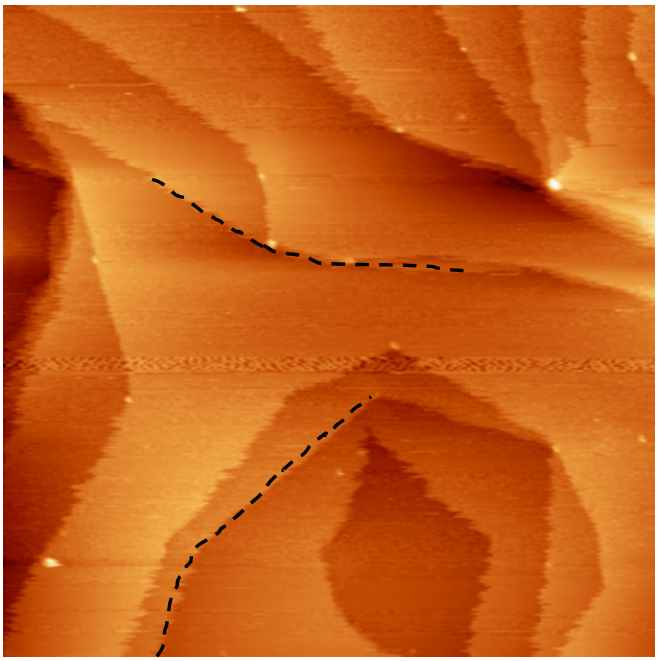

Fig. E2a. 06-11-2007, # 10, 300 nm x 300 nm, after S deposition, 13:27 pm

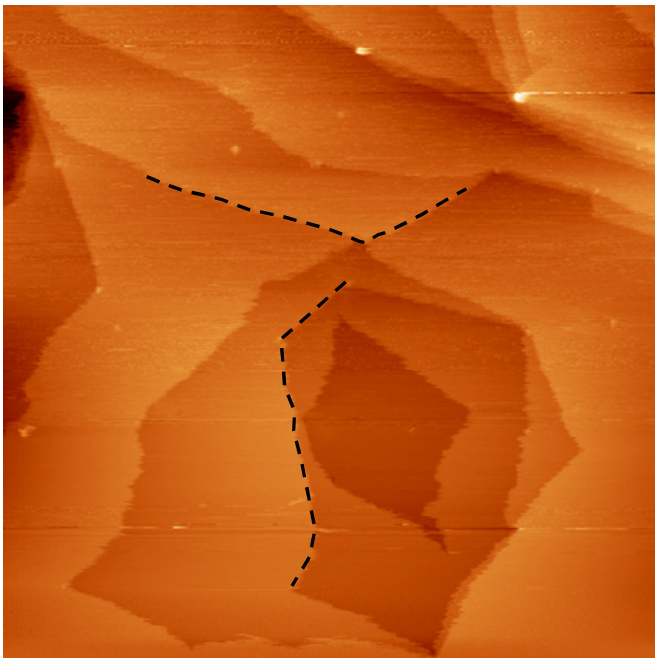

Fig. E2b. 06-11-2007, # 11, 300 nm x 300 nm, after Ag deposition, 13:56 pm

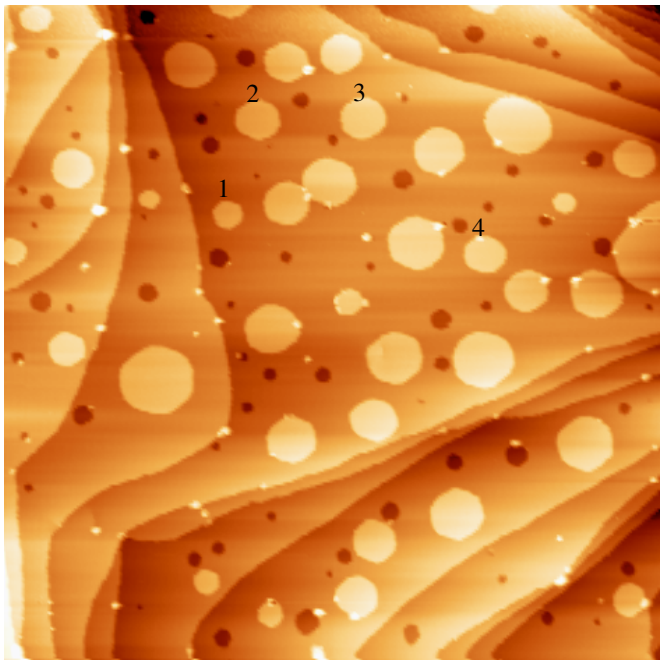


Fig. E3a. 07-19-2007, # 28, 300 nm x 300 nm, 5 min after S deposition, 14:55 pm

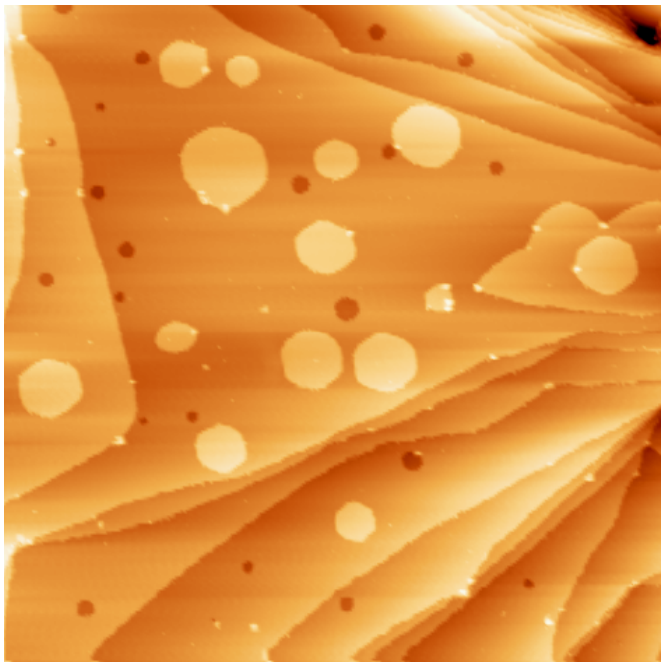

Fig. E3b. 07-19-2007, # 142, 300 nm x 300 nm, after S deposition, 16:58 pm

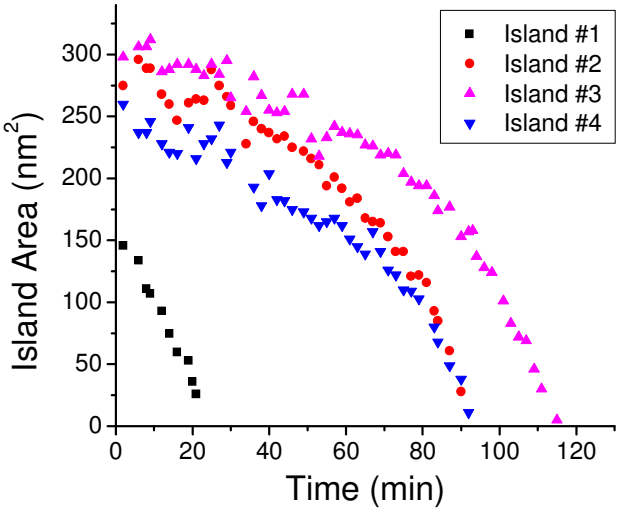


Fig. E3c. Decay with time of the area of selected small islands

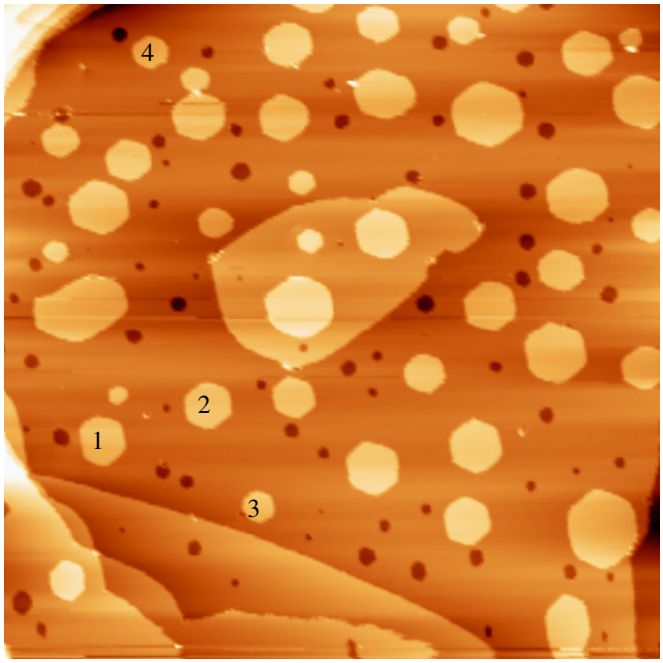


Fig. E4a. 08-16-2007, # 27, 300 nm x 300 nm, right after S deposition, 16:51 pm

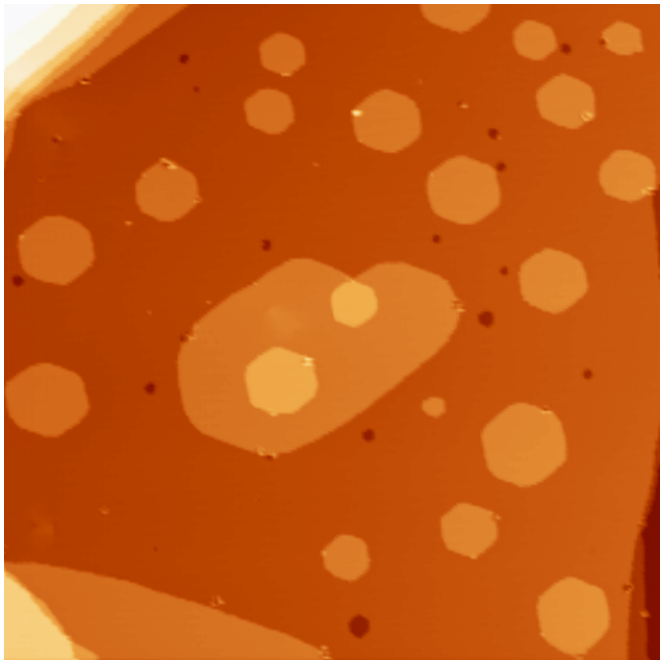

Fig. E4b. 08-16-2007, # 156, 300 nm x 300 nm, after S deposition, 19:07 pm

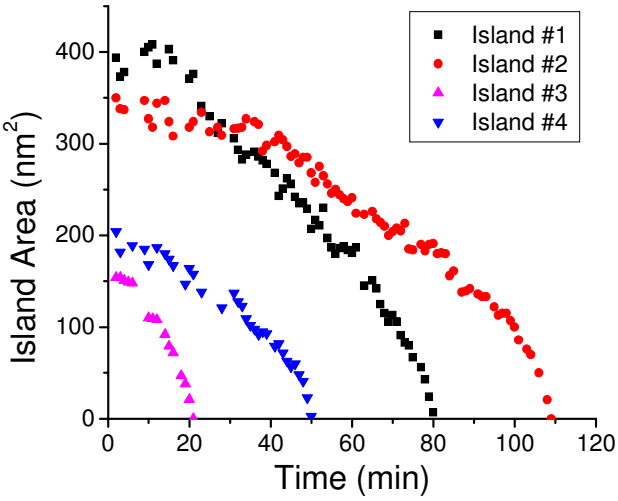


Fig. E4c. Decay with time of the area of selected small islands

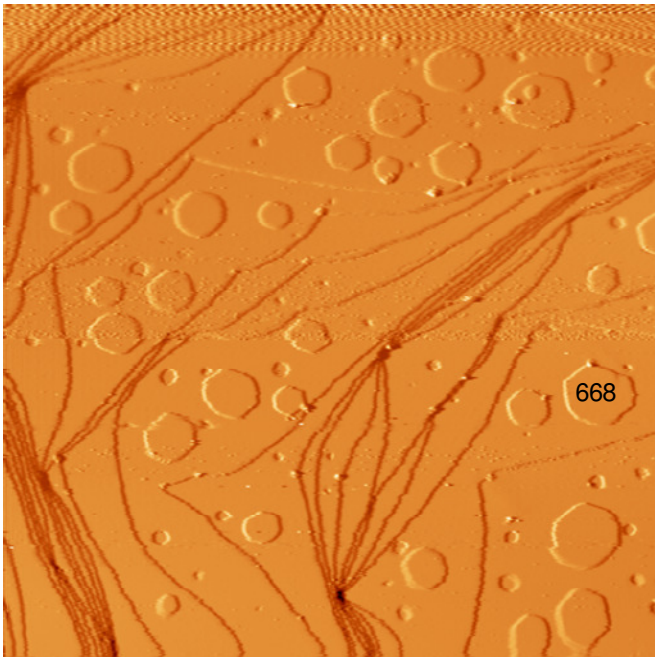


Fig. E5a. 06-28-2007, # 10, 300 nm x 300 nm, right before S deposition

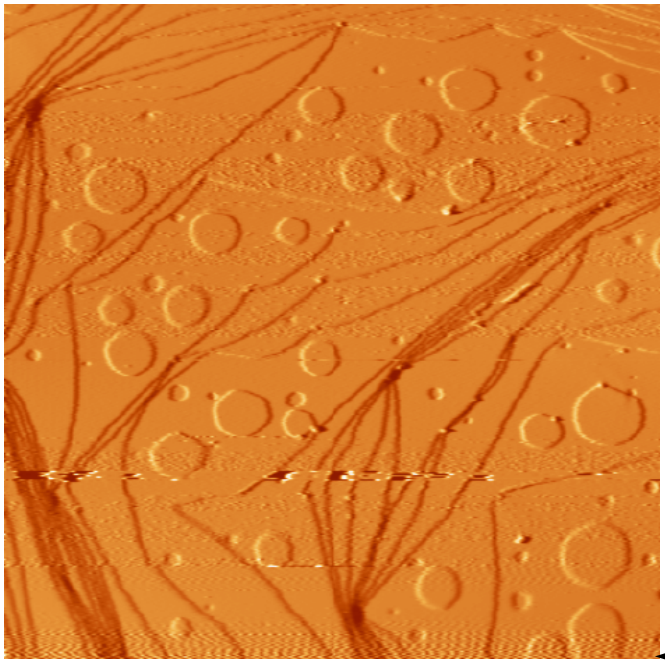


Fig. E5b. 06-28-2007, # 11, 300 nm x 300 nm, during S deposition, scanning is from bottom to top

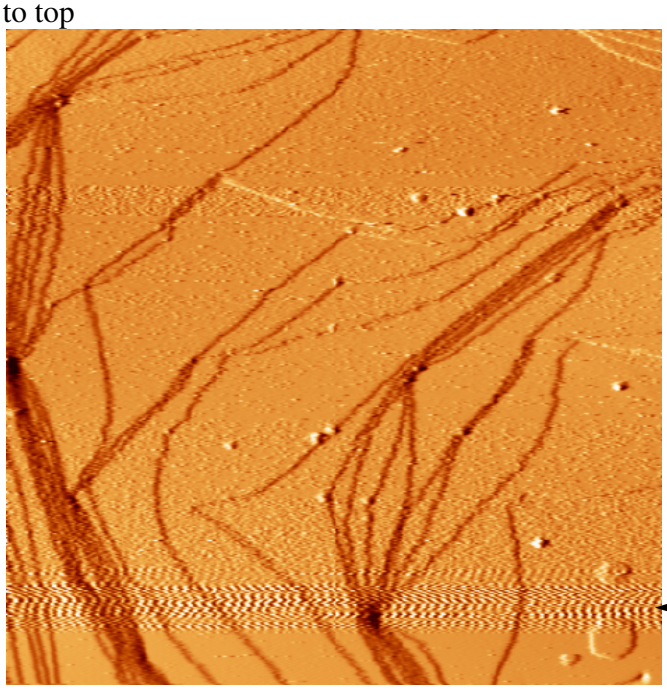


Fig. E5c. 06-28-2007, # 10, 300 nm x 300 nm, right after S deposition

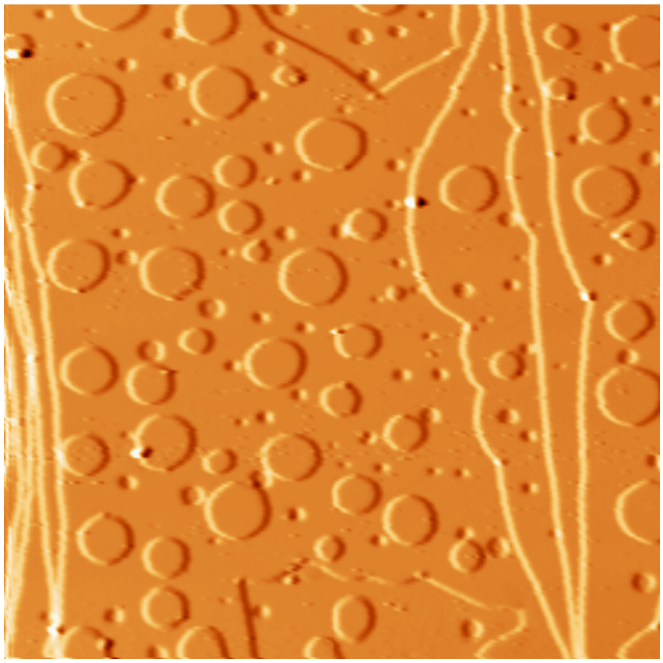

Fig. E6a. 08-09-2007, # 21, 300 nm x 300 nm, before S deposition, 15:40 pm

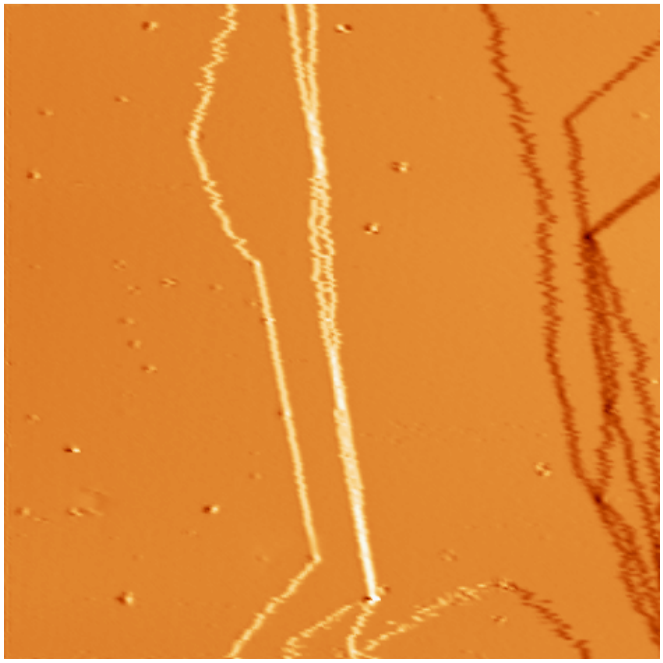

Fig. E6b. 08-09-2007, # 33, 300 nm x 300 nm, after S deposition, 15:50 pm

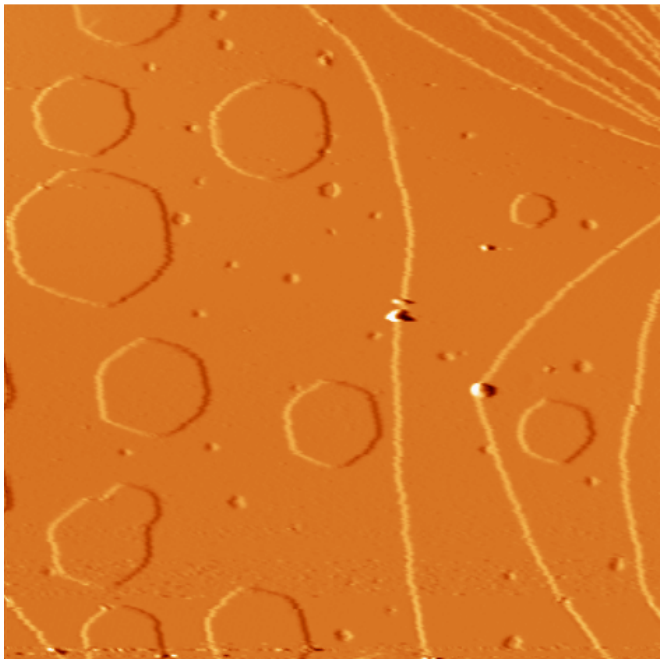

Fig. E6c. 12-18-2006, # 23, 200 nm x 200 nm, after Ag deposition, 17:05 pm

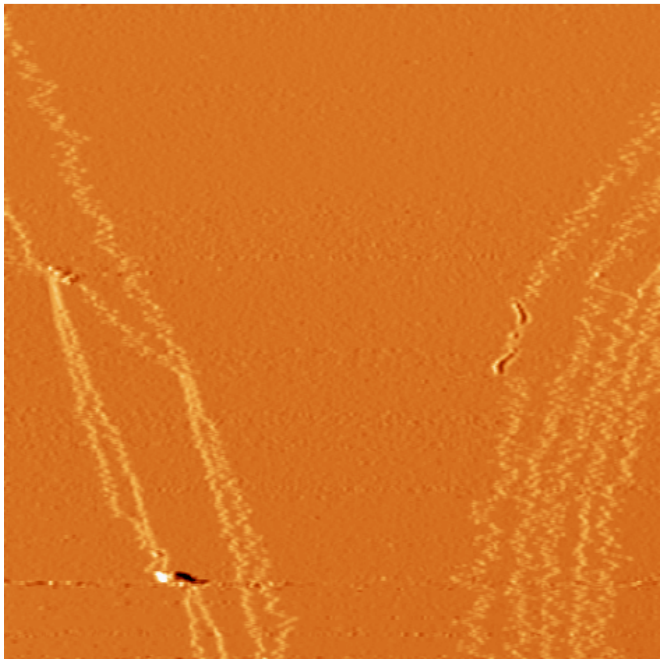

Fig. E6d. 12-18-2006, # 36, 190 nm x 190 nm, after S deposition, 17:35 pm

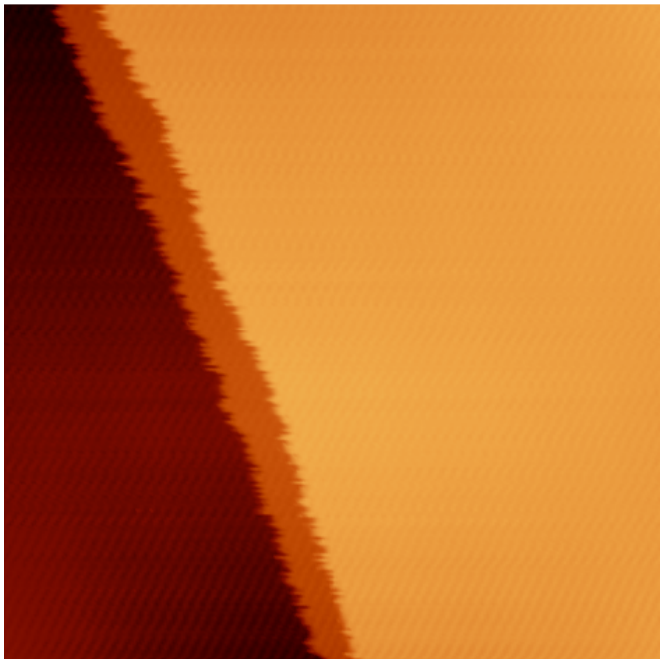

Fig. E7a. 02-14-2007, # 3, 50 nm x 50 nm, clean Ag(111)

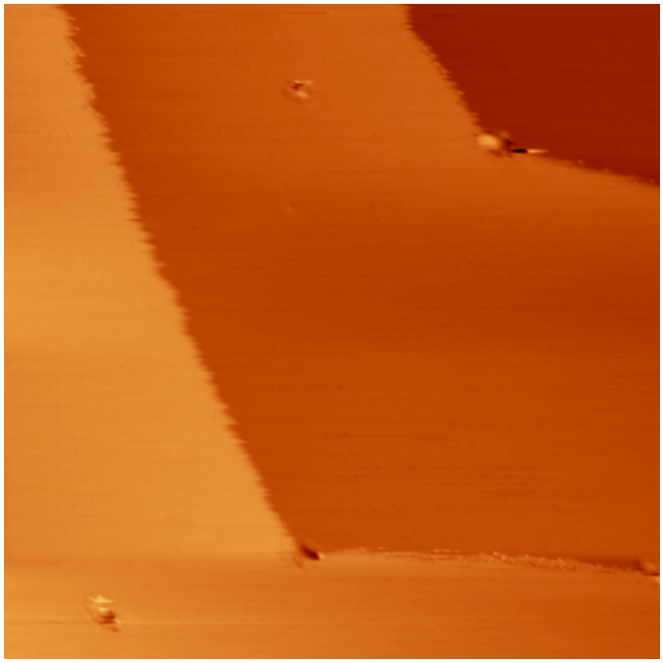

Fig. E7b. 09-06-2007, # 31, 50 nm x 50 nm, 2.5 mML S

Fig. E7c. 08-20-2007, # 63, 45 nm x 45 nm, 11 mML S

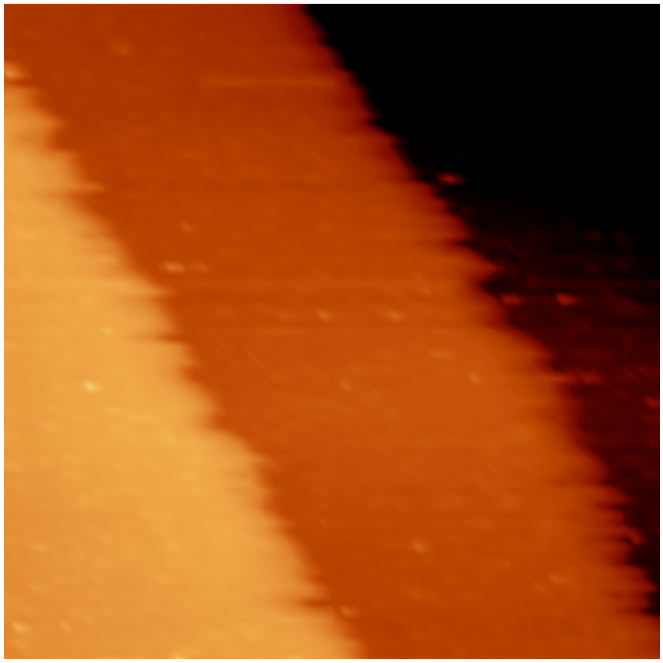

Fig. E7d. 06-28-2007, # 14, 50 nm x 50 nm, 25 mML S

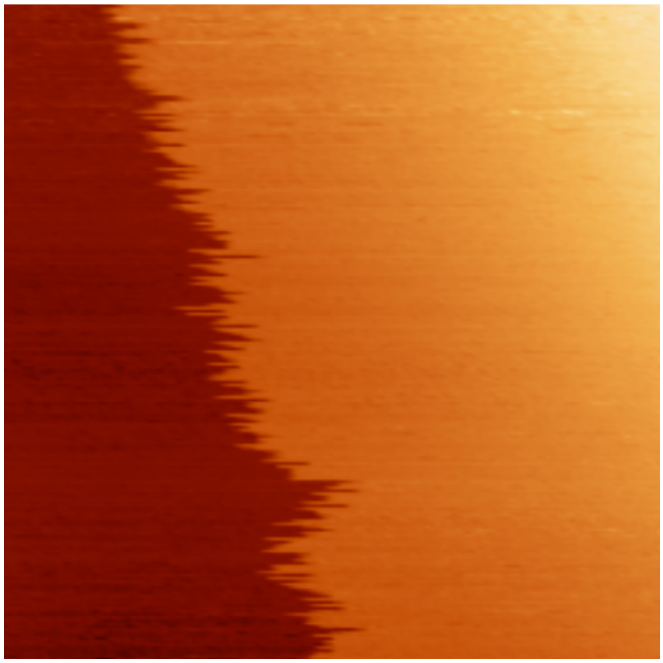

Fig. E7e. 12-18-2006, # 14, 50 nm x 50 nm, 95 mML S

# CHAPTER 4. THE EFFECT OF CHALCOGENS (O, S) ON COARSENING OF NANOISLANDS ON METAL SURFACES

A paper published in *Surface Science*

Mingmin Shen, Da-Jiang Liu, C. J. Jenks, J. W. Evans, and P. A. Thiel

**Abstract**

In this article, we review some of our recent work concerning sulfur adsorption on Ag(111), and the effect of sulfur on coarsening of nanoscale Ag islands. We find that sulfur accelerates coarsening, but that a finite threshold coverage exists, below which the sulfur decorates step edges and does not affect coarsening kinetics. Furthermore, below room temperature, and at coverages above the threshold, an ordered sulfur structure develops. This structure contains long rows of $Ag_3S_3$ trimers as its dominant motif, and its development coincides with inhibition of coarsening. Taken in the context of published literature, these observations suggest that acceleration of coarsening of metal nanofeatures by adsorbed chalcogens is a general effect, and that metal-chalcogen clusters are the agents of metal mass transport. Possible models are discussed.

## 1. Introduction

When an assemblage of particles coarsens, material is transferred from smaller to larger particles. Thermodynamically, evolution toward larger features is driven by the reduction in the total surface energy of an ensemble of three-dimensional clusters, or in the total line energy of two-dimensional (2D) islands. Coarsening, a.k.a. ripening, is important in fields as diverse as pharmaceuticals, where it can limit shelf life of nanosuspensions [1]; metallurgy, where it can weaken precipitation-hardened steels [2]; and geology, where it can yield large and valuable gemstones [3].

Coarsening *on surfaces* is important in at least two applied areas: heterogeneous catalysis, where sintering (coarsening) of supported metal particles can lead to catalyst deactivation [4]; and nanoscience, where coarsening of nanoparticles can be either desirable (e.g. a tool to narrow the size distribution) or undesirable (making particles larger than an optimal size) [5, 6]. Coarsening on surfaces is also important from a fundamental perspective. This is true because the study of coarsening kinetics sheds light on the atomic-scale mechanisms and energetics of basic surface processes, including surface diffusion and attachment/detachment at step edges.

Coarsening on clean surfaces, especially of metal islands on metal surfaces, has received considerable attention [7-11]. Ripening in the presence of adsorbates has received much less scrutiny, but there is abundant evidence that adsorbates can induce metal surface rearrangements other than coarsening, such as faceting [12], step bunching [13], pitting [14], smoothening during growth (surfactant effect) [15, 16], and reconstruction [17, 18]. It is quite likely that an understanding of the kinetics and mechanism of adsorbate-induced coarsening can be extended to help understand some of these processes as well.

One type of adsorbate-metal surface combination is of particular interest to us with regard to coarsening—chalcogens (O, S, Se, …= X) adsorbed on surfaces of coinage metals (Ag, Cu, Au = M). This is an important combination, since surfaces or nanoscale particles of the coinage metals are involved in several specific applications. These include ethylene epoxidation [19-22], surface-enhanced Raman spectroscopy [23], and self-assembled alkanethiol monolayers [24-26]. Furthermore, O and S are ubiquitous adsorbates.

There are isolated reports which, viewed as a whole, suggest that adsorbed chalcogens may generally accelerate coarsening of metallic features on coinage metal

surfaces. As early as 1967, Perdereau and Rhead [27] noted that adsorbed S increases the surface diffusion coefficient of Ag by a factor of $10^4$. More recently, Reutt-Robey et al. showed that adsorbed O can facilitate the faceting of vicinal Ag(110) at room temperature [12]. McCarty et al. demonstrated that low coverages of S accelerate coarsening of Cu islands on Cu(111) [28, 29], and Friend et al. showed that S promotes mass transport on Au(111) at room temperature and above [30-33]. Cooper et al. [34, 35] reported that nanoscale features on Au(111) decay rapidly in air, but very slowly in ultrahigh vacuum; later work in our laboratory indicated that the adsorbate responsible for this effect was most probably O or $H_2O$ [36].

Our work has shown that low coverages of O accelerate coarsening of Ag nanoislands on Ag(100) [36, 37]. The acceleration is illustrated by the series of scanning tunneling microscopy (STM) images in Fig. 1. Visual comparison of the top panel (without oxygen) and the bottom panel (with oxygen) shows that oxygen causes a more rapid decrease in the density, and increase in the average size, of the Ag islands.

There are two main mechanisms by which surface features can ripen.[38] The first, and most common, is Ostwald ripening. This usually relies on equilibrium between the clusters or islands and a dilute 2D gas. According to the Gibbs-Thomson relation, the equilibrium vapor pressure of this gas is higher for smaller features, leading to net mass transfer from smaller to larger features via the gas. (This thermodynamic treatment may underestimate the variation in vapor pressure as a function of size, especially for small particles [39].) The second is Smoluchowski ripening, in which the clusters or islands themselves diffuse, and randomly collide and merge. Smaller particles move faster [40], leading to preferential loss. In the case of O/Ag(100) (Fig. 1), we found that oxygen not only

changes the kinetics of Ag island ripening, but also the mechanism—from Smoluchowski ripening on the clean surface, to Ostwald ripening with oxygen [37].

Section 2 of this paper provides a review of our recent work, together with new results, for the system sulfur on Ag(111). In Section 3, we place this work in context and outline the challenges and opportunities that remain. Experimental details are given elsewhere [41].

**2. Sulfur on Ag(111)**

Before considering S-induced coarsening, a review of this adsorption system is necessary. S/Ag(111) has been studied previously with low-energy electron diffraction (LEED) and STM, at room temperature [42-44]. At S coverages above about 0.4 monolayers (ML, defined as the ratio of S atoms to Ag atoms in the (111) plane), a ($\sqrt{7}$ x $\sqrt{7}$)R19$^o$ phase (abbreviated $\sqrt{7}$) develops. This phase has been assigned as a reconstruction in which the top layer resembles $Ag_2S$(111) [42, 44].

Our work has shown that below room temperature, S forms ordered structures in which the dominant motif is a long row of dots [41], examples of which can be seen in Fig. 2. The dot-rows align with the close-packed Ag rows in the substrate. The dot-row features are very robust, since they are observed over a wide range of coverage (0.03 to 0.4 ML) and with variable inter-row spacings—although the spacing between dots within rows is constant. The dot-rows are also very dynamic at 200 K, with locations and lengths of rows often fluctuating over a period of a minute or two (the typical time between STM images). Upon heating to room temperature, at 0.10 ML, the dot-rows disorder reversibly.

The dots are planar $Ag_3S_3$ clusters, wherein the Ag atoms form an inner triangle and the S decorates the sides of the triangle [41]. This conclusion rests mainly on two results

from density functional theory (DFT). First, from DFT, the stability of the trimers is comparable to that of other possible adsorbates, i.e. various Ag-S moieties or chemisorbed S adatoms. Second, the dimensions of the clusters as measured in STM can be simulated from DFT results, using the Tersoff-Hamann method [45], and good agreement with experiment is obtained. The most distinctive dimension is the height, which is anomalously low in both theory and experiment: 0.14 nm and 0.13 nm, respectively. This is to be compared with the height of the ion cores, 0.22-0.23 nm. Presumably, the height is low because the electronegative sulfur atoms on the edges withdraw electron density. The good agreement between the experimental and theoretical heights supports the assignment of the dots as trimers. We also suggest[41], based on DFT, that the √7 structure observed at high coverage at room temperature could consist of $Ag_3S_3$ clusters, rather than a AgS-like overlayer [44] (noting that the two structures are related by rather small atomic displacements).

The $Ag_3S_3$ clusters, however, account for only 20-30% of the total sulfur. Evidence of the remaining S can be seen in the regions between the dot-rows. These regions have variable average heights and in some of them, a short-range (√3 x √3)R30$^o$ structure can be identified[41], while other regions appear to have different (but thus far unidentified) structures. It is rather remarkable that the dot-rows seem insensitive to the matrix in which they exist.

Next, consider coarsening. Typically, our experimental approach is to deposit a submonolayer coverage of Ag by physical vapor deposition in UHV, under conditions where nucleation and growth of Ag adatom islands occurs. The subsequent evolution of these islands on the Ag(111) terraces is then followed with STM.

The effect of sulfur on the Ag islands is illustrated in Fig. 3. The distribution of Ag islands on the clean surface is shown in Fig. 3a. This distribution coarsens very slowly at 300 K, and in fact there would be no measurable change over a period of a few minutes. However, after brief S exposure producing an S coverage of only 0.019 ML, the islands disappear completely over that period, as shown in Fig. 3b and 3c—images taken 3 and 4 minutes after S exposure, respectively. From experiments in which the coarsening kinetics are slower than in Fig. 3, i.e. at lower temperature, we have determined that the mechanism is Ostwald ripening (as it would be also on the clean Ag(111) surface [9, 46-48]). This was done by monitoring sequential STM images, which provided unequivocal evidence that islands shrink or grow, rather than diffusing significantly.

However, sulfur does not facilitate coarsening under all conditions. We have found that there is a lower limit of S coverage, about 0.010 ML, below which it has no significant effect on the coarsening kinetics. This lower limit roughly corresponds to the density of Ag atoms at step edges. Upon increasing S coverage by just a few hundredths of a monolayer, to 0.012 ML, coarsening accelerates significantly. This indicates that S first saturates step edges, and that S at Ag step edges does not influence the kinetics of Ag mass transport [49]. Only when S is free to exist on terraces can it influence the rearrangement of the Ag islands. We calculate that step saturation with S corresponds to only 1 S for every 2 edge Ag atoms. Thus, Ag is in no sense corralled in the inner part of islands, and it is quite reasonable that Ag detachment is not significantly impeded even when the steps are saturated with S.

There is another condition under which sulfur fails to accelerate Ag island transformations. Development of the dot-row structure appears to quench coarsening. This is illustrated in Fig. 4. In Fig. 4a, an ensemble of Ag islands has been prepared; conditions have

been tailored to make the islands small and ramified. Figure 4b, taken 2 hours later, shows that this ensemble is quite stable in the absence of S. After adsorption of 0.12 ML of S at 200 K, Fig. 4c shows that significant coarsening has occurred in a short period of time, leading to fewer but larger islands. At the same time, the dot-row structure has formed, as shown by the higher-magnification image in Fig. 4d. *Remarkably, the Ag islands do not coarsen further at 200 K—they are locked in place.* This is shown by Fig. 4e, taken 45 min after Fig. 4c-d. In other words, coarsening accelerates at some intermediate S coverage, but shuts down again when S coverage becomes too high.

Is the ordered dot-row structure linked to the arrested coarsening of the Ag islands, or is its existence in Fig. 4c-e just a coincidental consequence of the higher S coverage? To answer this, we can take advantage of the fact that the dot-rows disorder upon heating to 300 K. When a surface such as Fig. 4c-d is heated to room temperature, the Ag islands disappear completely, although S coverage remains constant. This strongly suggests that the correlation between the dot-row structure and slower ripening is not coincidental. Its exact relationship to coarsening is a subject of ongoing investigation in our laboratory. Additional evidence that the dot-row structure inhibits coarsening comes from observations of pitting on surfaces free of Ag-islands: rather than extract Ag from step edges, the S tends to consume Ag from the terraces. This is indicative of inhibited Ag mass transport.

In summary, we have found that S on Ag(111) accelerates coarsening of nanoscale features, very much like O on Ag(100). However, this acceleration occurs only under conditions where a minimum coverage has been exceeded, which we interpret to mean that S first decorates step edges and that this modification of step edges does not influence coarsening. Furthermore, the acceleration occurs only if a static dot-row structure is absent.

**3. Discussion and Perspectives**

The effect of sulfur on coarsening of nanosized features on Ag(111) surfaces is part of a larger issue, namely, whether chalcogens generally accelerate coarsening on surfaces of coinage metals and, if so, whether there is a common underlying mechanism. The work reviewed in this article adds to the body of literature, presented in Section 1, suggesting that accelerated coarsening is indeed a general phenomenon. However, this work also reveals that the effect can be blocked if S coverage is either too high or too low, points that had not been recognized previously.

With regard to establishing whether a general mechanistic and energetic picture exists, this is certainly an open challenge. What are some of the possibililties? As a starting point, note that the two systems we have studied— O/Ag(100) and S/Ag(111)—both exhibit Ostwald (not Smoluchowski) ripening. The same is true for S/Cu(111) [29]. In Ostwald ripening, the two key processes—either of which can be rate-limiting—are attachment-detachment from island edges, and diffusion of metal-atom carriers across terraces. The effective activation barrier for Ostwald ripening has the form $E_{OR} = E_d + E_{form} + E_{attach}$, where $E_d$ is the terrace diffusion barrier, $E_{form}$ is the energy difference associated with forming the metal-atom carrier, and $E_{attach}$ is any extra barrier, above the terrace diffusion barrier, to attachment at step edges[7, 10]. See Fig. 5a. The term $E_{atttach}$ is zero for terrace-diffusion-limited kinetics, and this describes the coarsening kinetics of the surfaces being considered here when they are in their clean (adsorbate-free) state. The term $E_{form}$ controls the density of metal carriers on terraces. Note that acceleration generally requires a reduction in $E_{OR}$. However, there exist circumstances in which the change in $E_{OR}$ cannot be used to *quantitatively* predict the magnitude of the change in coarsening rate [29, 49].

3.1 First scenario: Mass transport by M adatoms

One possibility is that the adsorbate could change the above energetics, but leave the basic process unchanged—in other words, that individual metal atoms remain as the main agents of mass transport.

Consider first that the adsorbate might change the energetics at the step edge, relative to the adsorbate-free surface, leaving the other energetic quantities unchanged. More specifically, the adsorbate might raise $E_{attach}$ for the M atom above zero. However, this would inhibit, not enhance, coarsening, so it can be ruled out. On the other hand, the adsorbate might reduce the barrier for initial movement of a metal atom away from the island. This case is shown by the dotted curve in Fig. 5a. However, this would not affect $E_{form}$, which just depends on the difference between the energies of the M adatom at the step edge and on the terrace, not on finer details of the potential energy surface. Thus, the population of M on the terraces would not be affected.

For S/Ag(111), we assert that there is no significant $E_{attach}$. This is because a minimum coverage is necessary to saturate step edges, and below the minimum coverage, S has no effect on the coarsening rate relative to the clean surface kinetics.

Next, consider the possibility that the adsorbate modifies the diffusion of Ag adatoms across terraces through indirect interactions, e.g. strain fields. However, the amount of S on terraces necessary to accelerate coarsening is very small—less than 0.01 ML—so this seems implausible. Very low coverages were also reported to accelerate coarsening for S/Cu(111) [29] and for O/Ag(100) [36, 50].

3.2 Second scenario: Mass transport by M-X clusters

The above line of reasoning leads to the conclusion that the adsorbate forms an M-X cluster that participates in mass transport. The energetics must be such that $E_{OR}$ with the adsorbate is less than $E_{OR}$ for the clean metal. This can be true if $E_d$ or $E_{form}$ or $E_{attach}$ (or some combination) is less positive than for the clean metal. But more importantly, the chalcogen changes the basic process, such that mass transport is no longer dominated by diffusion of single metal atoms, but rather by clusters that serve as carriers of metal. Essentially two such models have been suggested thus far.

In the first cluster-carrier model, an intact cluster detaches from a step edge and diffuses across terraces, re-attaching when it encounters another step edge [36]. A second species, with a lower M:X ratio, must also be able to attach/detach and diffuse. This is because edges of smaller islands must have a way to become repopulated with X as coarsening proceeds, in accord with experimental observation [36]. The constituents of such a shuttle pair could, for instance, be $MX_2$ and X, respectively. This type of cluster-based model is illustrated in Fig. 5b. This model was proposed for O/Ag(100), partly on the basis of evidence that O interacts very strongly with step edges, even changing the step orientation [36]. However, it is not apparent that this model is compatible with a finite threshold coverage for coarsening, as we have observed for S/Ag(111). [A finite threshold for coarsening can be inferred from the published data for S/Cu(111) as well (see Fig. 1 of Ref. [29]), although it was not noted explicitly.] If a lower threshold is generally observed, that would go far toward excluding this model. Careful coverage-dependent studies are warranted in other systems.

In the second cluster-carrier model, only metal atoms detach from step edges, but close to the step edge they form chalcogen-metal clusters. These M-X clusters can diffuse

across terraces, and are in dynamic equilibrium with adsorbed M and X. If they dissociate close to a step edge, they may contribute M atoms back to the step. This mechanism is illustrated in Fig. 5c. It was proposed originally for S/Cu(111), because a transition between terrace-diffusion-limited and attachment-detachment-limited-like kinetics observed in that system could be explained qualitatively by an appropriate kinetic model [29]. It is broadly compatible with the data for S/Ag(111) as well [49].

In summary, the two cluster-based models differ primarily in whether the species that attaches/detaches from step edges is an intact cluster, or a single metal atom. They also differ in whether or not a secondary shuttle is necessary. Only one of the two models (Fig. 5c) is compatible, in an obvious way, with a threshold coverage for accelerated coarsening. In both models, the main carrier is an M-X cluster. As emphasized by Feibelman, ripening can occur quickly even if the M-X clusters diffuse more slowly than individual M adatoms, because slower diffusion can be compensated by higher carrier density, together with higher density of M per carrier [28]. Neither model, to date, has been adapted to explain the arrested coarsening presented in Section 2.

These two cluster-based mechanisms represent two extremes, and intermediate cases are also viable. For instance, a cluster such as MX might detach (attach) from a cluster edge, then react with X to form $MX_2$ as the main carrier of M atoms.

In the S/Cu(111) system, it was proposed that the clusters primarily responsible for mass transport are $Cu_3S_3$, based on an observed third-order coverage-dependence of the ripening rate [29]. However, $Cu_3S_3$ clusters have not been imaged directly on Cu(111), even below room temperature [51, 52]. In our system, $Ag_3S_3$ clusters can be imaged directly, below room temperature, perhaps because their formation energy is negative [41, 49]

whereas it is positive for the $Cu_3S_3$ clusters [28]. ($Ni_3S_3$ clusters have also been reported recently, in STM studies on Ni(111) [53].) However, more direct proof that these trimers enhance the ripening kinetics is desirable. This is particularly true because DFT indicates that other clusters, notably $MX_2$, are also quite stable on the (111) surfaces of Cu and Ag [49]. Even though such clusters have not yet been observed directly, it seems likely that they make a significant contribution to coarsening.

## 4. Conclusions

For three metal-chalcogen systems—O/Ag(100), S/Ag(111), and S/Cu(111)— the adsorbate serves to accelerate coarsening. In one of these systems, S/Ag(111), our work has shown that coarsening is unaffected if the S coverage is too low, and inhibited if dense rows of $Ag_3S_3$ trimers are present. Mechanistically, metal-chalcogen clusters are implicated as major agents of mass transport in all three systems. A challenge in the field is to establish whether accelerated metal coarsening is indeed a universal effect in coinage metal-chalcogen systems, as suggested by the work thus far, and if so, whether a general energetic and mechanistic picture can be developed.

## Acknowledgments

This work was supported primarily by NSF Grants CHE-0414378 and CHE-0809472. DJL was supported by the Division of Chemical Sciences, Basic Energy Sciences, US Department of Energy (USDOE). The work was performed at the Ames Laboratory which is operated for the USDOE by Iowa State University under Contract No. DE-AC02-07CH11358.

**References**

[1] L. Lindfors, P. Skantze, U. Skantze, M. Rasmusson, A. Zackrisson, U. Olsson, Langmuir 22 (2006) 906-910.

[2] S. Yamasaki, H.K.D.H. Bhadeshia, Mat. Sci. Technol. 19 (2003) 1335-1343.

[3] K. Miyazaki, Contr. Mineralogy Petrology 108 (1991) 118-128.

[4] C.T. Campbell, Surf. Sci. Rep. 27 (1997) 3-111.

[5] H. Brune, Surf. Sci. Rep. 31 (1998) 121-229.

[6] H. Brune, "Growth of Metal Clusters at Surfaces" in: K.H. Meiwes-Broer (Ed.), Metal Clusters at Surfaces, Berlin, 2000, pp. 67-105.

[7] M. Zinke-Allmang, L.C. Feldman, M.H. Grabow, Surf. Sci. Rep. 16 (1992) 377.

[8] W. Theis, N.C. Bartelt, R.M. Tromp, Phys. Rev. Lett 75 (1995) 3328-3332.

[9] K. Morgenstern, G. Rosenfeld, G. Comsa, Phys. Rev. Lett. 76 (1996) 2113.

[10] M. Giesen, Prog. Surf. Sci. 68 (2001) 1-153.

[11] H. Brune, "Creating Metal Nanostructures at Metal Surfaces Using Growth Kinetics" in: E. Hasselbrink (Ed.), Handbook of Surface Science, Amsterdam, 2008, pp. 761-786.

[12] J.S. Ozcomert, W.W. Pai, N.C. Bartelt, J.E. Reutt-Robey, Phys. Rev. Lett. 72 (1994) 258-261.

[13] E.R. Frank, R.J. Hamers, J. Catalysis 172 (1997) 406-413.

[14] A. Klust, R.J. Madix, J. Chem. Phys. 126 (2007) 084707.

[15] A. Pimpinelli, J. Villain, Physics of Crystal Growth, Cambridge, Cambridge University Press, 1998.

[16] T. Michely, J. Krug, Islands, Mounds, and Atoms: Patterns and Processes in Crystal Growth Far from Equilibrium, Berlin, Springer Verlag, 2004.

[17] F. Besenbacher, J. NØrskov, Prog. Surf. Sci. 44 (1993) 5-66.

[18] P.A. Thiel, P.J. Estrup, "Metal surface reconstructions" in: A.T. Hubbard (Ed.), The Handbook of Surface Imaging and Visualization, Boca Raton, Florida, 1995, p. 407.

[19] X.E. Verykios, F.P. Stein, R.W. Coughlin, Catalysis Rev. 22 (1980) 197-234.

[20] D.J. Sajkowski, M. Boudart, Catal. Rev. 29 (1987) 325-360.

[21] R.A. van Santen, H. Kuipers, Adv. Catal. 35 (1987) 265-321.

[22] J.G. Serafin, A.C. Liu, S.R. Seyedmonir, J. Mol. Cat. A 131 (1998) 157-168.

[23] K.A. Willets, R.P. Van Duyne, Ann. Rev. Phys. Chem. 58 (2007) 267-297.

[24] F. Schreiber, J. Phys.: Cond. Matter 16 (2004) R881-R900.

[25] A. Ulman, Self-Assembled Monolayers of Thiols (Thin Films), New York, Academic Press, 1998.

[26] C.D. Dimitrakopoulos, D.J. Mascaro, IBM J. Res. Dev. (2001)

[27] J. Perdereau, G.E. Rhead, Surf. Sci 7 (1967) 175-187.

[28] P.J. Feibelman, Phys. Rev. Lett. 85 (2000) 606-609.

[29] W.L. Ling, N.C. Bartelt, K. Pohl, J. de la Figuera, R.Q. Hwang, K.F. McCarty, Phys. Rev. Lett. 93 (2004) 166101.

[30] B.K. Min, A.R. Alemozafar, M.M. Biener, J. Biener, C.M. Friend, Topics in Catalysis 36 (2005) 77-90.

[31] M.M. Biener, J. Biener, C.M. Friend, Langmuir 21 (2005) 1668-1671.

[32] M.M. Biener, J. Biener, C.M. Friend, Surf. Sci 601 (2007) 1659-1667.

[33] C.M. Friend, J. Phys. Chem. 110 (2006) 15663.

[34] B.H. Cooper, D.R. Peale, J.G. McLean, R. Phillips, E. Chason, "Mass flow and stability of nanoscale features on Au(111)" in: H.A. Atwater, E. Chason, M.H. Grabow, M.

Lagally (Eds.), Evolution of Surface and Thin Film Microstructure: MRS Symposium Proceedings, Warrendale, PA, 1993, p. 37.

[35] D.R. Peale, B.H. Cooper, J. Vac. Sci. Technol. A 10 (1992) 2210-2215.

[36] A.R. Layson, J.W. Evans, P.A.Thiel, Phys. Rev. B 65 (2002) 193409.

[37] A.R. Layson, J.W. Evans, V. Fournée, P.A. Thiel, J. Chem. Phys. 118 (2003) 6467-6472.

[38] G. Rosenfeld, K. Morgenstern, M. Esser, G. Comsa, Appl. Phys. A 69 (1999) 489-496.

[39] C.T. Campbell, S.C. Parker, D.E. Starr, Science 298 (2002) 811-814.

[40] J.-M. Wen, S.-L. Chang, J.W. Burnett, J.W. Evans, P.A. Thiel, Phys. Rev. Lett. 73 (1994) 2591-2593.

[41] M. Shen, D.-J. Liu, C. Jenks, P.A. Thiel, J. Phys. Chem. C 112 (2008) 4281-4290.

[42] K. Schwaha, N.D. Spencer, R.M. Lambert, Surf. Sci 81 (1979) 273-284.

[43] G. Rovida, F. Pratesi, Surf. Sci 104 (1981) 609-624.

[44] M. Yu, D.P. Woodruff, C.J. Satterley, R.G. Jones, V.R. Dhanak, J. Phys. Chem. C 111 (2007) 3152-3162.

[45] J. Tersoff, D.R. Hamann, Phys. Rev B 32 (1985) 805.

[46] K. Morgenstern, G. Rosenfeld, E. Laegsgaard, F. Besenbacher, G. Comsa, Phys. Rev. Lett. 80 (1998) 556-559.

[47] K. Morgenstern, G. Rosenfeld, G. Comsa, M.R. SØrensen, B. Hammer, E. Lægsgaard, F. Besenbacher, Physical Review B 63 (2001) 045412-1.

[48] M. Shen, J.-M. Wen, C.J. Jenks, P.A. Thiel, D.-J. Liu, J.W. Evans, Phys. Rev B 75 (2007) 245409.

[49] M. Shen, D.-J. Liu, C. Jenks, P. Thiel, J. Evans, J. Chem. Phys. submitted (2008)

[50] A.R. Layson, P.A. Thiel, Surf. Sci. 472 (2001) L151-L156.

[51] E. Wahlström, I. Ekvall, T. Kihlgren, H. Olin, S.A. Lindgren, L. Wallden, Phys. Rev. B 64 (2001) 155406.

[52] E. Wahlström, I. Ekvall, H. Olin, S.A. Lindgren, L. Wallden, Phys. Rev. B 60 (1999) 10699.

[53] M. Yamada, H. Hirashima, A. Kitada, K. Izumi, J. Nakamura, Surf. Sci. 602 (2008) 1659-1668.

**Figure Captions**

**Fig. 1.** Two sequences of STM images, following deposition of 0.3 ML Ag on Ag(100). Image size: 100 nm x 100 nm. Panels (a-c) show the coarsening of the clean surface at 250 K, at various times after deposition. (a) 25 min (b) 89 min (c) 160 min. Panels (d-f) show the coarsening of the surface at 250 K, after exposure to 20 L oxygen. (d) 9 min after deposition (e) 77 min (f) 167 min. Note that the total time elapsed in (c) and (f) are very similar.

**Fig. 2.** STM image of Ag(111) with 0.10 ML of adsorbed sulfur at 200 K. Image size: 30 nm x 30 nm.

**Fig. 3.** Sequence of STM images of Ag(111). (a) After deposition of 0.8 ML Ag at 300 K. (b) 3 min after deposition of 0.019 ML S at 300 K. (c) Same as (b), 1 min later. Image size is 300 nm x 300 nm in (a), and 250 nm x 250 nm in (b-c).

**Fig. 4.** Sequence of STM images of Ag(111). (a) After deposition of 1.2 ML Ag at 135 K, then heating to 200 K. (b) Follows (a), after 120 minutes in ultrahigh vacuum at 200 K. (c) After deposition of 0.12 ML S at 200 K. (d) Same as (c), but higher magnification so that dot-rows are visible. (e) Same as (d), after 45 min in vacuum at 200 K. Image size in (a-c) is 200 nm x 200 nm, and in (d-e) it is 70 nm x 70 nm.

**Fig. 5.** (a) Schematic of the possible potential energy surface of a M adatom near a step edge. (b, c) Schematic representations of the two cluster-based mechanisms for accelerated coarsening. For clarity, only processes and species involved in net mass transfer between the edge of the small M island, and the edge of the large M island or terrace, are shown. The cluster is arbitrarily shown with $MX_2$ stoichiometry. In (b), the cluster detaches and attaches intact at step edges. The adatom X at top serves as the shuttle to repopulate the edge of the smaller island, but this could in principle be any species with a lower M:X stoichiometry than

the main carrier. In (c), metal adatoms attach and detach at step edges, forming clusters on the terraces.

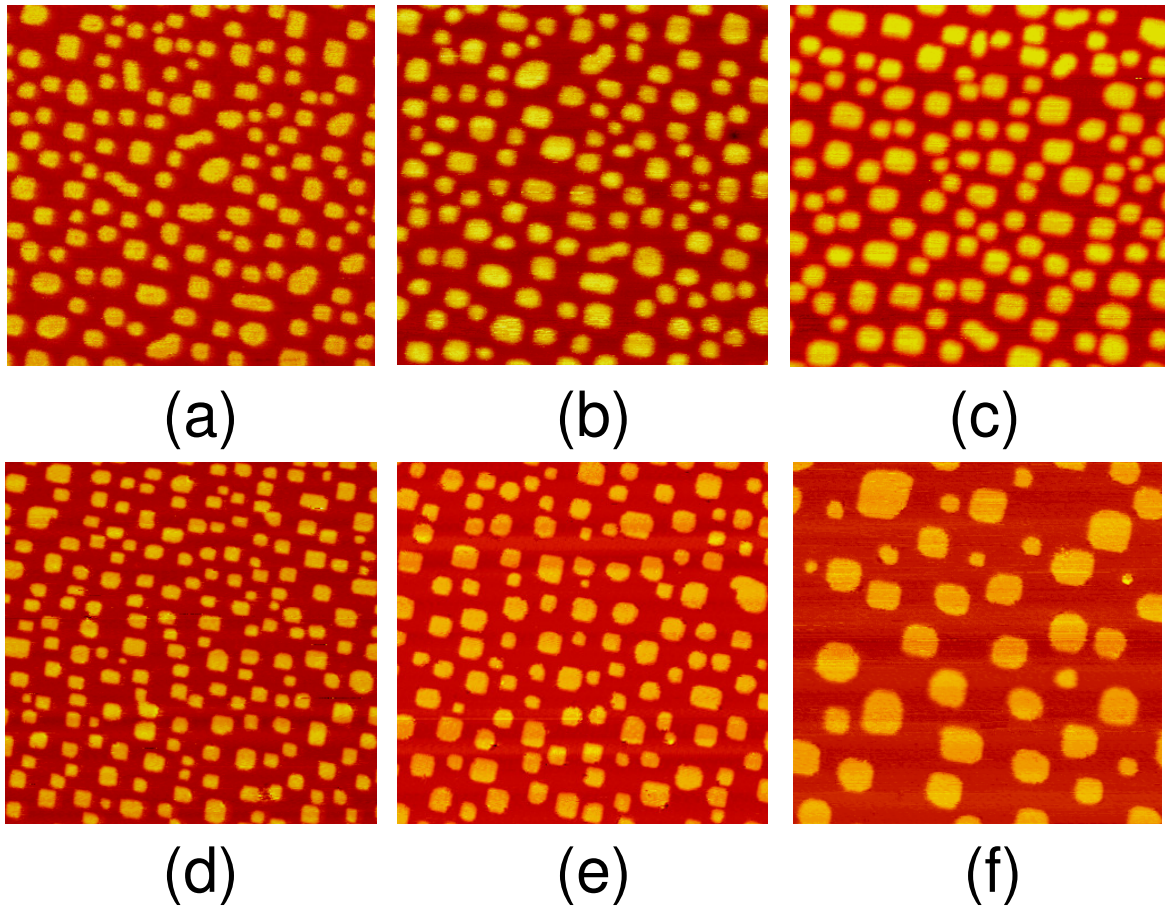


Figure 1

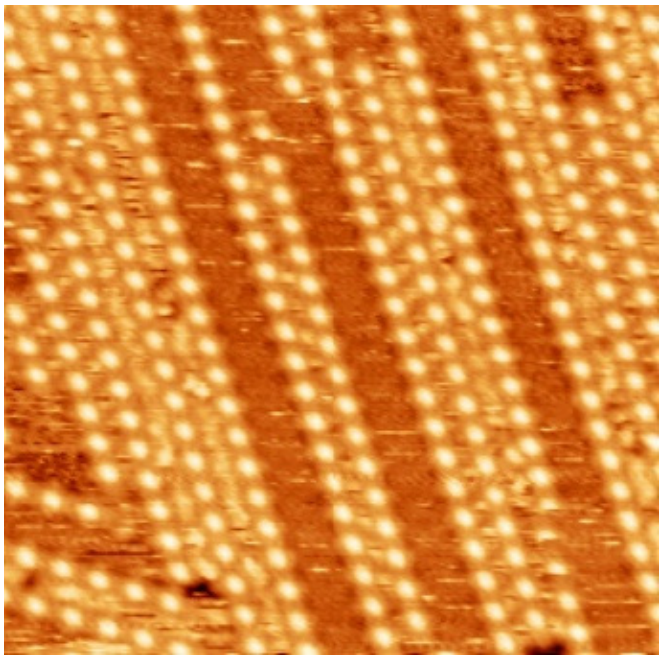

Figure 2

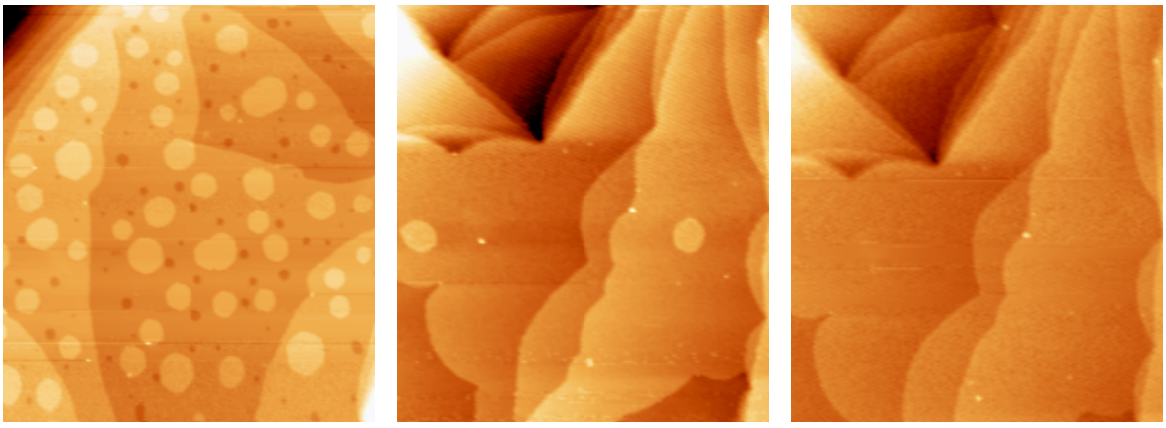


Figure 3

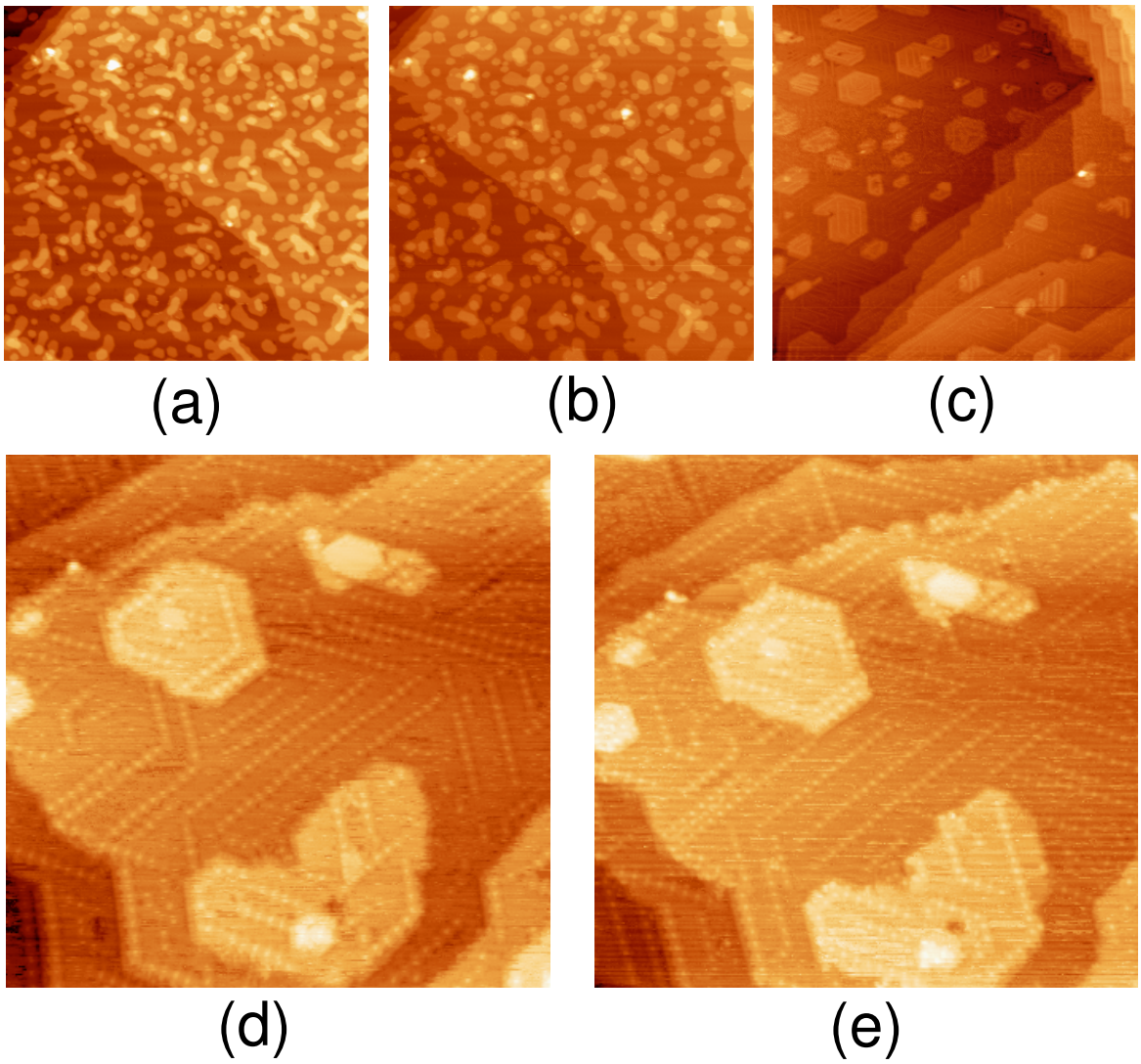


Figure 4

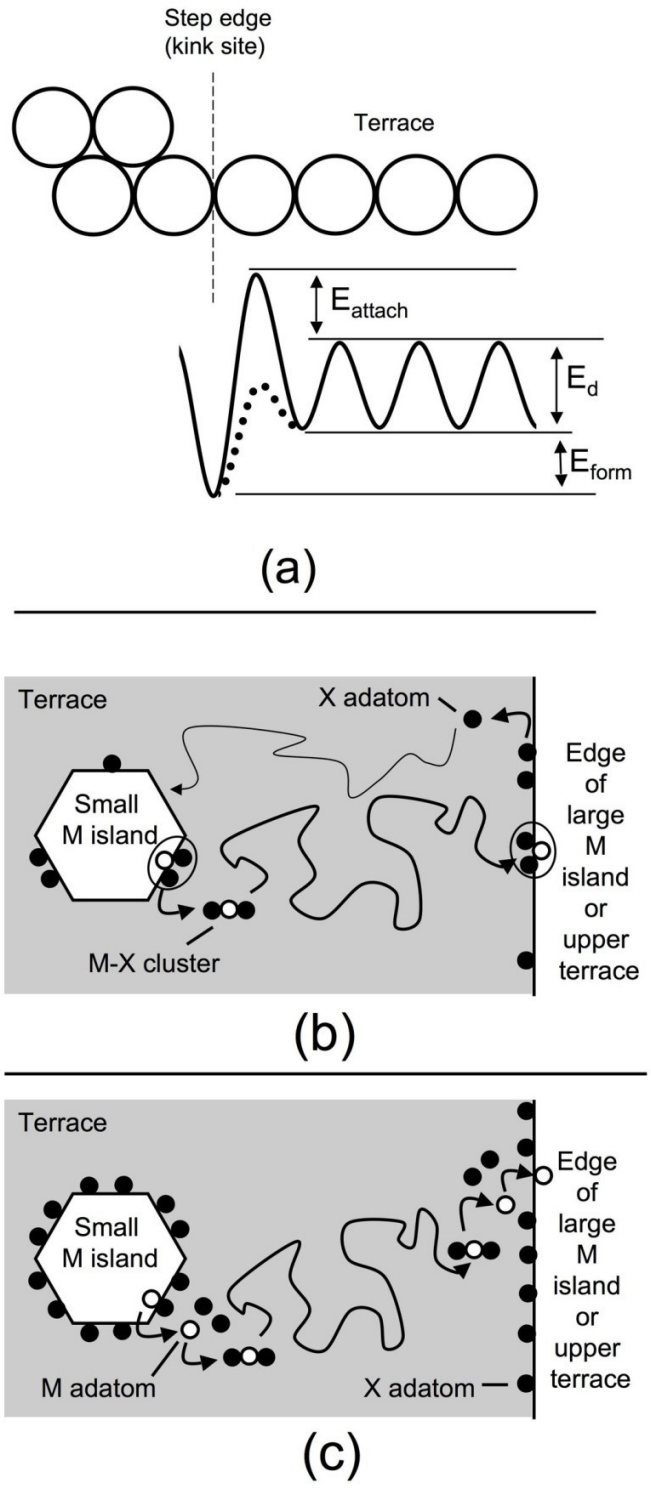


Figure 5

**Appendix: Supplemental Data below Room Temperature.**

Here we present additional, relevant data concerning the effect of S on coarsening of Ag islands on Ag(111). The data span different S coverages, both before and after Ag deposition. The coverage of deposited Ag ranges from about 0.3 to 0.8 ML, and this variation appears to be insignificant for the purposes of this work. In contrast to the experiments described in Ch. 3 and Appendix E, coarsening is studied ***below*** room temperature (RT).

1. S deposition (0.057 ML) followed by Ag deposition (~ 0.3 ML) at 250 K

Fig. A1 shows STM images before and after Ag deposition on the 0.057 ML S/Ag(111) surface at 250 K. The surface forms rough step edges with S adsorption at 250 K (Fig. A1a). No dot-row structure is found. No Ag islands are found after 0.3 ML Ag deposition as seen in Fig. A1b. This means that at 250 K, S adsorption higher than the critical S coverage can also lead to fast Ag island decay as for the room temperature case described in Chapter 3.

2. Ag deposition (~0.2 ML) followed by S deposition (0.004 ML) at 225 K

Fig. A2 shows STM images before and after S deposition on the Ag/Ag(111) surface at 225 K. As seen in Fig. A2a, hexagonal Ag islands form on the clean Ag(111) surface after 0.2 ML Ag deposition. The area of the Ag islands is unchanged after S deposition and no obvious change happens except that the two islands on the bottom right coalesce to form one island and the Ag islands become more round than hexagonal (Fig. A2b and c). As presented in Chapter 2, no obvious change (e. g. step faceting) can be found if the S coverage is lower than 0.01 ML at 200 K. Here the S coverage is only 0.004 ML and it is too low to form any structure or to cause fast island decay.

3. Ag deposition (~ 0.8 ML) followed by S deposition (0.135 ML) at 225 K

Fig. A3 shows STM images before and after S deposition on the Ag/Ag(111) surface at 225 K. Right before S deposition, layers of hexagonal islands form on the clean Ag(111) surface and only local coalescence takes place (Fig. A3a). The S deposition takes 15 to 20 min. Fig. A3b shows that significant coarsening has occurred in a short period of time during S deposition, leading to fewer but larger islands. At the same time, the dot-row structure forms as shown by the inset, a higher magnification image. Remarkably, the Ag islands do not coarsen further at this temperature. So after the sulfur has reached a certain coverage, it fails to accelerate the Ag islands' transformation and development of the dot-row structure appears to quench coarsening.

The following parts (part 4 to 11) show a series of in situ S deposition on Ag/Ag(111) surface with different S coverages at 200 K.

4. Ag deposition (~0.4 ML) followed by in situ S deposition (0.009 ML) at 200 K

Fig. A4 shows a series of STM images before, during, and after S deposition with final S coverage at 0.009 ML at 200 K. As shown in Fig. A4a, b, and c, it is easy to tell that almost nothing happens during S deposition with this low S coverage. Fig. A4d shows the surface at 2 hours after S deposition. Comparing it with the surface right after S deposition in Fig. A4c, we can find that only local coalescence happens and no coarsening happens, which is the same as for Ag islands on the clean Ag(111) surface. As reported earlier in Chapter 2, 0.009 ML S adsorption on Ag(111) surface is not high enough to form any kind of structures (faceting step edge or dot-row) and it does not lead to any Ag island transformation.

5. Ag deposition (~ 0.3 ML) followed by in situ S deposition (0.021 ML) at 200 K

Fig. A5 shows a series of STM images before, during, and after S deposition with final S coverage at 0.021 ML at 200 K. Some Ag islands disappear during S deposition as marked with circles in Fig. A5a and b. After S deposition, no other obvious change happens (Fig. A5c).

6. Ag deposition (~ 0.3ML) followed by in situ S deposition (0.036 ML) at 200 K

Fig. A6a shows an STM image after Ag deposition on the clean Ag(111) surface. As is mentioned in the main text, this ensemble of Ag islands is quite stable in the absence of S. Our image quality during and right after S deposition is poor, so here we show the surface 35 min and 142 min after S deposition, in Fig. A6b and A6c, respectively. As we can see from Fig. A6b, the Ag island density after S deposition is much lower than that of the clean surface in Fig. A6a. After scanning the same surface for another ~ 110 min, some circled small islands disappear via Ostwald ripening and no other change is obvious after all the small islands disappear. So at this S coverage (0.036 ML), when only a few dot-rows form, the sulfur does not totally quench coarsening, and Ostwald ripening can still proceed for Ag islands after S deposition.

7. Ag deposition (~ 0.3 ML) followed by in situ S deposition (0.14 ML) at 200 K

Fig. A7 shows STM images before, during, and after S deposition on the Ag/Ag(111) surface at 200 K. Small Ag islands become smaller or even disappear and some large Ag islands become smaller, forming irregular shapes during S deposition, as shown from Fig. A7b to A7d. After S deposition ends, Ag islands do not coarsen further. As we look closer at the surface as in Fig. A7e, the dot-row structure already forms throughout the whole Ag(111) surface at a coverage of 0.14 ML, and it appears to quench coarsening.

8. Ag deposition (~ 0.7 ML) followed by in situ S deposition (0.28 ML) at 200 K

Fig. A8 shows STM images before and after S deposition on the Ag/Ag(111) surface at 200 K. It is clear that the island density decreases greatly after S deposition (Fig. A8b) compared to the density on the clean surface (Fig. A8a). The dot-row structure forms after S deposition; Ag islands and vacancy pits become irregular in shape. The formation of the dot-row structure stops further coarsening after S deposition.

9. Ag deposition (~ 0.3 ML) followed by in situ S deposition (0.35 ML) at 200 K

Fig. A9 shows STM images before, during, and after S deposition on the Ag/Ag(111) surface at 200 K. As the dot-row structure starts to form (Fig. A9b), Ag islands get smaller due to fast coarsening, which is more obvious in the lower half of Fig. A9c. When the dot-row structure forms completely, no more coarsening happens. So based on our observations in parts 6 to 9, we are able to conclude that fast island decay only happens during dot-row formation before it covers the whole surface, and once the structure covers, it blocks coarsening. By scanning another area of the surface, we find an even lower Ag island density and some vacancy pits have already formed, as shown here in Fig. A9d. Presumably, this is due to a higher local S coverage in this region. This means the STM tip has a shielding effect by the tip holder during S deposition, so the S coverage of the second part is slightly higher than in the region that was scanned during deposition.

10. Ag deposition (~ 0.5 ML) followed by in situ S deposition (0.49 ML) at 200 K

Fig. A10 shows a series of STM images before, during, and after 0.49 ML S deposition on Ag/Ag(111) at 200 K. As shown in Fig. A10 b and A10c, facet step edge and dot-row structures form, and Ag island density decreases greatly during S deposition. Some irregularly-shaped vacancy pits also form during and after S deposition. Another region of the same surface shows no Ag islands and only vacancy pits as in Fig. A10e. At higher

magnification, the second region shows a √7 structure in the encircled area, the same as Fig. A2b' in the Appendix of Chapter 2. The tip shielding effect presumably causes the second scanning region to have a real S coverage of ~ 0.5 ML, which leads to the √7 structure formation.

11. Ag deposition (~ 0.4 ML) followed by in situ S deposition (0.73 ML) at 200 K

Fig. A11a and A11b show STM images before and after 0.73 ML S deposition on the Ag/Ag(111) surface at 200 K. It is clear that the Ag island density is high on the Ag/Ag(111) surface in Fig. A11a. Irregularly-shaped Ag islands form without any dot-row structure or √7 structure. Although the surface here in Fig. A11b is similar to Fig. A2b in chapter 2 in low magnification, the S coverage at this point is much higher than the ideal S coverage for forming √7 structure (0.43 ML), and we are not able to see fine structure due to high S coverage.

12. S deposition (0.066 ML) followed by Ag deposition (~ 0.3 ML) at 200 K

Fig. A12 shows STM images before and after Ag deposition on 0.066 ML S/Ag(111) at 200 K. As shown in Fig. A12a, the dot-row structure forms. After depositing 0.3 ML Ag onto this S preadsorbed surface, no typical features such as we normally have for Ag deposition on clean Ag(111) as in Fig. A9a, are observed. Instead, irregularly-shaped islands with dot-row structure as in Fig. A12b and inset form on this surface, and no coarsening happens afterwards. This is the same as we reported in the main part of this chapter (Fig. 4d and 4e): Irregularly-shaped islands with dot-row structure form after depositing S onto Ag/Ag(111). So the same conclusion is reached, regardless of the sequence of deposition.

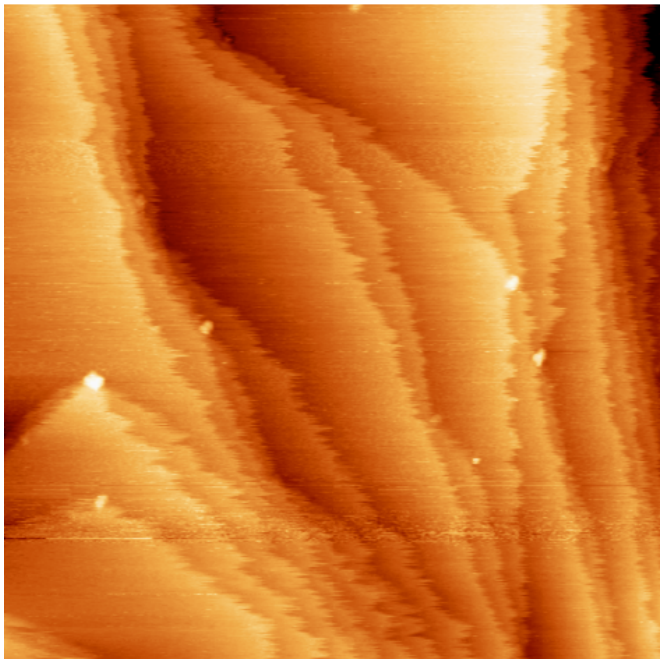

Fig. A1a. 06-25-2007, # 11, 200 nm x 200 nm, after S deposition, 250 K

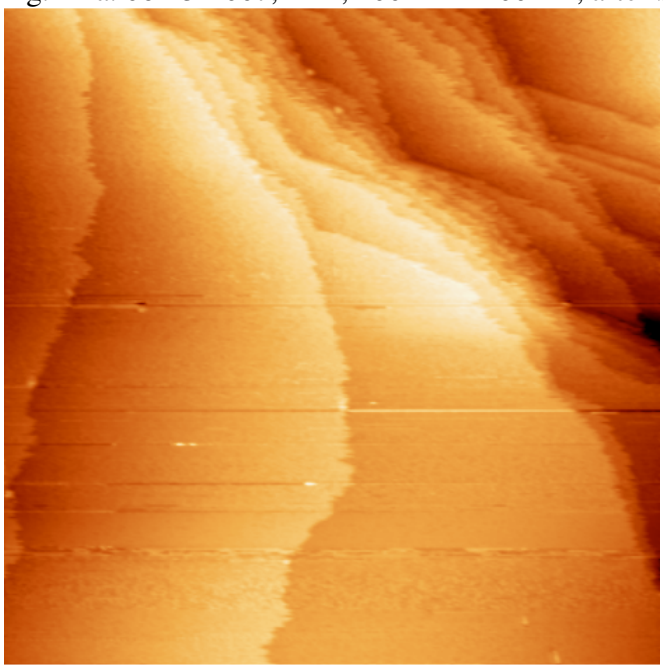

Fig. A1b. 06-25-2007, # 27, 200 nm x 200 nm, after Ag deposition, 250 K

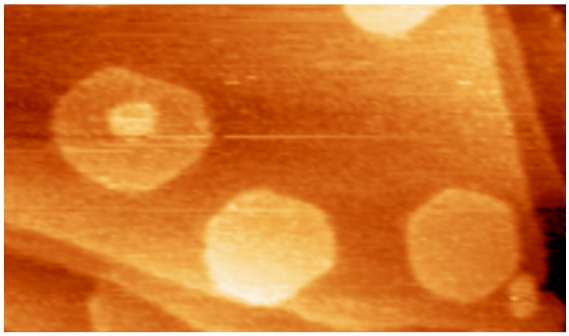

Fig. A2a. 12-28-2006, # 39, 120 nm x 70 nm, clean Ag

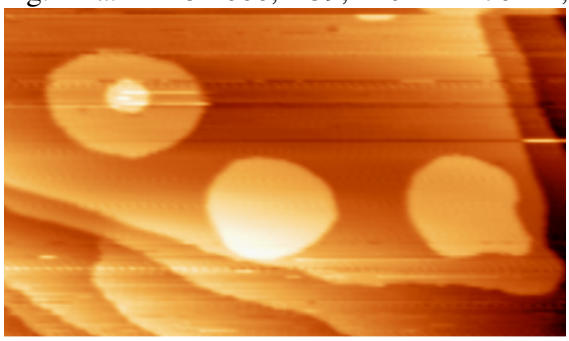

Fig. A2b. 12-28-2006, # 47, 120 nm x 70 nm, 30 min after S deposition, 19:50 pm

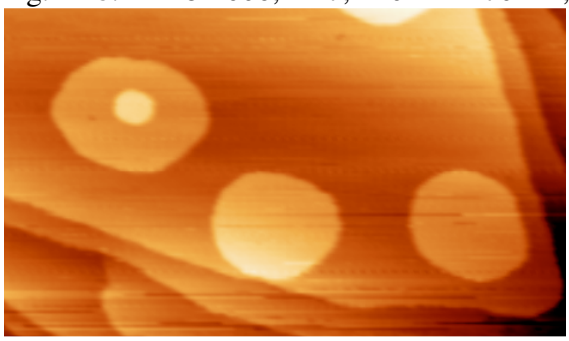

Fig. A2c. 12-28-2006, # 82, 120 nm x 70 nm, 152 min after S deposition, 21:52 pm

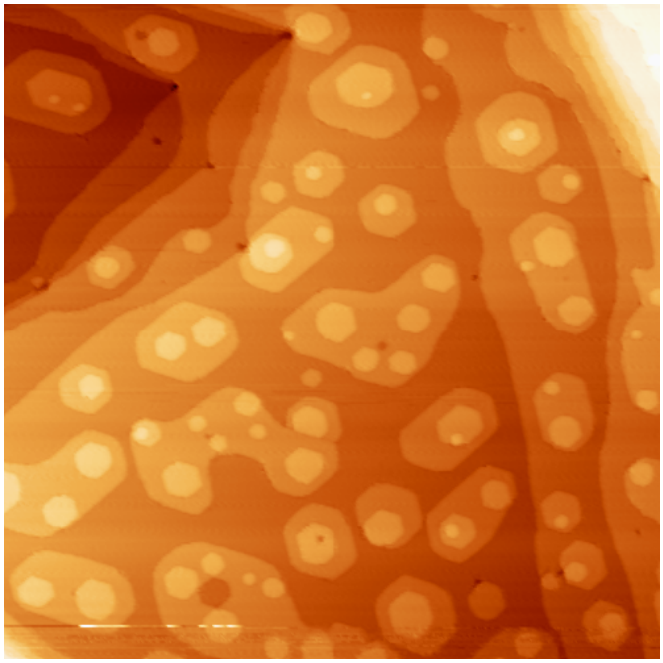

Fig. A3a. 01-03-2007, # 51, 200 nm x 200 nm, after Ag deposition, 225 K, 19:48 pm

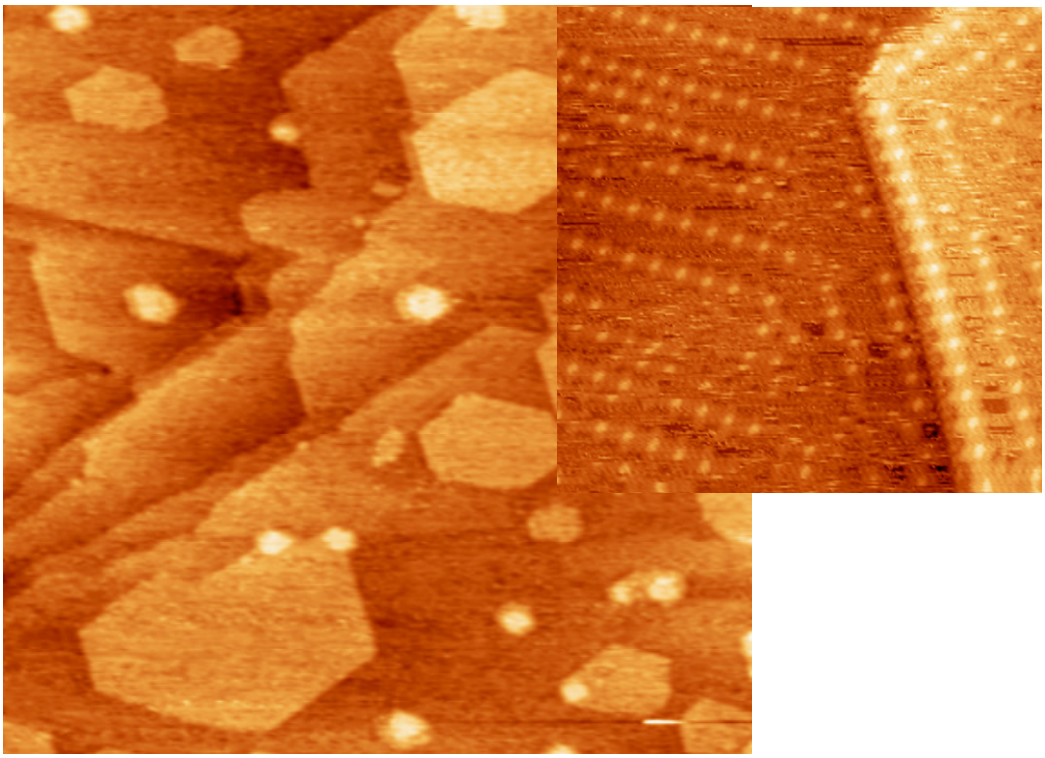

Fig. A3b. # 61, 200 nm x 200 nm, 5 min after S deposition, 225 K, 20:40 pm, Inset: 30 nm x 30 nm

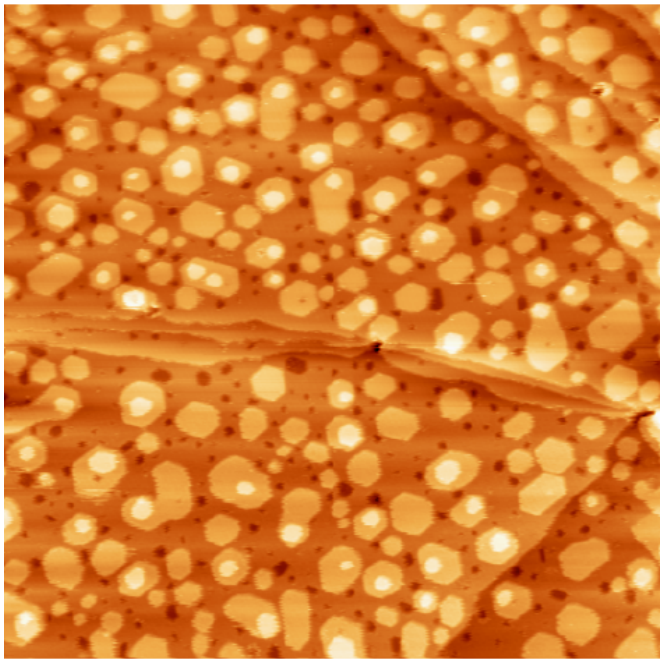

Fig. A4a. 02-26-2008, # 25, 140 nm x 140 nm, after Ag deposition, 200 K, 18:40 pm

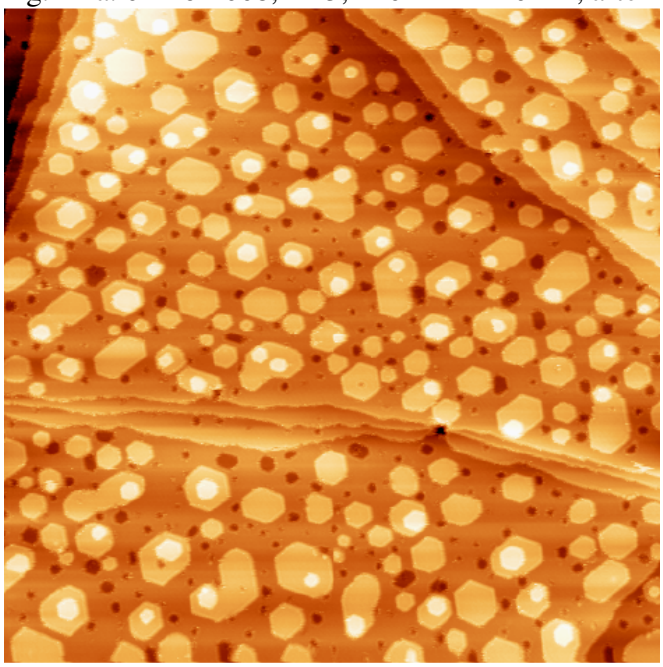

Fig. A4b. 02-26-2008, # 28, 140 nm x 140 nm, during S deposition, 200 K, 18:45 pm

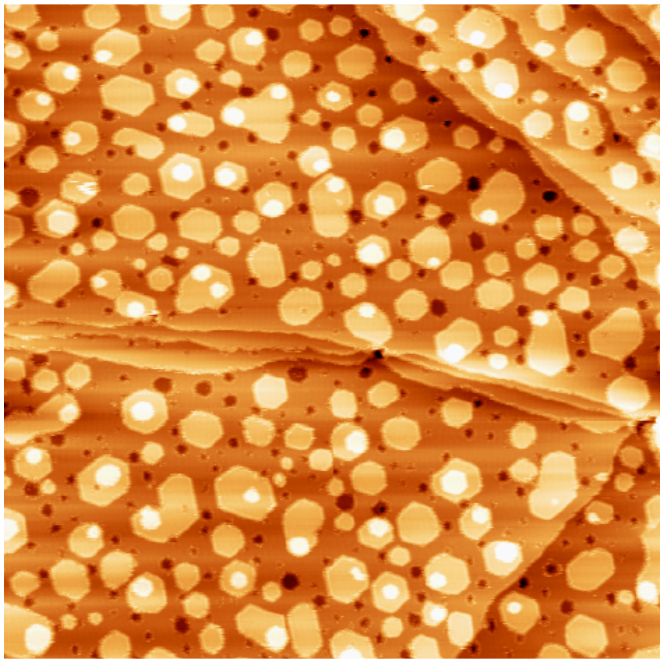

Fig. A4c. 02-26-2008, # 30, 140 nm x 140 nm, right after S deposition, 200 K, 18:48 pm

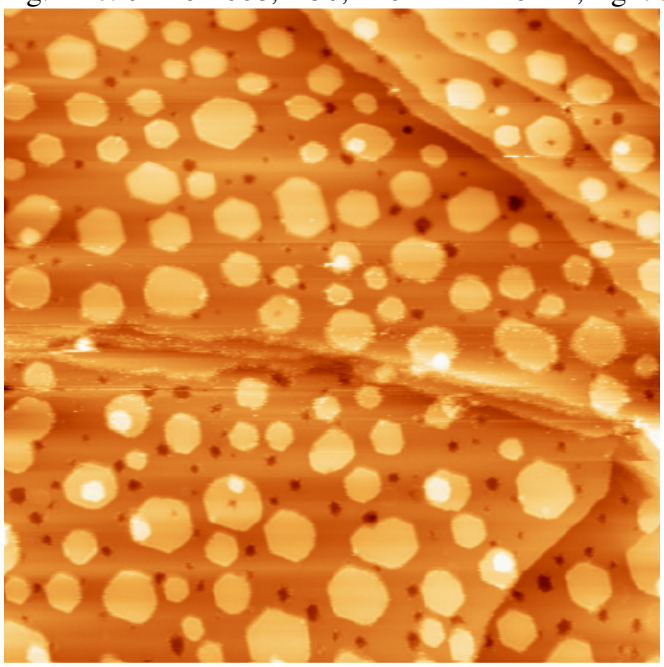

Fig. A4d. 02-26-2008, # 86, 140 nm x 140 nm, after S deposition, 200 K, 20:36 pm

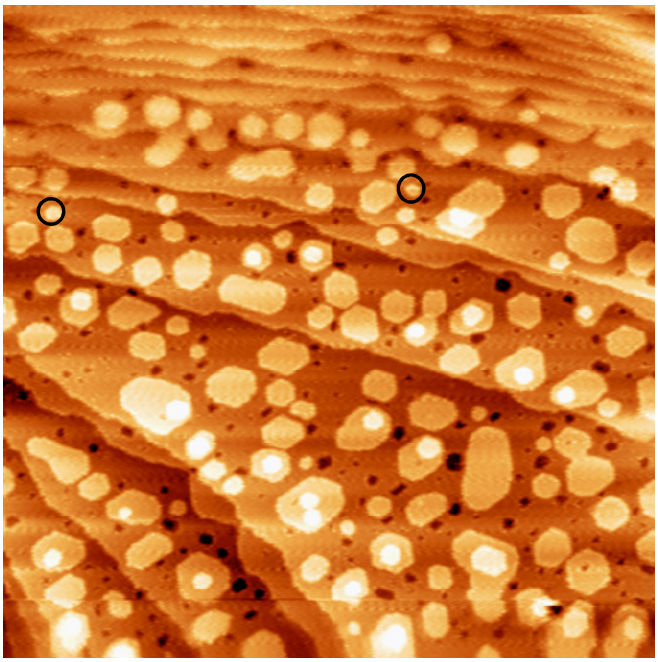

Fig. A5a. 02-19-2008, # 28, 110 nm x 110 nm, after Ag deposition, 200 K, 19:32 pm

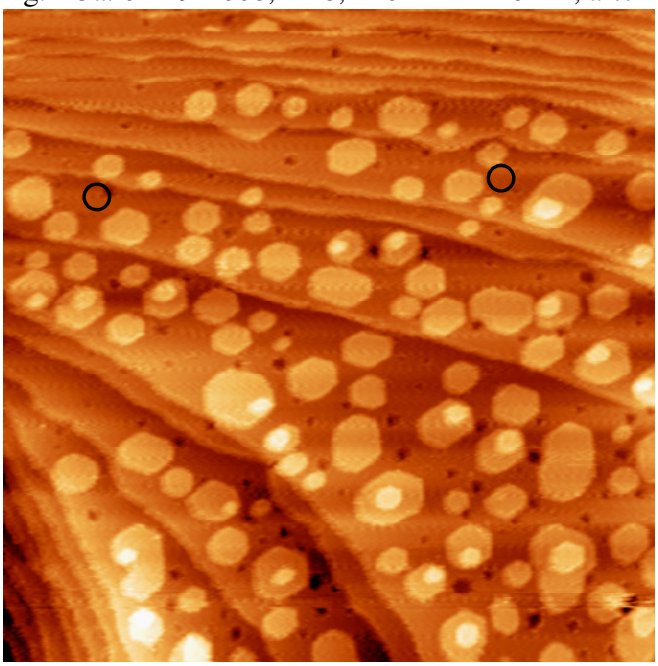

Fig. A5b. 02-19-2008, # 37, 110 nm x 110 nm, during S deposition, 200 K, 19:48 pm

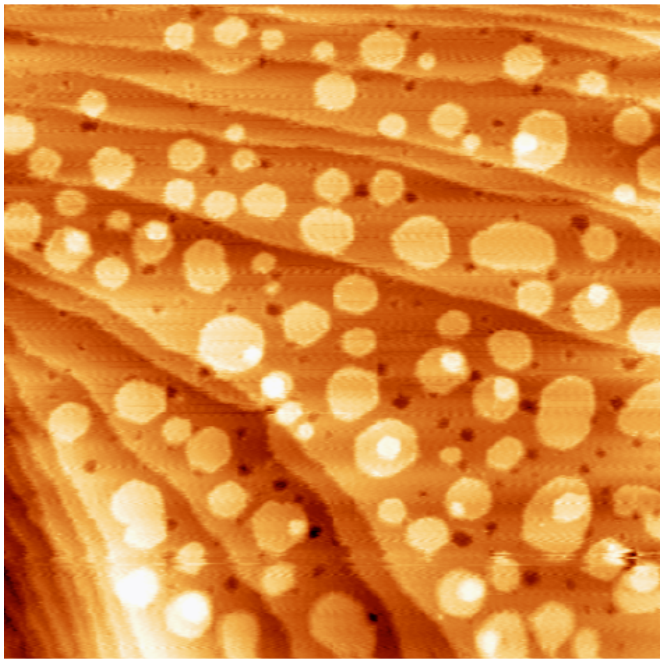

Fig. A5c. 02-19-2008, # 42, 110 nm x 110 nm, after S deposition, 200 K, 19:56 pm

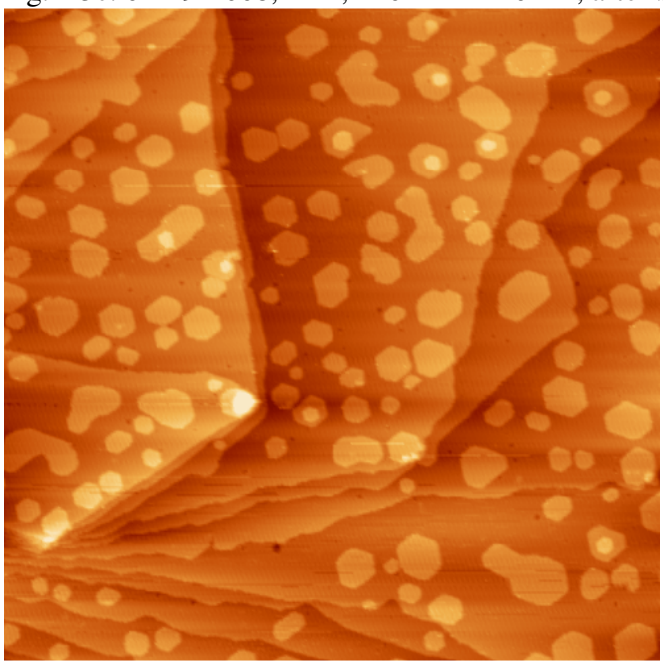

Fig. A6a. 04-10-2008, # 20, 200 nm x 200 nm, after Ag deposition, 200 K, 17:25 pm

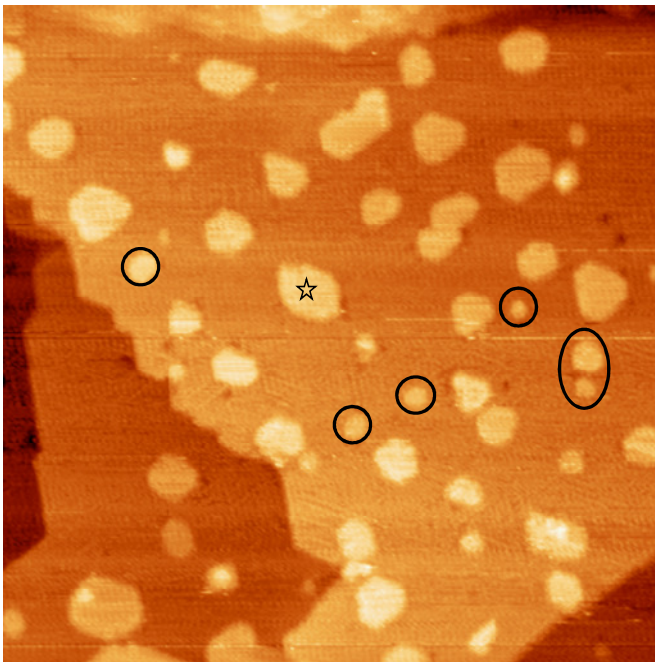

Fig. A6b. 04-10-2008, # 57, 200 nm x 200 nm, after S deposition, 200 K, 19:10 pm

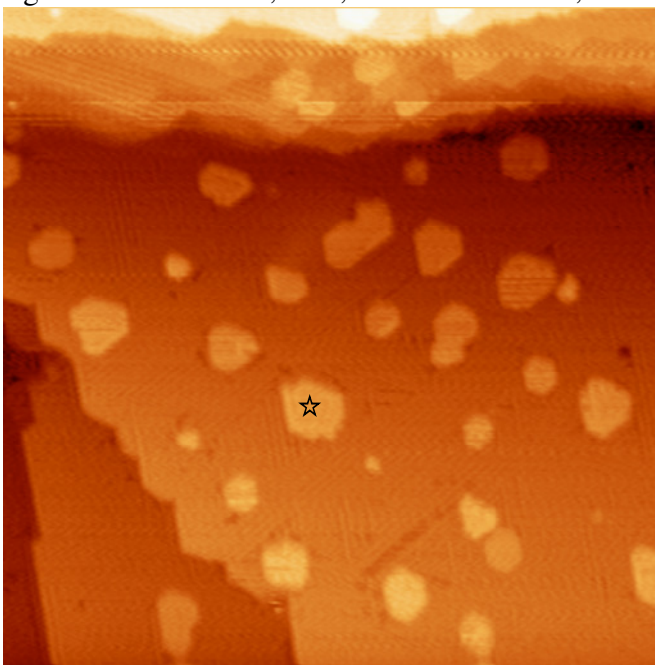

Fig. A6c. 04-10-2008, # 103, 200 nm x 200 nm, after S deposition, 200 K, 20:42 pm

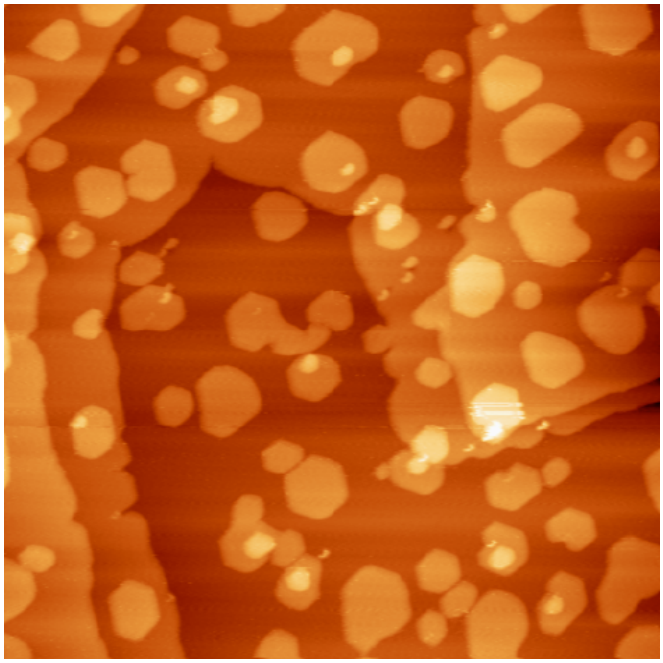

Fig. A7a. 05-14-2007, # 14, 250 nm x 250 nm, before S deposition, 200 K, 16:24 pm

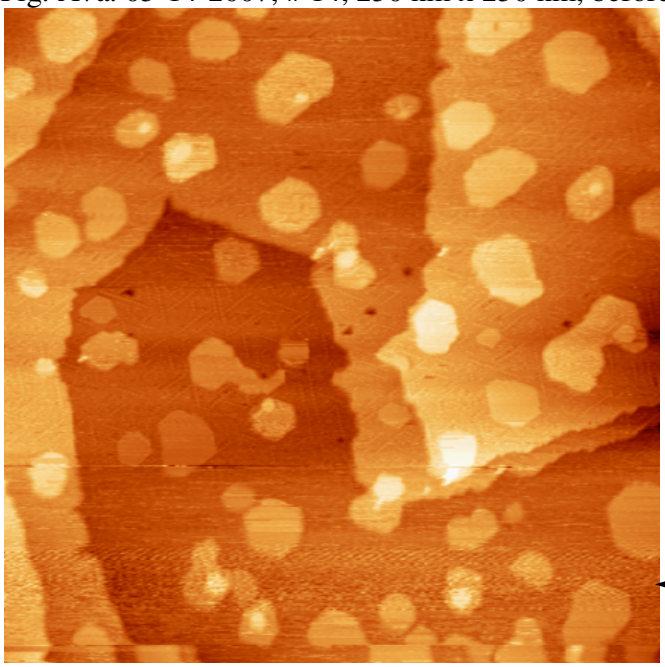


Fig. A7b. 05-14-2007, # 19, 250 nm x 250 nm, during S deposition, 200 K, 16:35 pm

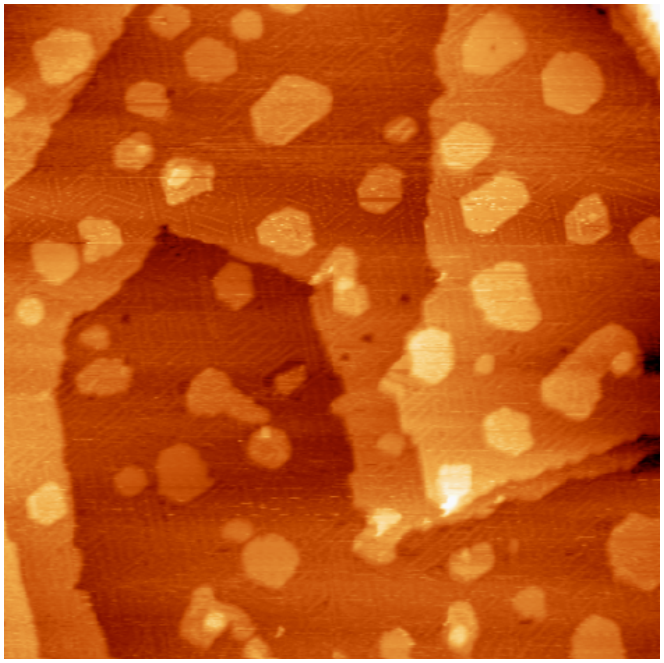

Fig. A7c. 05-14-2007, # 20, 250 nm x 250 nm, during S deposition, 200 K, 16:37 pm

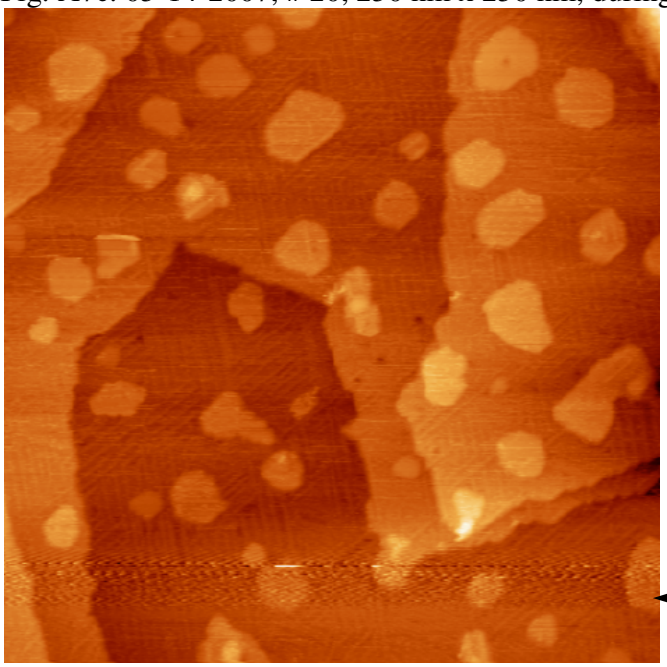


Fig. A7d. 05-14-2007, # 21, 250 nm x 250 nm, after S deposition, 200 K, 16:39 pm

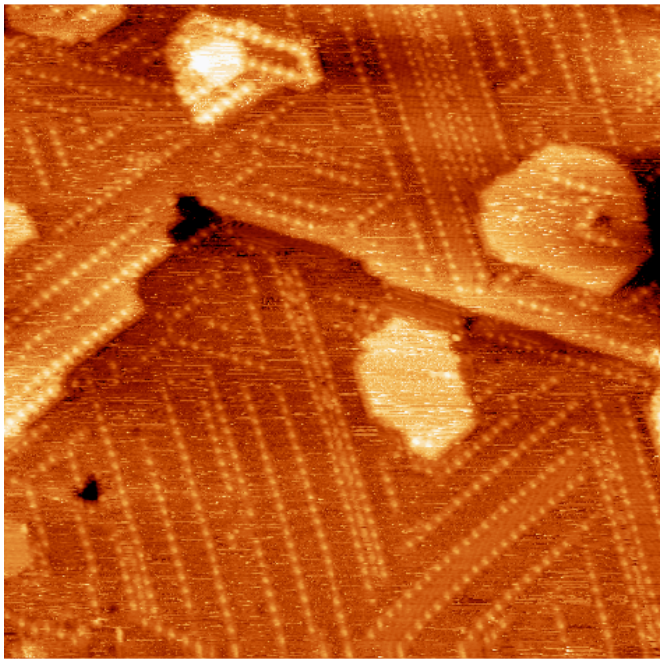

Fig. A7e. 05-14-2007, # 25, 80 nm x 80 nm, after S deposition, 200 K, 16:50 pm

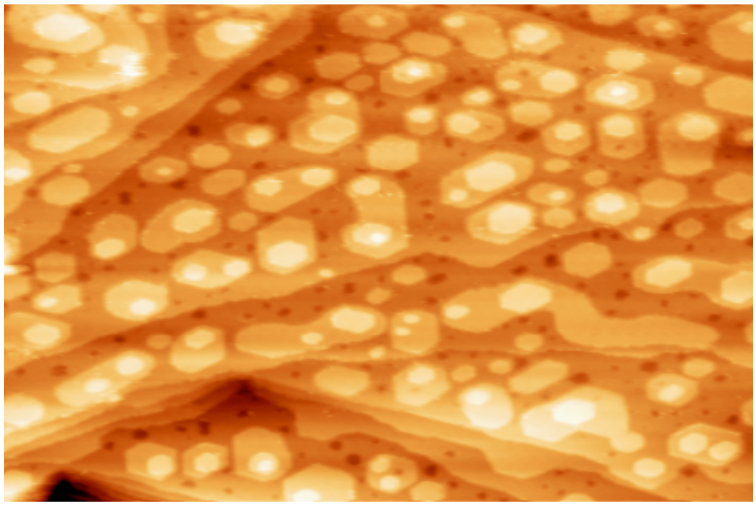

Fig. A8a. 04-23-2007, # 10, 120 nm x 80 nm, after Ag deposition, 200 K

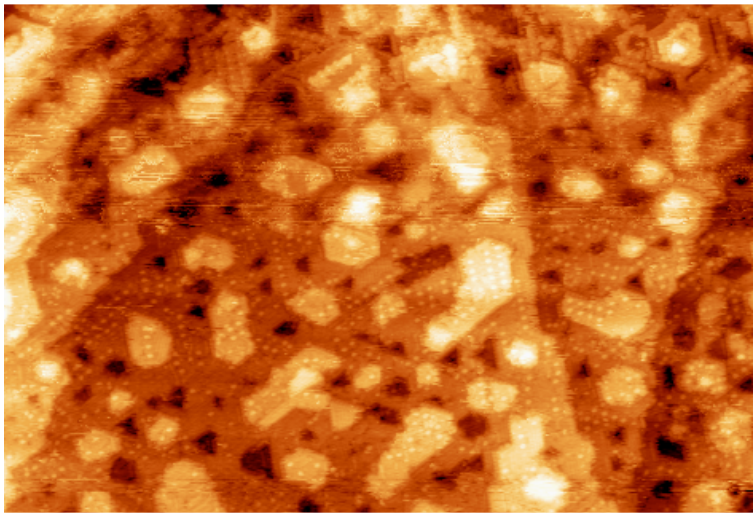

Fig. A8b. 04-23-2007, # 21, 120 nm x 80 nm, after S deposition, 200 K

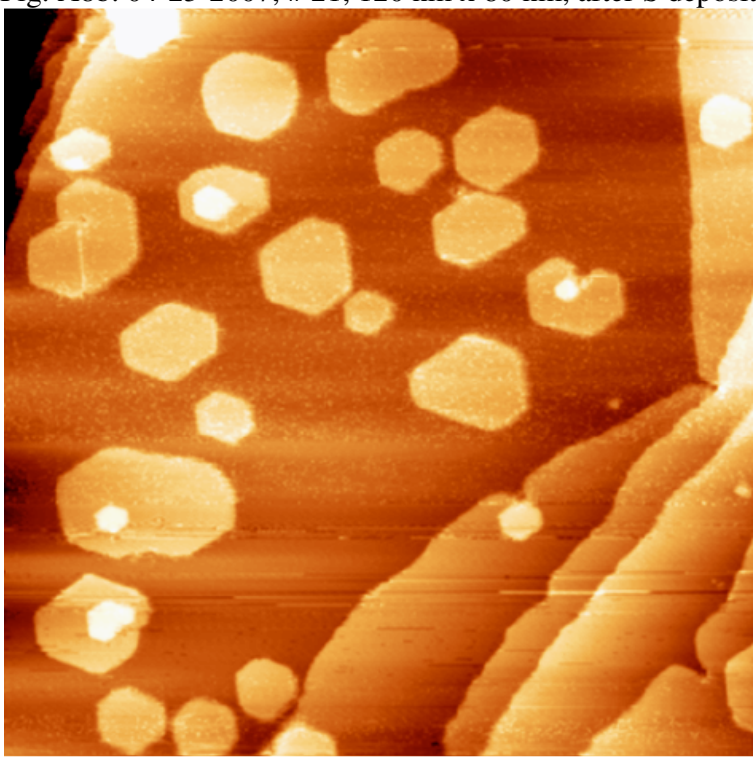

Fig. A9a. 04-30-2007, # 29, 150 nm x 150 nm, right before S deposition, 200 K, 19:11 pm

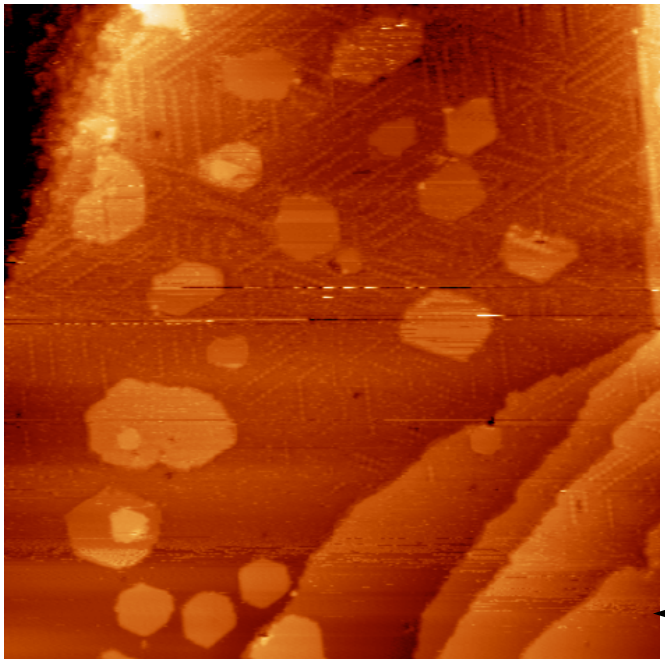


Fig. A9b. 04-30-2007, # 30, 150 nm x 150 nm, during S deposition, 200 K, 19:14 pm

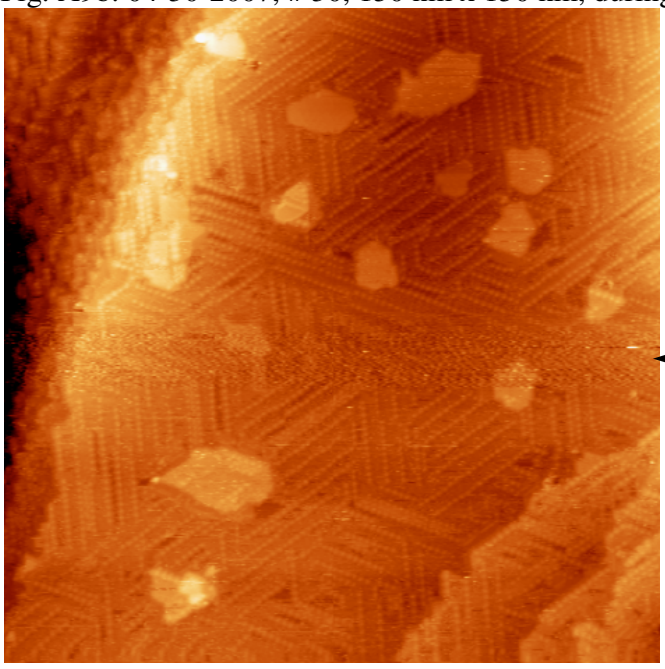


Fig. A9c. 04-30-2007, # 31, 150 nm x 150 nm, during S deposition, 200 K, 19:16 pm

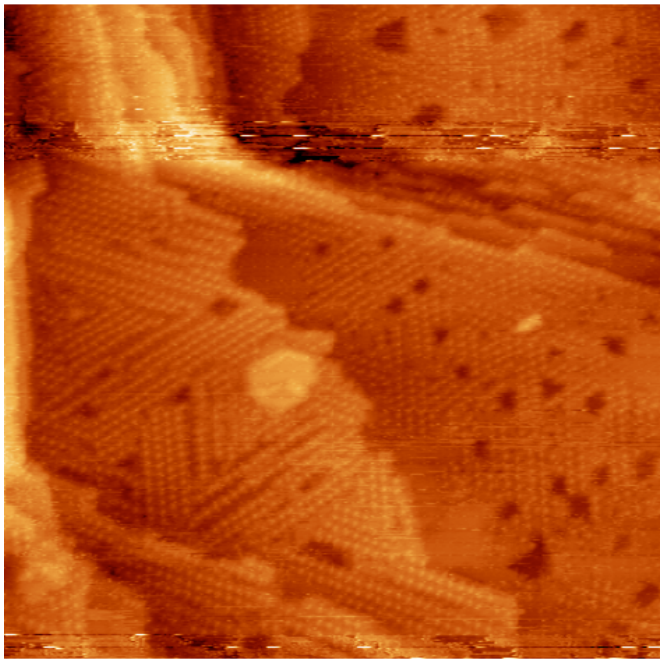

Fig. A9d. 04-30-2007, # 37, 100 nm x 100 nm, after S deposition, 200 K, 19:40 pm Another region of the surface

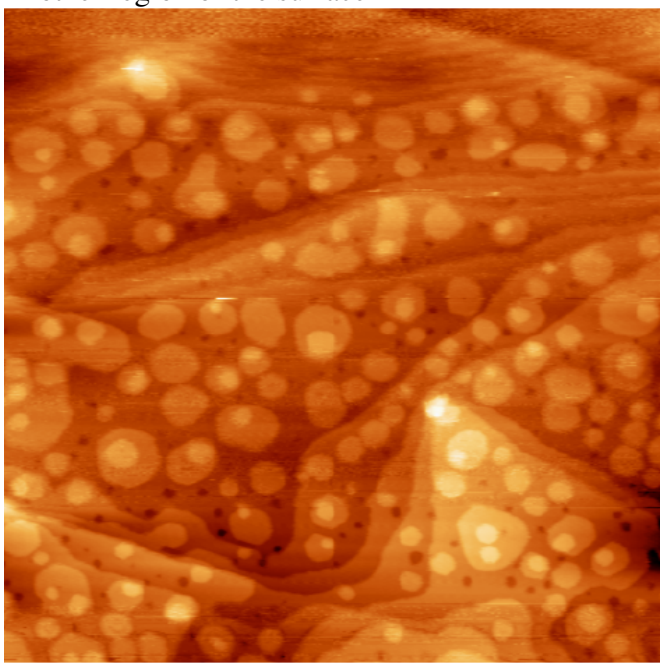

Fig. A10a. 04-19-2007, # 10, 150 nm x 150 nm, after Ag deposition, right before S deposition, 200 K, 16:05 pm

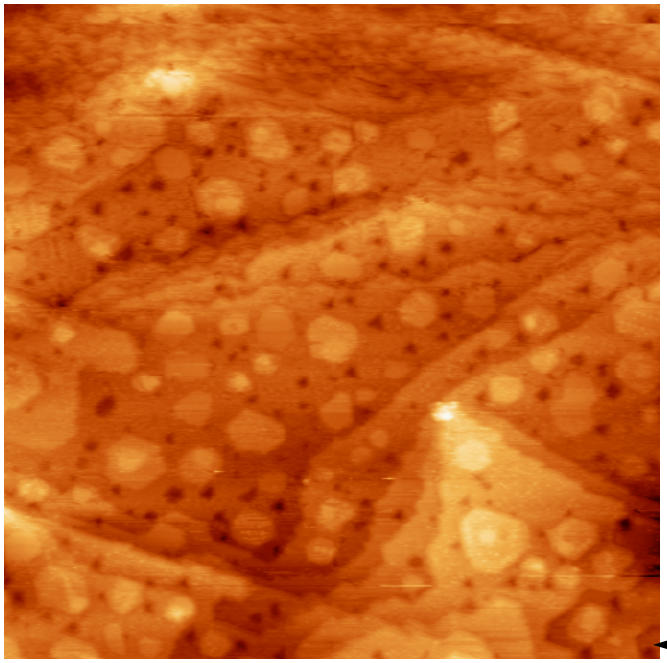


Fig. A10b. 04-19-2007, # 11, 150 nm x 150 nm, during S deposition, 200 K, 16:07 pm

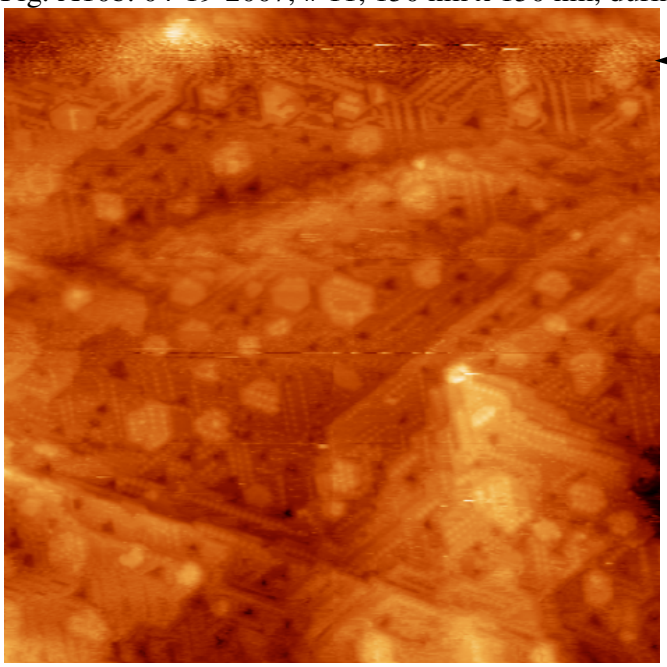


Fig. A10c. 04-19-2007, # 12, 150 nm x 150 nm, during S deposition, 200 K, 16:09 pm

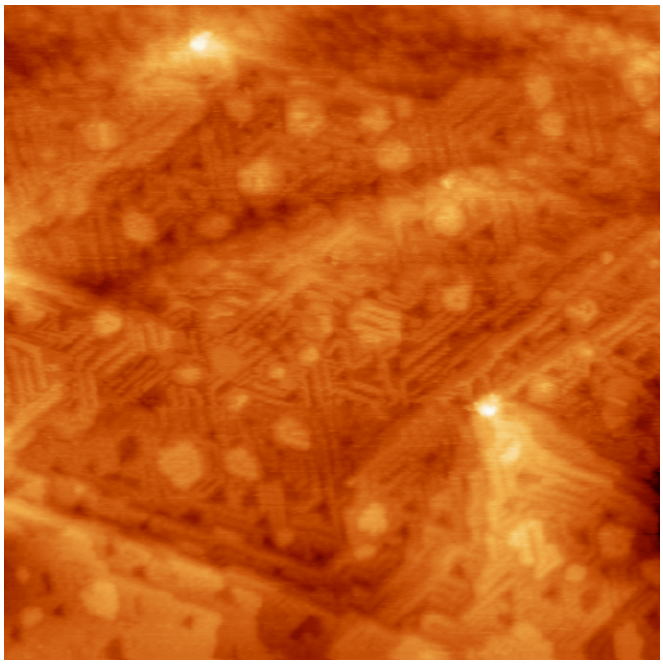

Fig. A10d. 04-19-2007, # 13, 150 nm x 150 nm, right after S deposition, 200 K, 16:11 pm

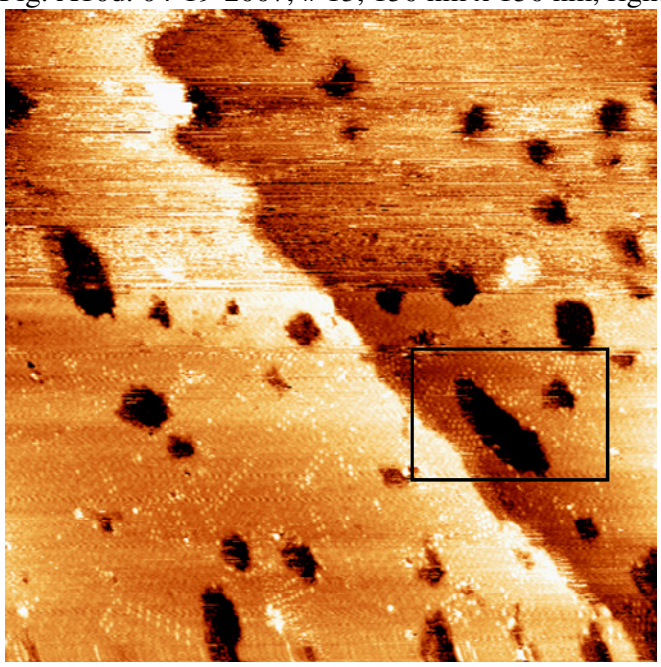

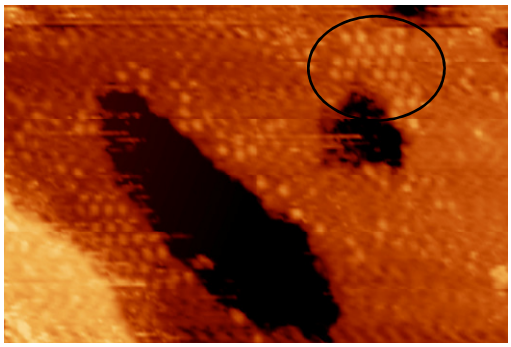

Fig. A10e. 04-19-2007, # 19, 100 nm x 100 nm, after S deposition, 200 K, 16:26 pm
Other region of the surface
04-19-2007, zoom in for #19, 30 nm x 20 nm, after S deposition, 200 K,

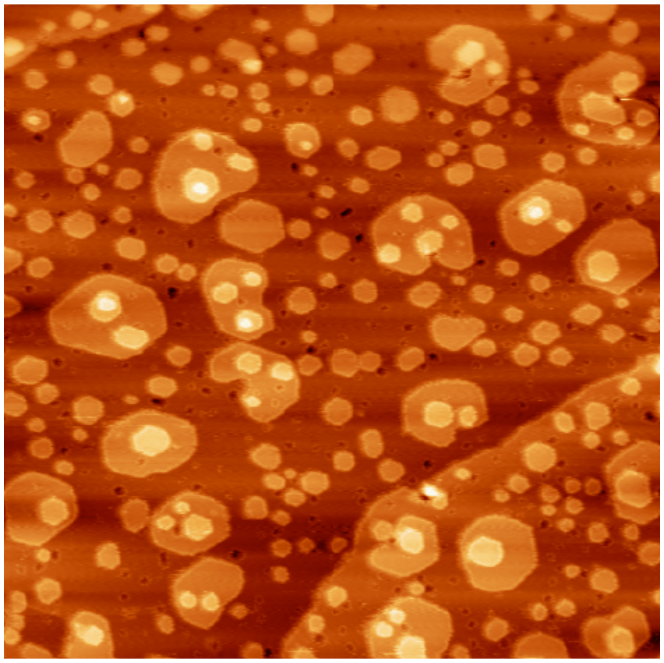

Fig. A11a. 05-07-2007, # 24, 140 nm x 140 nm, right before S deposition, 200 K, 16:35 pm

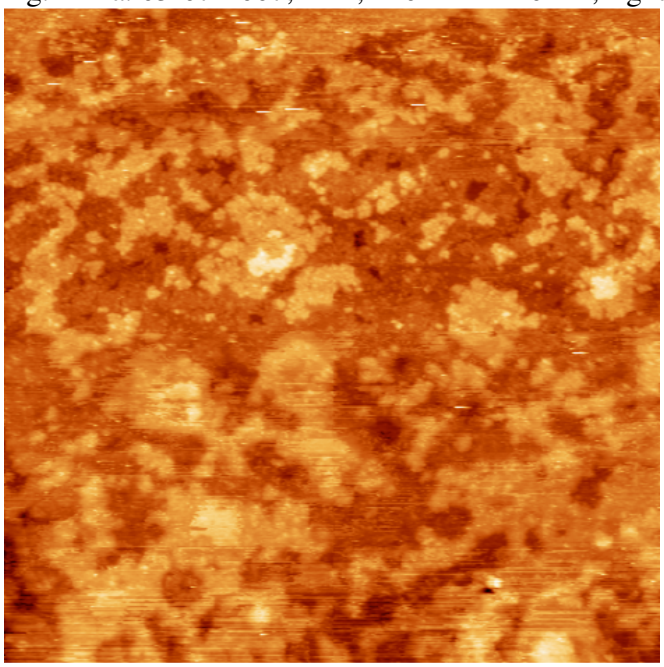

Fig. A11b. 05-07-2007, # 29, 140 nm x 140 nm, after S deposition, 200 K, 16:45 pm

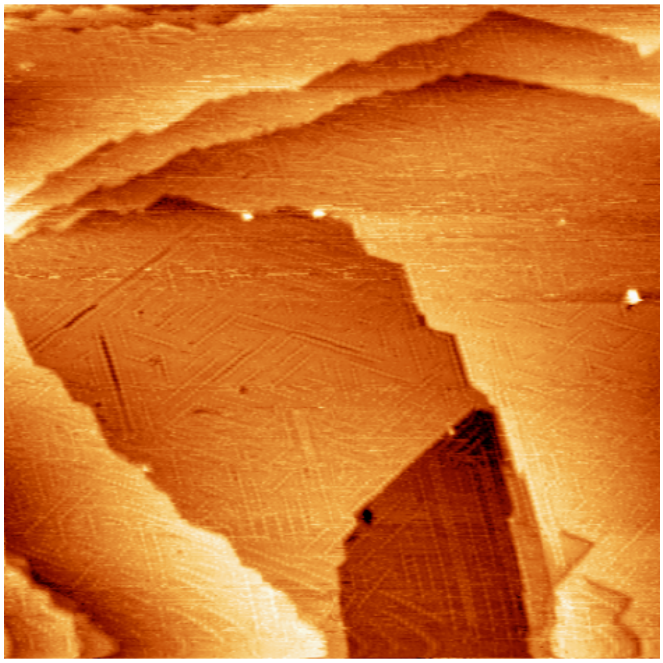

Fig. A12a. 06-14-2007, # 21, 200 nm x 200 nm, after S deposition, 200 K, 16:20 pm

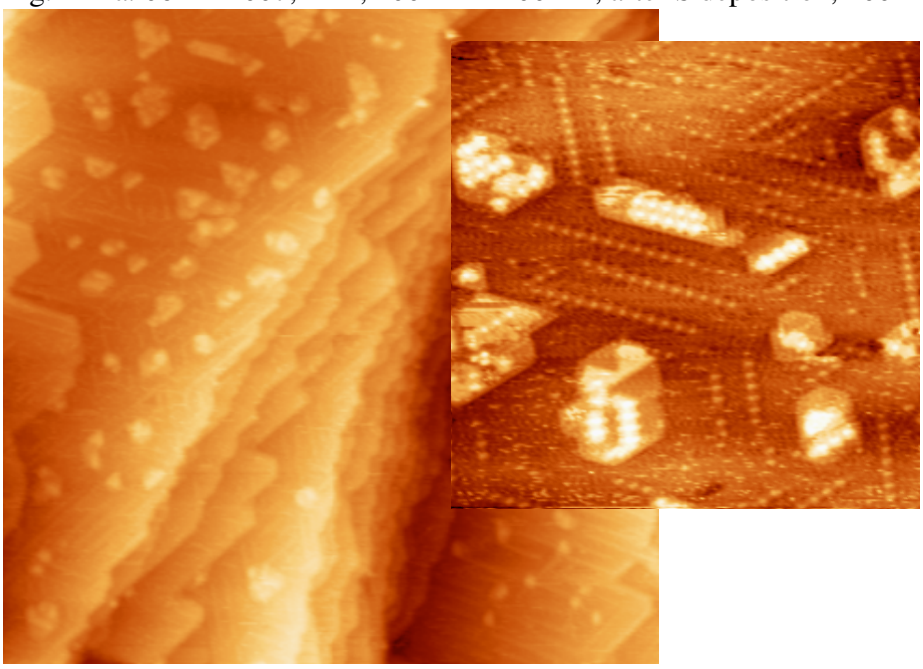

Fig. A12b. 06-14-2007, # 30, 200 nm x 200 nm, after Ag deposition, 200 K, 17:07 pm
Inset: 06-14-2007, # 35, 50 nm x 50 nm, after Ag deposition, 200 K, 17:27 pm

# CHAPTER 5. S EFFECTS ON Ag/Ag(100) COARSENING

A paper to be submitted

Mingmin Shen, Selena M. Russell, Da-Jiang Liu, James W. Evans, and Patricia A. Thiel

**ABSTRACT**

Scanning tunneling microscopy studies have revealed that adsorption of S can have a strong effect on coarsening of Ag islands on Ag(100) at 300 K.

## 1. INTRODUCTION

Studies of coarsening and coagulation phenomena were introduced about 100 years ago.[1,2] Coarsening on surfaces is important in at least two applied areas: heterogeneous catalysis, where sintering (coarsening) of supported metal particles can lead to catalyst deactivation [3]; and nanoscience, where coarsening of nanoparticles can be either desirable (e.g. a tool to narrow the size distribution) or undesirable (making particles larger than an optimal size) [4,5]. Coarsening on surfaces is also important from a fundamental perspective. This is true because the study of coarsening kinetics sheds light on the atomic-scale mechanisms and energetics of basic surface processes, including surface diffusion and attachment/detachment at step edges.

Coarsening on clean surfaces, especially of metal islands on metal surfaces, has received considerable attention [6-10]. Ripening in the presence of adsorbates has received much less scrutiny, but there is abundant evidence that adsorbates can induce metal surface rearrangements other than coarsening, such as faceting [11], step bunching [12], pitting [13], smoothening during growth (surfactant effect) [14,15], and reconstruction [16,17]. It is quite likely that an understanding of the kinetics and mechanism of adsorbate-induced coarsening can be extended to help understand some of these processes as well.

There are isolated reports which, viewed as a whole, suggest that adsorbed chalcogens may generally accelerate coarsening of metallic features on coinage metal surfaces. As early as 1967, Perdereau and Rhead [18] noted that adsorbed S increases the surface diffusion coefficient of Ag by a factor of $10^4$. More recently, Reutt-Robey et al. showed that adsorbed O can facilitate the faceting of vicinal Ag(110) at room temperature [11]. McCarty et al. demonstrated that low coverages of S accelerate coarsening of Cu islands on Cu(111) [19,20], and Friend et al. showed that S promotes mass transport on Au(111) at room temperature and above [21-24]. Cooper et al. [25,26] reported that nanoscale features on Au(111) decay rapidly in air, but very slowly in ultrahigh vacuum; later work in our laboratory indicated that the adsorbate responsible for this effect was most probably O or $H_2O$ [27].

There are two main mechanisms by which surface features can ripen.[28] The first, and most common, is Ostwald ripening. This usually relies on equilibrium between the clusters or islands and a dilute 2D gas. According to the Gibbs-Thomson relation, the equilibrium vapor pressure of this gas is higher for smaller features, leading to net mass transfer from smaller to larger features via the gas. (This thermodynamic treatment may underestimate the variation in vapor pressure as a function of size, especially for small particles [29].) The second is Smoluchowski ripening, in which the clusters or islands themselves diffuse, and randomly collide and merge. Smaller particles move faster [30], leading to preferential loss.

Our work has shown that low coverages of O accelerate coarsening of Ag nanoislands on Ag(100) [27,31]. We found that oxygen not only changes the kinetics of Ag island ripening, but also the mechanism—from Smoluchowski ripening on the clean surface, to Ostwald ripening with oxygen [31]. Recently, we found that trace amounts of S were shown to greatly enhance coarsening of Ag adatom islands on Ag(111), but only above a critical coverage

where all step edges are saturated with S.[32] This picture is consistent with our DFT results demonstrating the stability and mobility of various metal-S clusters, together with our analysis of coarsening kinetics based on non-linear reaction-diffusion equations incorporating appropriate mechanisms and rates for cluster formation.

In the present work, we describe the effect of adsorbed S on the coarsening of Ag islands on the Ag(100) surface.

## 2. EXPERIMENTAL PROCEDURES

The Ag(100) sample used in these studies was grown at the Ames Laboratory Materials Preparation Center.[33] The surface was oriented perpendicular to the <100> direction to within 0.25°. The sample was polished to a mirror finish using 6, 1, and 0.25 μm diamond paste. All experiments were carried out in a stainless steel ultrahigh vacuum (UHV) chamber with base pressure of $1 \times 10^{-10}$ Torr, equipped with an ion gun and with a retarding field analyzer (RFA) for Auger electron spectroscopy (AES). One part of the chamber contained an Omicron variable-temperature Scanning Tunneling Microscope (STM) with RHK SPM 100 controller. All STM images were acquired using electrochemically-etched W tips[34] at the stated temperature, 300 K. Typical tunneling conditions were -1.5 V and 1.0 nA. WSxM program was used for data analysis.[35] In the other part of the chamber, the sample was cleaned by repeated cycles of $Ar^+$ sputtering (15 min, 20 mA, 1.0 kV, T = 300 K) followed by annealing. This procedure was carried out until no impurities could be detected by AES, and until images acquired with the STM showed large terraces on the order of at least 100 nm in width, together with a very low density of apparent impurities as evidenced by a lack of pinning sites of steps.

For our study of adatom island coarsening and decay, deposition of Ag on the Ag(100) single-crystal surface was performed using an Omicron EFM3 UHV evaporator containing Ag (99.99% pure) as the deposition source. The Ag flux was held fixed at ~0.018 monolayers (ML)/s and S coverage is around 0.3 ML in all experiments. Sulfur deposition was then performed by exposing the sample to $S_2$ generated by a solid-state electrochemical Ag|AgI|$Ag_2S$|Pt cell following the design of Wagner.[36] With the electrochemical evaporator, the S flux was in the range of 1 to 12 mML/minute.

Only Ag and S were detected by AES on the surface after S deposition—not iodine or oxygen. Sulfur coverage was determined after each run using the S(LMM)/Ag(MNN) AES intensity ratio, where the letters in parenthesis denote electronic levels, and combination indicates the electronic energy transitions involved. We adopted a calibration that was published by Schwaha, Spencer and Lambert (SSL) in 1979[37] derived largely from Low Energy Electron Diffraction (LEED) but corroborated by temperature-programmed desorption and work function measurements by another group.[38]

The computational work was performed by Dr. Da-Jiang Liu in the Ames Laboratory.

**3. ISLAND DECAY KINETICS: EXPERIMENTAL ANALYSIS**

Figure 1 show a series of STM image snapshots at different S coverage and time with 0.3 ML Ag/Ag(100). Column (a) is the S-free surface where $\theta_S = 0$. Our STM movie reveals that the evolution of Ag islands on Ag(100) surface proceeds through island diffusion and coalescence, i. e., Smoluchowski ripening (SR), which is consistent with earlier reports about this system.[39-41] There is no observable Ostwald ripening (OR) even for very small islands (about 8 atoms in length). Column (b) shows a different study after S has been deposited on the surface to a coverage, $\theta_S$, of 0.034. After S deposition, smaller islands decay very slowly

without totally disappearing. This means OR occurs after S deposition. It is clear here that most Ag islands stay square shaped with some of the edges slightly rounding off. Column (c) reveals OR with $\theta_S = 0.083$. Ag islands stay between square and round shaped with some smaller islands disappearing with time. Column (d) shows the STM images at $\theta_S = 0.12$. All Ag islands are rounded and island density decreases with time through OR. SR can still occur when two islands are close enough as shown here in the first image of this column. Column (e) reveals fast island decay via OR at $\theta_S = 0.21$. Here all the Ag islands rotate 45° with respect to the original Ag island orientation on the clean Ag(100) surface. The rotated Ag islands also show rounded corners.

High magnification STM images of island shape change at different S coverages are shown in Figure 2. It gives a better view of how the Ag island shape changes with increasing S adsorption.

Figure 3 shows STM images with even higher S coverage, $\theta_S = 0.27$. Square Ag islands are irregularly shaped and no obvious island decay occurs. Fig. 2c shows a high magnification image of the S-adsorbed surface at 0.27 ML S with patterned structure,[42] which is formed by domains of p(2x2) and $(\sqrt{17}x\sqrt{17})R14^o$ structure shown as inset with S coverage at 0.36 ML for a better view. We had a very strong tip effect with S coverage at 0.27 ML for observing coarsening effect. When scanning the same area, island density got lower and some pits formed. When moving to another unscanned area, high island density as right after S deposition was observed again. It is possible that the formation of this patterned structure blocks island ripening.

Figure 4 shows how Ag island density decreases with time at different S coverages. For the clean Ag(100) surface, the Ag island density decrease mainly happens in the first

5000 s (~1.5h). No more local coalescence is observed after the first 1.5 h with STM and there is an almost constant island density curve. S deposition usually starts about 3000 to 4000 s after Ag deposition. When the S coverage ranges from ~ 0.03 ML to 0.16 ML, the island density curves are very similar to each other, and the curves continue decreasing slowly with S adsorption, which is clearly different from the clean surface curve. However, for experiments with $\theta_S = 0.21$, the Ag island density curve decreases more strongly after S deposition.

In Figure 5, we present the averaged decay rate of small islands via OR for various island sizes (sizes ranging from 9 to 23 atoms in length) at different S coverages. As shown in the plot, the island decay rate does not increase much until the Ag islands rotate 45° with respect to the original Ag island orientation on the clean Ag(100) surface. This is also consistent with our island density curves, which show that a stronger decrease is observed when the S coverage reaches $\theta_S = 0.21$. The nonlinear variations of individual island areas with time at different S coverages (shown in Figure 6) are indicative of terrace-diffusion (TD) limited decay.

More direct evidence for TD-limited decay is shown in Figure 7 for the decay of the circled island with time at $\theta_S = 0.21$. The decay of this island depends greatly on the surrounding islands. The island first decays slowly with a smaller island (indicated with arrow) present nearby, and once the nearby smaller island disappears, a much higher rate is observed.

## 4. COARSENING OF 2D NANOCLUSTERS ON Ag(100) SURFACE

For 2D clusters in homoepitaxial systems, the default expectation is that coarsening should be dominated by OR, although SR is observed for Ag islands on clean Ag(100).

Diffusion of material across terraces is driven by differences in the chemical potentials of these nanoclusters (islands or pits) as a function of size.[43,44] Smaller clusters with higher chemical potentials shrink, while larger clusters with lower chemical potentials grow in size. There are two standard scenarios for mass transport in OR. The first is transport via adatoms (ORA) from smaller to larger islands or from larger to smaller pits. The second is transport via vacancies (ORV) from smaller to larger pits or from larger to smaller islands.[45,46]

The effective energy for different pathways on clean Ag(100) is given by the equations below.

$E_{eff}(SR) = E_e + \phi + \delta_{KES}$

$E_{eff}(ORA) = E_d(ad) + E_{form}(ad)$

$E_{eff}(ORV) = E_d(vac) + E_{form}(vac) + \delta_{ES}(vac)$

The energetic quantities are defined as: NN interaction energies ($\phi$), formation energy ($E_{form}$), adatom and vacancy diffusion barriers ($E_d$), ES step edge barriers ($\delta_{ES}$), edge diffusion barrier for close-packed edges ($E_e$), and kink ES barrier ($\delta_{KES}$). The values of these quantities for the clean surface are given in Table 1.[45,46]

Table 1: Known values of energetic parameters for clean Ag(100). NN interaction energies ($\phi$), formation energy ($E_{form}$), adatom and vacancy diffusion barriers ($E_d$), ES step edge barriers ($\delta_{ES}$), edge diffusion barrier for close-packed edges ($E_e$), and kink ES barrier ($\delta_{KES}$). All units are in eV.

| | $\phi$ | $E_{form}$(ad) | $E_{form}$(vac) | $E_d$(ad) | $E_d$(vac) | $\delta_{ES}$ (ad) | $\delta_{ES}$ (vac) | $E_e$ | $\delta_{KES}$ |
|---|---|---|---|---|---|---|---|---|---|
| Ag(100) | 0.21 | 0.42 | 0.36 | 0.43 | 0.37 | 0.07 | 0.07? | 0.25 | 0.16 |

So these three different pathways are energetically different as shown here in Table 2.[45]

Table 2: Effective activation barriers for coarsening via various pathways on Ag(100)

| | $E_{eff}$(ORA) | $E_{eff}$(ORV) | $E_{eff}$(SR) | Note |
|---|---|---|---|---|
| Ag(100) | 0.85 eV | 0.73 eV + $\delta_{ES}$ | 0.62 eV | SR wins |

For the clean Ag/Ag(100) surface, $\delta_{ES}$(vac) is about 0..07 eV, and it leads to $E_{eff}$(ORV) = 0.8 eV. In this case, only SR is favored. [45]

## 5. COARSENING OF 2D NANOCLUSTERS ON Ag(100) SURFACE WITH S ADSOPTION

To explain the observed accelerated OR decay rate of Ag islands, the easiest way to think of the accelerated OR is to lower the OR effective activation barrier either through ORA or ORV. We considered different scenarios for the enhanced mass transport.

One scenario is due to the formation of a mobile Ag-S complex, as for the S/Ag(111) surface. The requirement for accelerated coarsening with S adsorption is that the effective barrier for coarsening (the sum of the diffusion barrier and formation energy) for the complex should be smaller than $E_{eff}$(ORA) ≈ 0.85 eV for the S-free system. One possibility is that the Ag-S complex directly detaches from step edges incorporating the S which was initially bound at those steps. However, this may lead to some smaller islands being depleted of S and thus becoming "frozen" rather than dissolving. One resolution of this dilemma is that S, in addition to Ag-S complexes, can detach from step edges and thus replenish depleted islands. An alternative model is that just Ag adatoms detach from step edges and that the Ag-S complexes form on the terraces.[47,48] However, our preliminary DFT analysis has not identified any suitable stable Ag-S complexes on Ag(100), prompting consideration of other possible scenarios.

In our examination of coarsening of Ag adatom islands on the clean Ag(100) surface, we have noted that the ORV mechanism is likely to be inhibited by the presence of a

substantial additional barrier, $\delta_{ES}$(vac), for vacancy interlayer transport. However, if the presence of the adsorbate greatly reduced this barrier, it could enhance or "catalyze" the ORV process. Recall that the terrace diffusion barrier for vacancies, $E_d$(vac) ≈ 0.36 eV, is significantly below that for adatoms.[49] Preliminary DFT analysis indicates that the formation energy for vacancies, $E_{form}$ ≈ 0.37 eV, is also significantly below $E_{form}$ ≈ 0.43 eV for adatoms. Consequently, $E_{eff}$(ORV) ≈ 0.73 + $\delta_{ES}$(vac) which is reduced to around 0.7 eV if an adsorbate can eliminate $\delta_{ES}$. This barrier is somewhat above $E_{eff}$(SR) ≈ 0.62 eV, but ORV (which would be TD-limited) has an advantage with respect to size scaling and thus could potentially become the dominant mechanism. The potential for S to reduce the ES barrier is aided by the feature that S likely resides at kink sites on step edges, the location where interlayer attachment and detachment of vacancies (or adatoms) occurs. Another possibility is that with the adsorption of S adatoms on Ag(100) surface, the periphery diffusion barrier for Ag adatoms, $E_e$, may get higher and it will lead to a higher effective activation barrier for SR, so that ORV can have lower barrier than SR.

## 6. DIFFERENT ADSORPTION SITES ON Ag/Ag(100) AND AG ISLAND SHAPE CHANGE

There are mainly three different adsorption sites for S adatoms on Ag/Ag(100) surface as shown here in Figure 8. One is the 3f-hollow site along the close-packed step edge. Here the nearby Ag atoms form a (111) microfacet and an adsorbed S atom can have three nearest neighbor binding Ag atoms (-4.6 eV, preliminary DFT result). The second is the 4f-hollow site on terraces. Adsorbed S adatoms can have four nearest neighbor binding Ag atoms (-5.06 eV, preliminary DFT result). The third is a site along a less-stable <001> type step edge. Such a step edge can be regarded as a (110) microfacet. The site consists of two

Ag atoms together with three other Ag atoms in lower terrace. S adsorption at this kink site is quite similar to that on the Ag(110) surface and binding is strong (-4.98 eV, preliminary DFT result).

Comparing the DFT results for these three different adsorption sites, it is clear that the kink site and 4f-hollow site are more favored. But for clean, two-dimensional Ag islands, the close-packed step edge dominates the surface and hence the island shape is square. With S adsorption requiring kink sites as favored adsorption sites, the <001> type step edge will be stabilized by increasing S coverage. All this leads to the orientation change for Ag islands forming more kink sites.

When oxygen adatoms adsorb on Ag(100) surface, they also prefer kink sites. The accelerated coarsening as OR is analogous to S on Ag/Ag(100).[32]

As shown in Figure 8, when the S adatom goes to the (111) microfacet site, the nearby corner Ag atom marked with a star will tend to move away so that S adatom can stay at a new formed kink site. With S coverage increases, more S adatoms will attach to the 3f-hollow sites and give a higher chance for corner Ag atoms to move away. This leads to a higher coarsening rate with increasing S coverage.

**7. COMPARISON BETWEEN S AFFECTED COARSENING ON Ag/Ag(100) AND Ag/Ag(111)**

Our current study points out that OR occurs on S adsorbed Ag/Ag(100) surface instead of SR on S-free Ag/Ag(100), and there is no stable cluster corresponding to the accelerated OR coarsening rate on S/Ag/Ag(100) system with increasing S coverage at 300 K. Island decay reveals TD-limited OR via vacancies. As reported previously,[32] coarsening kinetics in S/Ag/Ag(111) system at 300 K reveals two different stages. When S coverage is

below a critical value of 8-10 mML, there is no significant deviation from the TD-limited OR observed for the S-free Ag/Ag(111). When S coverage goes even a few mML higher above the critical value, there is dramatic acceleration in coarsening (by a factor of more than 100) with AD-like behavior as shown in the inset of Figure 5. The differences between these two systems are caused by different medium. For S/Ag/Ag(100), OR is mediated by single vacancies, while for S/Ag/Ag(111), Ag-S clusters mediate fast coarsening via OR above a critical value.

**8. CONCLUSION**

At 300 K, adsorbed S on Ag/Ag(100) causes the ripening mechanism change from SR to OR at S coverages from 0.03 ML to 0.21 ML. The Ag island decay rate for OR increases with increasing S coverage. Ag islands change from square to round with increasing S coverage, and change orientation at S coverage higher than 0.16 ML. No more coarsening occurs when S coverage increases to 0.27 ML, where ordered structures are also visible. Preliminary DFT results indicate that S adatoms prefer (110) microfacet sites along <001>-type steps than 3f-hollow sites along close-packed step edge.

**Reference**

(1) Ostwald, W. *Lehrbuch der Allgemeinen Chemie*Leipzig, Germany, 1896; Vol. 2.

(2) Smoluchowski, M. *Physica Z* **1916**, *17*, 557 and 585.

(3) Campbell, C. T. *Surface Sci. Reports* **1997**, *27*, 3.

(4) Brune, H. *Surface Sci. Reports* **1998**, *31*, 121.

(5) Brune, H. Growth of Metal Clusters at Surfaces. In *Metal Clusters at Surfaces*; Meiwes-Broer, K. H., Ed.; Springer: Berlin, 2000; pp 67.

(6) Zinke-Allmang, M.; Feldman, L. C.; Grabow, M. H. *Surface Sci. Reports* **1992**, *16*, 377.

(7) Theis, W.; Bartelt, N. C.; Tromp, R. M. *Phys. Rev. Lett* **1995**, *75*, 3328.

(8) Morgenstern, K.; Rosenfeld, G.; Comsa, G. *Phys. Rev. Lett.* **1996**, *76*, 2113.

(9) Giesen, M. *Progress in Surface Science* **2001**, *68*, 1.

(10) Brune, H. Creating Metal Nanostructures at Metal Surfaces Using Growth Kinetics. In *Handbook of Surface Science*; Hasselbrink, E., Ed.; Elsevier: Amsterdam, 2008; Vol. 3: Dynamics; pp 761.

(11) Ozcomert, J. S.; Pai, W. W.; Bartelt, N. C.; Reutt-Robey, J. E. *Phys. Rev. Lett.* **1994**, *72*, 258.

(12) Frank, E. R.; Hamers, R. J. *J. Catalysis* **1997**, *172*, 406.

(13) Klust, A.; Madix, R. J. *J. Chem. Phys.* **2007**, *126*, 084707.

(14) Pimpinelli, A.; Villain, J. *Physics of Crystal Growth*; Cambridge University Press: Cambridge, 1998.

(15) Michely, T.; Krug, J. *Islands, Mounds, and Atoms: Patterns and Processes in Crystal Growth Far from Equilibrium*; Springer Verlag: Berlin, 2004.

(16) Besenbacher, F.; Norskov, J. *Prog. Surf. Sci.* **1993**, *44*, 5.

(17) Thiel, P. A.; Estrup, P. J. Metal surface reconstructions. In *The Handbook of Surface Imaging and Visualization*; Hubbard, A. T., Ed.; CRC Press: Boca Raton, Florida, 1995; pp 407.

(18) Perdereau, J.; Rhead, G. E. *Surf. Sci* **1967**, *7*, 175.

(19) Feibelman, P. J. *Phys. Rev. Lett.* **2000**, *85*, 606.

(20) Ling, W. L.; Bartelt, N. C.; Pohl, K.; de la Figuera, J.; Hwang, R. Q.; McCarty, K. F. *Phys. Rev. Lett.* **2004**, *93*, 166101.

(21) Min, B. K.; Alemozafar, A. R.; Biener, M. M.; Biener, J.; Friend, C. M. *Topics in Catalysis* **2005**, *36*, 77.

(22) Biener, M. M.; Biener, J.; Friend, C. M. *Langmuir* **2005**, *21*, 1668.

(23) Biener, M. M.; Biener, J.; Friend, C. M. *Surf. Sci* **2007**, *601*, 1659.

(24) Friend, C. M. *J. Phys. Chem.* **2006**, *110*, 15663.

(25) Cooper, B. H.; Peale, D. R.; McLean, J. G.; Phillips, R.; Chason, E. Mass flow and stability of nanoscale features on Au(111). In *Evolution of Surface and Thin Film Microstructure: MRS Symposium Proceedings*; Atwater, H. A., Chason, E., Grabow, M. H., Lagally, M., Eds.; Materials Research Society: Warrendale, PA, 1993; Vol. 280; pp 37.

(26) Peale, D. R.; Cooper, B. H. *J. Vac. Sci. Technol. A* **1992**, *10*, 2210.

(27) Layson, A. R.; Evans, J. W.; P.A.Thiel. *Phys. Rev. B* **2002**, *65*, 193409.

(28) Rosenfeld, G.; Morgenstern, K.; Esser, M.; Comsa, G. *Appl. Phys. A* **1999**, *69*, 489.

(29) Campbell, C. T.; Parker, S. C.; Starr, D. E. *Science* **2002**, *298*, 811.

(30) Wen, J.-M.; Chang, S.-L.; Burnett, J. W.; Evans, J. W.; Thiel, P. A. *Phys. Rev. Lett.* **1994**, *73*, 2591.

(31) Layson, A. R.; Evans, J. W.; Fournée, V.; Thiel, P. A. *J. Chem. Phys.* **2003**, *118*, 6467.

(32) Shen, M. M.; Liu, D. J.; Jenks, C. J.; Thiel, P. A.; Evans, J. W. *Journal of Chemical Physics* **2009**, *130*.

(33) Single crystals were synthesized at the Materials Preparation Center, Ames Laboratory USDOE, Ames, IA, USA. See: www.mpc.ameslab.gov.

(34) Chen, C. J. *Introduction to Scanning Tunneling Microscopy*; Oxford University Press: New York, 1993.

(35) Horcas, I.; Fernandez, R.; Gomez-Rodriguez, J. M.; Colchero, J.; Gomez-Herrero, J.; Baro, A. M. *Review of Scientific Instruments* **2007**, *78*.

(36) Wagner, C. *Journal of Chemical Physics* **1953**, *21*, 1819.

(37) Schwaha, K.; Spencer, N. D.; Lambert, R. M. *Surface Science* **1979**, *81*, 273.

(38) Rovida, G.; Pratesi, F. *Surface Science* **1981**, *104*, 609.

(39) Wen, J.-M.; Chang, S.-L.; Burnett, J. W.; Evans, J. W.; Thiel, P. A. *Physical Review Letters* **1994**, *73*, 2591.

(40) Wen, J.-M.; Evans, J. W.; Bartelt, M. C.; Burnett, J. W.; Thiel, P. A. *Physical Review Letters* **1996**, *76*, 652.

(41) Pai, W. W.; Swan, A. K.; Zhang, Z.; Wendelken, J. F. *PHYSICAL REVIEW LETTERS* **1997**, *79*, 3210.

(42) Selena M. Russell, et al, in preparation

(43) Ratke, L.; Voorhees, P. W. *Growth and Coarsening: Ostwald Ripening in Materials Processes*; Springer: Berlin, 2002.

(44) Zinke-Allmang, M.; Feldman, L. C.; Grabow, M. H. *Surface Science Reports* **1992**, *16*, 377.

(45) Shen, M. M.; Wen, J. M.; Jenks, C. J.; Thiel, P. A.; Liu, D. J.; Evans, J. W. *Physical Review B* **2007**, *75*, 245409.

(46) Thiel, P. A.; Shen, M.; Liu, D. J.; Evans, J. W. *Journal of Physical Chemistry C* **2009**, *113*, 5047.

(47) Feibelman, P. J. *Physical Review Letters* **2000**, *85*, 606.

(48) Ling, W. L.; Bartelt, N. C.; Pohl, K.; de la Figuera, J.; Hwang, R. Q.; McCarty, K. F. *Physical Review Letters* **2004**, *93*, 166101.

(49) Da-Jiang Liu, in preparation.

**Figure Caption**

**Figure 1**. STM snapshots showing Ag island coarsening on Ag(100) at different time with different S coverages at room temperature, Ag coverages are all 0.3 ML. Column (a), clean Ag/Ag(100), 86, 145, 210 min after Ag deposition; column (b), 0.034 ML S on Ag/Ag(100), 78, 120, 154 min after Ag deposition (14, 58, 90 min after S deposition); column (c), 0.083 ML S on Ag/Ag(100), 90, 155, 215 min after Ag deposition (20, 85, 145 min after S deposition); column (d), 0.12 ML S on Ag/Ag(100), 78, 124, 168 min after Ag deposition (9, 55, 99 min after S deposition); column (e), 0.21 ML S on Ag/Ag(100), 99, 150, 204 min after Ag deposition (2, 53, 107 min after S deposition). All STM images are 50 nm x 50 nm.

**Figure 2**. High magnification STM images showing island shape at different S coverages. (a) clean Ag(100); (b) 0.034 ML S; (c) 0.083 ML S; (d) 0.12 ML S; (e) 0.12 ML S; (f) 0.21 ML S. All images are 10 nm x 10 nm.

**Figure 3**. STM images at S coverage of 0.27 ML. (a) clean Ag/Ag(100), 3 min after Ag deposition with 0.3 ML Ag, 150 nm x 100 nm; (b) 10 min after S deposition (114 min after Ag deposition, 150 nm x 100 nm; (c) high magnification image showing structure formed after S deposition, 45 nm x 45 nm; inset shows S on Ag(100) structure with 0.36 ML S for a better view of the two different structures at room temperature, 23 nm x 23 nm.

**Figure 4**. Ag island density decay with time at 0.3 ML Ag on Ag(100).

**Figure 5**. Averaged island decay rate at different S coverages on Ag/Ag(100). Inset shows island decay rate on Ag/Ag(111).

**Figure 6**. Ag island decay with time at different S coverages. (a) 0.083 ML S; (b) 0.12 ML S.

**Figure 7**. Island decay with time at S coverage of 0.21 ML. Insert STM images shows how nearby small island affects the decay of circled island. STM is 50 nm x 50 nm.

**Figure 8**. Schematic diagram showing 2D Ag islands on Ag(100) with different adsorption sites. Bright circles represent lower layer Ag atoms; dark circles represent upper layer Ag atoms. Yellow circles represent S adatoms.

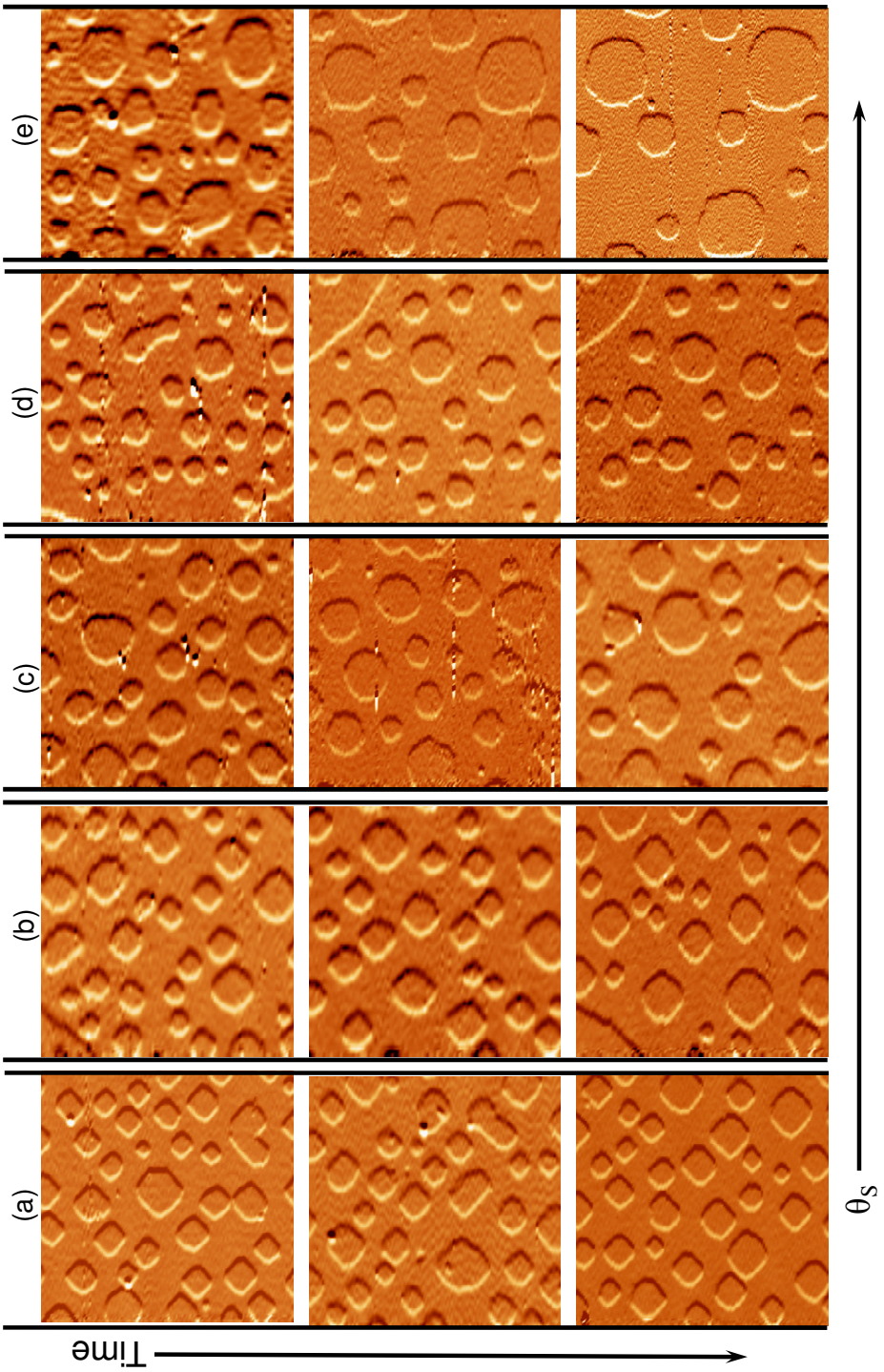


Figure 1

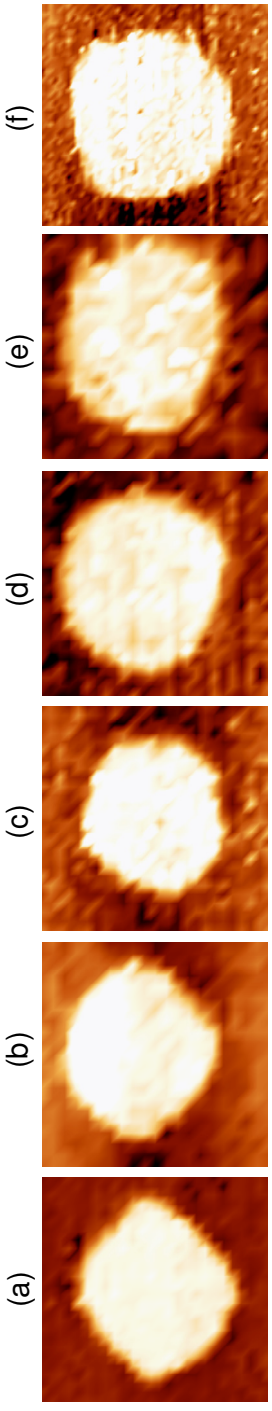


Figure 2

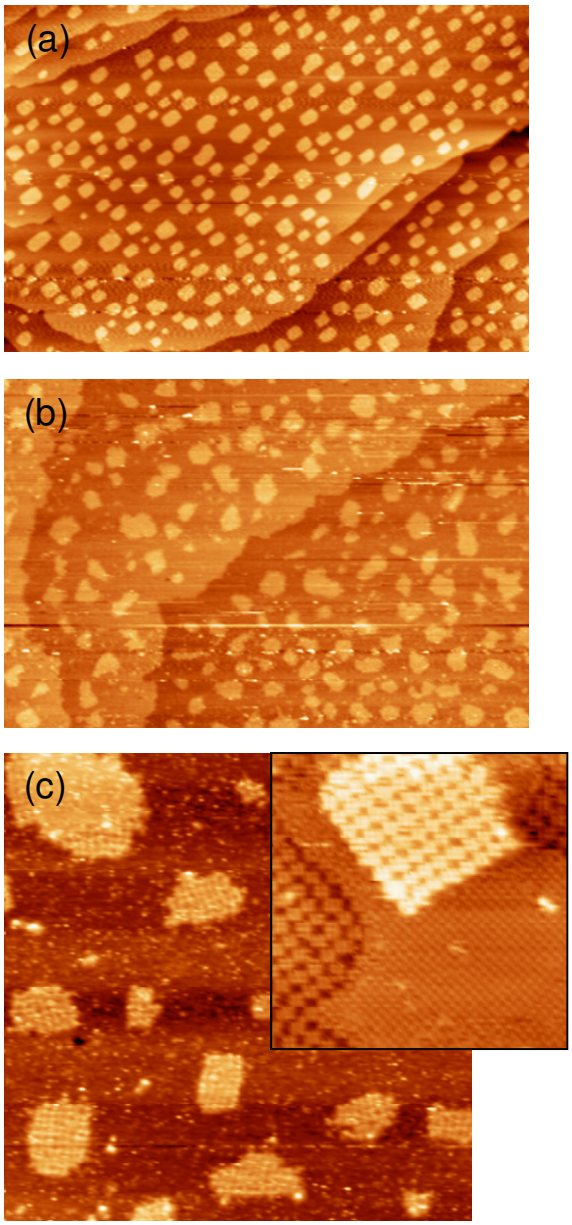


Figure 3

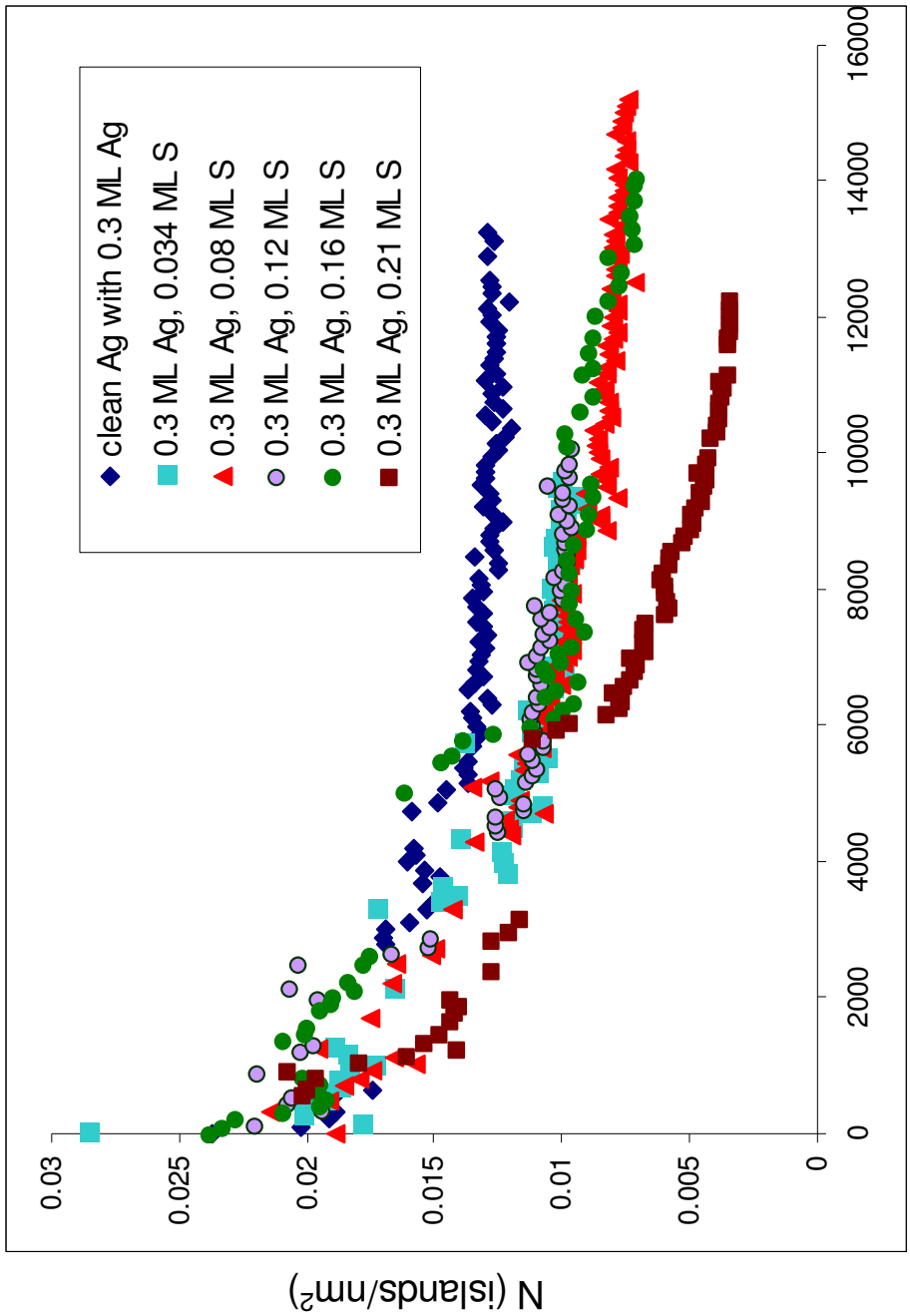


Figure 4

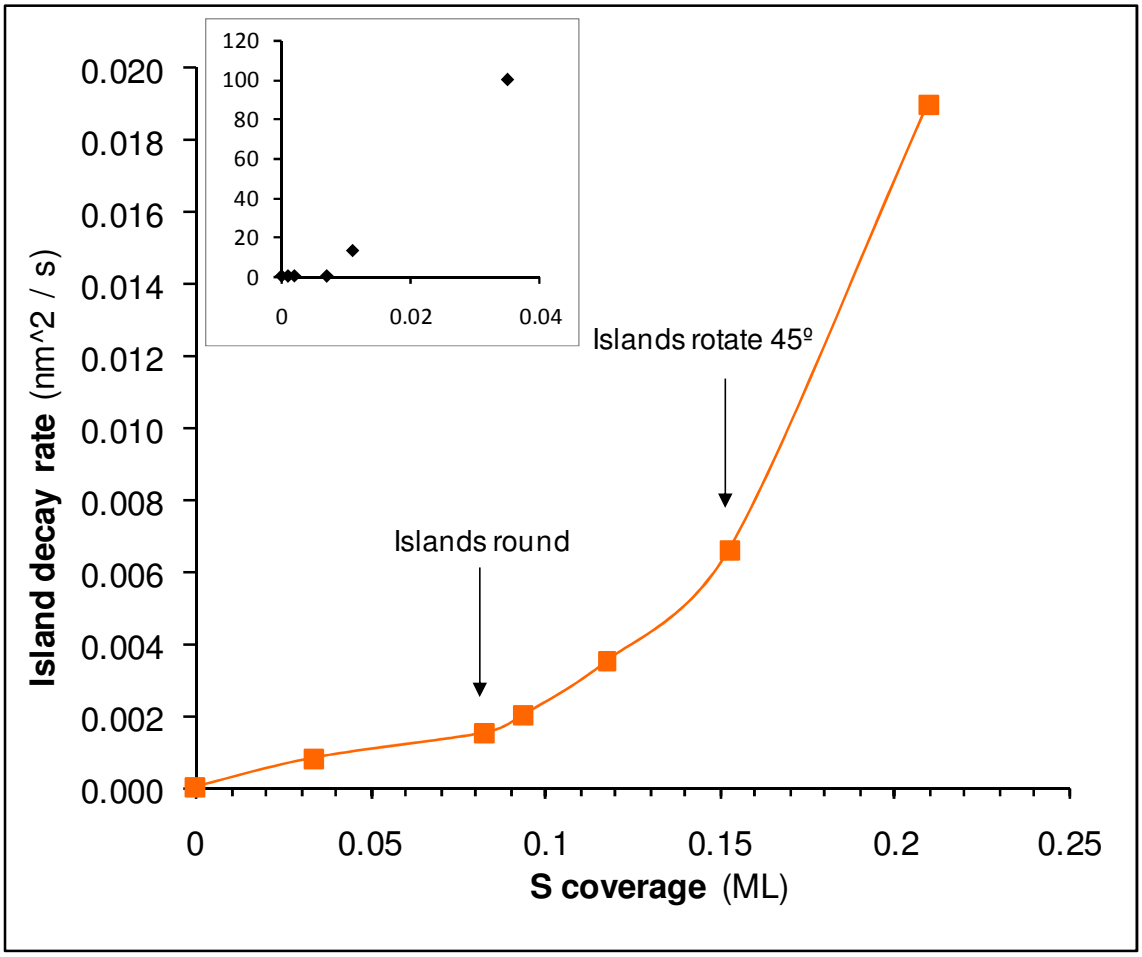


Figure 5

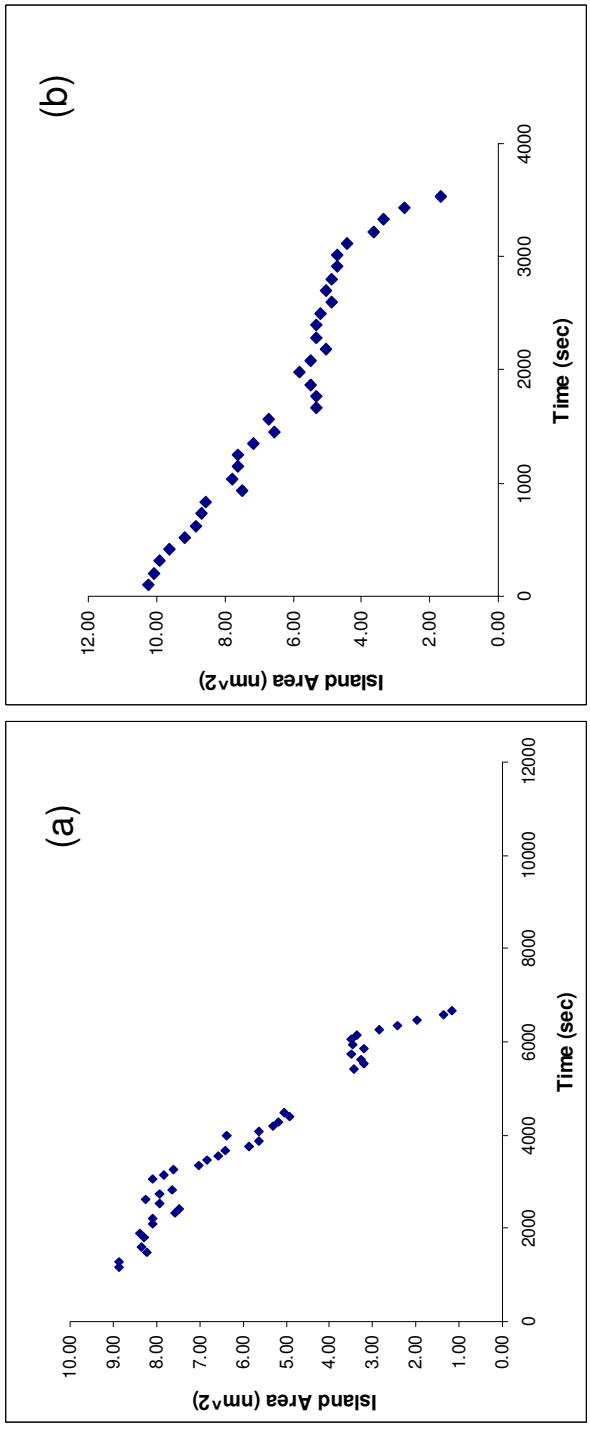


Figure 6

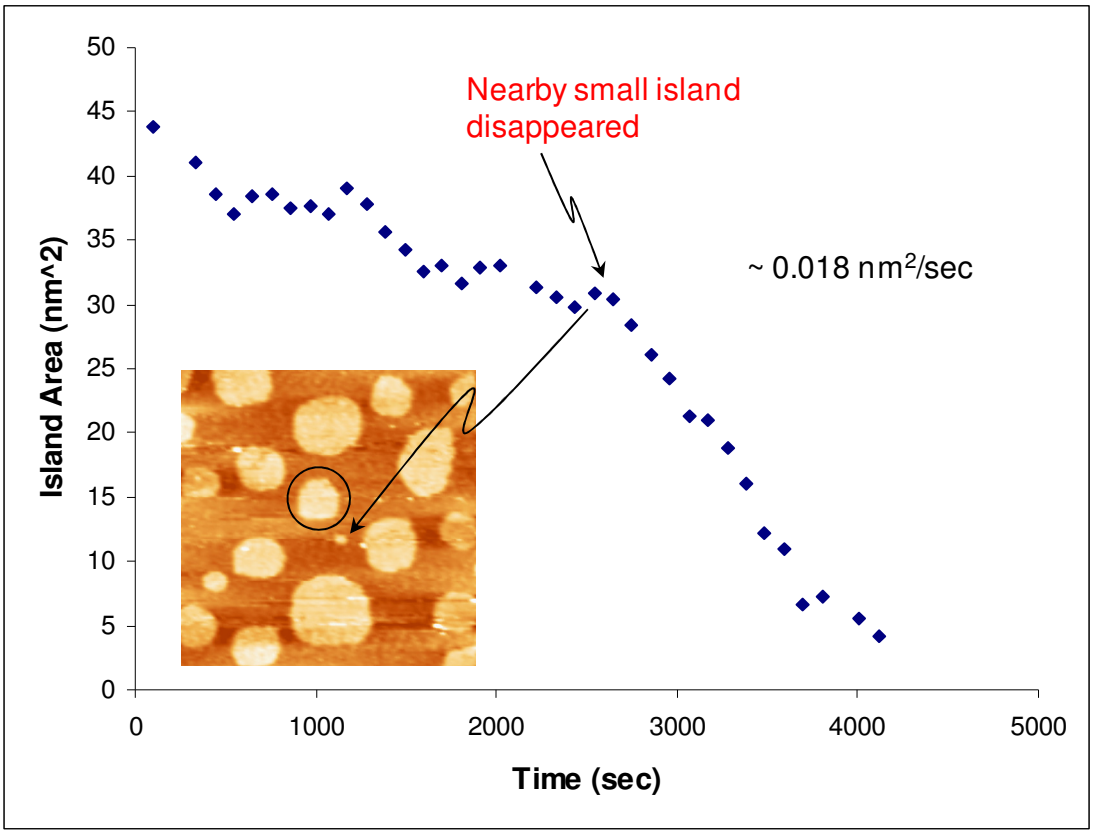


Figure 7

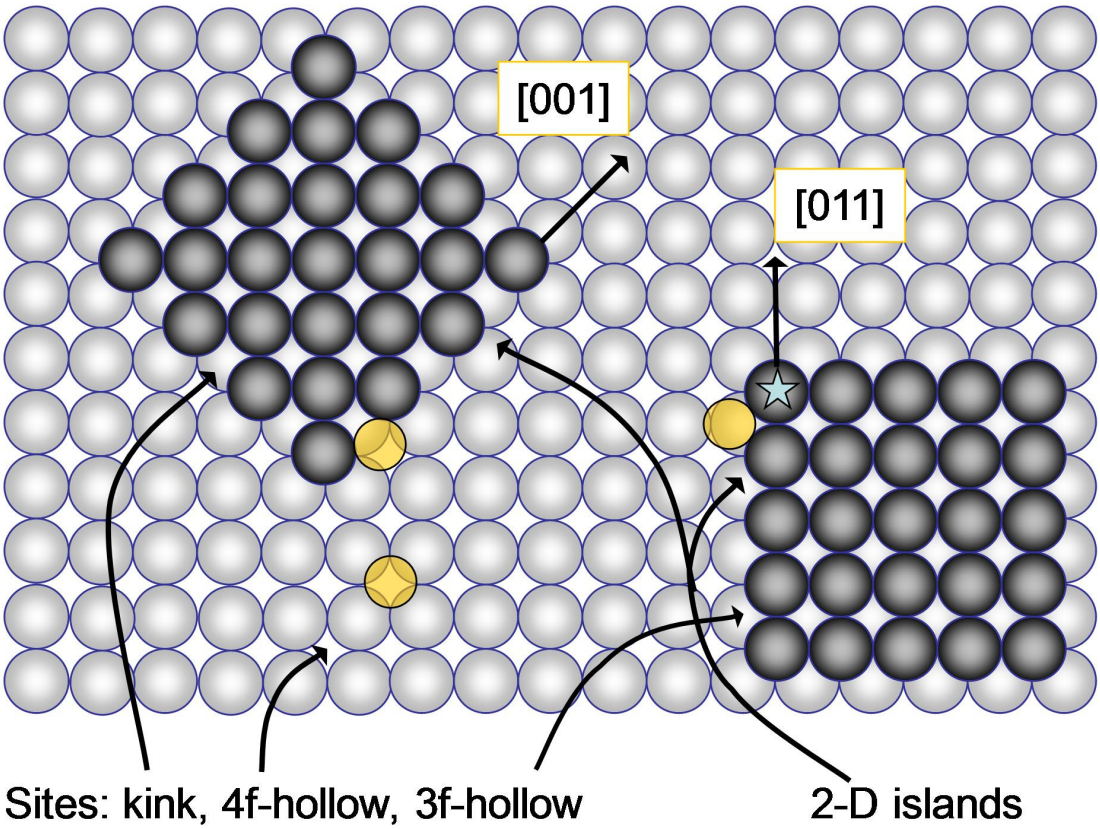


Figure 8

# CHAPTER 6. PREPARATION OF Ag(111) SINGLE CRYSTAL SURFACES

## 1. Introduction

Sample preparation is a basic challenge in ultra-high vacuum (UHV) studies. The goal is to get large, perfect terraces on which to study various phenomena. The routine procedure for sample preparation consists of repetitive sputtering and annealing cycles. In the literature[1-3], researchers have consistently reported using annealing temperatures higher than 800 K for Ag(111). In our experience with Ag(111), annealing at high temperatures, up to ~1000 K, can indeed lead to good STM images of large terraces, but the sample can only be used for a few months before the large terraces are lost, and the surface becomes irreversibly rough. The reason for this has been unknown to us, and to our knowledge it has not been addressed in the literature, although it is extremely important from a practical perspective. In this paper, we analyze the probable cause from a materials science perspective.

The growth of a single crystalline sample cannot be perfect, and defects, such as point defect (e.g. lattice vacancies, substitution impurity atoms, etc.), linear defects (commonly called dislocations), and planar defects (stacking faults and grain boundaries) can always be found in the bulk sample. The presence of defects, mainly dislocations strongly influences many of the properties of materials. For dislocations, it is well-known that a terminal point cannot exist inside the crystal, even though a dislocation forms within the bulk during crystal growth.[4] At sufficiently high temperatures, where the thermal diffusion of atoms becomes

active, dislocations actually move, which leads to the appearance of dislocations on the surface after annealing.

Studies of bulk recrystallization[5,6] have shown that when the annealing temperature, T, is 0.3 $T_m$ to 0.5 $T_m$ (where $T_m$ is the melting point), surface diffusion is sufficient for surface atoms to rearrange. If $T > 0.5\ T_m$, bulk recrystallization can happen, especially for soft metals (e.g. Ag), and this is due to the motion of dislocations which formed during crystal growth. This is termed primary recrystallization. The driving force for this recrystallization is the stored dislocation energy.[7]

When primary recrystallization is complete, the structure is not yet stable, and further growth of the recrystallized grains may occur. Grain growth may be divided into two types, normal grain and abnormal grain growth (AGG) or secondary recrystallization. Normal grain growth, in which the microstructure coarsens uniformly, is classified as a continuous process. AGG is a discontinuous process in which the microstructure becomes unstable and a few grains may grow excessively, consuming the smaller recrystallized grains. AGG often occurs during further annealing after the primary recrystallization event in metals.[8] It has long been known that small strains produce large effects on AGG. As initially proposed by Burton et al.,[9] for a singular surface free of dislocations, the surface growth rate will be almost 0 at very low driving forces. That means for a sample free of dislocations, the rate of primary recrystallization and AGG will be close to zero. Frank[10] reported that dislocations (screw and edge) can enhance the growth rate. Thus, it is expected that with an increasing number of dislocations, the growth rate will increase particularly at low driving forces.

Upon annealing a cold worked metal at an elevated temperature, recovery occurs first, via annihilation and rearrangement of the dislocations. The microstructural changes during

recovery are relatively homogeneous and do not usually affect the boundaries between the deformed grains; these changes in microstructure are shown schematically in Figure 1b. In recovery, the dislocation structure is not completely removed, but reaches a metastable state (Fig. 1b). A further restoration process called recrystallization may occur in which new dislocation-free grains are formed within the deformed or recovered structure (Fig. 1c). These then grow and consume the old grains, resulting in a new grain structure with a low dislocation density (Fig. 1d).Although recrystallization removes the dislocations, the material still contains grain boundaries, which are thermodynamically unstable. Further annealing may result in grain growth, in which the smaller grains are eliminated, the larger rains grow, and the grain boundaries assume a lower energy configuration (Fig. 1e). In certain circumstances this normal grain growth may give way to the selective growth of a few large grains (Fig. 1f), a process known as abnormal grain growth or secondary recrystallization. [7]

These concepts regarding recrystallization and grain growth were developed in the materials science community for polycrystalline materials that are originally in a highly-deformed state originating, for example, from cold working. However, we believe that some of the concepts can be used to understand our samples - for which the beginning state is nominally that of a single-grain single-crystal - as well.

We have studied the effect of annealing temperature, in ultrahigh vacuum, on Ag(111) single crystal samples. Surface changes have been monitored with STM and LEED, while bulk changes have been monitored with Laue diffraction. The Ag(111) sample gave reproducible terrace-step surface morphologies, adequate for surface studies but with a high dislocation density, after annealing at T ≈ 550-600 K. The sample started to have abnormal grain growth at 800 K and exhibited Ag(100)-like features after treatment at 900 K. after

direct heating at T > 1000 K, large terraces appeared on the surface, but the bulk sample itself was heavily recrystallized.

**2. Experimental details**

The Ag(111) sample used in these studies was grown by the Ames Laboratory Materials Preparation Center (MPC)[11] using Bridgman growth. High purity Ag was arc melted and dropcast into a copper chilled mold under high purity argon. The dropcast ingot was placed in an alumina Bridgman style crucible and heated under a diffusion vacuum to 1423 K to outgas the ingot and crucible. Once at temperature the chamber was backfilled with high purity argon to a pressure of 25 psi to minimize any evaporative losses during the growth. The ingot was withdrawn from the heat zone at a rate of 4 mm/h. Four different samples were used in our study. Each sample size was 3 mm × 9 mm × 1.5 mm. The surface was oriented perpendicular to the <111> direction within 0.25°. Each sample was polished to a mirror finish using 6, 1, and 0.25 μm diamond paste.

Experiments were performed in two separate stainless steel, ultrahigh vacuum (UHV) chambers, which will be named here chambers I and II. Most experiments were carried out in chamber I, which had a base pressure of $1\times10^{-10}$ Torr. Chamber I was equipped with an Omicron variable-temperature scanning tunneling microscope (VTSTM) and reverse-view Vacuum Microengineering LEED-Auger optics. In one part of the chamber, the sample was cleaned by repeated cycles of $Ar^+$ sputtering (15-30 min, 20 mA, 1.0 -1.5 kV, T = 300 K) followed by annealing at various temperatures (600 K, 800 K, 900 K, and ~ 1000 K) until no impurities could be detected by Auger electron spectroscopy (AES). The STM morphology was monitored after the sample had been cooled to room temperature. Typical tunneling conditions were +1.5 V and 1.0 nA. Samples A, B, and C were studied in Chamber I.

LEED experiments after annealing at T > 900 K were performed in Chamber (II), which had a base pressure of 0.8 to 1.0 × $10^{-10}$ Torr, and was equipped with both an Omicron HRLEED system, and a Physical Electronics Auger electron spectroscopy (AES). Temperatures were measured using a Mikron infrared pyrometer and two set of K-type (W-Re) thermocouple located at the back of the sample plate. Sample D was studied in Chamber II.

Temperatures higher than 650 K were monitored using an infrared pyrometer (Mikron). Possible sources of error in the measurements include film deposition on the window of the UHV chamber (due to evaporation from the sample and other sources), stray radiation from the heater, and thermal gradients (poor conductivity) across the sample. The variation of measured temperature across the sample, based upon five different pyrometer readings taken from a Ag sample D in Chamber II, was ± 10 K. In Chamber I, lower temperatures (< 650 K) were monitored using two sets of K-type thermocouple (chromel-alumel) located at different spots on the sample manipulator and also were based on the experimental temperature curve for resistive heating in VTSTM provide by the manufacturer (Omicron). In Chamber II, lower temperatures were measured using W-Re thermocouple.

A Philips PW1729/00 X-ray Generator Back-Reflection Laue Camera was used to obtain Laue patterns. It was operated at 20 kV and 40 mA, with a sample-to-film distance of 70 mm using Mo radiation.

**3. Results and Interpretation**

Figure 2 shows a series of STM images and line profiles of the Ag(111) surface after annealing at different temperatures. The first image of the whole series (a) was recorded at room temperature (RT) after final annealing at ~ 550 K (sample A, chamber I). As seen from

figure 2a, a typical terrace is about 100 to 200 nm wide. The step height (~ 0.24 nm) is shown in the line profile. It corresponds to the Ag(111) step height predicted from the bulk structure. We have been getting reproducible STM results using ~ 600 K annealing for more than two and a half years with the same sample, althouth these surfaces have a significant density of screw dislocations (see below).

Figure 2b is the STM image taken at RT after annealing at a temperature of ~ 800 K (sample B, chamber I). Small terraces (only about 20 nm wide) and step bunches can be observed in this situation. The line profile shows that the step height is still ~ 0.24 nm. Larger terraces are difficult to locate on this surface. Figure 2c and 2c' show STM images of this surface after final annealing at ~ 900 K (sample B, chamber I). The surface still has many step bunches, and now square shaped islands are present as well, as shown in Figure 2c. The insert (Figure 2c') is a 50 nm x 50 nm image with a step that is ~0.20 nm high, according to the line profile. The square shaped islands and step height are typical of the Ag(100) surface morphology. Therefore, parts of the surface have undergone grain growth, and formed a (100)-like structure. After even higher temperature annealing (950 K) (sample B, chamber I), the surface shows domains with different reflectivity, as observed with the naked eye. We attribute this to further grain growth and formation of grain boundaries. No terraces can be observed at all in STM images obtained after 950 K annealing. The STM image after direct annealing higher than 1000 K (sample C, chamber I) is shown in figure 2d. This exhibits large terraces and the typical Ag(111) step height (0.24 nm ). After the high temperature annealing, terraces as large as $500 \times 500$ nm$^2$ can be obtained.[12]

Figure 3 shows a typical STM image with dislocations after annealing at 550 to 600 K. The derivative mode image in Fig. 3b gives a better view of dislocations, as marked with

arrows. We have counted this kind of dislocations in sample A in more than 80 images of area 200 nm × 200 nm to 400 nm × 400 nm over a period of 2 years. From this we found the dislocation density was in a range of $5\times10^{-5}$ to $1.5\times10^{-4}/nm^2$ with an average of $8.2\times10^{-5}/nm^2$. Here we want to note that there is also some kind of protrusion underneath the surface in various places, and we did not count that as a dislocation. No obvious decrease in dislocation density was found over the lifetime of the sample, with annealing at 550-600 K. We were not able to count the dislocation density for the sample annealed at higher temperature (> 800 K) due to the bad STM image quality. But for the surface annealed directly above 1000 K (Sample C, Chamber I), there were no noticeable dislocations, as shown in Fig. 1d.

Figure 4 shows a series of LEED patterns obtained at RT after annealing at various temperatures. After annealing at ~ 550 K (sample A, chamber I), a pattern with 6-fold symmetry is observed. The LEED spot size is small and consistent with the 100-200 nm wide terraces observed in STM. The uneven spot size and brightness is due to the tilting of the sample manipulator and no adjustment can be made in this chamber. For the sample annealed at ~ 800 K (sample B, chamber I), a pattern with near 6-fold symmetry is also observed, but the diffraction spots are split, as shown by the red circles in figure 4b. At this point, the sample starts to undergo grain growth and forms facets with different orientations. The facets are still (111) domains, as indicated by the STM morphology and the near 6-fold symmetry pattern in LEED. After annealing above 900 K (sample D, chamber II), LEED patterns are obtained in chamber II where there is an ability to adjust sample orientation. After annealing at ~ 900 K, with the same experimental condition (sample position), the central spot surrounded by a red circle in Figure 4c is not centered. Both 6-fold and 4-fold symmetries, shown as solid lines and dashed lines, can be observed in the LEED pattern in figure 4c. The

four-fold symmetry is consistent with the square-shaped adatom islands and 2.0 Å Ag(100) step height observed in the STM images. The orientation of part of the surface has also changed, based on the shifted (0,0) spot position. Upon 900 K annealing, the sample undergoes further grain growth and forms both (111) and (100) faces on the surface. No LEED pattern was taken on this particular sample after direct annealing at T >1000 K, but other authorsa[3,13] report a sharp (1×1) LEED pattern.

The Laue back-reflection pattern provides information about the orientation of a single crystal sample. Figure 5 shows the Laue patterns of different Ag(111) samples before and after annealing in UHV at different temperatures. Prior to insertion into the UHV chamber each sample has a surface perpendicular to the [111] axis within 0.25°, as shown in figure 5a (same for all fresh samples). They are originally good single crystalline samples. After a long history of sputtering and annealing at T < 600 K (sample A, chamber I), the Laue pattern remains the same as that of the fresh sample (figure 5a), and it is not shown here. After repeated cycles of sputtering at room temperature and annealing at ~ 800 K (sample B, chamber I), the surface becomes misoriented by more than10° from the [111] axis, and split spots can be observed in the pattern as shown in Figure 5b. This is consistent with the split spots in the LEED pattern (figure 4b). Hence, we conclude that the sample starts to undergo grain growth at 800 K. The high misorientation angle of 10° accounts for the fact that no large terraces can be observed with STM. No regular Laue pattern can be found after annealing at higher temperature (> 1000 K) (sample C, chamber I), as shown in figure 5c. This means the sample is not a single crystal any longer, although it still may show a sharp LEED pattern with large terraces on the surface. The annealing history of different samples is shown in Table A.

**4. Discussion**

Dannenberg et al[14] reported that normal grain growth happened in 80-nm-thick sputter-deposited Ag films up to 556 K. This is also in the temperature range we use to anneal our sample A. Koo and Yoon[15,16] studied the dependence of grain growth in silver on annealing temperature and atmosphere and found that in a vacuum of $10^{-4}$ Torr, AGG occurred at temperatures between 750 K and 1000 K. Also at higher temperature (T > 1000 K), close to the melting point, grain growth was found to be normal grain and smooth surface could be observed with optical microscopy. The Ag(111) surface shows a screw dislocation density of $5 \times 10^{-5}$ to $1.5 \times 10^{-4}$/nm$^2$, after heating no higher than 600 K. We postulate that these dislocations contribute to grain growth, and eventually disappear, at annealing temperatures higher than 800 K.

Studies[17,18] have shown that both Cu and Ag films will have AGG by thermal annealing whenever a special texture is formed during film deposition. During AGG, the initial <111> texture transforms completely into <001>. Important contributions to the driving force for grain growth are the reduction in free energy due to a reduction in grain boundary area, the anisotropy of surface and interface energies, and the anisotropy of the elastic strain-energy density.[18-20] In fcc (face-centered cubic) thin films, surface energy minimization often promotes the growth of grains with (111) planes parallel to the film surface.[18-20] In contrast, strain energy minimization can lead to abnormal growth of (001) oriented grains. For fcc metals, such as Cu and Ag, the (100)-oriented grains have the lowest stresses in the plane of the film surface and the lowest strain energy density, so from strain energy minimization, the (100) texture should be favorable in an fcc film.[18-20] For Ag single

crystals, the surface energy difference for the three low index surfaces is fairly small[21-23], so the minimization of strain energy may play the most important role in determining the grain growth. This explains why the Ag(100) feature shows up with annealing at ~ 900 K.

## 5. Conclusions

At annealing temperatures of 550-600 K, the Ag(111) surface can be reproducibly obtained. Grain growth at T > 800 K is due to dislocation defects, and this kind of recrystallization in this stage causes growth of (100) oriented grains. Direct annealing higher than 1000 K can lead to normal grain growth and surfaces with large, flat (111) terraces.

## ACKNOWLEDGEMENTS

This work was supported by NSF Grant CHE-0414378. It was performed at the Ames Laboratory which is operated for the US Department of Energy by Iowa State University under Contract No. W-7405-Eng-82.

## REFERENCES

(1) Poensgen, M.; Wolf, J. F.; Frohn, J.; Giesen, M.; Ibach, H. *Surface Science* **1992**, *274*, 430.

(2) Vrijmoeth, J.; van der Vegt, H. A.; Meyer, J. A.; Vlieg, E.; Behm, R. J. *PHYSICAL REVIEW LETTERS* **1994**, *72*, 3843.

(3) Morgenstern, K.; Rosenfeld, G.; Comsa, G. *Surface Science* **1999**, *441*, 289.

(4) Suzuki, T.; Takeuchi, S.; Yoshinaga, H. *Dislocation Dynamics and Plasticity*; Springer-Verlag, 1991.

(5) Higo, M.; Fujita, K.; Tanaka, Y.; Mitsushio, M.; Yoshidome, T. *Applied surface science* **2006**, *252*, 5083.

(6) Porter, D. A.; Easterling, K. E. *Phase transformations in metals and alloys*; CRC press, 1992.

(7) Humphreys, F. J.; Hatherly, M. *Recrystallization and related annealing phenomina*; Elsevier, 2004.

(8) KOO, J. B.; YOON, D. Y.; HENRY, M. F. *Metallurgical and Materials Transactions A* **2002**, *33*, 3803.

(9) Burton, W. K.; Cabrera, N.; Grank, E. C. *The Philosophical Transactions of the Royal Society A* **1951**, *243*, 299.

(10) Frank, F. C. *Journal of Crystal Growth* **1981**, *51*, 367.

(11) Note. *Single crystals were synthesized at the Materials Preparation Center, Ames Laboratory USDOE, Ames, IA, USA. See: www.mpc.ameslab.gov.*

(12) Cox, E.; Li, M.; Chung, P.-W.; Ghosh, C.; Rahman, T. S.; Jenks, C. J.; Evans, J. W.; Thiel, P. A. *Physical Review B* **2005**, *71*, 115414.

(13) Morgenstern, K.; Rosenfeld, G.; Comsa, G. *PHYSICAL REVIEW LETTERS* **1996**, *76*, 2113.

(14) Dannenberg, R.; Stach, E.; Groza, J. R.; Dresser, B. J. *Thin Solid Films* **2000**, *379*, 133.

(15) Koo, J. B.; Yoon, D. Y. *Metallurgical and Materials Transactions a-Physical Metallurgy and Materials Science* **2001**, *32*, 469.

(16) Koo, J. B.; Yoon, D. Y. *Metallurgical and Materials Transactions a-Physical Metallurgy and Materials Science* **2001**, *32*, 1911.

(17) Zhang, H. M.; Zhang, Y.; Xu, K. W. *Journal of Crystal Growth* **2005**, *285*, 427.

(18) Greiser, J.; Mullner, P.; Arzt, E. *Acta Materialia* **2001**, *49*, 1041.

(19) Thompson, C. V.; Carel, R. *Journal of the Mechanics and Physics of Solids* **1996**, *44*, 657.

(20) Floro, J. A.; Thompson, C. V.; Carel, R.; Bristowe, P. D. *Journal of Materials Research* **1994**, *9*, 2411.

(21) Vitos, L.; Ruban, A. V.; Skriver, H. L.; Kollar, J. *Surface Science* **1998**, *411*, 186.

(22) Mehl, M. J.; Papaconstantopoulos, D. A. *Physical Review B* **1996**, *54*, 4519.

(23) Tyson, W. R.; Miller, W. A. *Surface Science* **1977**, *62*, 267.

Table A: Annealing history of different samples

| Sample | Annealing T | STM | LEED | Laue |
|---|---|---|---|---|
| A | 550-600 K | Terrace 100-200 nm wide | 6-fold pattern | good |
| B | 800 K | Small terrace about 20 nm wide | Near 6f-pattern, diffused spots | > 10º off |
| | 900 K | Step bunch, square islands | | |
| | 950 | | | |
| C | > 1000 K | Large terrace, 500 nm wide | Sharp 6f-pattern | No pattern |
| D | 550-600 K | | 6-fold pattern | |
| | 900 K | | 6f and 4f pattern | |

Figure Captions

1. Schematic diagram of the main annealing processes. (a) deformed state; (b) recovered; (c) partially recrystallized; (d) fully recrystallized; (e) grain growth; (f) abnormal grain growth. (From Humphreys, F. J.; Hatherly, M. *Recrystallization and related annealing phenomina*; Elsevier, 2004. With permission)
2. Ag(111) STM after annealing at (a) 550-600 K, 300 nm x 300 nm; (b) 770-800 K, 150 nm x 150 nm; (c) ~900 K, 300 nm x 300 nm, inset shows 50 nm x 50 nm view of the surface; (d) > 1000 K, 300 nm x 300 nm; (a')-(d') line profiles for the scanning.
3. Ag(111) STM after annealing at 550-600 K showing dislocations, 200 nm x 200 nm: (a) 2D mode; (b) derivative mode.
4. LEED pattern of Ag(111) surface after annealing at (a) ~ 550 K, at an incident energy of 109 eV; (b) ~ 800 K, at an incident energy of 138 eV; (c) ~ 900 K, at an incident energy of 85 eV.
5. Laue back-scattering pattern of Ag(111) single crystal (a) Fresh sample; after annealing at (b) ~ 800 K; (c) > 980 K.

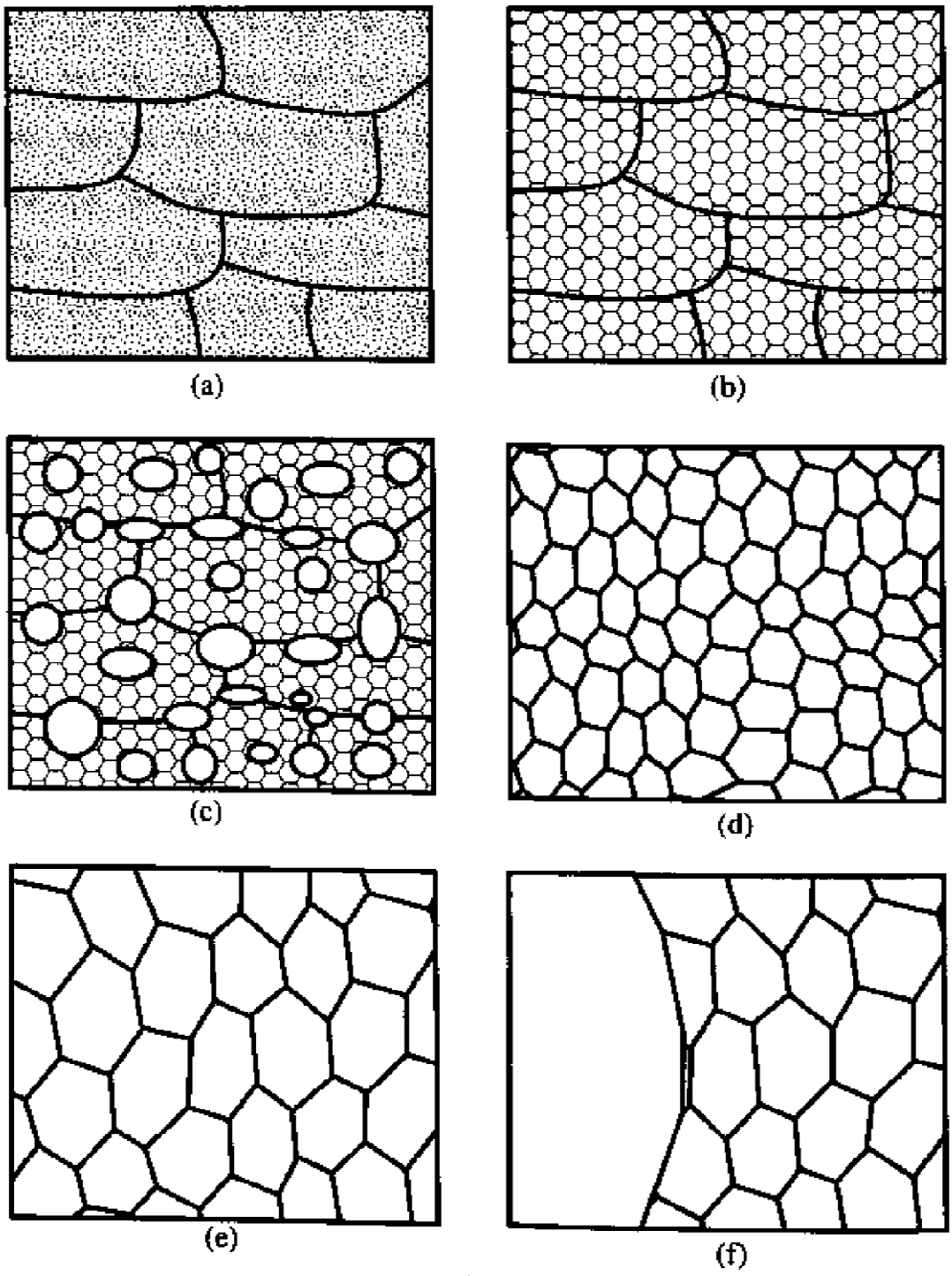


Figure 1

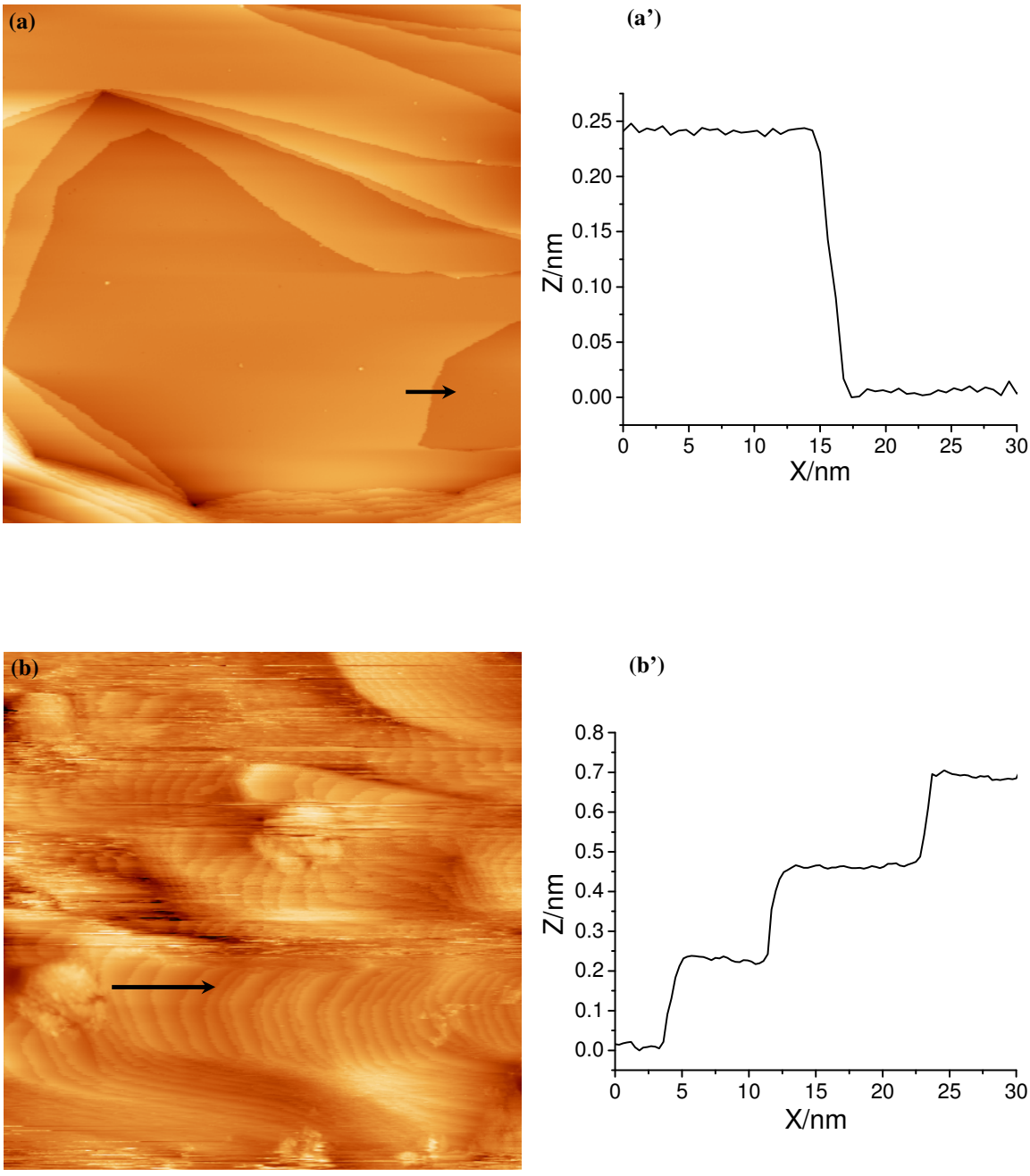


Figure 2

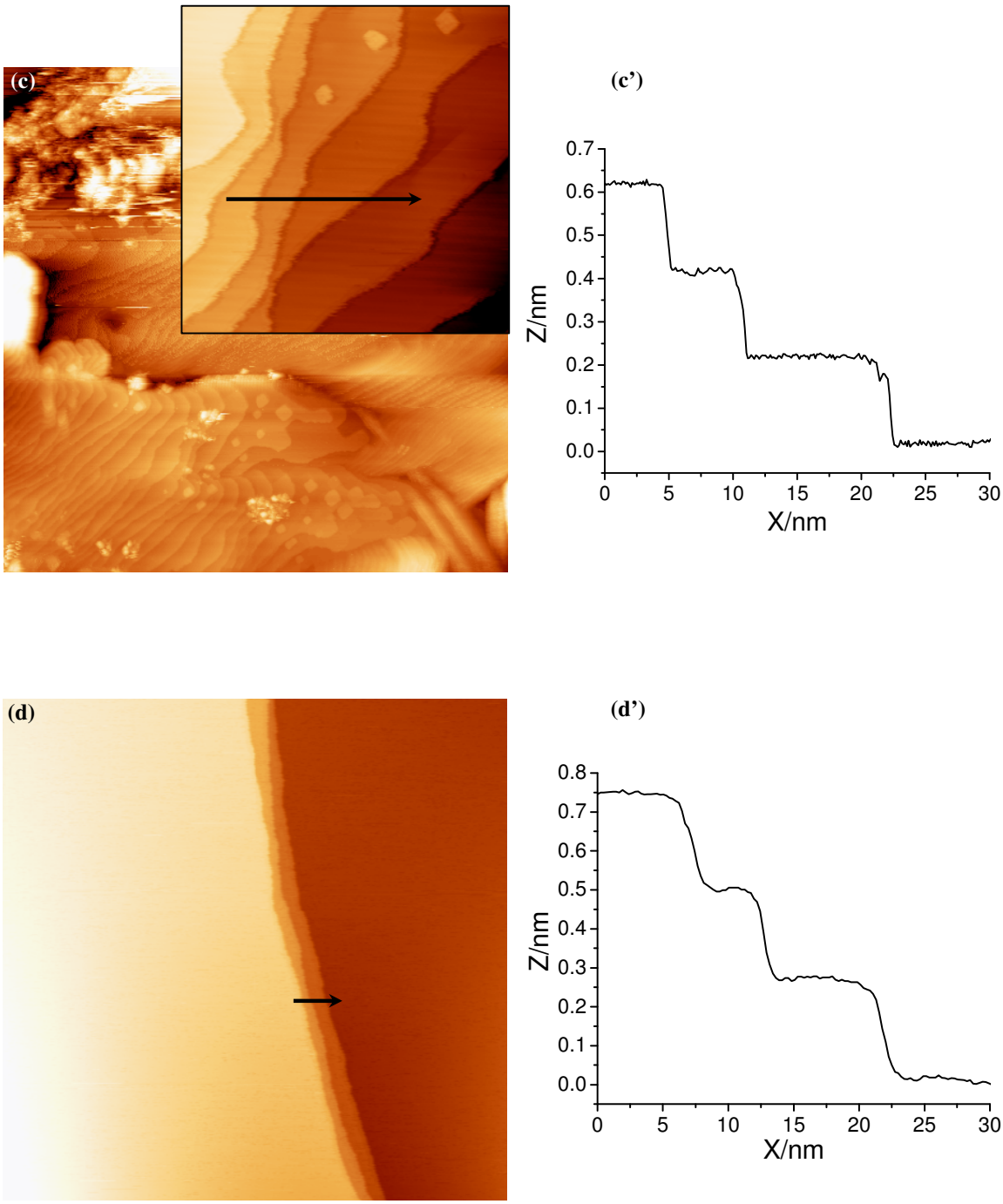


Figure 2 (Cont.)

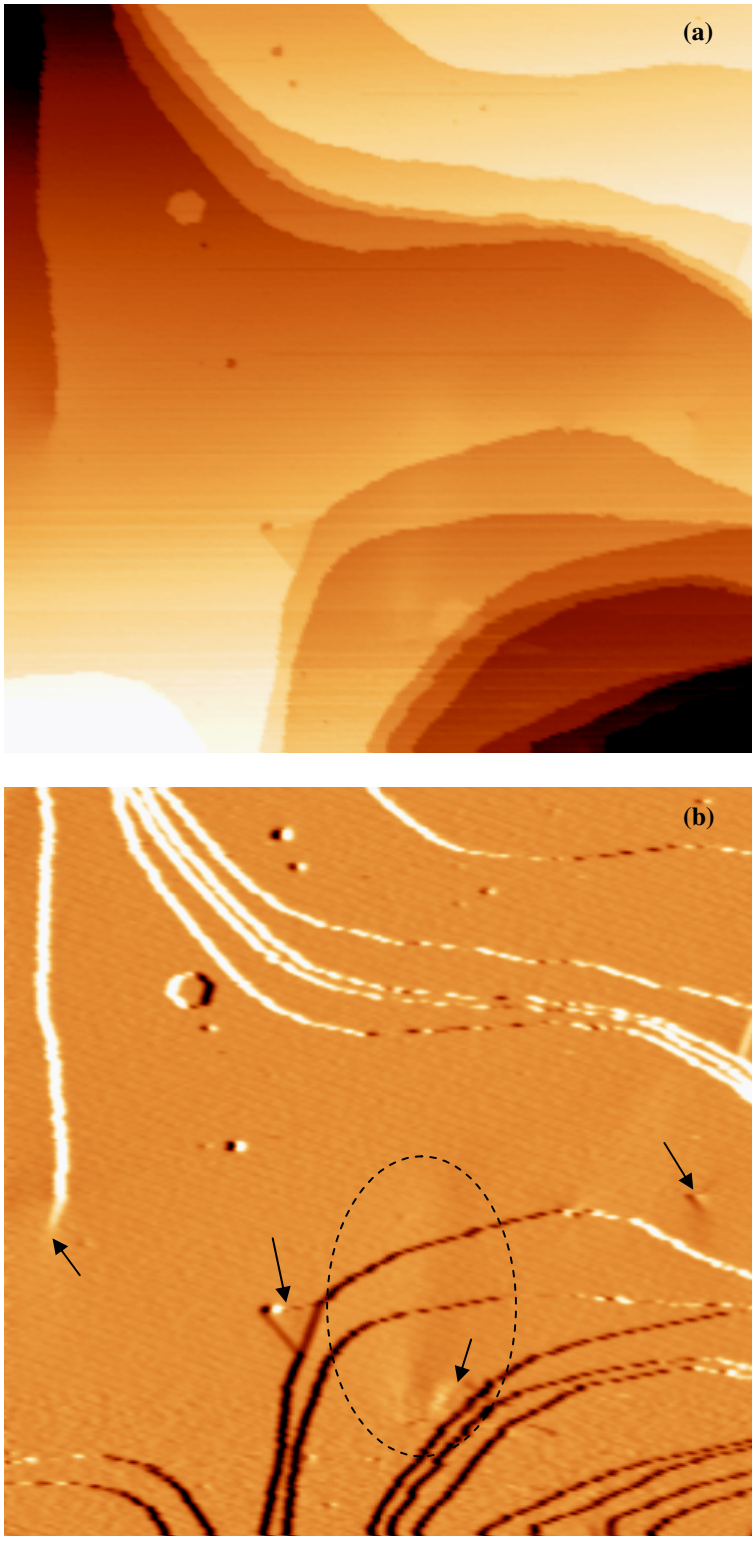


Figure 3

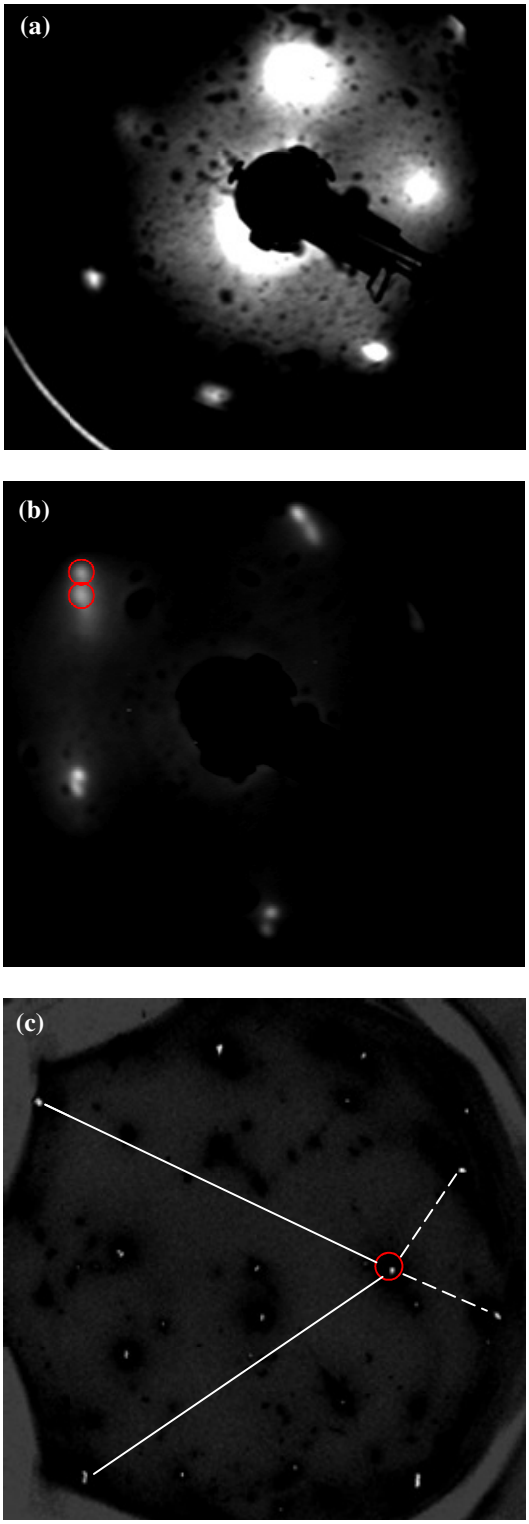


Figure 4

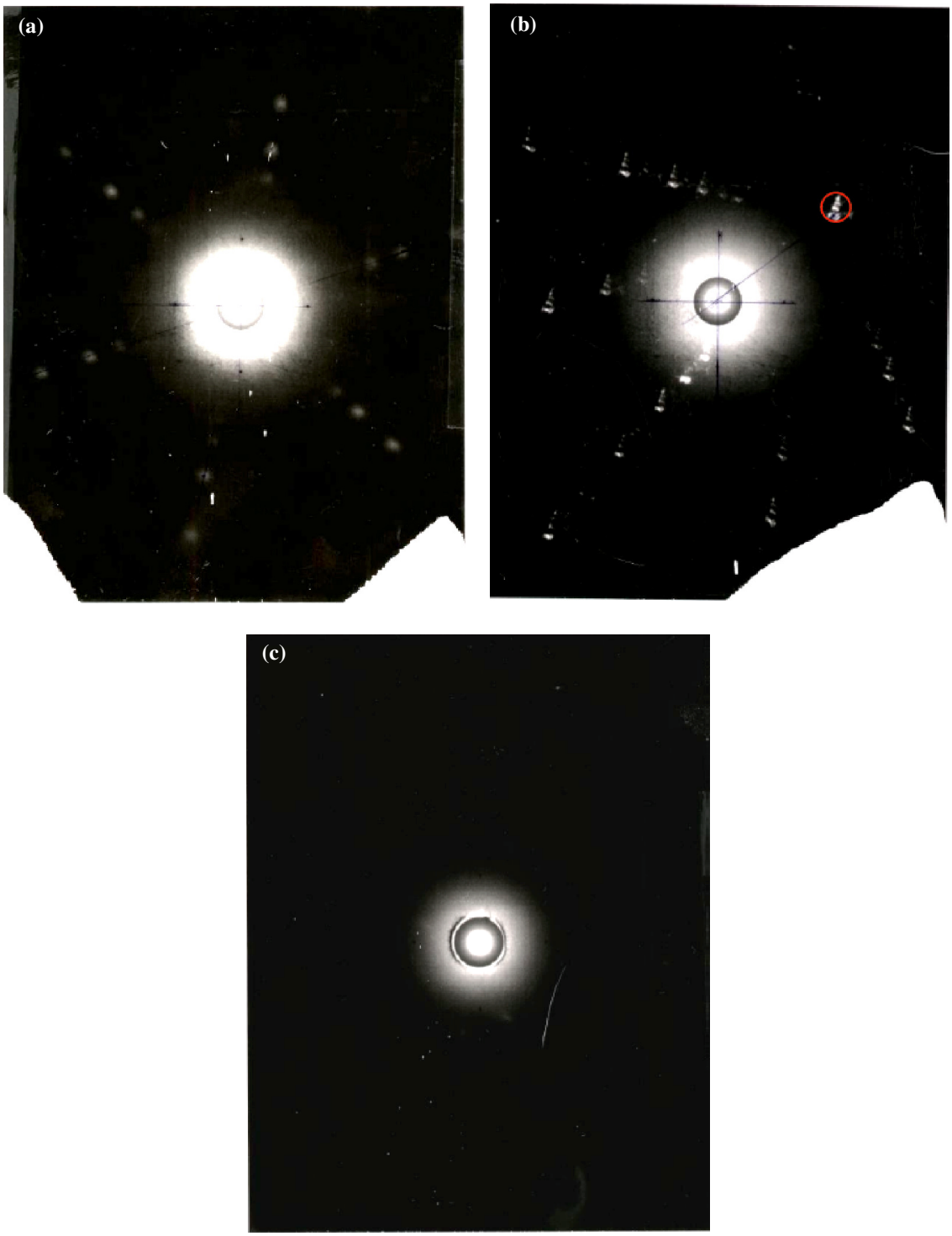


Figure 5

# CHAPTER 7. GENERAL CONCLUSION

The work presented in this dissertation clearly shows that the adsorption on Ag(111) causes structure formation. S adsorption also has a strong effect on coarsening of both Ag/Ag(111) and Ag/Ag(100) systems.

1. At 200 K, adsorbed S self-organizes into a distinctive dot-row structure and into other forms of adsorbed S. The dot-row structure exists over a coverage range that spans an order of magnitude (0.03 to 0.4 ML). A strong case, based partly on energy calculations and the height of the dots in STM, can be made for assigning the dots as $Ag_3S_3$ clusters in a matrix of adsorbed S. The dot-row structure undergoes two reversible transitions, one of which may be transformation to a Ag-Ag chain structure. Dynamics of ordering during adsorption, and equilibrium fluctuations, can be observed. DFT lends insight into the viability of other structures in this rich system, including a new candidate for the well-known ($\sqrt{7}$ x $\sqrt{7}$)R19$^o$ phase we found at higher S coverage (> 0.5 ML).

2. Trace amounts of S were shown to greatly enhance coarsening of Ag adatom islands on Ag(111), but only above a critical coverage where all step edges are saturated with S. This picture is consistent with our DFT results demonstrating the stability and mobility of various metal-S clusters, together with our analysis of coarsening kinetics based on non-linear reaction-diffusion equations incorporating appropriate mechanisms and rates for cluster formation. In contrast to the other systems mentioned above, one of the stable clusters, $Ag_3S_3$, which can contribute to enhanced coarsening has been observed directly by STM as a component of S adlayer structures on Ag(111) at around 200 K (Again, we note that other clusters such as $AgS_2$ could provide even greater enhancement).

3. For three metal-chalcogen systems—O/Ag(100), S/Ag(111), and S/Cu(111)— the adsorbate serves to accelerate coarsening. In one of these systems, S/Ag(111), our work has shown that coarsening is unaffected if the S coverage is too low, and inhibited if dense rows of $Ag_3S_3$ trimers are present. Mechanistically, metal-chalcogen clusters are implicated as major agents of mass transport in all three systems. A challenge in the field is to establish whether accelerated metal coarsening is indeed a universal effect in coinage metal-chalcogen systems, as suggested by the work thus far, and if so, whether a general energetic and mechanistic picture can be developed.

4. At 300 K, adsorbed S on Ag/Ag(100) causes the ripening mechanism change from Smoluchowski ripening (SR) to Ostwald ripening (OR) at S coverages from 0.03 ML to 0.21 ML. The Ag island decay rate for OR increases with increasing S coverage. Ag islands change from square to round with increasing S coverage, and change orientation at S coverage higher than 0.16 ML. No more coarsening occurs when S coverage increases to 0.27 ML, where ordered structures are also visible. Preliminary DFT results indicate that S adatoms prefer (110) microfacet sites along <001>-type steps than 3f-hollow sites along close-packed step edge.

# APPENDIX I. RIPENING OF MONOLAYER VACANCY PITS ON METAL SURFACES: PATHWAYS, ENERGETICS AND SIZE-SCALING FOR Ag(111) VERSUS Ag(100)

A paper published in *Physical Review B*

Mingmin Shen, J.-M. Wen, C.J. Jenks, P.A. Thiel, Da-Jiang Liu, and J.W. Evans

## ABSTRACT

Scanning tunneling microscopy studies have revealed that monolayer-deep vacancy pits typically coarsen at 300 K via Smoluchowski ripening (SR) on Ag(111) surfaces and instead via Ostwald ripening (OR) on Ag(100) surfaces. We elucidate the underlying atomistic processes, the relevant energetics with some input from Density Functional Theory analysis, and also the scaling of the ripening rate with mean pit size. Size scaling for SR reflects the size-dependence of the pit diffusion coefficient, so we also discuss observed deviations from classical theories. SR dominates OR for pits on Ag(111) primarily due to its significantly lower effective energy barrier. However, the effective barrier for OR is not lower than that for SR for pits on Ag(100), and one must also account for distinct size scaling of these pathways to explain the dominance of OR. We also briefly discuss the dependence on temperature of the dominant ripening pathway and the ripening behavior for adatom islands.

## I. INTRODUCTION

Coarsening or ripening phenomena are ubiquitous for two-phase materials from solid alloys to surface deposits to liquid droplets [1]. The driving force for evolution is reduction of the excess free energy associated with the interface regions between the two phases. The most common mechanism for coarsening of convex domains or aggregates of a minority

phase embedded in a majority phase is Ostwald ripening. This mechanism involves mass transfer between smaller and larger aggregates leading to growth of the latter. This is a curvature-driven process reflecting the higher chemical potential of smaller aggregates.

One class of two-phase systems with an embedded minority phase is provided by single-atom-high islands for adlayers with lower pre-coalescence coverages on low-index single-crystal metal surfaces. These island distributions are typically formed by deposition of up to roughly 0.3 monolayers and are embedded in a very dilute two-dimensional gas phase of adatoms. Another class is provided by single-atom-deep vacancy pits embedded in the surrounding terrace. Such distributions of pits can be formed either by sputtering of the surface, or by depositing adlayers with higher near-monolayer coverages as described below. These classes of systems are ideally suited for fundamental studies of coarsening phenomena in two-dimensions [2,3,4]. In this paper, we focus on analysis of the latter, vacancy pit ripening, for Ag single-crystal surfaces.

Previous experimental studies have revealed a stark contrast in the ripening mechanism observed for monolayer-deep vacancy pits on the (111) and (100) faces of an Ag single-crystal substrate at 300 K. Smoluchowski ripening (SR), i.e., vacancy pit diffusion and coalescence, occurs for pits on Ag(111) [2,5]. In contrast, Ostwald ripening (OR), i.e., dissolution of smaller pits and associated growth of larger pits, occurs for pits on Ag(100) [6]. The corresponding difference in ripening pathways is also observed at 300 K if the substrate is Cu rather than Ag [3]. In this paper, we will determine the origin of this differing behavior for Ag(111) versus Ag(100) by examining the following factors:

(i) Possible underlying atomistic mass transport processes contributing to ripening. We emphasize that the mass transport underlying OR could potentially be dominated by either

terrace diffusion of adatoms or of isolated vacancies. For SR in the systems of interest here, it is commonly accepted that periphery diffusion of adatoms along the step edges bounding pits is the dominant factor in pit diffusion. See Fig.1 for a schematic of these atomistic processes.

(ii) Overall or effective barriers, $E_{eff}$, for these ripening pathways. We shall decompose these effective barriers into their various components, and determine these either from utilization of previous experimental data or from previous or new Density Functional Theory calculations.

(iii) Scaling of the ripening rate with mean pit size. This basic behavior can be formulated in terms of simple generic equations which have essentially the same for form either of the above mentioned OR or SR ripening mechanisms. See the discussion immediately below.

For our formulation of size scaling, we let $L_{av} = L_{av}(t)$ denote the mean linear size or "diameter" of vacancy pits at time t, where $L_0$ gives the initial value. These quantities, as well as other lengths introduced below, are measured in dimensionless units of the surface lattice constant, a. Then, we identify $K = dL_{av}/dt$ as the coarsening or ripening rate. For either OR or SR, the key quantities $L_{av}$ and K satisfy the scaling forms [4,7]

$$L_{av}(t) \approx L_0 \, (1 + t/\tau)^n \text{ with characteristic time } \tau = \tau_0 \exp[E_{eff}/(k_B T)], \quad (1)$$

and correspondingly

$$K \approx \nu \exp[-E_{eff}/(k_B T)] \, (L_{av})^{-m} \text{ with } m = n^{-1} - 1 \text{ and } \nu = (L_0)^{1/n} \, n/\tau_0. \quad (2)$$

Here, $E_{eff}$ denotes the effective or overall activation barrier for the ripening process, T denotes the surface temperature, and $k_B$ is the Boltzmann constant. Often temporal scaling behavior for ripening is formulated in terms of the average center-to-center pit separation $L_{isl}$

~ $\varphi^{-1/2}$ $L_{av}$, where $\varphi$ denotes the areal coverage of the pits. Since $\varphi$ is constant during ripening, $L_{isl}$ and $L_{av}$ exhibit the same temporal scaling.

For OR, one has that n=1/3 [so m=2] in the regime where mass transport is limited by terrace-diffusion [4], and n=1/2 [so m=1] in the regime of attachment-detachment limited mass transport [4]. For the attachment-detachment-limited OR, there exists a significant additional barrier inhibiting attachment to pits. See Appendix A. For SR, we assume that the diffusion coefficient for vacancy pits of "large" linear size L scales like [8]

$$D_{pit}(L) \approx D_0 \exp[-E_{eff}/(k_B T)] \, L^{-\beta}, \qquad (3)$$

where $E_{eff}$ will also correspond to the effective energy for ripening in (1) and (2). Then, a simple Smoluchowski-type rate equation analysis of ripening kinetics reveals that the scaling forms (1) and (2) apply with $n = 1/(2+\beta)$ [so $m = 1+\beta$] [7,9]. See again Appendix A. Clearly, a comprehensive analysis of the ripening rates for competing pathways includes both determination of the relevant energetics and assessment of size-scaling. This type of analysis seems to be lacking in the existing literature, but we shall see that it is needed to explain the experimentally observed behavior for vacancy pit ripening on Ag surfaces.

In Sec. II, we briefly review experimental observations on ripening of vacancy pits on Ag surfaces. Then, a description underlying atomistic processes and a detailed analysis of the energetics for OR of vacancy pits on Ag surfaces follows in Sec. III. Next, a description of the atomistic processes and an analysis of the energetics for SR of vacancy pits on these surfaces is provided in Sec. IV. A comparison of ripening rates for OR and SR incorporating appropriate size-scaling behavior is provided in Sec. V. Finally, conclusions are provided in Sec. VI as well as a brief discussion of analogous issues for ripening of adatom islands.

## II. REVIEW OF EXPERIMENTAL OBSERVATIONS

Procedures for our own sample preparation can be found in Ref. [10] for Ag(100), and in Ref. [11] for Ag(111). Extensive previous data for vacancy pit ripening on Ag(111) is available from studies of Morgenstern and coworkers, and their sample preparation procedures are described in Ref.s [2,5,12-14]. All observations of pit ripening where made utilizing scanning tunneling microscopy on single-crystal surfaces with broad terraces under ultra-high-vacuum conditions.

**Vacancy pit ripening and diffusion behavior for Ag(111).** As indicated in Sec. I, distributions of pits are conveniently formed by sputtering of large terraces on an Ag(111) surface. Previous studies [2,5] of large arrays of vacancy pits on Ag(111) at 300 K have revealed that evolution is dominated by SR. For pits with diameters in the range $L_0 \sim 15$-60, a significant reduction in the pit density occurs on the time scale of ~1 hour at 300 K. Our own studies also find this behavior. No island dissolution is observed, although this cannot be ruled out for some of the smallest islands, so that coarsening occurs either primarily or exclusively by SR. In new studies, we have observed similar SR of smaller ensembles of vacancy pits confined on a finite terrace surrounded mainly by ascending steps, so that pit ripening behavior is isolated from the higher terraces by the presence of a step-edge barrier (see below). However, one edge of this terrace was bounded by a descending step, and we observe that as the tip scans across this descending terrace from the lower to the upper terrace of interest, occasionally small pits are formed due to a tip effect. Subsequently, these disappeared relatively quickly due to coalescence.

Previous studies have also provided a detailed analysis of the diffusivity of these monolayer vacancy pits. The initial study of pit diffusion at 300 K found a size-scaling exponent of $\beta \approx 2.0$, i.e., $D_{pit}(L) \sim L^{-2}$ [12]. A subsequent study examining behavior for

various T revised the estimate of this exponent to $\beta \approx 1.5$ at 300 K (although statistics were more limited), and it was observed that $\beta$ tends to increase with T [13]. This later study also extracted an effective barrier varying from $E_{eff} \approx 0.6$ eV for smaller L≈13 to $E_{eff} \approx 0.5$ eV for larger L≈80 [13]. We will both utilize and elucidate these results in Sec. IV and Sec. V.

Another significant observation comes from previous studies [14], and also our own experiments, where an adatom island exists in the immediate vicinity of one or more vacancy pits. This island is observed to dissolve with its area decaying non-linearly in time as is indicative of diffusion-limited decay [2,3]. See Appendix A. However, essentially none of its atoms fill the neighboring vacancy pits, but rather attach to more distant ascending steps. This feature provides direct support for the commonly recognized existence of a large Ehrlich-Schwoebel step-edge barrier, $\delta_{ES}$ (in excess of the terrace diffusion barrier), which strongly inhibits downward transport of adatoms in the Ag/Ag(111) system [2].

**Vacancy pit ripening and diffusion behavior for Ag(100).** In these studies, distributions of pits were created as follows. Deposition of 0.8-0.9 monolayers at 300 K produced adlayer morphologies with an incomplete first layer containing irregular vacancy clusters formed due to coalescence and percolation of adatom islands. There was also a low population of second layer islands. A short time after deposition (with the temperature maintained at 300 K), the second layer atoms were incorporated into the first layer and the irregular vacancy clusters restructured to form an array of separated near-square vacancy pits.

Analysis of the evolution of arrays of dozens of vacancy pits with size $L_0$~20-60 on a large terrace at 300 K reveals noticeable coarsening over a period of 6 hours almost exclusively due to OR. While ripening was dominated by OR, we emphasize that the vacancy pits were <u>not</u> completely immobile during the ripening process. In fact, significant pit

diffusion was observed. One can track the motion of the center of mass of individual pits for a period of time over which their size does not vary significantly. See Fig. 2a. In this way, we are able to estimate the diffusion coefficients, $D_{pit}(L)$, for pits of various linear sizes, L. We have determined $D_{pit}$ for eighteen vacancy pits on Ag(100) with linear dimensions in the range $L \approx 25 \pm 10$. These data, which reveal an average diffusion coefficient of $D_{pit}(L \approx 25) \approx 3.5 \times 10^{-3}$ $a^2/s$, are shown in Fig. 2b.

In the following analysis, we will propose that large vacancy pits and adatom islands on Ag(100) with the same size have roughly equal diffusion coefficients. See also Sec. V. This is generically true in the "continuum regime" of very large sizes $L >> L_c$, where $L_c \approx 70$ at 300 K is the mean separation between kinks on a close-packed step edge (see below). In this regime, the size-scaling exponent for cluster diffusion mediated by periphery diffusion satisfies $\beta = 3$ [8]. However, we will also claim that this rough equality of island and pit diffusion coefficients applies for the regime of smaller sizes L≈10-35. Here, the size-scaling exponent $\beta \approx 2.3$ has been shown to deviate significantly below the continuum value for adatom islands [15]. Thus, by our assumption, $\beta \approx 2.3$ for vacancy pits in this size range. Experimental support for our proposal is provided in Fig. 2b, where we also show a subset of our previous data [10] for diffusion coefficients, $D_{isl}$, of nine adatom islands with a range of smaller linear sizes $L \approx 13 \pm 5$ yielding an average value of $D_{isl}(L \approx 13) \approx 1.5 \times 10^{-2}$ $a^2/s$. Our data for adatom islands or vacancy pits separately are not extensive enough to assess size scaling. However, together the data are consistent with our proposal for similar diffusion coefficients of islands and pits with a common size scaling exponent of $\beta \approx 2.3$. (Note that Ref.[6] made the misleading assertion that the diffusion coefficient for vacancy pits is

smaller than that for adatom islands. This assertion was based on a neglect of the decrease of diffusion coefficient with pit or island size.)

## III. ENERGETICS FOR OSTWALD RIPENING OF VACANCY PITS

Traditionally, ripening in submonolayer metal homoepitaxial systems has invariably been expected to occur via the OR pathway [4]. Thus, we first analyze the associated OR energetics for vacancy pits. These results are summarized again in Sec.V. We thereby provide insight into why OR is inefficient for vacancy pits on Ag(111), but more efficient on Ag(100). As indicated in Sec. I, there are potentially two mass transport pathways which could contribute to OR in these systems (see Fig.1a):

(i) adatom transport (ORA) where the overall effect is that single adatoms detach from the edges of larger pits, climb up onto and diffuse across the surrounding terrace, and then descend into the smaller pits attaching to their edges;

(ii) vacancy transport (ORV) where the overall effect is that single vacancies detach from the edges of smaller pits, then diffuse across the terrace and attach to the edges of larger pits (a process involving only intra-layer hopping of atoms).

For adatom transport (ORA), one can apply the Gibbs-Thomson relation [4] to determine the equilibrium density (per site), $\rho_{ad}$, of single adatoms on the upper or lower terraces immediately adjacent to the edge of a pit. If R denotes the local "pedal" radius [16] of the pit, and $\gamma>0$ denotes the local step energy per atom, then one has that

$$\rho_{ad}(R) = \rho_0 \exp[-\gamma/(k_B T R)], \text{ where } \rho_0 \sim \exp[-E_b/(k_B T)]. \quad (4)$$

Here, $\rho_0$ gives the equilibrium density adjacent to a straight step, and $E_b>0$ denotes the effective detachment energy from such a step [4,16]. The ratio $\gamma/R$ is constant along the step

edge for equilibrated pit shapes [16], and often one interprets $\gamma$ as a mean step energy and R as a mean radius. Thus, adatoms diffuse from regions of higher density surrounding larger pits to those of lower density around smaller pits. Since such atoms must surmount the additional Ehrlich-Schwoebel step-edge barrier, $\delta_{ES}$, in both climbing out of and descending into pits, the effective barrier for this ripening pathway is given by $E_{eff}(ORA) = E_d(ad) + E_b + \delta_{ES}$, where $E_d(ad)$ is the adatom terrace diffusion barrier. More precisely, this result applies for significant step-edge barriers (the case of relevance here) where the associated characteristic Ehrlich-Schwoebel length, $L_{ES} = \exp[\delta_{ES}/(k_BT)]-1$, far exceeds pit separations.

For vacancy transport (ORV), the equilibrium density of single vacancies surrounding a pit of radius R has the Gibbs-Thomson [4] form

$$\rho_{vac}(R) = \rho_0 \exp[+\gamma/(k_BTR)], \text{ with } \rho_0 \text{ and } E_b \text{ as above} \quad (5)$$

(for pairwise adspecies interactions). Thus, single vacancies diffuse from regions of higher density around smaller pits to those of lower density around larger pits. Since no step edge barrier need be surmounted for this intralayer process, the effective barrier for this ripening pathway is $E_{eff}(ORV) = E_d(vac) + E_b$, where $E_d(vac)$ is the vacancy terrace diffusion barrier.

**Absence of OR for vacancy pits on Ag(111).** First, consider the adatom transport pathway (ORA) on Ag(111). The value of the adatom terrace diffusion barrier of $E_d(ad) = 0.10$ eV is well established from both theory and experiment [17]. Appendix B gives our consistent estimate from Density Functional Theory (DFT) analysis. If $\phi$ denotes the nearest-neighbor (NN) bond energy for a pair of Ag adatoms on the Ag(111) surface, then the detachment energy on fcc(111) surfaces satisfies $E_b = 3\phi$ noting that three bonds are broken when an atom detaches from a kink site along a step edge. A previous DFT study using a 4×4

supercell reported a somewhat high value of $\phi$=0.24 eV [18]. However, our own DFT analysis reveals a surprisingly slow convergence with increasing lateral supercell size to the more precise value of $\phi$=0.19 eV for a 6×6 supercell. See Appendix B. If one uses the commonly adopted value for the "large" step edge barrier of $\delta_{ES} \approx 0.13$ eV [2], then one obtains for the OR pathway mediated by adatom transport a value of $E_{eff}(ORA) \approx 0.8$ eV. In Sec. IV, we shall see that this is significantly higher than the effective barrier for SR indicating this OR pathway may be inactive.

Second, consider the vacancy transport pathway (ORV). While this pathway has the advantage that no step edge barrier need be surmounted, a critical factor is the efficiency of vacancy diffusion. To assess this factor, we have performed DFT calculations to determine the terrace diffusion barrier for single vacancies. We find that $E_d(vac) = 0.58$ eV for a 3×3 supercell which is reasonably consistent with a previous estimate using semi-empirical potentials [19]. See Appendix B. This high value should be expected since vacancy diffusion occurs via hopping of an adjacent atom into an isolated vacancy, and its motion is highly constrained. Thus, one obtains for the OR pathway mediated by vacancies an even larger value of $E_{eff}(ORV) = E_d(vac) + 3\phi > 1.1$ eV which will be shown to be far too high for OR to be operative.

**OR for vacancy pits on Ag(100).** First, consider the adatom transport pathway (ORA) on Ag(100). The adatom terrace diffusion barrier has the value $E_d(ad) = 0.40$-$0.45$ eV from theory and experiment [17,20]. See Appendix B for our own consistent DFT estimate. Also, it is known from analysis of experimental studies of kinetic roughening during multilayer growth that a step edge barrier exists only along close-packed edges with a low value of $\delta_{ES}$

= 0.07 eV [17,20,21]. The detachment energy satisfies $E_b = 2\phi$ on fcc(100) surfaces for NN adatom bond energy $\phi$, noting that two bonds are broken upon detaching an adatom from a kink site. A previous DFT estimate gave $\phi = 0.22$ eV [22] which is slightly above our own estimates. See Appendix B. Thus, we conclude that the effective barrier for OR by adatom transport is $E_{eff}(ORA) \approx 0.9$ eV.

Second, the vacancy transport pathway (ORV) again has the advantage that no ES barrier need be surmounted, although that would not be a major impediment for Ag(100). However, another significant factor is suggested by previously available semi-empirical analyses of energetics [19,23]. These indicate that the activation barrier for single vacancy diffusion is generally comparable to or even somewhat lower than for adatom diffusion on metal(100) surfaces. This contrasts behavior on metal(111) surfaces. Roughly speaking, vacancy diffusion involves adatom motion reminiscent of escape from a kink along a step edge for which the barrier is the sum of a low step diffusion barrier and the NN interaction $\phi$. For a more precise analysis, we apply DFT to obtain $E_d(vac) = 0.35$ eV for the Ag(100) surface from a 3×3 supercell. See Appendix B. Thus, the effective barrier for OR by vacancy diffusion is $E_{eff}(ORV) \approx 0.8$ eV. This value is lower than $E_{eff}(ORA)$ indicating that vacancy transport should dominate adatom transport pathway in the observed OR process. It remains to explain why this pathway is more efficient than SR which we shall see in Sec. IV has a lower effective barrier.

## IV. ENERGETICS FOR SMOLUCHOWSKI RIPENING OF VACANCY PITS

As indicated in Sec. I, the ripening rate for SR and its scaling with mean vacancy pit size is determined by the diffusion coefficient for the large pits and the scaling of this

diffusion coefficient with pit size. For Ag(100) and Ag(111) surfaces, pit or island diffusion is believed to be mediated by periphery diffusion of adatoms along step edges [2,5,15,24-27]. We now discuss the corresponding energetics. Results are also summarized in Sec.V. The traditional continuum treatment of cluster diffusion mediated by periphery-diffusion predicts a diffusion coefficient of the form (3) with scaling exponent $\beta=3$ [2,8]. This diffusion coefficient is also proportional to the product of the adatom step edge mobility, $\sigma_e \sim \exp[-E_{mob}/(k_BT)]$, and the density of adatom carriers, $\rho_{edge} \sim \exp[-\phi/(k_BT)]$, for mass transport along the step edge. The effective energy for the mobility satisfies $E_{mob} = E_e + \delta_{KES}$, where $E_e$ is the barrier for diffusion of adatoms along straight close-packed steps, and $\delta_{KES}$ is the additional kink rounding barrier (sometimes referred to as the kink Ehrlich-Schwoebel barrier); $\phi$ is the NN pair interaction as above. Thus, the effective activation energy for cluster diffusion and for ripening in this treatment satisfies $E_{eff}(SR) = E_{mob} + \phi = E_e + \phi + \delta_{KES}$ (continuum). The carriers are identified as edge adatoms since isolated edge vacancies have a higher barrier for diffusion along straight steps.

However, as noted in Sec. III, deviations from classic continuum scaling with $\beta<3$ are often observed [13,15]. To understand this behavior, one can utilize atomistic models for periphery diffusion which provide a realistic treatment of the numerous distinct types of adatom hops and barriers for edge diffusion associated with different local step configurations. Such models exclude detachment, but satisfy detailed-balance for all allowed edge hops. Most such studies have focused on adatom island diffusion rather than vacancy pit diffusion. However, the key concepts deriving from the former studies should apply for vacancy pits. It is convenient to introduce a characteristic length corresponding to the typical

separation between kinks on equilibrated close-packed step edges, $L_c \approx \exp[\varepsilon_{kink}/(k_BT)]$, where $\varepsilon_{kink} \approx \phi/2$ is the kink creation energy. Since $\varepsilon_{kink} \approx 0.11$ eV for an Ag(100) surface [3], consistent with our use of $\phi \approx 0.22$ eV, one has that $L_c \approx 70$ at 300 K as mentioned above. For Ag(111), $\varepsilon_{kink} \approx 0.10$ eV [4] and $L_c \approx 70$ at 300 K are slightly smaller. In general terms, the primary component of the deviation from continuum scaling occurs for L smaller than $L_c$ due to faceting of the vacancy pit (or adatom island) shapes. Another secondary component occurs with significant kink rounding barriers for L smaller than the so-called kink Ehrlich-Schwoebel length, $L_{KES} = \exp[\delta_{KES}/(k_BT)] - 1$.

More specifically, these deviations from classic behavior associated with facetted clusters reflect the difficulty to nucleate a new outer vacant row (or filled row) of sites on an otherwise perfect close-packed pit (or island) step edge [27-29]. This process is a necessary component of long-range cluster diffusion. If new outer rows are not created, the cluster can never move outside of a rectangle inscribing it for an Ag(100) surface, or a hexagon inscribing it for an Ag(111) surface. We now analyze the associated energetics for periphery diffusion models with no detachment and thus no background equilibrium density of isolated vacancies (adatoms) on the terrace surrounding the pit (island). For adatom islands, the density of isolated adatoms on a perfect close-packed step, $\rho_{edge} \sim \exp[-\phi/(k_BT)]$, is low as these atoms would rather be incorporated at kink sites elsewhere on the island periphery. To nucleate a new outer filled row on this edge, another adatom must detach from a kink site on another edge and round a corner (with effective barrier of $\sim E_e + \phi + \delta_{KES}$) in order to aggregate with this lone atom before it is re-incorporated at a kink. Thus, accounting for the T-dependence of $\rho_{edge}$, one obtains a total effective barrier of $E_{eff}(SR) \approx E_e + 2\phi + \delta_{KES}$

(facetted) [27]. For vacancy pits, the picture is analogous. The density of isolated vacancies on a perfect close-packed step edge is again $\rho_{edge} \sim \exp[-\phi/(k_B T)]$. To nucleate a new outer vacant row on this edge, an atom adjacent to this vacancy could be transported away to a distant kink site (with effective barrier $E_e + \phi + \delta_{KES}$). See the top portion of the schematic Fig.1b which illustrates this process. This again leads to the result that $E_{eff}(SR) \approx E_e + 2\phi + \delta_{KES}$ (facetted).

To create isolated vacancies on perfect outer step edge of a vacancy pit within these periphery diffusion models, it is necessary for a highly-coordinated atom to be extracted from a straight step edge, i.e., to extract a triply-coordinated atom for Ag(100), and a quaduply-coordinated atom for Ag(111). In contrast for adatom islands, it is not necessary to extract any highly-coordinated adatoms from step edges in order to achieve nucleation of new rows and thereby long-range island diffusion. Returning to consideration of vacancy pits, it should be noted that the effective barrier for extraction of a highly-coordinated atoms from some central portion of a straight step edge is in fact equal to $E_{eff}(SR)$. (This is most easily seen by noting that the reverse process corresponds to corner or kink rounding with a barrier of $E_e + \delta_{KES}$. Thus, using detailed-balance, the barrier for extraction equals this value plus the energy difference of $2\phi$ between initial and final configurations.) However, again using detailed-balance arguments, one might anticipate that the effective barrier for sliding an atom out of a highly-coordinated corner site of the pit and along a step edge equals the lower value of $E_e+2\phi$. This is confirmed by analysis using semi-empirical potentials for Ag(100), where the kink rounding barrier is significant [23]. Thus, for pits on Ag(100), one expects that most

isolated vacancies on outer edges are created by this "corner sliding" process. See the lower left portion of the schematic Fig.1b which illustrates this process.

The above analysis does not address deviations from continuum size scaling as this requires a more detailed analysis. See Ref. [27, 28] for a more complete discussion. Here, we just summarize the results. In the regime of strongly facetted islands or pits, one has that $\beta \to 1$ for $\delta_{KES} = 0$. For the case of significant kink rounding barriers with L below $L_{KES}$, one finds even lower values of $\beta$ at least for adatom islands [27]. In practice, observed behavior is often in the crossover regime between the continuum and completely facetted limits. Thus, the effective $\beta$ is expected to decrease with decreasing T (or L), and the effective energy, $E_{eff}(SR)$, should increase with decreasing T (or L). These features are in fact observed in the experimental data for vacancy pit diffusion on Ag(111) [13].

**Vacancy Pit diffusion on Ag(111).** Here, one finds that $E_e \approx 0.28$-$0.31$ eV is large, $\delta_{KES} \approx 0.05$ eV is small [11,30], and $\phi \approx 0.19$ eV as in Sec. III. Thus, one estimates that $E_{eff}(SR) \approx 0.52$-$0.55$ eV (continuum) and $E_{eff}(SR) \approx 0.7$ eV (facetted). The former value is reasonably consistent with experimental results for vacancy pit diffusion of $E_{eff}(SR) \approx 0.5$ eV for larger L [2,13]. However, as noted in Sec. III, the experimentally observed $\beta \approx 1.5$ deviates significantly below the continuum value. Correspondingly, the experimentally observed $E_{eff}(SR) \approx 0.6$ eV for small pit sizes is somewhat above the continuum theory value, but below the completely-facetted value.

**Vacancy Pit diffusion on Ag(100).** Here, one has that $E_e = 0.25$ eV based on DFT analysis [31]. We estimate that $\delta_{KES} \approx 0.16$ eV [21,26,27], and $\phi \approx 0.21$ eV from Sec. III. Thus, it follows that $E_{eff}(SR) \approx 0.62$ eV (continuum) and $E_{eff}(SR) \approx 0.8$ eV (facetted). Unfortunately,

there has been no previous experimental determination of $E_{eff}(SR)$ for adatom island or vacancy pit diffusion. However, related studies of periphery-diffusion-mediated relaxation of step edge nanostructures [25] suggest values in this range. For example, we have estimated that the initial rate of decay of the height of a 10×10 square protrusion on a close packed step edge equals 7 a/s at 300 K [25] versus 0.14 a/s at 260 K [32]. This corresponds to a value of $E_{eff}(SR) \approx 0.67 \pm 0.1$ eV although we caution that there is considerable uncertainty in our estimates of decay rates. As noted in Sec. III, the experimentally observed value of $\beta \approx 2.3$ for adatom islands is below the continuum value. We assume that this value $\beta \approx 2.3$ also applies for vacancy pits, and consequently expect that $E_{eff}(SR)$ should be somewhat above the value predicted from continuum theory.

## V. ANALYSIS OF SMOLUCHOWSKI VERSUS OSTWALD RIPENING RATES

Integrating all of the results for energetics from Sec. III and Sec. IV to determine appropriate effective energy barriers for ripening (as summarized in Table I), we now provide a comparison of rates for SR and OR of vacancy pits for Ag(111) and Ag(100).

**Vacancy pit ripening on Ag(111).** We compare the rates (2) for SR and OR (=ORA here):

$$K_{SR} \approx \nu_{SR} \exp[-0.56/(k_B T)](L_{av})^{-2.5} \text{ versus } K_{ORA} \approx \nu_{ORA} \exp[-0.80/(k_B T)](L_{av})^{-1}, \quad (6)$$

in units of $s^{-1}$ with $k_B T$ in eV. For SR, we have used $\beta = 1.5$ (so $m = 2.5$), and $E_{eff} = 0.56$ eV which is somewhat above the value of $E_{eff}(SR)$ from continuum theory. For ORA, adatom mass transport is inhibited by a step-edge barrier, $\delta_{ES} \approx 0.13$ eV, with an associated characteristic Ehrlich-Schwoebel length $L_{ES} = \exp[\delta_{ES}/(k_B T)] - 1 \approx 152$ at 300 K. Since $L_{ES}$ is somewhat above the typical pit separation of ~100, we have used the attachment-detachment-limited exponent $m = 1$ (although the effective value could be somewhat higher). See

Appendix A. For a quantitative comparison, it remains to assess the prefactors. Based on analysis of experimental data in Appendix C, we assign $\nu_{SR} \approx 10^{11.1}$ $s^{-1}$ and $\nu_{ORA} \approx 10^{11.3}$ $s^{-1}$, so that $K_{SR} \approx 47\ (L_{av})^{-2.5}$ versus $K_{ORA} \approx 0.007\ (L_{av})^{-1}$ at 300 K. This implies that SR should dominate OR below a crossover size of $L_{SR \to OR} \approx 350$. See Fig.3a. Thus, for the experimental size range, $L_{av} \approx 30$-50, it follows that SR should completely dominate at 300 K (as observed). For higher temperatures around 350 K, the crossover size decreases to $L_{SR \to OR} \approx 94$ and the typical experimental $L_{av}$ is larger than at 300K, so OR should become competitive with SR.

**Vacancy pit ripening on Ag(100).** We compare the rates (2) for SR and OR (=ORV here):

$$K_{SR} \approx \nu_{SR} \exp[-0.65/(k_B T)](L_{av})^{-3.3} \text{ versus } K_{ORV} \approx \nu_{ORV} \exp[-0.80/(k_B T)](L_{av})^{-2}, \quad (7)$$

in units of $s^{-1}$ with $k_B T$ in eV. For SR, we have used $\beta$=2.3 and $E_{eff}$ = 0.65 eV somewhat above the prediction of continuum theory. This choice of $\beta$ is based on the assumption that vacancy pits and adatom islands of the same size have similar diffusion coefficients. Some experimental data supporting this claim was provided in Sec. II. In addition, we have run simulations of the atomistic model for periphery-diffusion-mediated cluster diffusion described in Ref. [27]. Results from these simulations at 300 K choosing $\phi$ = 0.2 and $\delta_{KES}$ = 0 support this claim for sizes above L=30 (cf. $L_c \approx 70$). The pit diffusion coefficient is somewhat lower than the island diffusion coefficient for smaller sizes, but this could reflect limitations of our treatment of periphery diffusion (which is likely too inhibited for concave step edge geometries characteristic of pits). For OR=ORV, we have used that ORV is terrace-diffusion-limited, resulting in a scaling exponent m=2. Based on analysis of experimental data in Appendix C, we assign $\nu_{SR} \approx 10^{12}$ $s^{-1}$ and $\nu_{ORV} \approx 10^{13.3}$ $s^{-1}$, so that $K_{SR} \approx 10\ (L_{av})^{-3.3}$

versus $K_{ORV} \approx 0.8\ (L_{av})^{-2}$ at 300 K. This implies that OR should dominate SR above a crossover size of $L_{SR \rightarrow OR} \approx 7$. See Fig.3b. Thus, for the experimental size range, $L_{av} \approx 35$, it follows that OR should dominate at 300 K (as observed). For lower temperatures around 275 K, the crossover size increases to $L_{SR \rightarrow OR} \approx 22$ and the typical experimental $L_{av}$ is smaller than at 300 K, so SR should become competitive with OR (although both processes are very slow at this temperature).

We caution that there are significant uncertainties in the above analyses. Fairly small changes in effective energies produce significant changes in the rates. Also, there is considerable uncertainty in prefactors, and these also have an effect on the rates. However, we believe that the above analysis of ripening rates and their crossover with vacancy pit size captures the essential features of ripening on Ag surfaces.

## V. CONCLUSIONS

The distinct ripening behavior for vacancy pits on Ag(111) versus Ag(100) surfaces has been elucidated in terms of the underlying atomistic mass transport pathways, the energetics of those pathways, and the scaling of the ripening rate with pit size. OR of vacancy pits on Ag(111) is inoperative primarily due to a large effective barrier. This large barrier derives in part from the presence of a large Ehrlich-Schwoebel step edge barrier if one considers mass transport via single adatoms, or from a high terrace diffusion barrier if one considers mass transport via single vacancy diffusion. OR of vacancy pits is operative on Ag(100) where mass transport is dominated by single vacancy diffusion in part due to its lower terrace diffusion barrier (relative to that for single adatoms). SR is also inhibited relative to OR for Ag(100) due to the relatively large size of the pits. The type of analysis

presented above can be extended to compare ripening mechanisms for vacancy pits on Cu(100) and Cu(111) surfaces [3].

The above approach is also effective in elucidating the different ripening mechanisms observed for adatom islands at 300 K, either on Ag [2,6] or Cu [3,15] single-crystal surfaces. Interestingly, adatom islands ripen via ORA on Ag(111) [6], in contrast to SR for vacancy pits on Ag(111). For ORA of adatom islands (unlike pits), the step edge barrier need not be surmounted during mass transport. Furthermore, adatom islands ripen via SR on Ag(100) [2], in contrast to OR for vacancy pits on Ag(100). OR is inhibited for islands relative to pits in part due to the higher diffusion barrier for adatoms of $E_d(ad) \approx 0.43$ eV compared to that for vacancies of $E_d(vac) \approx 0.35$ eV. Appendix D provides a more detailed analysis of OR versus SR pathways for adatom islands on Ag surfaces.

**ACKNOWLEDGEMENTS**

MS, JMW, CJJ, PAT and JWE were supported for work by NSF Grant CHE-0414378. DJL was supported by the Division of Chemical Sciences, US Department of Energy (DOE) - BES. The work was performed at Ames Laboratory which is operated for the US DOE by Iowa State University under Contract No. DE-AC02-07CH11358.

**APPENDIX A: OR AND SR RIPENING KINETICS**

For Ostwald ripening, analysis of kinetics is based on consideration of the evolution of a single pit or island of "diameter" L = L(t) within a sea of other islands which are described as an effective medium. Evolution is determined by solving a boundary value problem for the quasi-steady-state diffusion equation for mass transport across the surface with the appropriate boundary conditions. At the island or pit edge, one requires that the normal gradient of carrier density at the island edge is given by the ratio of the "excess

density" at island edge to the attachment length, $L_{attach} = \exp[\delta/(k_B T)] - 1$, where $\delta$ denotes any extra barrier for attachment. This excess density is the difference between the density on a terrace and the equilibrium Gibbs-Thomson density for the curved step edge (see Sec. III). When $\delta=0$, so $L_{attach}=0$, this boundary condition forces the terrace density to equal the equilibrium density. Another boundary condition is imposed at a "large" distance from the island or pit which corresponds to the average island or pit separation $L_{isl} \sim \varphi^{-1/2} L_{av} \sim \varphi^{-1/2} L$, where $\varphi$ denotes the areal coverage of the embedded phase. Specifically, one sets the carrier density to a constant corresponding to the equilibrium density at the edge of islands or pits with mean size $L_{av}$. Solving this boundary value problem after linearizing the boundary conditions for small curvature of island or pit edges yields [1,4,33]

$$d/dt\ L \sim D\rho_0\gamma\, L^{-1}\, [L_{attach} + L \ln(\varphi^{-1/2})]^{-1}\, [L/L_{av} - 1], \qquad (8)$$

where D is the terrace diffusion coefficient, and $\rho_0$ and $\gamma$ are defined in Sec. III. It follows that $dL/dt \sim -1/L$, as $L \to 0$, in the attachment-detachment-limited regime of large $L_{attach}$ (so that pit or island area $A \sim L^2$ decays linearly), and $dL/dt \sim -1/L^2$, as $L \to 0$, in the terrace-diffusion-limited regime of small $L_{attach}$ (so that areas decay non-linearly as mentioned in Sec.II).

Substitution of (8) into the continuity equation for the pit or island size distribution and extraction of self-similar scaling solutions leads to time-scaling for $L_{av}$ of the form (1) with n=1/2 for attachment-detachment-limited ripening and n=1/3 for terrace-diffusion-limited ripening [1,4,33]. In our applications, $\delta=0$ and $L_{attach}=0$ for terrace-diffusion-mediated intralayer transport, whereas $\delta=\delta_{ES}$ and $L_{attach}=L_{ES}$ for attachment-detachment-limited interlayer transport of adatoms in the presence of a step-edge barrier.

For Smoluchowski Ripening of vacancy pits, an analysis of the evolution of the mean linear pit size, $L_{av}$, is based on a simple rate equation analysis for the mean pit density, $N_{pit} \sim \varphi(L_{av})^{-2}$, for areal coverage $\varphi$ of islands or pits. It is expected that [7,9]

$$d/dt\ N_{pit} \sim -D_{pit}(L_{av})\ (N_{pit})^2 \sim -D_0 \exp[-E_{eff}/(k_BT)]\ (N_{pit})^{(4+\beta)/2}, \quad (9)$$

which can be readily integrated to obtain time evolution of the form (1) for $L_{av} \sim \varphi^{1/2}\ (N_{pit})^{-1/2}$ with $n = 1/(2+\beta)$. The treatment of SR kinetics for adatom islands is essentially identical.

**APPENIDX B: DFT ANALYSIS OF ENERGETICS**

Our DFT studies were performed using the Vienna *ab initio* simulation package (VASP) [34,35]. We employ the Generalized Gradient Approximation (GGA) with the Perdew-Burke-Ernzerhof (PBE) exchange-correlation functional [36] and the projector augmented wave (PAW) method [37]. We use the DFT theory equilibrium bulk lattice constant of 0.417 nm for fcc Ag. For the Ag(111) surface, calculations were performed on five-layer slabs of Ag substrate separated by ~1.2 nm of vacuum. For the Ag(100) surface, four-layer slabs of substrate separated by ~1.9 nm of vacuum were used. We checked for the effects of substrate atom relaxation. These effects are generally very small in calculations of adatom diffusion or NN adatom interactions, but are significant for vacancy diffusion. Results for diffusion barriers are presented in Table II, and for NN adatom interactions in Table III. These Tables also show the size of the lateral supercell used in the calculations, as well as the numbers of k-points and thus the sensitivity of results on this choice. Of particular note is the slow convergence with increasing supercell size of the NN adatom interaction, $\phi$, for the Ag(111) surface. See Ref. [38] for similar observations on slow convergence for a strained-layer heteroepitaxial system.

**APPENDIX C: PREFACTOR DETERMINATION FOR SCALING RELATIONS**

For quantitative comparison of Ostwald ripening (ORA or ORV) and Smoluchowski ripening (SR) rates, it is necessary to assess the prefactors in (2). This is achieved here by matching the experimentally observed rates for ripening with the scaling forms (2).

For ORA of pits on Ag(111), one might expect that the prefactor is not readily assessed since SR dominates in this system. However, attachment-detachment-limited decay of single vacancy pits has been observed for special geometries at 300 K [1,39]. Consequently, one can exploit the feature that the observed (constant) rate of decay to zero of pit area, A, equals 1/3.6 times the (constant) rate of increase of the mean pit area, $A_{av}$, for attachment-detachment-limited OR of an array of pits [40]. Using that $dA/dt \approx -0.04$ site/s from Ref. [1] and Ref. [39], we obtain that $dA_{av}/dt \approx 0.011$ site/s at 300 K. Since $A_{av} \approx \pi/4 (L_{av})^2$, it follows that

$$K_{ORA} = dL_{av}/dt \approx 0.007 (L_{av})^{-1} \text{ at } 300K. \quad (10)$$

Then, using $E_{eff} = 0.8$ eV yields a prefactor in (2) equals $\nu = \nu_{ORA} \approx 10^{11.3}$ $s^{-1}$ for Ag(111).

For ORV of pits on Ag(100), our data at 300 K with $\varphi \approx 0.2$ ML indicates that the pit density decreases from an initial value of $N_{pit} \approx 1.2 \times 10^{-4}$ /site to $N_{pit} \approx 0.76 \times 10^{-4}$ /site after 6 hours. Using

$$N_{pit} \approx \varphi(L_{av})^{-2} \approx N_0(1 + t/\tau)^{-2/3} \quad (11)$$

for terrace-diffusion-limited ORV, consistent with (1), yields $\tau \approx 27130$ sec, and

$$K_{ORV} = dL_{av}/dt \approx 0.8 (L_{av})^{-2} \text{ at } 300 \text{ K}. \quad (12)$$

Using $E_{eff} \approx 0.8$ eV then yields a prefactor in (2) of $\nu = \nu_{ORV} \approx 10^{13.3}$ $s^{-1}$ for Ag(100).

For SR of pits on Ag(111) at 300 K, using the data in Ref. [5] with $\varphi \approx 0.15$ ML, the pit density decreases from an initial value of $N_{pit} \approx 1.0 \times 10^{-4}$/site to $N_{pit} \approx 0.67 \times 10^{-4}$/site after 61 min. Using

$$N_{pit} = \varphi(A_{av})^{-1} \approx 4\pi^{-1}\varphi(L_{av})^{-2} \approx N_0(1 + t/\tau)^{-0.57} \quad (13)$$

with $\beta \approx 1.5$ yields $\tau \approx 3090$ sec and

$$K_{SR} = dL_{av}/dt \approx 47\ (L_{av})^{-2.5} \text{ at 300 K.} \quad (14)$$

Then, using $E_{eff} \approx 0.56$ eV yields a prefactor in (2) of $\nu = \nu_{SR} \approx 10^{11.1}$ $s^{-1}$ for Ag(111).

For SR of pits on Ag(100) surface at 300 K, we assume the same kinetics for vacancy pits and adatom islands. Then, we can use the result from Ref. [14] that $L_{av}/L_0 \approx 1.93$ for t = 1667 sec together with $\beta \approx 2.3$ to obtain from (1) an estimate of $\tau \approx 6410$ sec and

$$K_{SR} = dL_{av}/dt \approx 2\ (L_{av})^{-3.3} \text{ at 300 K.} \quad (15)$$

Then, using $E_{eff} \approx 0.65$ eV yields a prefactor in (2) of $\nu = \nu_{SR} \approx 10^{11.3}$ $s^{-1}$. An alternative strategy exploits our result for $D_{pit}(L \approx 25) = 3.5 \times 10^{-3}$ $a^2/s$ at 300 K together with $\beta \approx 2.3$ and $E_{eff} \approx 0.65$ eV to estimate that $D_0 \approx 10^{11.5}$ $a^2/s$. A refined analysis based on (9) but incorporating appropriate $\varphi$-dependence [7] indicates that

$$\nu = \nu_{SR} \approx (2+\beta)4\varphi(1-\varphi^{1/2})^{-2} D_0 \approx 10^{12.5}/s \text{ for } \varphi \approx 0.2 \text{ ML.} \quad (16)$$

Thus, we choose $\nu = \nu_{SR} \approx 10^{12}$ $s^{-1}$ for vacancy pit ripening on Ag(100).

**APPENDIX D: OR VERSUS SR FOR ADATOM ISLANDS**

For adatom islands on Ag(111), OR occurs via adatom transport (ORA) given the far lower terrace diffusion barrier for adatoms compared with vacancies, and noting that no step edge barrier need be surmounted. Our estimate of effective barrier, $E_{eff}(OR) = E_d(ad)+3\phi \approx$ 0.67 eV, is quite close to the experimental estimate of 0.71 eV [39]. Note that this effective

energy is significantly lower than the value 0.8 eV for ORA of vacancy pits. ORA of adatom islands is terrace-diffusion-limited so that one has that

$$K_{ORA} = \nu_{ORA} \exp[-0.67/(k_B T)] \, (L_{av})^{-2}. \quad (17)$$

Analysis of the ripening data in Ref.[2] indicates that $\nu_{ORA} \approx 10^{12.3}$ $s^{-1}$, so that $K_{ORA} \approx 12$ $(L_{av})^{-2}$ at 300 K.

Characterization of the kinetics of SR of adatom islands on Ag(111) is more difficult as this process is not observed experimentally at 300 K. However, adatom islands are mobile and their diffusivity has been characterized [13]. The effective activation barrier was estimated as $E_{eff}(SR) \approx 0.53$ eV [13], quite close to the experimental estimates for vacancy pits, and consistent with continuum theory estimate (for either pits or islands) of 0.54 eV. The experimental estimate for the size scaling exponent of $\beta \approx 1.6$ [13] is also close to that for vacancy pits. Thus, one concludes that the diffusivity of islands and pits of the same size on Ag(111) is quite similar. Then, we can adopt the expression for $K_{SR}$ for pits in (6) to describe SR of islands. In this case, using (17), one finds a crossover from SR of adatom islands to ORA as the typical size increases above $L_{SR \to OR} \approx 10$. This is consistent with experimental observations of OR as typical island sizes in Ref. [2] and Ref.[5] exceed this crossover value.

For adatom islands on Ag(100), SR dominates coarsening at 300 K. Estimation of the effective barrier yields $E_{eff}(SR) = E_e + \phi + \delta_{KES} \approx 0.65$ eV (continuum), as for vacancy pits. Utilizing the size scaling exponent for adatom island diffusion of $\beta \approx 2.3$, one has

$$K_{SR} = \nu_{SR} \exp[-0.65/(k_B T)] \, (L_{av})^{-3.3}. \quad (18)$$

Analysis of ripening data in Ref. [15] indicates that $\nu_{SR} \approx 10^{11.2}$ $s^{-1}$, so that $K_{SR} \approx 2.2\ (L_{av})^{-3.3}$ at 300 K.

Characterization of the kinetics of OR of adatom islands on Ag(100) by adatom transport (ORA) is more difficult. The effective activation barrier can be estimated from $E_{eff}(ORA) = E_d(ad) + 2\phi \approx 0.85$ eV. The prefactor of the ripening rate is not known, but adopting a similar value to that for OR of vacancy pits on Ag(100) yields $K_{ORA} \approx 10^{13} \exp[-0.85/(k_BT)]\ (L_{av})^{-2}$. This in turn implies a crossover from SR to ORA when the typical island size exceeds $L_{SR \rightarrow OR} \approx 18$, a value above typical experimental sizes in Ref. [6].

Surprisingly, for adatom islands on metal(100) surfaces, one should not discount the possibility of OR by vacancy transport (ORV). The lower terrace diffusion barrier for vacancies compared with adatoms can compensate for any inhibition due to the required interlayer transport. For Ag(100), the effective barrier for ORV is $E_{eff}(ORV) = E_d(vac) + 2\phi + \delta_{ESV} \approx 0.75 + \delta_{ESV}$, where $\delta_{ESV}$ denotes any additional barrier for interlayer transport of vacancies. If $\delta_{ESV}$ is below 0.1 eV, then ORV has an energetic advantage over ORA. Note while ripening of adatom islands on Cu(100) occurs via SR at 300 K, ORV dominates at around 340 K [41,42].

**REFERENCES**

[1] L. Ratke and P.W. Voorhees, *Growth and Coarsening* (Springer, Berlin, 2001).

[2] K. Morgenstern, Phys. Stat. Sol. (b) 242, 773 (2005).

[3] M. Giesen, Prog. Surf. Sci. 68, 1 (2001)

[4] M. Zinke-Allmang, L.C. Feldman, and M.H. Grabow, Surf. Sci. Rep. 16, 377 (1992).

[5] G. Rosenfeld, K. Morgenstern, M. Esser, and G. Comsa, Appl. Phys. A 69, 489 (1999).

[6] J.-M. Wen, J.W. Evans, M.C. Bartelt, J.W. Burnett, and P.A. Thiel, Phys. Rev. Lett. 76, 652 (1996).

[7] C.R. Stoldt, C.J. Jenks, P.A. Thiel, A.M. Cadilhe, and J.W. Evans, J. Chem. Phys. 111, 5157 (1999).

[8] S.V. Khare, N.C. Bartelt, and T.L. Einstein, Phys. Rev. Lett. 75, 2146 (1995).

[9] P. Meakin, Physica 165A, 1 (1980).

[10] J.-M. Wen, S.-L. Chang, J.W. Burnett, J.W. Evans, and P.A. Thiel, Phys. Rev. Lett. 73, 2591 (1994).

[11] E. Cox, M. Li, P.-W. Chung, C. Ghosh, T.S. Rahman, C.J. Jenks, J.W. Evans, and P.A. Thiel, Phys. Rev. B 71, 115414 (2005).

[12] K. Morgenstern, G. Rosenfeld, B. Poelsema, and G. Comsa, Phys. Rev. Lett. 74, 2058 (1995).

[13] D.C. Schlosser, K. Morgenstern, L.K. Verheij, G. Rosenfeld, F. Besenbacher, and G. Comsa, Surf. Sci. 465, 19 (2000).

[14] K. Morgenstern, G. Rosenfeld, and G. Comsa, Phys. Rev. Lett. 76, 2113 (1996).

[15] W.W. Pai, A.K. Swan, Z. Zhang, and J.F. Wendelken, Phys. Rev. Lett. 79, 3210 (1997).

[16] By virtue of Wulff's construction for equilibrium island or pit shapes, the ratio of local step energy to the local pedal radius, $\gamma/R$, equals the product of the local step stiffness and the local curvature, $\tilde{\gamma}\kappa$. Both quantities are constant along the step edge. See W.K. Burton, N. Cabrera, and F.C. Frank, Proc. R. Soc. 243, 40 (1951).

[17] J.W. Evans, P.A. Thiel, and M.C. Bartelt, Surf. Sci. Rep. 61, 1 (2006).

[18] K. Fichthorn and M. Scheffler, Phys. Rev. Lett. 84, 5371 (2000).

[19] P. Stoltze, J. Phys.: Cond. Mat. 6, 9495 (1994).

[20] P.A. Thiel and J.W. Evans, J. Phys. Chem. B 108, 14428 (2004).

[21] K.J. Caspersen, A.R. Layson, C.R. Stoldt, V. Fournee, P.A. Thiel, and J.W. Evans, Phys. Rev. B 65, 193407 (2002).

[22] P. Feibelman, unpublished.

[23] H. Mehl, O. Biham, I. Furman, and M. Karimi, Phys. Rev. B 60, 2106 (1999).

[24] N. Quaas, M. Wenderoth, and R.G. Ulbrich, Surf. Sci. 550, 57 (2004).

[25] C.R. Stoldt, A.M. Cadilhe, C.J. Jenks, J.-M. Wen, J.W. Evans, and P.A. Thiel., Phys. Rev. Lett. 81, 2950 (1998).

[26] W.W. Pai, J.F. Wendelken, C.R. Stoldt, P.A. Thiel, J.W. Evans, and D.-J. Liu, Phys. Rev. Lett. 86, 3091 (2001)

[27] D.-J. Liu and J.W. Evans, Phys. Rev. B 66, 165407 (2002).

[28] P. Jensen, N. Combe, H. Larralde, J.L. Barratt, C. Misbah, and A. Pimpinelli, Eur. Phys. J. B 11, 497 (1999).

[29] G. Mills, T.R. Mattsson, L. Mollnitz, and H. Metiu, J. Chem. Phys. 111, 8639 (1999).

[30] H. Brune, H. Roder, K. Bromann, K. Kern, J. Jacobsen, P. Stoltze, K. Jacobsen, and J.K. Norskov, Surf. Sci. 349, L115 (1996).

[31] B.D. Yu and M. Scheffler, Phys. Rev. B 55, 13916 (1997).

[32] C.R. Stoldt, Ph.D. thesis, Iowa State University (1999).

[33] F. Hausser and A. Voigt, Phys. Rev. B 72, 035437 (2005).

[34] G. Kresse and J. Hafner, Phys. Rev. B 47, R558 (1993).

[35] G. Kresse and J. Furthmueller, Phys. Rev. B 54, 11169 (1996).

[36] J.P. Perdew, K. Burke and M. Ernzerhof, Phys. Rev. Lett. 77, 3865 (1996).

[37] G. Kresse and D. Joubert, Phys. Rev. B 59, 1758 (1999).

[38] W. Luo and K. Fichthorn, Phys. Rev. B 72, 115433 (2005).

[39] K. Morgenstern, G. Rosenfeld, E. Laegsgaard, F. Besenbacher and G. Comsa, Phys. Rev. Lett. 80, 556 (1998).

[40] N.C. Bartelt, W. Theis, and R.M. Tromp, Phys. Rev. B 54, 11741 (1996).

[41] J.B. Hannon, C. Klunker, M. Giesen, H. Ibach,, N.C. Bartelt, and J.C. Hamilton, Phys. Rev. Lett. 79, 2506 (1997).

[42] C. Klunker, J.B. Hannon, M. Giesen, H. Ibach, G. Boisvert, and L.L. Lewis, Phys. Rev. B 58, R7556 (1998).

## TABLES

**Table I.** Summary of our estimates for the values of key energies (in eV) for Ag(111) and Ag(100) surfaces. Uncertainties are indicated in the text. Also shown are effective energies for OR of vacancy pits via adatom transport (ORA) and via vacancy transport (ORV), and for SR of vacancy pits where pit diffusion is mediated by periphery diffusion. The associated energy is estimated from continuum theory. Values are used for the analysis in Sec.V are slightly modified (see the text) or rounded-off.

| | $\phi$ | $E_d$(ad) | $E_d$(vac) | $\delta_{ES}$ | $E_e$ | $\delta_{KES}$ | $E_{eff}$(ORA) | $E_{eff}$(ORV) | $E_{eff}$(SR) |
|---|---|---|---|---|---|---|---|---|---|
| Ag(111) | 0.19 | 0.10 | 0.58 | 0.13 | 0.30 | 0.05 | 0.80 | 1.15 | 0.54 |
| Ag(100) | 0.21 | 0.43 | 0.35 | 0.07 | 0.25 | 0.16 | 0.92 | 0.77 | 0.62 |

**Table II:** DFT estimates of terrace diffusion barriers for isolated adatoms and vacancies.

| Surface | Species | Supercell size | $k$ points | $E_d$ (eV) |
|---|---|---|---|---|
| Ag(100) | Adatom | 2×2 | (4 4 1) | 0.433 |
| | | | (6 6 1) | 0.429 |
| Ag(100) | Vacancy | 3×3 | (2 2 1) | 0.328 |
| | | | (4 4 1) | 0.376 |
| | | | (6 6 1) | 0.351 |
| Ag(111) | Adatom | 2×2 | (10 10 1) | 0.010 |
| Ag(111) | Vacancy | 3×3 | (4 4 1) | 0.485 |
| | | | (6 6 1) | 0.580 |

**Table III:** DFT estimates of NN adatom interaction energies, ϕ. To determine ϕ, a single NN pair of adatoms is placed within each supercell. Note that for the smallest 2×2 supercell, the adatoms form a linear chain, so one must account for two NN interactions per supercell. In all other cases, there is a single isolated NN pair of adatoms within each supercell.

| Surface | Supercell size | *k* points | $\phi$ (eV) |
|---|---|---|---|
| Ag(100) | 2×2 | (10 10 1) | 0.226 |
| | 3×3 | (10 10 1) | 0.216 |
| | 4×4 | (10 10 1) | 0.183 |
| Ag(111) | 2×2 | (12 12 1) | 0.233 |
| | 3×3 | (6 6 1) | 0.153 |
| | 4×4 | (4 4 1) | 0.229 |
| | 5×5 | (4 4 1) | 0.200 |
| | 6×6 | (2 2 1) | 0.196 |

FIGURE CAPTIONS

**Figure 1**: Schematics for atomistic processes underlying ripening of vacancy pits for an fcc(100) crystal geometry. Grey atoms represent the top surface layer. White atoms represent the underlying layer exposed within the monolayer pits. (a) Possible mass transport pathways operative in OR involving single adatoms (ORA) and single vacancies (ORV) diffusing between different sized vacancy pits. There are higher concentrations of isolated adatoms around the bigger pit, and of isolated ad-vacancies around the smaller pit. Black adatoms are diffusing on top of the grey surface layer. (b) Periphery-diffusion processes underlying diffusion of vacancy pits. We indicate nucleation of a new empty row on the top edge of the left pit (by removal of an adatom adjacent to an isolated vacancy). We also indicate the dominant process leading to formation of an isolated vacancy on the lower edge, i.e., corner sliding. See Sec. IV for related discussion. The overall motion of the center of masses (indicated by $\times$) of the pits, potentially leading to coalescence, is also shown by a meandering path.

**Figure 2**: (a) Center-of-mass motion at 300 K for a vacancy pit on Ag(100) with 950 missing atoms (S: starting position; F: final position after ~500 min.); (b) log D - log L plot showing diffusion coefficients, D, for set of 18 pits with L=25±15 (grouped within large dashed circle) *plus* D for set of 9 islands with L=13±5 (grouped within small dashed circle). Dashed line through the centers of these dashed circles has a slope of about -2.3 corresponding to the size scaling exponent determined in Ref. [15] for adatom islands. The D-values in Ref.[15] are systematically lower than here perhaps reflecting a slightly lower T in those studies, or perhaps strain effects due to the higher island density.

**Figure 3**: Crossover from SR to OR in coarsening rates, K, with increasing linear pit size, L, at 300 K for: (a) Ag(111); (b) Ag(100).

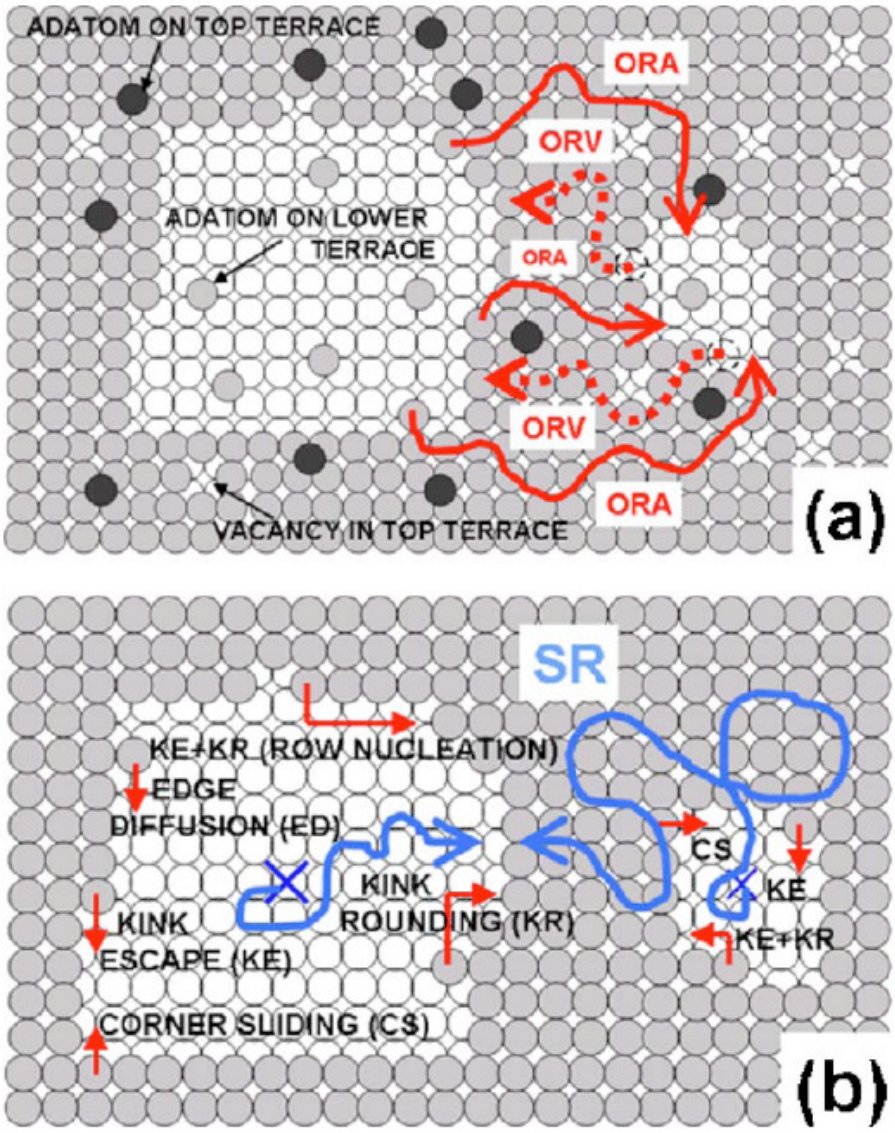


Figure 1

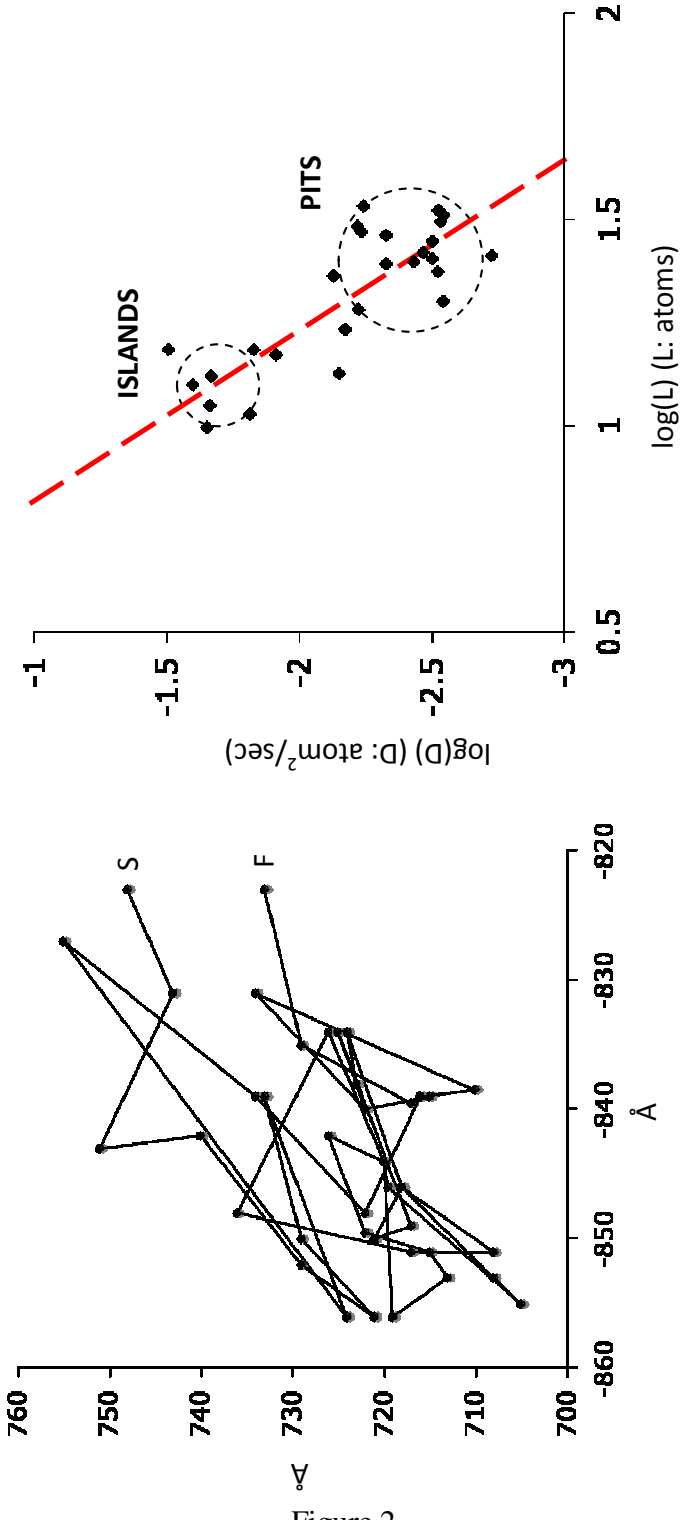


Figure 2

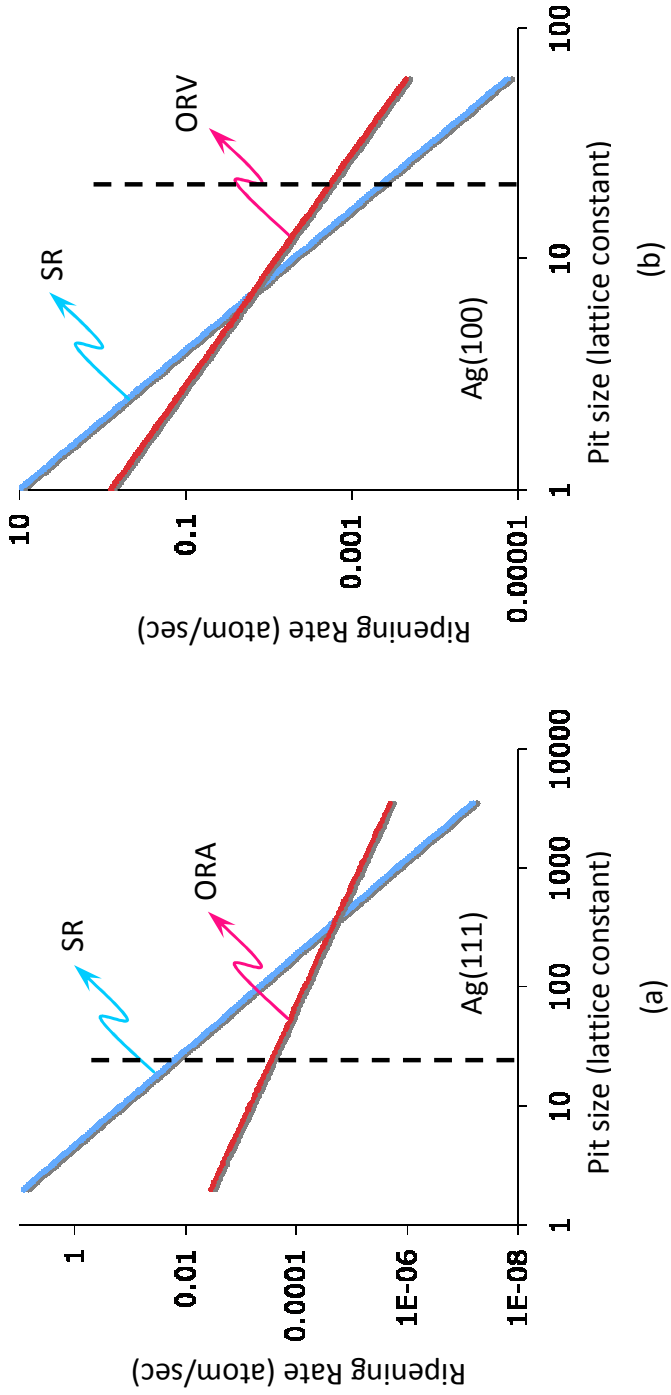


Figure 3

# APPENDIX II. PIT DECAY ON Ag(111) WITH AND WITHOUT $O_2$ EXPOSURE AND Ag ON Ag(111) WITH $O_2$ EXPOSURE

In Appendix I, we explored the coarsening of vacancy pits on Ag(111) and Ag(100) surfaces. Here we analyze pit decay near ascending step edges on Ag(111), with and without $O_2$ exposure. Ag island coarsening on Ag(111) with $O_2$ exposure at different temperatures is also analyzed in this part.

## Experimental Description.

### Pit decay

The Ag(111) single crystal sample was cleaned by repeated cycles of $Ar^+$ sputtering (15-30 min, 20 mA, 1.0 -1.5 kV, T = 300 K) followed by annealing at ~ 525 K until no impurities could be detected by Auger electron spectroscopy (AES). The STM morphology was monitored after the sample had been cooled to room temperature. Typical tunneling conditions were +1.5 V and 1.0 nA. This low temperature annealing led to insufficient surface restoration, and vacancy pits introduced by sputtering could still be observed sometimes on the surface after annealing. Clean surface STM images were obtained immediately after the final cycle of sputtering and annealing. Oxygen exposure STM was achieved by backfilling the chamber. The surface was scanned during oxygen exposure.

### Ag on Ag(111) with $O_2$ exposure

For our study of adatom island, deposition of Ag on the Ag(111) single-crystal surface was performed using an Omicron EFM3 UHV evaporator containing Ag (99.99% pure) as the deposition source. The Ag flux was held fixed at 0.01-0.02 monolayers (ML)/s in all experiments. For lower than room temperature experiments, the sample was usually cooled with liquid nitrogen. Sample temperature, $T_s$, was measured by means of a silicon

diode at the cooling stage, which surrounded the sample holder on all sides but one. There was a temperature offset between the cooling stage and the sample. We took $T_s = T_{diode} + A(T_{diode})$, where $A(T_{diode})$ was provided by the manufacturer (Omicron). Oxygen exposure STM was achieved by backfilling the chamber at different pressure. The surface was scanned during and/or after oxygen exposure.

**Results.**

**Pit decay**

Figure 1 shows the decay of a vacancy pit on the Ag(111) clean surface when it approaches a pair of adjacent, ascending step edges. Based on our earlier studies of Ag deposition on Ag(111) surface and the features of this sample,[1,2,3] it is clear that the ascending step edges, and the parallel edge of the pit, are A-type steps. There are two stages. Between 0 and 25 minutes, the pit shrinks at a rate of ~ 4.08 $nm^2$/min. In this period, the two ascending steps approach and merge. Simultaneously, the bottom pit becomes increasingly triangular, as its A-steps shorten relative to its B-steps. After about 25 minutes, the pit shrinks at a much slower rate of 0.15 $nm^2$/min. (This number is based on a much longer observation time than shown in Fig. 1.) This is lower by a factor of ~ 27 than the earlier rate. In this second stage, the pit continues to reshape, moving away from the ascending step and becoming more hexagonal.

We attribute the convergence of the two upper step edges in Fig. 1, at about 18 minutes, to the fact that atoms are leaving the lower step edge to fill the pit and, in fact, the lowest of the two extended step edges is moving to the left, while the upper one is static. This shows that the source of atoms to fill the pit is not the two-dimensional gas of Ag adatoms, but rather the step edge itself.

Figure 2 shows another vacancy pit approaching a step edge. In this case, it is a small pit embedded in a larger pit. By comparing it to the position of the pit in Figure 1, it is clear that this pit also approaches an A-type ascending step edge. It gives a decay rate of ~ 4.01 $nm^2$/min, entirely consistent with the results in Fig.1.

Figure 3 shows the decay of a vacancy pit which approaches a B-type step, which is different than the ones in Figure 1 and 2, and the decay rate is ~ 9.31 $nm^2$/min, which is much higher than the rate near an A-type step.

Figure 4 shows another pit decaying parallel to a B-type step, and it gives a similar decay rate (~ 9.45 $nm^2$/min) as the one in Figure 3. In both Fig. 3 and 4, note that the border between the pit and the ascending step becomes longer than it was at initial contact. This stands in contrast to Fig. 2, where the border shrank.

Figure 5 shows the decay of a vacancy pit on the terrace while it is moving, relative to the step edge. When the pit first approaches the A-type step edge, the decay rate is ~ 4.10 $nm^2$/min. When it diffuses and approaches the B-type step edge, it decays much faster (~ 9.63 $nm^2$/min). Finally the small pit leaves the step edge.

Figure 6a-c are schematic diagrams showing a possible explanation for some of the different features of vacancy pit decay. The dark atoms enclosed in the middle hexagon in Fig. 6a are at the bottom of the vacancy pit. As reported elsewhere,[4,5] diffusion of adatoms is slower along B-steps than A-steps. Hence, the residence time on B-steps is enhances, as is the probability for nucleation of a new step edge line, i.e. for growth perpendicular to the B-type steps. This leads to the B-type steps to grow longer, relative to the A-type steps.

In Fig. 6b, the filled gray circles correspond to atoms that have partially filled the pit, after the vacancy pit has “touched” an ascending B-step edge on the right-hand side. These

atoms come mainly from the ascending step itself, rather than the two-dimensional adatom gas on top of terrace. Due to the slow migration of atoms along the B-step, these atoms nucleate and grow a new line of atoms along the B-step. Consequently, the B-step edge near the ascending step gets longer, consistent with the experimental data (Fig. 3 and 4).

As shown in Figure 6c, when the vacancy pit "touches" an ascending A-type step edge on its right, atoms from the ascending step edge can also fill the pit. Due to the smaller barrier to migration of atoms along the A-step, atoms will diffuse and stick to the B-steps. This leads to growth of B-steps, and eventually the triangular connection of the B-steps. When this is complete, there is no remaining boundary between the pit and the step edge, and the pit may diffuse away from the ascending step edge. This is what occurs in Fig. 1 and 5, where pits are adjacent to A-steps.

Morgenstern et al. (see ref. 5) have discussed by the atomic-scale mechanisms and energetics by which adatom islands and vacancy pits decay when they touch a step edge on Ag(111), and one expects the same arguments to apply here. Figure 7 is a schematic comparison of the effective barriers of different decay pathways. In this picture, the darkest circles represent atoms at the bottom of the pit, and white circles are atoms in the ascending step edge, while gray circles are atoms in the terrace that borders the pit. The general trend is that two-atom exchange processes, involving atoms in the ascending step edge itself, are favored with respect to a mechanism in which adatoms from a two-dimensional gas would cross downward over step edges. This is consistent with the experimental data, which indicates that the step edge becomes eroded as the pit fills in (Fig. 1 here and also Fig. 4 in Ref. 5). As pointed out by Morgenstern et al.,[5] two-atom exchange processes at B-steps have lower energy barriers than exchanges at A-steps. The energy barrier of an atom at an upper

B-step descending to a lower step edge by the exchange mechanism is only 0.38 eV. The presence of a kink at the lower step reduces the energy barrier by no more than 0.03 eV. For a straight A-step, the corresponding energy barrier is 0.73 eV. The number can be lowered by up to 0.20 eV when there is a kink at the lower step edge, but it is still significantly higher than the barrier at a B-step. The difference of the energy barriers of A- and B-steps explains the faster decay rate when a pit approaches an ascending B-step rather than an A-step.

Figure 8 shows the decay of a vacancy pit during oxygen exposure at a pressure of 8 $\times 10^{-10}$ Torr. As shown in these STM images, first the pit is not close enough to the ascending step edge, and suffers almost no change on its area. When the pit diffuses and touches the ascending A-step edge, a sudden increase occurs in the decay rate, and it shrinks at a rate of ~ 63.2 $nm^2$/min until the pit finally disappears. This is faster than for the clean surface, by a factor of ~15. It is possible that the presence of oxygen causes an even lower detachment barrier, and this leads to a much lower effective barrier for the atomic exchange processes.

**Ag on Ag(111) with $O_2$ exposure**

Figure 9 and 10 show a series of STM images before and after low oxygen exposure at different temperatures. No oxygen was detectable with Auger electron spectroscopy (AES) at low oxygen exposure.

Figure 9a and 9b show STM images of Ag on Ag(111) before and after about 12.3 L $O_2$ exposure (2 x $10^{-9}$ Torr for 102 min) at 135 K. Although the surface has been exposed to oxygen for more than 100 min, no change (ripening and/or coarsening) has been observed for dendritic Ag islands. This is the same as clean Ag/Ag(111) that no coarsening happens at 135 K.

Figure 10 shows STM images of Ag on Ag(111) before and after about 17.2 L $O_2$ exposure (2 x $10^{-9}$ Torr for 143 min) at 235 K and then heat up to room temperature (300 K). No obvious change is observed for hexagonal Ag islands at 235 K as shown in Fig. 10a and 10a'. After heating the same surface to 300 K, bigger hexagonal islands form and with snapshots shown in Fig. 10b and 10b', Ostwald ripening is observed, same as for clean Ag(111) at 300 K.

Figure 11a and 11b show STM snapshots of Ag on Ag(111) right after and 120 min after 2000 L $O_2$ exposure (8 x $10^{-7}$ Torr for 40 min) at 300 K. Right after oxygen exposure, as shown in Fig. 11a, hexagonal Ag islands still form. Over time, these Ag islands decay through Ostwald ripening, the same as clean Ag/Ag(111), but form more irregular shape other than hexagons.

Figure 12 shows a series of STM snapshots of Ag on Ag(111) at different temperatures after 2000 L $O_2$ exposure (8 x $10^{-7}$ Torr for 40 min) initially at 135 K. Fig. 12a and 12a' show STM images right after and 20 min after 2000 L oxygen exposure at 135 K. No coarsening is observed at this temperature. After heating the surface up to 200 K and observe for more than 50 min, some local coalescence happens with an example shown in the circles. Ostwald ripening is also observed with the island in square box getting smaller with time shown in Fig. 12b and 12b'. Fig. 12c and 12c' show the same surface right after and over 50 min after heating up to 250 K. More Ostwald is observed with smaller islands in rectangular boxes disappearing. Ag islands stay triangular or irregular shape, different from the near hexagonal-shaped islands with Ag deposition on clean Ag(111) at 235 K shown in Fig. 10a. Fig. 12d and 12d' show the same surface right after and 60 min after heating up to 300 K. Ostwald ripening leads to an obvious decrease in island density. Ag islands still stay

irregular shapes at 300 K with step edges not as straight as low oxygen exposure surface shown in Fig. 10b and 10b'.

For comparison, another set of Ag deposition experiment as in Fig.12 was done at 135 K without exposing to any oxygen. After heating the clean Ag/Ag(111) surface up to 200, 250, and 300 K, it is found that hexagonal Ag islands already form at 250 K and straight step edges form at 300 K (images not shown here). Here we also want to note that even with 2000 L oxygen exposure, no oxygen peak can be observed with AES, although oxygen seems to have an effect on Ag/Ag(111) surface structure.

**Reference**

(1) Cox, E.; Li, M.; Chung, P.-W.; Ghosh, C.; Rahman, T. S.; Jenks, C. J.; Evans, J. W.; Thiel, P. A. *Physical Review B* **2005**, *71*, 115414.

(2) Thiel, P. A.; Shen, M.; Liu, D.-J.; Evans, J. W. *Journal of Physical Chemistry C* **2009**, *113*, 5047.

(3) NOTE:The sample used in this study was oriented in the same way as in other studies of Ag(111) in this thesis. The A- and B-steps were identified in those studies from the orientation of triangular, dendritic Ag islands formed at 130 K, where the long arms are perpendicular to the A-steps. The A- and B-steps were also identified from studies of S adsorption at low coverage, in which the S adsorbs preferentially on the A-steps and causes faceting. The results of these two analyses are consistent. In the present study, it was assumed that a hexagonal pit exposed only A- and B-step edges.

(4) Freund, J. E.; Edelwirth, M.; Grimminger, J.; Schloderer, R.; Heckl, W. M. *Applied Physics A* **1998**, S787.

(5) Morgenstern, K.; Rosenfeld, G.; Comsa, G.; Sørensen, M. R.; Hammer, B.; Lægsgaard, E.; Besenbacher, F. *Physical Review B* **2001**, *63*, 045412.

Figure Caption:

1. Room temperature pit decay with ascending A-step. All STM images are 50 nm x 50 nm. (STM from 06-07-2006)

2. Room temperature pit decay for lowest layer pit with ascending A-step. All STM images are 30 nm x 30 nm. (STM from 07-12-2006)

3. Room temperature pit decay for second lowest layer pit with ascending B-step. All STM images are 30 nm x 30 nm. (STM from 07-12-2006)

4. Room temperature pit decay for highest layer pit with ascending B-step. All STM images are 30 nm x 30 nm. (STM from 07-12-2006)

5. Room temperature pit decay with different ascending steps. All STM images are 40 nm x 40 nm. (STM from 08-02-2006)

6. Schematic diagram of diffusion effects applied to vacancy pits. (a). A pit grows into a half hexagon with approaching to ascending B-step; (b) A pit grows into a "triangle" with approaching to ascending A-step.

7. Schematic energetic processes for atoms at an upper step edge descend via hopping down, exchanging with ascending A-step, and exchanging with ascending B-step mechanisms.

8. Room temperature pit decay oxygen exposure with pressure equals 8 x $10^{-10}$ Torr. All STM images are 40 nm x 40 nm. (STM from 07-24-2006)

9. STM images of Ag on Ag(111) at 135 K, 120 nm x 120 nm. (a) Clean Ag/Ag(111) before oxygen exposure; (b) After 12.3 L oxygen exposure with $O_2$ pressure at 2 x $10^{-9}$ Torr for 102 min. (STM from 10-05-2006, #55 and #85)

10. STM images of Ag on Ag(111), (a) Clean Ag/Ag(111) before oxygen exposure, 160 nm x 160 nm, 235 K; (a') After 7.2 L oxygen exposure with $O_2$ pressure at 2 x $10^{-9}$ Torr for 143 min, 160 nm x 160 nm, 235 K; (b) After oxygen exposure and heating up to 300 K, 120 nm x 120 nm; (b') 85 min after heating up to 300 K, 120 nm x 120 nm. (STM from 10-12-2006, #35, #75, #82, and #122)

11. STM images of Ag on Ag(111) at 300 K, 200 nm x 120 nm. (a) Right after 2000 L oxygen exposure with $O_2$ pressure at 8 x $10^{-7}$ Torr for 40 min; (b) 120 min after oxygen exposure. (STM from 09-17-2007, # 28 and #160)

12. STM images of Ag on Ag(111). (a) Right after 2000 L oxygen exposure with $O_2$ pressure at 8 x $10^{-7}$ Torr for 40 min at 135 K, 100 nm x 100 nm; (a') 20 min after oxygen exposure, 135 K, 100 nm x 100 nm; (b) After oxygen exposure and heating up to 200 K, 100 nm x 100 nm; (b') 53 min after heating up to 200 K, 100 nm x 100 nm; (c) After oxygen exposure and heating up to 250 K, 200 nm x 200 nm; (c') 52 min after heating up to 250 K, 200 nm x 200 nm; (d) After oxygen exposure and heating up to 300 K, 200 nm x 200 nm; (d') 60 min after heating up to 300 K, 200 nm x 200 nm. (STM from 11-12-2007, #6, #16, #20, #43, #50, #73, #77, and #105 )

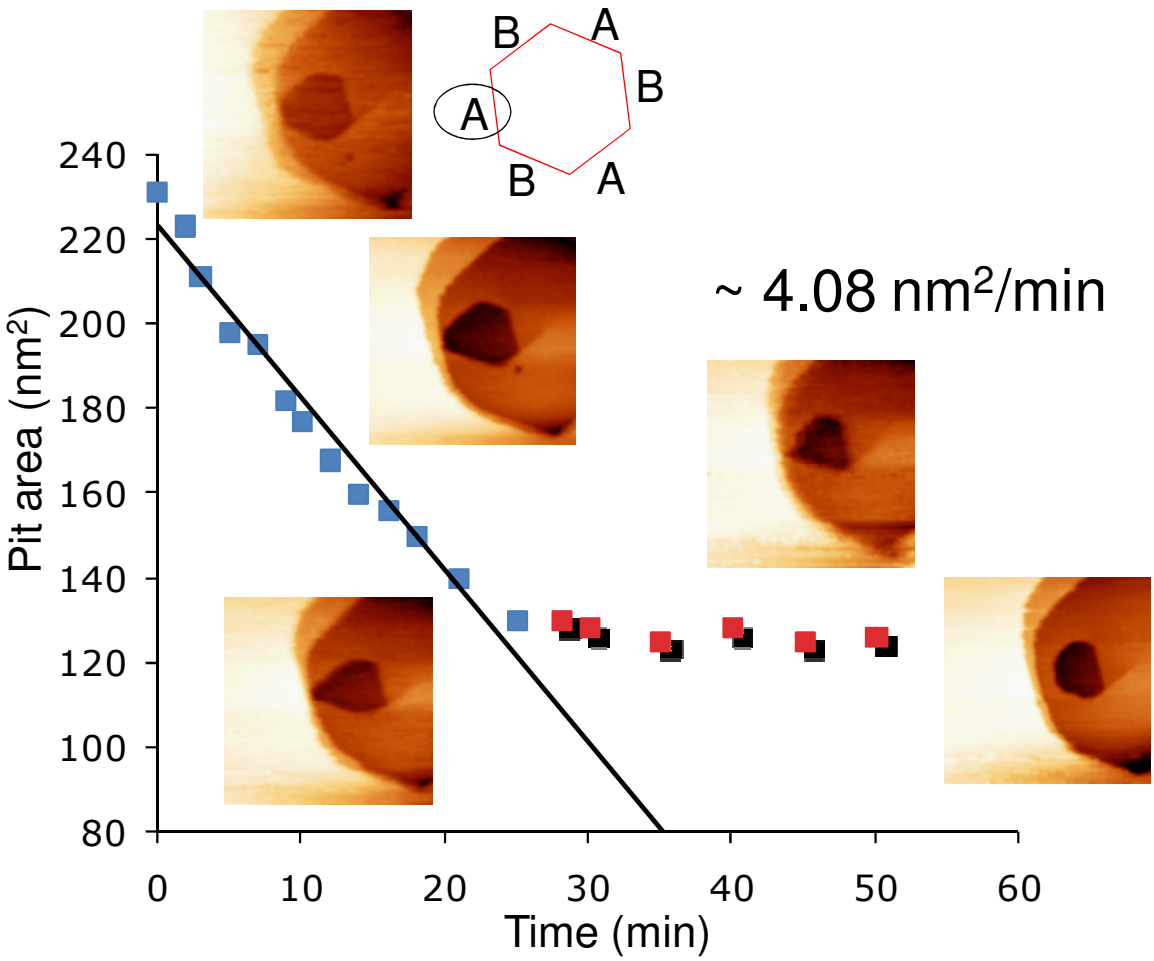


Figure 1

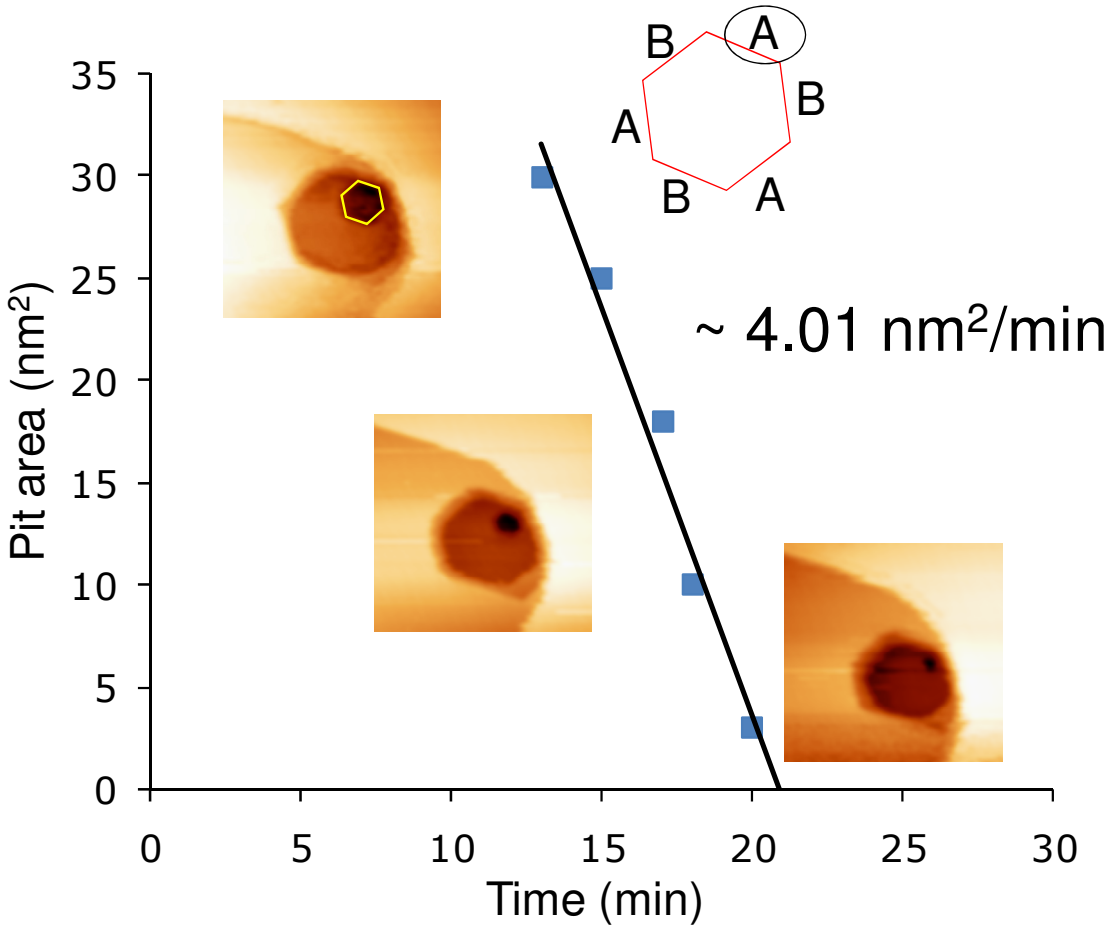


Figure 2

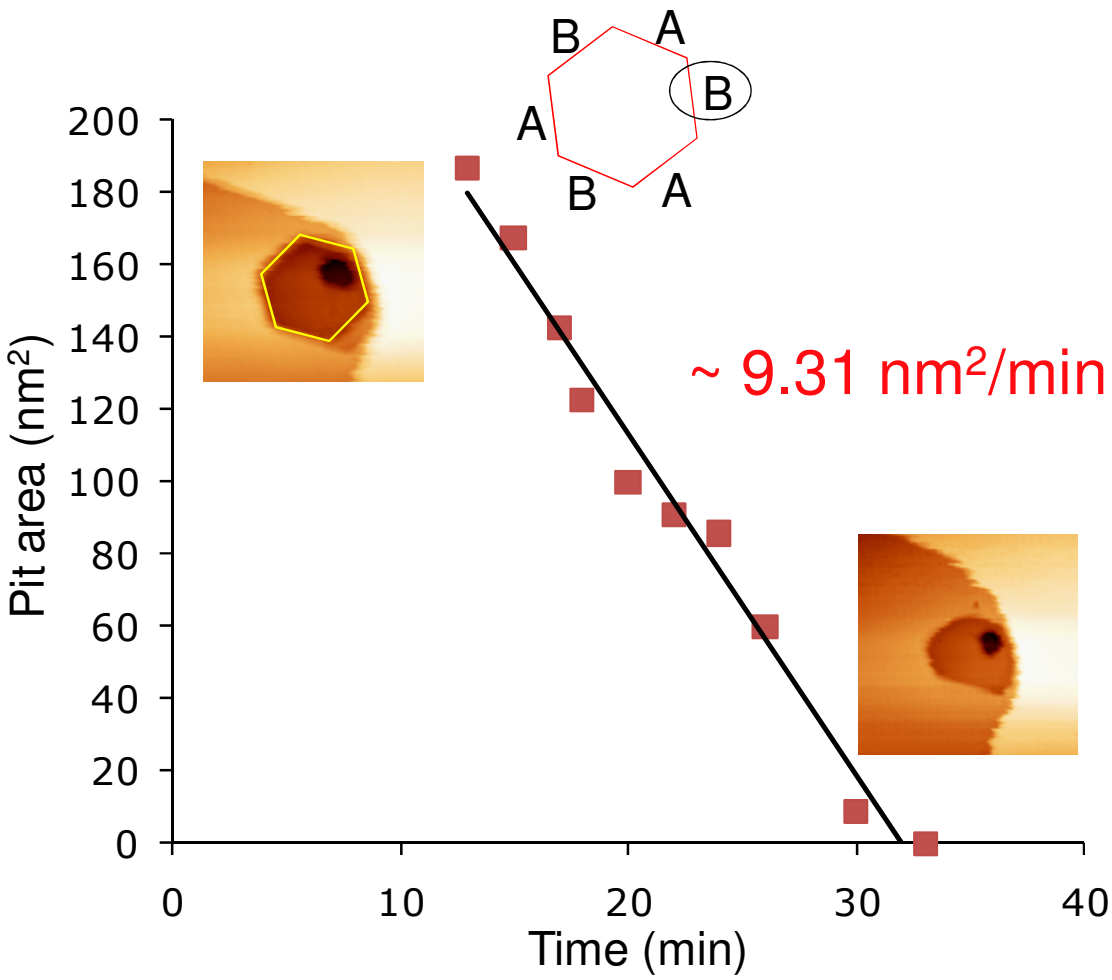


Figure 3

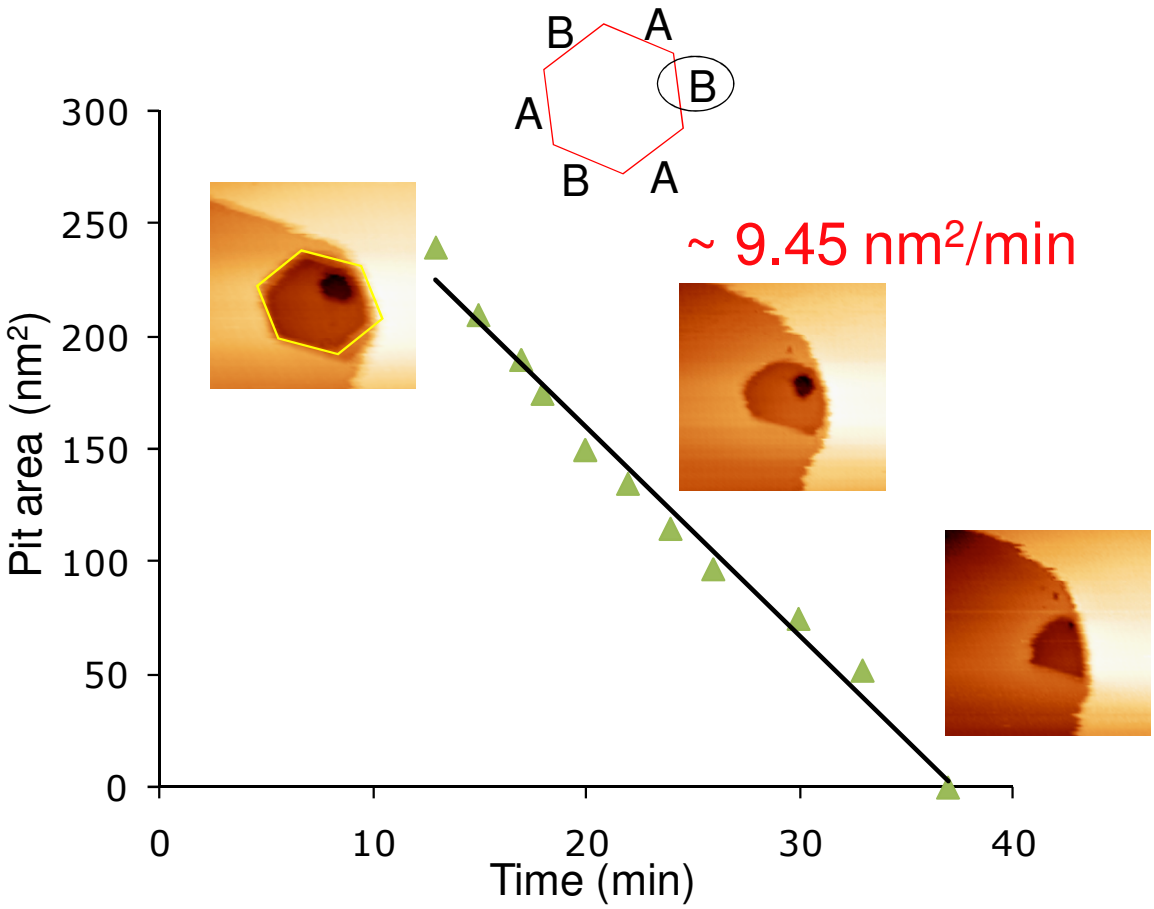


Figure 4

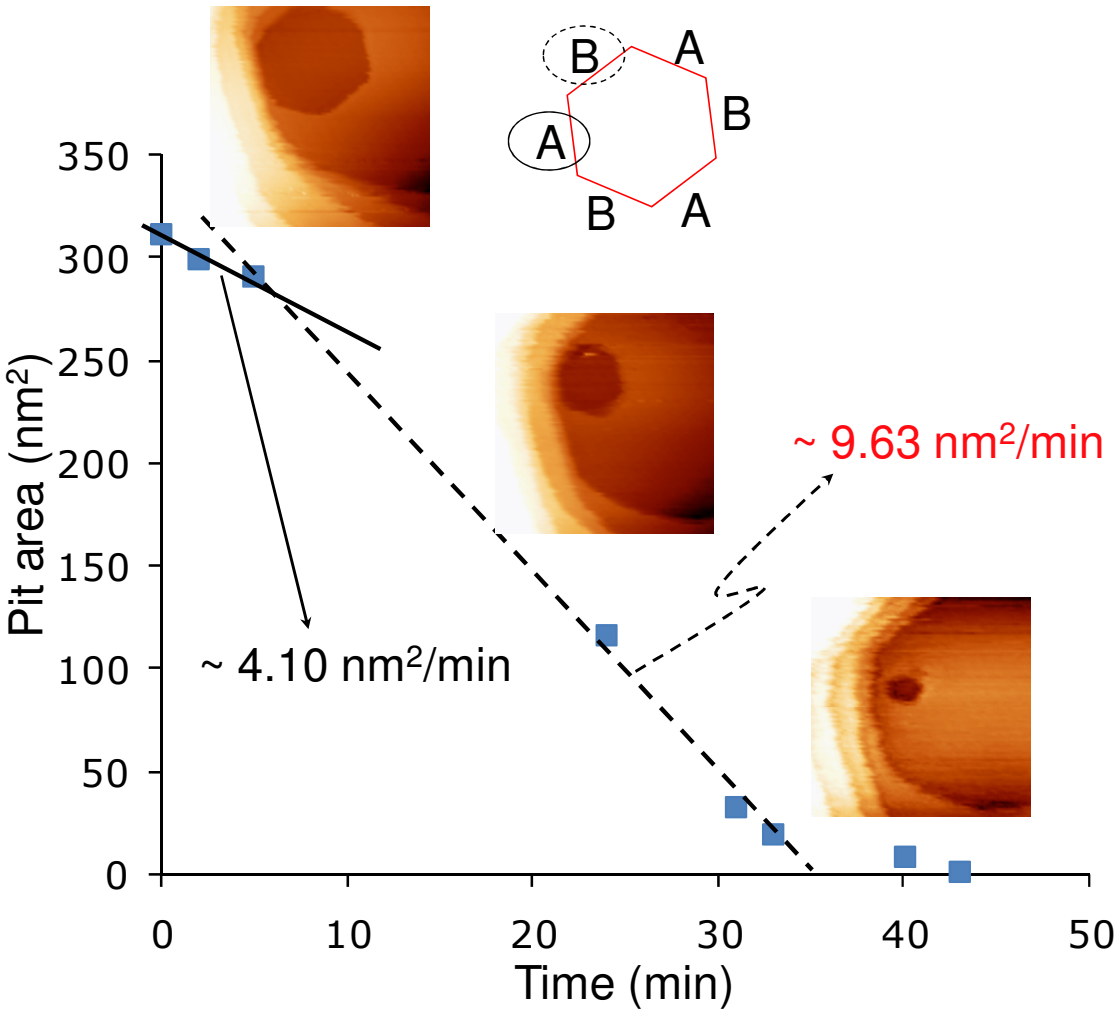


Figure 5

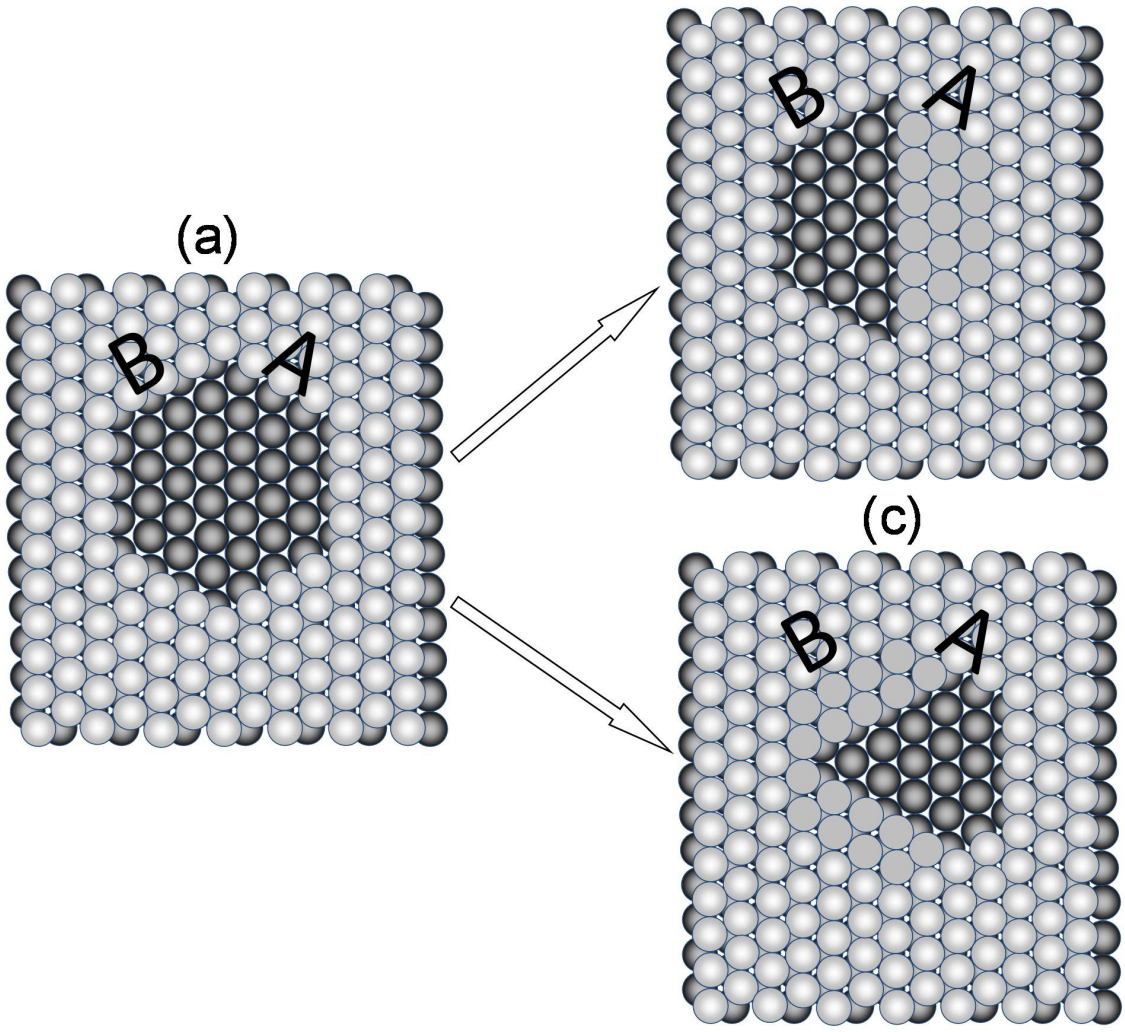


Figure 6

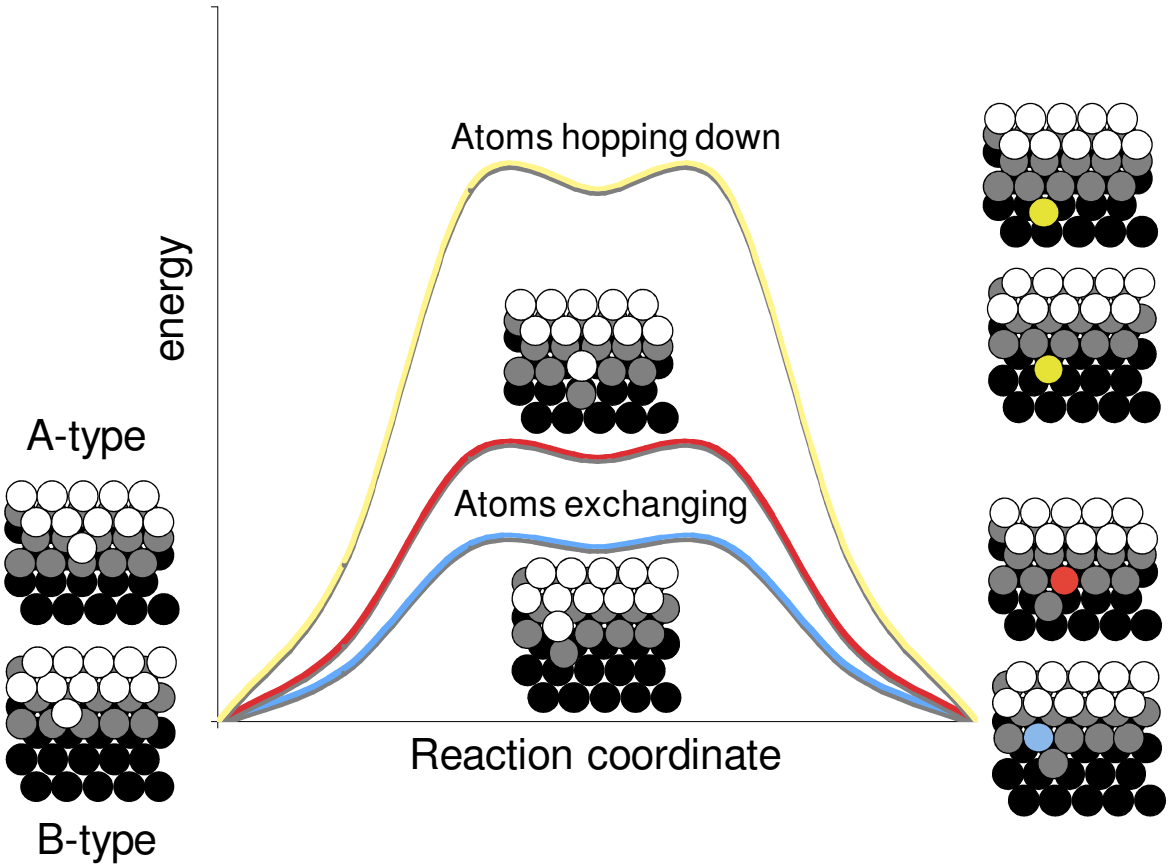


Figure 7

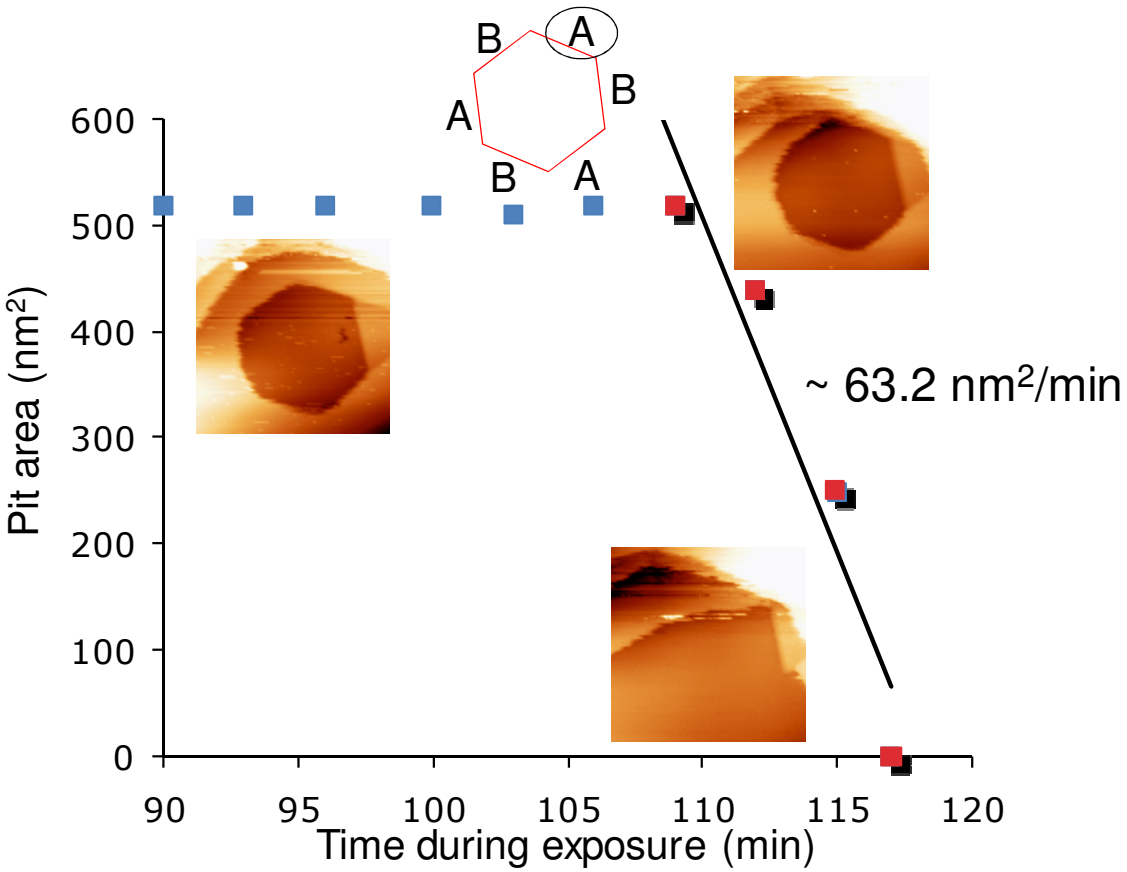


Figure 8

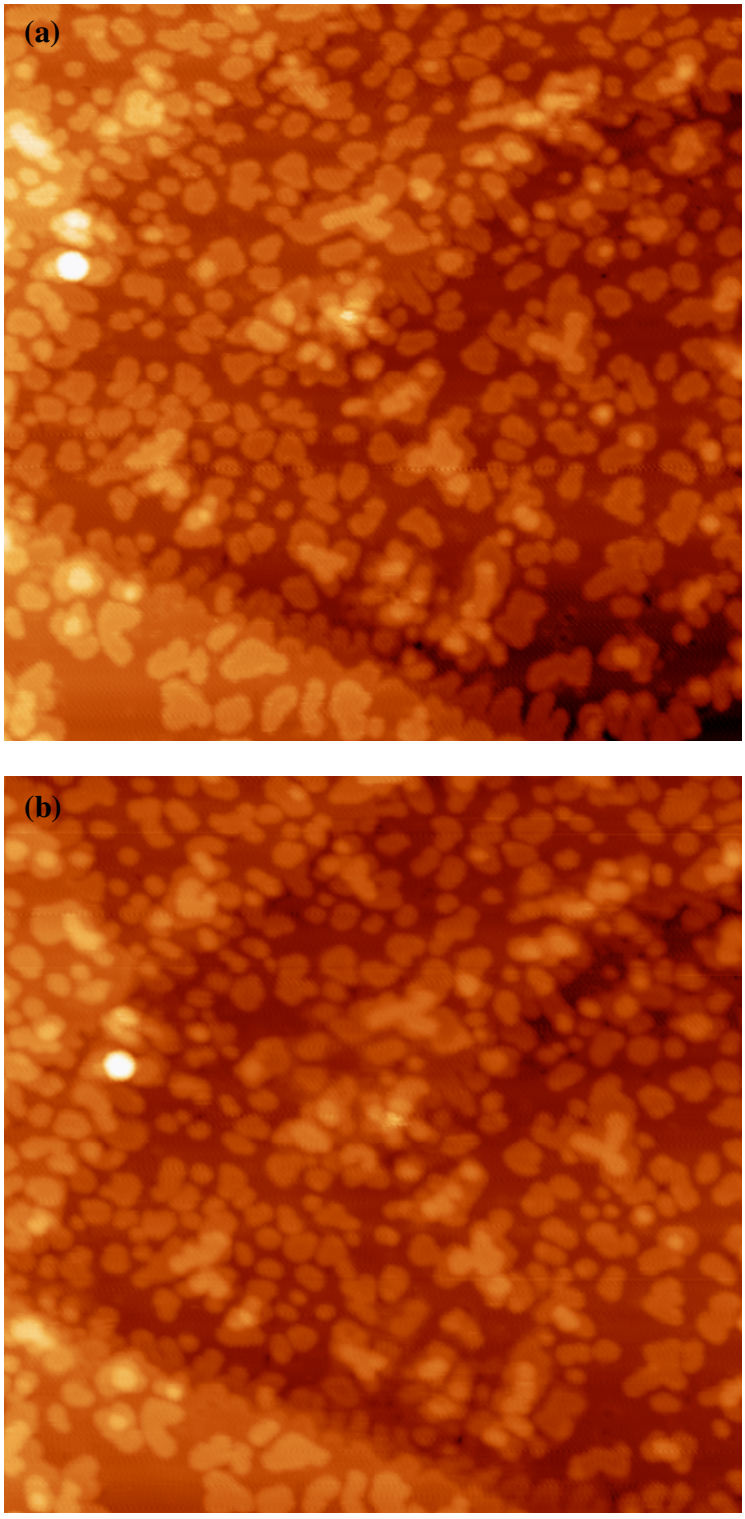


Figure 9

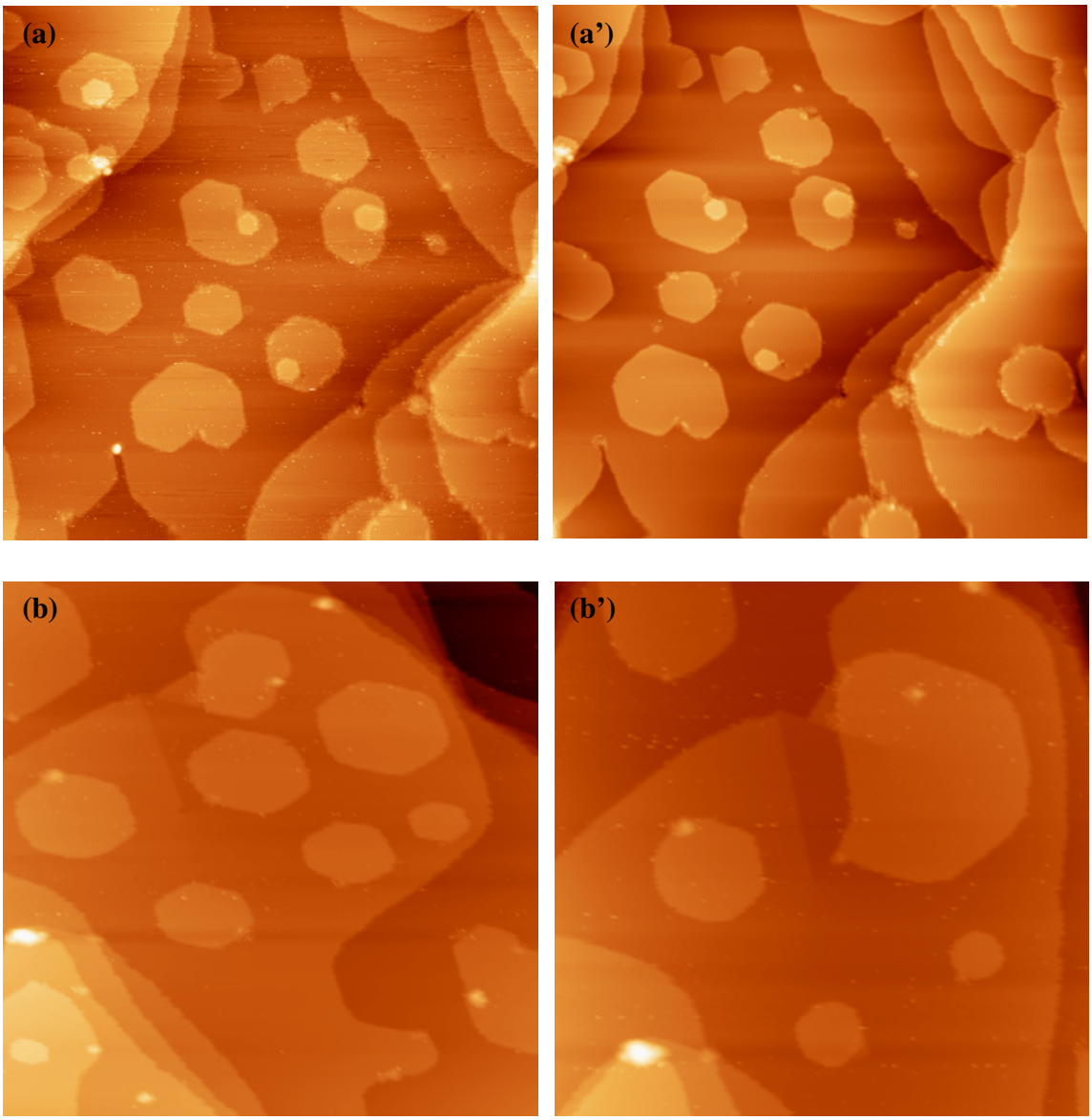


Figure 10

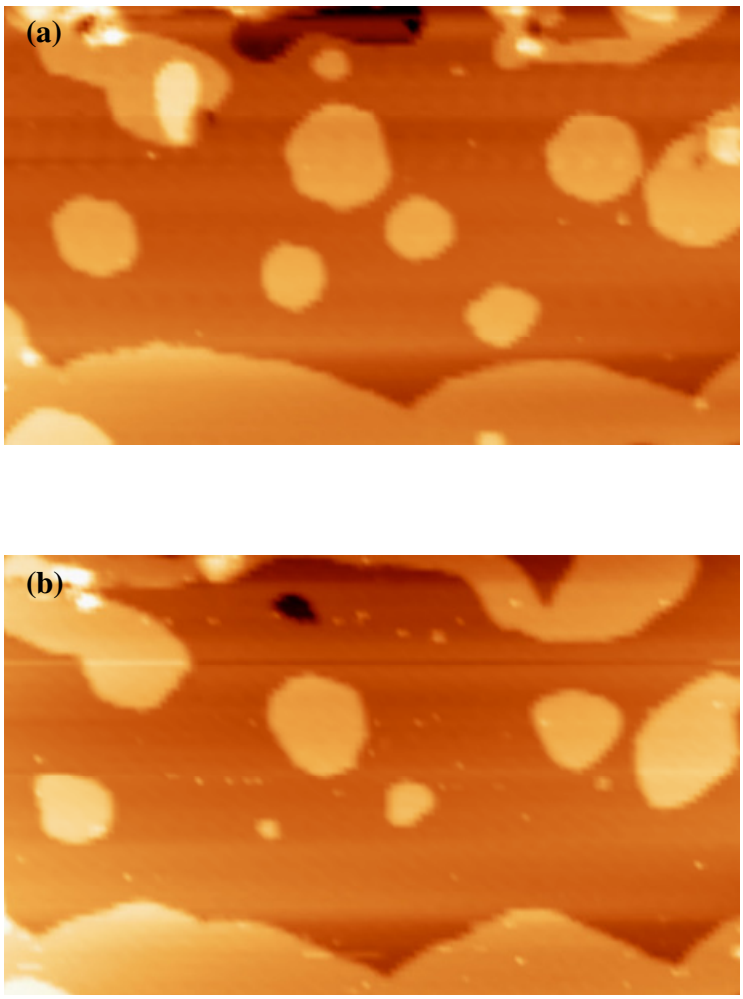


Figure 11

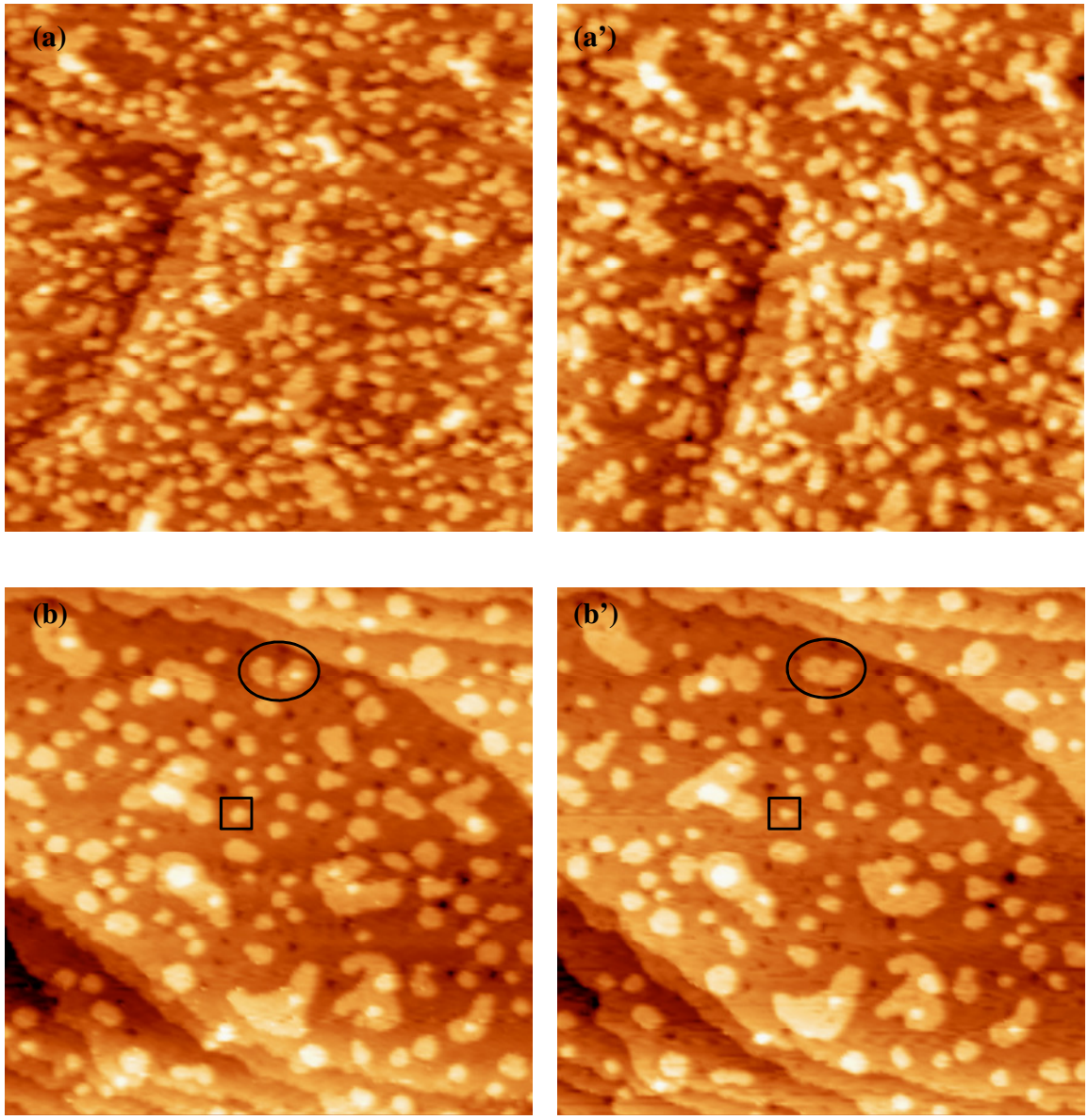


Figure 12

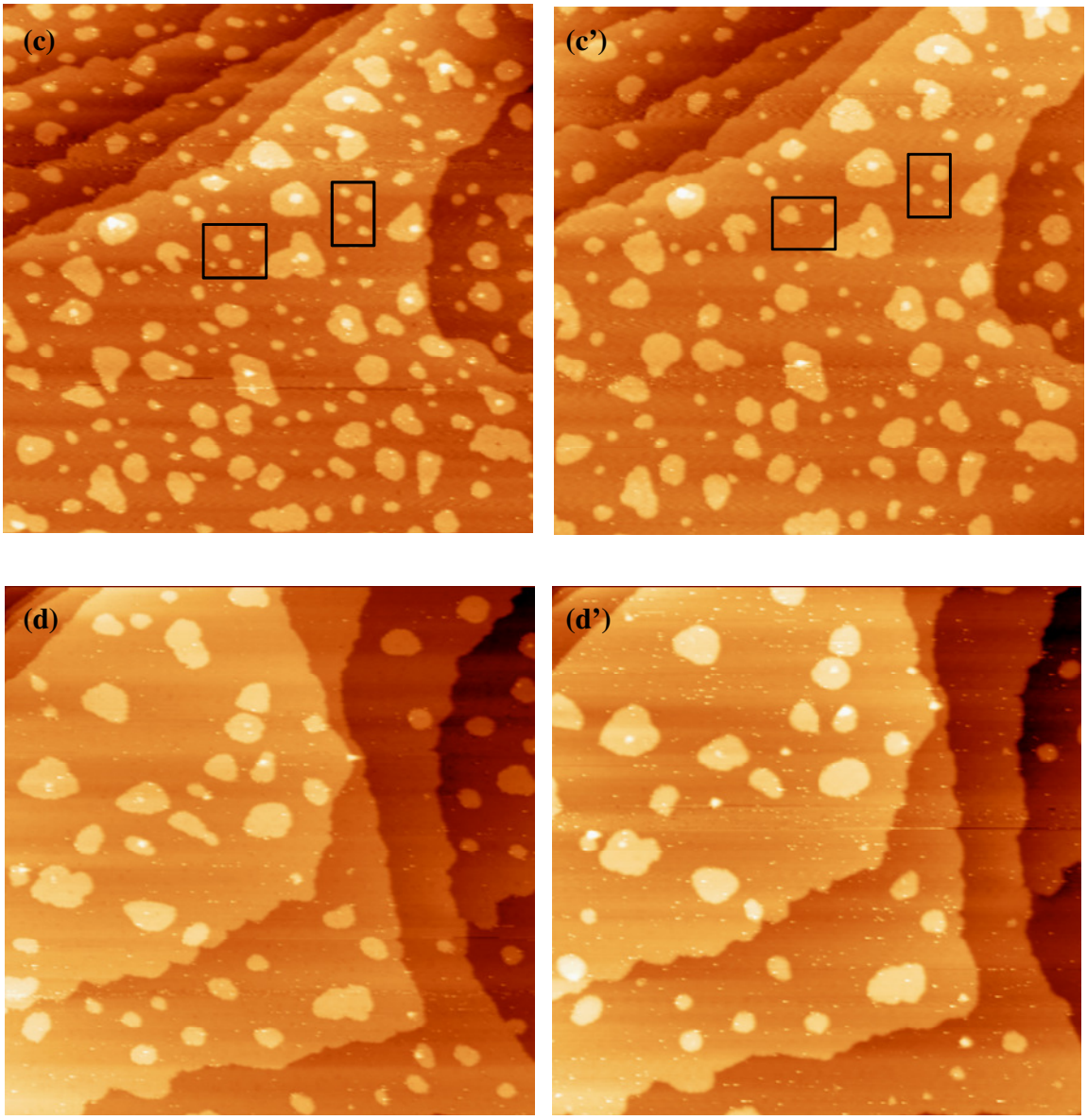


Figure 12 (Continued)

# APPENDIX III. PROCEDURE FOR OPERATING SULFUR EVAPORATOR

A solid-state electrochemical cell is especially convenient as a source for sulfur vapor deposition in surface science experiments. The cell was originally designed by Wagner[1] in the 1950s, and variations on its design have been in use[2-4]. The sulfur evaporator described in this report is based on the modification made by Heegemann et al[2].

The general design of our sulfur evaporator is shown in Fig.1 with its side view. The electrochemical cell is mounted onto a 2.75" flange that contains three electrical feedthroughs and a pair of thermocouple feedthroughs. The hole at the end of the glass tube helps the collimation. The shutter for the source is mounted on a linear motion feedthrough connected to a T-flange. It allows the Ta flag to move up and down to shield the sulfur beam to the sample surface. The evaporator is mounted to the STM part of the chamber (Fig. 3).

The electrochemical cell itself (Fig. 4) consists of:

Glass tube: This glass tube is used to isolate the cell anode and cathode. It is 7 mm OD, 5 mm ID, and 3" long. One open end is the original tube opening, and the other end is modified by the Chemistry glass shop to make a 2-3 mm hole.

3/16" OD 304 stainless steel tube: One end inserts into the glass tube to make an electrical connection, the other end attaches to the stainless steel rod that connects to the feedthrough C to allow an electrical connection and position adjustment.

W spring: This spring is made by wrapping 0.25 mm W wire around a 10-24 bolt. The spring provides an electrical connection and also applies force to the chemical pellets for good

contact. When properly placed, the pallets will give a resistance of 2 to 5 MΩ between the anode and cathode.

Ag sheet (0.05" thick, 4N purity, 3/16" in diameter): This is used as cathode for the electrochemical cell. It is cut from a large size Ag sheet by the machine in Ames Lab machine shop.

AgI and $Ag_2S$ pellet: These pellets are produced using an IR pellet handi-press borrowed from Dr. Lin's group. A ~ 2 mm thick $Ag_2S$ pellet (black) and 3-4 mm thick AgI pellet (yellow) are needed. Since the mold doesn't match our glass tube size, you need to use a razor blade to cut them so they can fit and move freely inside the glass tube. Later we had a new mold made from the machine shop in Chemistry Department and the pallets can fit the glass tube.

Pt wire (3N purity): One end is wired inside the glass tube in contact with the $Ag_2S$ pellet, and the other end is connected to the feedthrough A as the anode for the electrochemical cell.

W filament: 0.25 mm W wire is wrapped outside the glass tube around the chemical part of the cell to heat the cell. One end of the W wire connects to feedthrough C, the other end to feedthrough B. Here the cathode of the electrochemical cell and the heating coil share the same grounding feedthrough.

W-Re thermocouple: A pair of W-Re thermocouples covered with an isolating material is inserted through the stainless steel tube and attached to the end of the W spring connected to the Ag sheet for measuring the temperature of the cell.

The sulfur evaporator is operated by heating the cell to a temperature of ~200 °C and applying constant voltage to the anode and cathode of the cell to conduct electrochemical reaction. To do this, two different power supplies were used before we got the new power supply. The SL 100 DC power supply was used for heating the W coil. The brown-colored cable was used for electric connection outside the chamber with the red-taped (positive) clamp attaching to feedthrough B as shown in Fig. 5, and the other attaching to feedthrough C (grounding). The 6286 A DC power supply was used to apply voltage directly to the cell. The gray-colored cable was used for direct voltage supply with red-taped clamp (positive) attaching to feedthrough A, and the other to feedthrough C (grounding). Here the power supply was set to the range of 2.4 V, and we used two different multimeters to measure the voltage direct out of the power supply and from the feedthrough A to C. Due to the grounding issue, there was 5 to 15 mV difference between the two readings, and we used the voltage difference from the two feedthroughs as the cell voltage. The pair of thermocouple output was attached to another multimeter to give a reading of temperature in units of mV.

After we got the new power supply (XBT 32-3FTP DC power supply), channel 2 is used for heating and channel 1 is used to apply voltage to the cell with new cables. The cell voltage from the power supply has only a difference of less than 1 mV to the voltage measured from feedthrough A to C. We record the number from feedthrough A to C as cell voltage.

In order to limit the contamination during deposition to the lowest possible level, the W coil needs to be outgassed 2 to 3 times at a temperature ~ 180 °C after breaking vacuum with the shutter closed. We also need to check S flux after each new load of chemicals before

normal use. During each deposition run, we follow the same procedure to reach the final setting in order to yield a somewhat reproducible evaporation rate at certain setting. To do so, we follow a chart-flow shown here using heating current and cell voltage:

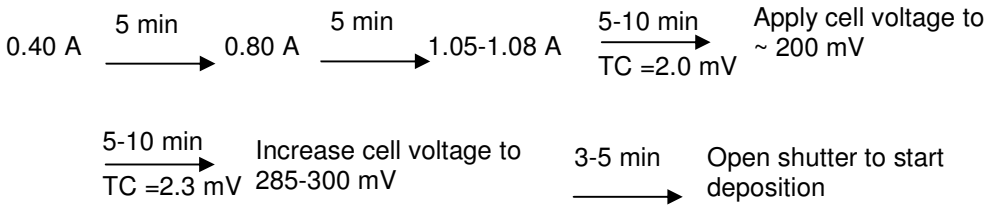


Once we reach the final operation setting, we lower down the linear motion for 8-9 mm to allow the beam go to the surface. For the first 2 to 3 runs, the pressure can rise to low $10^{-8}$ or high $10^{-9}$ Torr during deposition, but normally it can remain below 6 x $10^{-10}$ Torr. If the S coverage is low with normal setting, we usually let the cell sit at a cell voltage of ~ 315 mV for another 10 min, and then start deposition.

The cleanness of the deposited S adsorption is examined by Auger eletron spectroscopy (AES). For the first 2 to 3 runs, there will be some Cl residue on the surface coming from the outgas of the chemicals. Later, no evidence of codeposition of other elements is found, and the contamination by background gases is below the detection limit of the instrument. Table 1 summarizes the some settings as well as the measured coverage for the sulfur evaporator used here.

Table 1

| Trail | V of cell (mV) | Time of deposition | V(filament) (V) | I(filament) (A) | Cell temperature in mV | Auger intensity S/Ag | Sulfur coverage |
|---|---|---|---|---|---|---|---|
| 1 | 292 | 3.5 min | 4.8 | 1.08 | 2.1 | 0.81 | 0.49 |
| 2 | 285 | 5 min | 4.8 | 1.08 | 2.1 | 0.46 | 0.28 |
| 3 | 285.5 | 8 min | 4.8 | 1.08 | 2.1 | 0.36 | 0.22 |
| 4 | 276 | 3.7 min | 4.7 | 1.06 | 2.0 | 0.23 | 0.14 |
| 5 | 273.7 | 4 min | 4.6 | 1.05 | 2.0 | 0.1 | 0.055 |

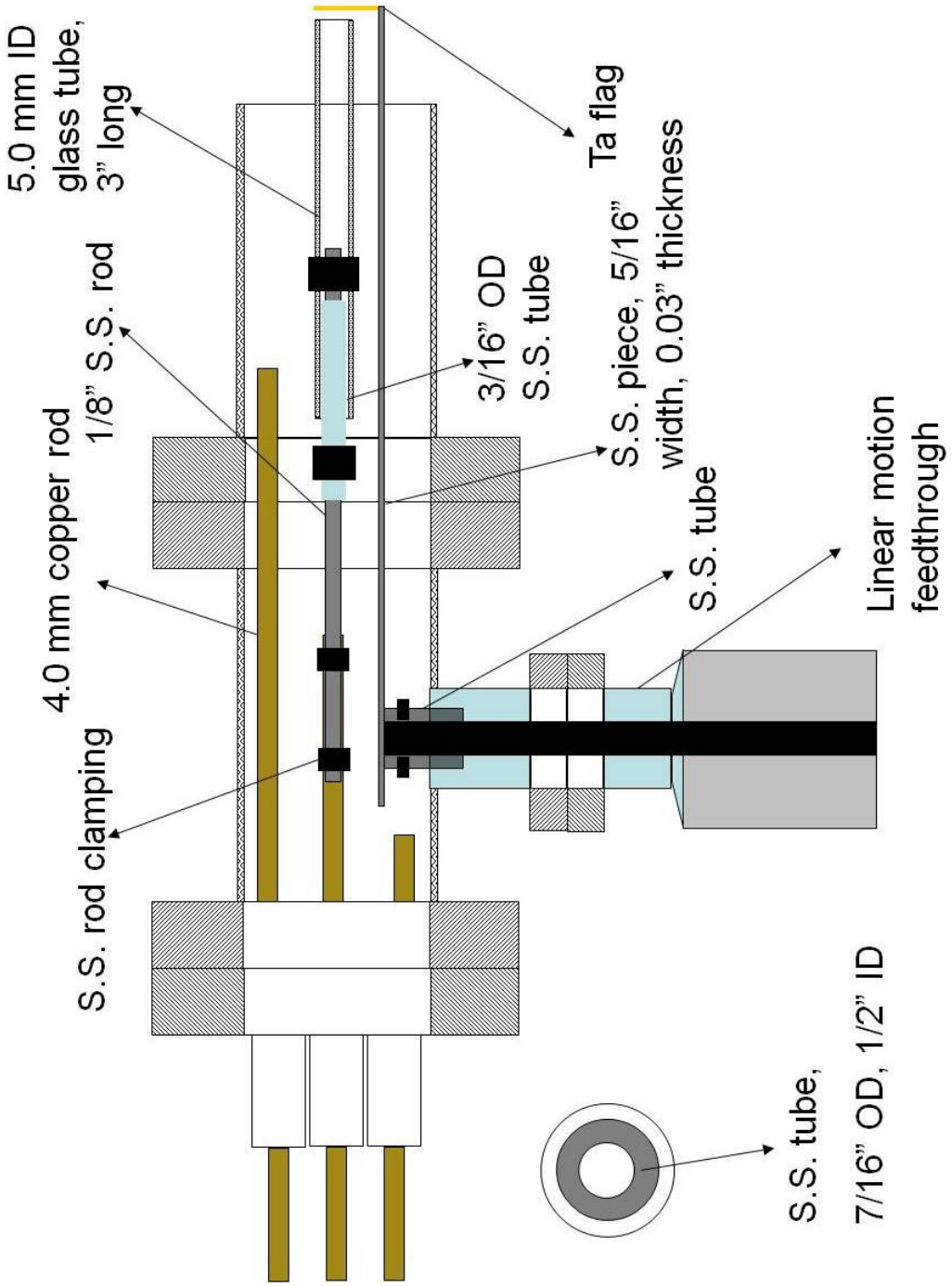


Figure 1. Side view of the S evaporator.

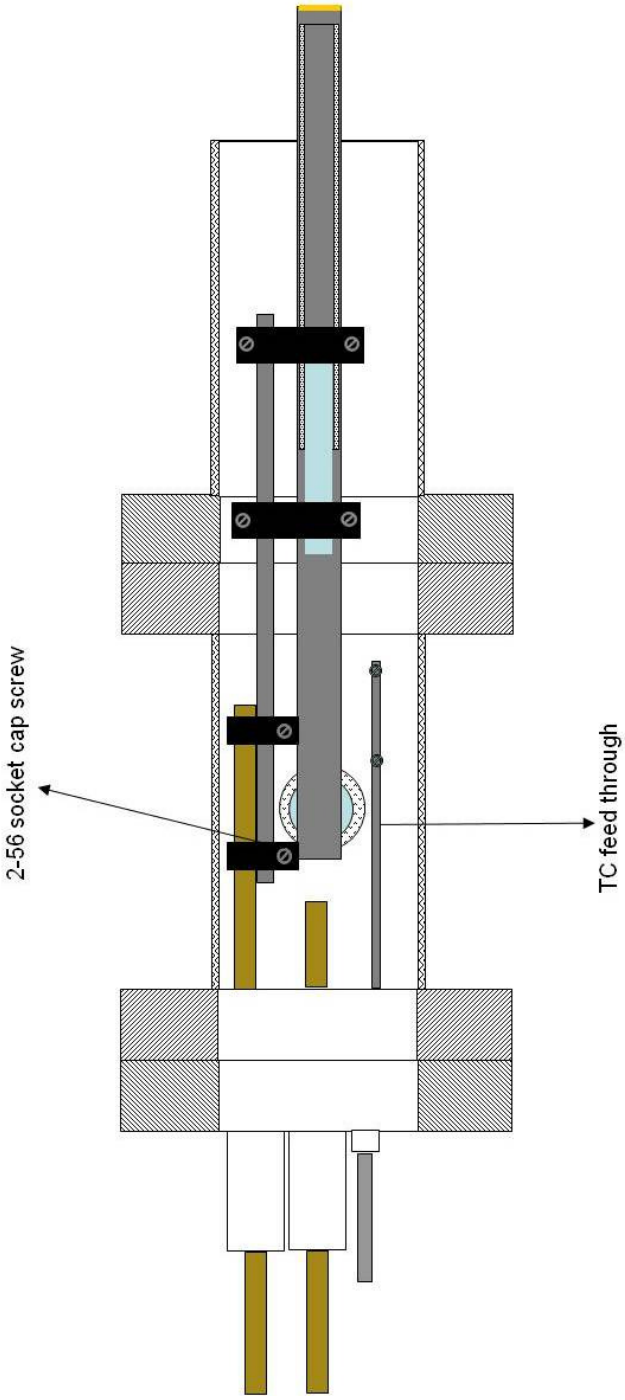


Figure 2. Top view of the S evaporator

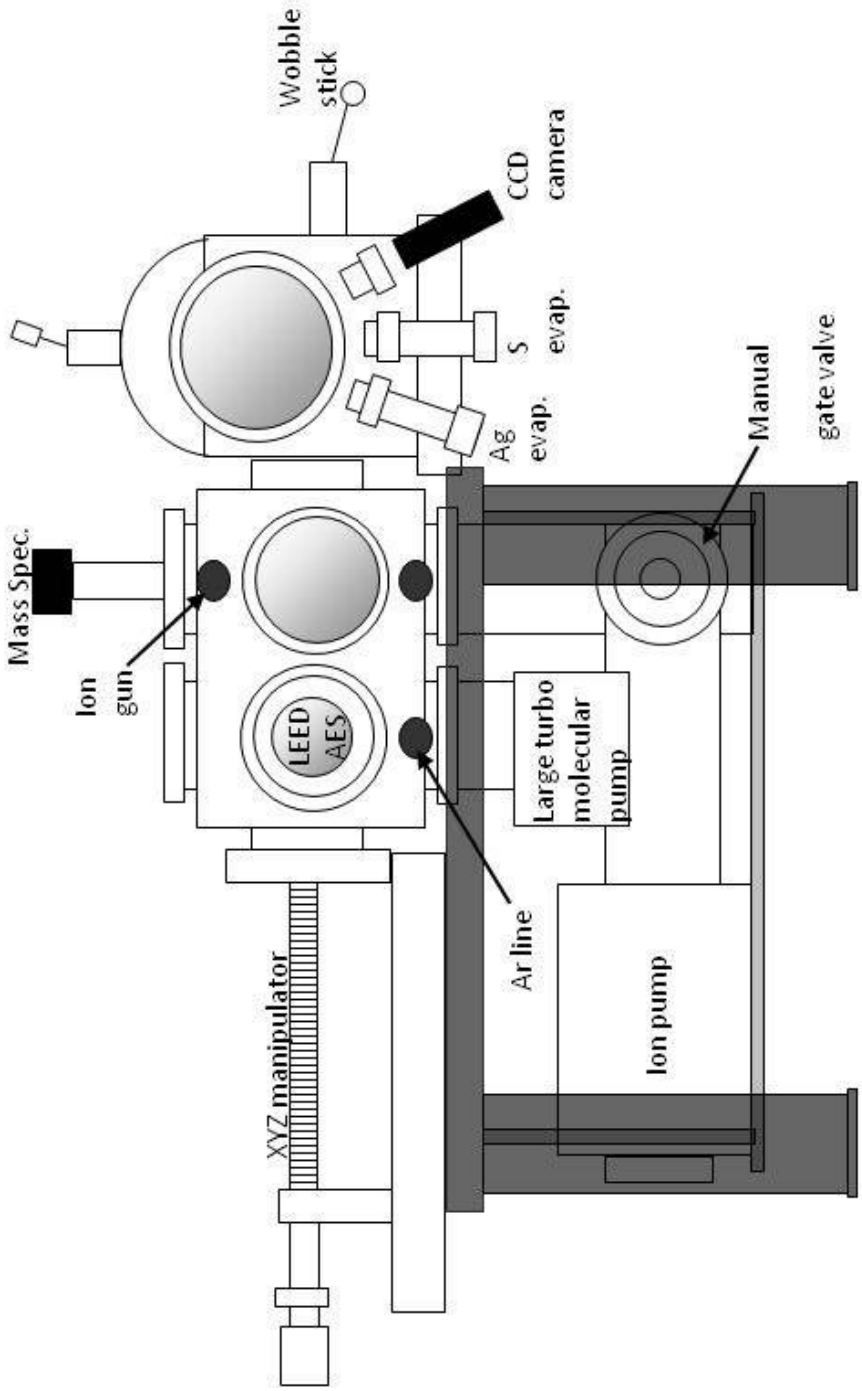


Figure 3. Side view of the UHV chamber.

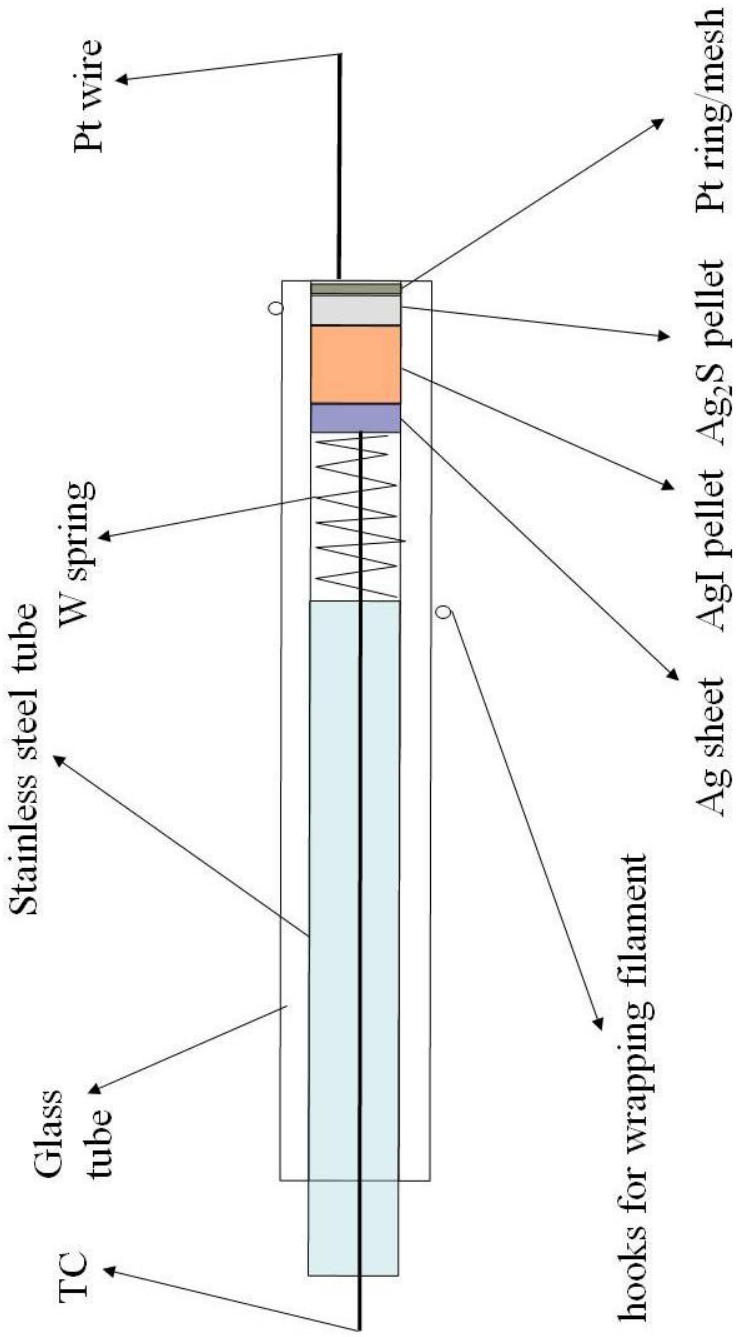


Figure 4. Glass tube setting.

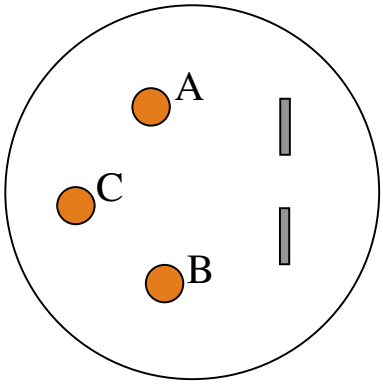


Figure 5. Front view of the S evaporator feedthrough

**Reference**

(1) Wagner, C. *Journal of Chemical Physics* **1953**, *21*, 1819.

(2) Heegemann, W.; Meister, K. H.; Bechtold, E.; Hayek, K. *Surface Science* **1975**, *49*, 161.

(3) Gallon, T. E.; Higginbotham, I. G.; Prutton, M.; Tokutaka, H. *Surface Science* **1970**, *21*, 224.

(4) Tokutaka, H.; Prutton, M.; Higginbotham, I. G.; Gallon, T. E. *Surface Science* **1970**, *21*, 233.

# APPENDIX IV. EXPERIMENTAL DATABASE

**Table Captions**

1. Break vacuum list
2. Brief STM list of Ag(111)
3. Detailed STM list of Ag(111)
4. Brief STM list of Ag(100)
5. Detailed STM list of Ag(100)

| Date | Nb page | Note |
|---|---|---|
| 3/14/2005 | 1-4 | Fix wobble stick |
| 4/12/2005 | 1-5 | Ceramic powder filled the chamber and used vacuum to clean |
| 5/10/2005 | 1-17 | Fix manipulator, and Teflon problem |
| 7/26/2005 | 1-100 | Fix wobble stick, clean LEED screen, polished sample, start designing S evaporator |
| 10/21/2005 | 2-47 | Refill Ag evaporator |
| 11/09/2005 | 2-67 | Fix Ag evaporator |
| 1/10/2006 | 2-80 | Refill Ag evaporator |
| 5/8/2006 | 4-7 | Fix ion pump feed-through, install new S evaporator, change TSP filaments |
| 9/7/2006 | 4-59 | Fix ion gun |
| 3/22/2007 | 5-24 | Refill S evaporator |
| 11/16/2007 | 5-111 | Refill S evaporator, refill Ag, change ion gun filament |
| 12/6/2007 | 5-119 | Fix S evaporator, , refill S evaporator |
| 01/22/2008 | 5-133 | Replace push-pull motion in STM part |
| 10/7/2008 | 6-59 | Fix STM pin grounding problem |
| 10/28/2008 | 6-68 | Fix S evaporator, refill S evaporator |
| 3/11/2009 | 6-138 | Refill S evaporator |

Table 1

| Date | experiment | $\Theta_{Ag}$/ML | $\Theta_S$/ML | STM image feature |
|---|---|---|---|---|
| 2/19/2006 | Clean surface after many cleaning cycles, RT | | | ~ 100 nm wide terrace with some vacancy pits |
| 2/21/2006 | Clean surface cooled to 135 K | | | Curly step edge after cooling |
| 2/23/2006 | Ag deposition at 135 K, and then heat up to 240 K | < 0.1 | | Curly step edge after cooling, only a few Ag islands |
| 3/13/2006 | Clean surface at room temperature | | | Vacancy pits coalesce via SR |
| 3/15/2006 | Cool to 124 K, Ag deposition at 135 K | ~ 0.1 | | Curly step edge, no obvious Ag islands |
| 3/20/2006 | Flash sample, Ag deposition at 125 K, then heat up to RT | < 0.2 | | Only see a few islands |
| 3/22/2006 | Clean surface at room temperature | | | Vacancy pits coalesce via SR, islands decay via OR |
| 3/23/2006 | Ag deposition at 130 K | < 0.5 | | Only see a few islands |
| 3/27/2006 | Ag deposition at 126 K, then heat up to 254 K | < 0.5 | | Only see a few islands |
| 3/30/2006 | Ag deposition at 75 K | < 0.4 | | A few small irregular shape islands on terrace. |
| 4/4/2006 | Cool the surface to 73 K and then heat up to RT | | | Curly step edge after cooling |
| 4/6/2006 | Ag deposition at 75 K and then heat up to RT | < 0.4 | | A few small irregular shape islands on terrace. |
| 4/13/2006 | Ag deposition at 75 K and then heat up to 250 K | < 0.5 | | Kind of square shape islands at < 200 K, hexagon at 250 K |
| 6/7/2006 | Clean surface after many cleaning cycles, RT | | | Pit decay near ascending A-type step edge |
| 6/15/2006 | Surface after exposure to 20 L $O_2$, RT | | | No obvious change |
| 7/12/2006 | Clean surface after many cleaning cycles, RT | | | Pit decay near different ascending step edges |
| 7/13/2006 | Surface after exposure to 20 L $O_2$, RT | | | No obvious change |
| 7/24/2006 | Surface after exposure to 9.84 L $O_2$, RT | | | Pit decay, no other obvious change |
| 8/2/2006 | Clean surface, RT | | | Pit decay near different ascending step edges |
| 8/3/2006 | Surface during exposure to 21.6 L $O_2$, RT | | | Irregular shape pit turned hexagonal |
| 10/3/2006 | Ag deposition at 133 K with high Ag flux | ~2.1 | | Layers of irregular shape Ag islands |
| 10/5/2006 | Ag deposition at 135 K followed by during $O_2$ exposure for 12.3 L | ~ 0.6 | | Irregular shape islands, mainly one layer, no obvious change after $O_2$ exposure |
| 10/10/2006 | Ag deposition at RT with high Ag flux | ~ 0.5 | | A few big hexagonal islands on terrace |
| 10/12/2006 | Ag deposition at 235 k and then during $O_2$ exposure for 17.2 L, then heat up to RT | ~ 0.4 | | No change at 235 K, islands perform OR at RT |
| 10/18/2006 | Ag deposition at 155 K and then heat up to 275 K, $O_2$ exposure at 275 K for 20 L, during and after | ~ 1.2 | | OR at 275 K |
| 10/24/2006 | Ag deposition at 135 K and then heat up to RT, $O_2$ exposure at RT for 20 L, during and after | ~ 1.2 | | OR at RT |
| 10/27/2006 | Ag deposition at 135 K and then heat up to RT | ~ 1.2 | | OR at RT |
| 11/1/2006 | Ag deposition at 135 K and then heat up to RT | ~ 1.2 | | OR at RT |

Table 2

| Date | experiment | $\Theta_{Ag}$/ML | $\Theta_S$/ML | STM image feature |
|---|---|---|---|---|
| 11/8/2006 | Ag deposition at RT and $O_2$ exposure at RT, 20 L | ~ 0.8 | | Islands and pits decay |
| 12/7/2006 | deposit S at RT, check STM at RT | | 0.884 | Rough step edge with root 7 by root 7 structure |
| 12/11/2006 | deposit S at RT, check STM at RT | | 0.341 | Rough step edge and adsorbed root 7 by root 7structure |
| | deposit more S, RT | | 0.462 | |
| 12/13/2006 | deposit S at RT, check STM at RT | | 0.042 | Fuzzy step edge, no big difference from clean surface |
| 12/14/2006 | sample of last night after depositing more S | | 0.12 | Fuzzy step edge |
| | sample of last night, heat at 0.6 A for 1 h, STM at RT | | 0.097 | |
| 12/18/2006 | deposit Ag at RT, then S at RT, STM at RT | ~ 0.4 | 0.095 | Ag islands disappear after S deposition, step edges are fuzzy |
| 12/21/2006 | deposit Ag at 150 K, then S at 150 K, STM at 150 K | ~ 0.1 | 0.451 | Dendritic Ag islands did not change |
| 12/28/2006 | deposit Ag at 225 K, then S at 225 K, STM at 225 K | ~ 0.2 | *< 0.005* | Ag island turned round with S |
| 1/3/2007 | deposit Ag at 135 K, heat up to 225 K, deposit S at 225 K, STM at 225 K, then heat up to RT | ~ 0.9 | 0.135 | Reduced island density after S deposition and show dot-row structure, islands turned irregular shape with no more decay |
| 1/8/2007 | deposit Ag at 135 K, heat up to 200 K, deposit S at 200 K, STM at 200 K, then cool back to 175 K | ~ 0.6 | 0.117 | Reduced island density after S deposition, dots are mobile at 200 K, but localized at 175 K |
| 1/11/2007 | deposit S at 135 K, heat up to 200 K, cool back to 135 K, heat up to RT, cool back to 200 K | | 0.094 | Dot row form at 200 K, and reversible between 200 k and 300 K, islands when cool back to 135 K again |
| 1/17/2007 | deposit S at 135 K, heat up to 175 K | | 0.122 | S islands formed dots at 175 K, not as clear as 200 K dots |
| 1/22/2007 | deposit S at 195 K, STM at 195 K | | 0.007 | No obvious change from clean Ag(111) surface |
| 1/25/2007 | deposit S at 195 K, STM at 195 K | | 0.031 | Facet step edge, only a few dots on terraces |
| 1/29/2007 | deposit S at 195 K, STM at 195 K | | 0.326 | Dot-row formation and pit formation |
| 2/1/2007 | deposit S at 195 K, STM at 195 K | | 0.173 | Dot-row formation |
| 2/5/2007 | deposit S at 195 K, STM at 195 K | | 0.030 | Facet step edge, only a few dots on terraces |
| 2/8/2007 | deposit S at 195 K, STM at 195 K | | 0.406 | Facet step edge, quite a few dots on terraces |
| 2/12/2007 | deposit S at 195 K, STM at 195 K | | 0.141 | Dot-row formation |
| 2/14/2007 | deposit S at 195 K, in situ STM at 195 K | | 0.109 | Facet step edge followed by dot-row formation |

Table 2 (continued)

| Date | experiment | $\Theta_{Ag}$/ML | $\Theta_S$/ML | STM image feature |
|---|---|---|---|---|
| 2/19/2007 | deposit S at 195 K, in situ STM at 195 K | | 0.043 | Facet step edge followed by some dot-row structure |
| 2/26/2007 | deposit S at 195 K, in situ STM at 195 K | | 0.051 | Facet step edge followed by some dot-row structure |
| 3/5/2007 | S deposition followed by Ag deposition at RT | ~ 0.3 | < *0.003* | Similar to cleans Ag(111) surface, OR for Ag islands, slow islands decay |
| 3/9/2007 | Ag deposition on clean Ag(111), RT | ~ 0.3 | | OR for Ag islands, slow island decay |
| 3/14/2007 | S deposition followed by Ag deposition at RT | ~ 0.3 | < *0.003* | Similar to clean Ag(111) surface, OR for Ag islands, slow islands decay |
| 4/10/2007 | Ag deposition at 130 K, then heat up to 200 K and deposit S | ~ 0.2 | 0.085 | No obvious change |
| 4/19/2007 | Ag deposition followed by in situ S deposition, 200 K | ~ 0.5 | 0.495 | Dot formation with consumption of Ag islands |
| 4/23/2007 | Ag deposition followed by in situ S deposition, 200 K and then heat up to RT, cool to 135 K, heat back to 200 K | ~ 0.7 | 0.280 | Dot formation with consumption of Ag islands and pit formation, rough step edge at RT with no islands |
| 4/26/2007 | Ag deposition followed by in situ S deposition, 200 K | ~ 0.6 | < *0.005* | Ag island density lowered after S deposition |
| 4/30/2007 | Ag deposition followed by in situ S deposition, 200 K | ~ 0.4 | 0.353 | Dot formation with consumption of Ag islands, pit formation |
| 5/7/2007 | Ag deposition followed by in situ S deposition, 200 K | ~ 0.4 | 0.735 | Dot formation with consumption of Ag islands, pit formation |
| 5/10/2007 | S deposition at 135 K, cycling between 135 K and 200 K | | 0.048 | Fragments of dot-row |
| 5/14/2007 | Ag deposition followed by in situ S deposition, 200 K | ~ 0.4 | 0.143 | Dot-row formation |
| 6/4/2007 | Ag deposition followed by in situ S deposition, 175 K | ~ 0.3 | 0.417 | Dot formation with consumption of Ag islands, pit formation |
| 6/7/2007 | Ag deposition after S deposition, RT | ~ 0.4 | < *0.003* | OR, slow island decay, similar to clean surface Ag deposition |
| 6/11/2007 | Ag deposition after S deposition, RT | ~ 0.4 | 0.032 | Rough step edge, no Ag island formation |
| 6/14/2007 | Ag deposition after S deposition, 200 K | ~ 0.3 | 0.066 | Smaller islands, low island density, dot-row structure |
| 6/25/2007 | Ag deposition after S deposition, 250 K | ~ 0.3 | 0.057 | Rough step edge, no Ag islands |
| 6/28/2007 | Ag deposition followed by in situ S deposition, RT | ~ 0.4 | 0.024 | Fast Ag island disappearance |
| 7/2/2007 | Ag deposition followed by in situ S deposition, RT | ~ 0.4 | 0.036 | Fast Ag island disappearance |
| 7/5/2007 | Ag deposition followed by in situ S deposition, RT | ~ 0.4 | 0.007 | Slow island decay, AD-OR? |

Table 2 (continued)

| Date | experiment | $\Theta_{Ag}$/ML | $\Theta_S$/ML | STM image feature |
|---|---|---|---|---|
| 7/9/2007 | Ag deposition followed by in situ S deposition, RT | ~ 0.4 | 0.011 | Fast island decay, > 500 $nm^2$/min |
| 7/19/2007 | Ag deposition followed by in situ S deposition, RT | ~ 0.4 | < 0.001 | Slow island decay, AD-OR? |
| 8/2/2007 | Ag deposition followed by in situ S deposition, RT | ~ 0.3 | 0.020 | Fast Ag island disappearance |
| 8/9/2007 | Ag deposition followed by S deposition, RT | ~ 0.3 | 0.048 | Rough step edge, all islands disappeared |
| 8/16/2007 | Ag deposition followed by S deposition, RT | ~ 0.3 | 0.003 | Slow island decay, AD-OR? |
| 8/20/2007 | S deposition at RT, line profile | | 0.002 to 0.013 | Step edge got rougher |
| 9/4/2007 | S deposition at RT, line profile | | <0.001 | Similar to clean Ag(111) surface |
| 9/6/2007 | S deposition at RT, line profile | | 0.002 | Similar to clean Ag(111) surface |
| 9/10/2007 | S deposition at RT, line profile | | 0.017 | Rough step edge after S deposition |
| 9/17/2007 | Ag deposition at RT and $O_2$ exposure at RT, 2000 L | ~ 0.4 | | Similar to clean surface |
| 10/29/2007 | Ag deposition at RT and $O_2$ exposure at RT, 2000 L | ~ 0.3 | | Similar to clean surface |
| 11/12/2007 | Ag deposition at 135 K, $O_2$ exposure at 135 K for 2000 L, heat up to 200 K, 250 K, and RT | ~ 0.2 | | Curly step edge |
| 11/15/2007 | Ag deposition at 135 K, heat up to 200 K, 250 K, and RT | ~ 0.2 | | Step edge straight compare to the one with $O_2$ exposure |
| 2/13/2008 | Ag deposition followed by in situ S deposition, 200 K | ~ 0.2 | 0.017 | Image quality not good |
| 2/19/2008 | Ag deposition followed by in situ S deposition, 200 K | ~ 0.3 | 0.021 | No obvious difference from clean surface |
| 2/26/2008 | Ag deposition followed by in situ S deposition, 200 K | ~ 0.4 | 0.009 | No obvious difference from clean surface |
| 4/10/2008 | Ag deposition followed by in situ S deposition, 200 K | ~ 0.3 | 0.036 | Dot formation with consumption of Ag islands |
| 4/17/2008 | Ag deposition followed by in situ S deposition, 200 K | ~ 0.5 | 0.200 | Dot formation with consumption of Ag islands |
| 4/24/2008 | deposit S at 132 K, heat up to 200 K, cool back to 135 K, heat up to RT, cool back to 200 K | | 0.515 | Formation of root 7 by root 7 structure |
| 5/1/2008 | S deposition at 133 K, cycling between 135 K and 200 K | | 0.320 | Dot row form at 200 K, reversible between 200 k and 300 K |

Table 2 (continued)

| Ag(111) data list | | | | | | | |
|---|---|---|---|---|---|---|---|
| **Date** | **Image** | **What?** | **θAg/ML** | **θs/ML** | **Lab Nb Pg** | **File name** | **Note** |
| 2-19-06 | all | After many cycles of RT sputtering, ~ 520 K anneal | | | 2-116 | 02-19-2006 | |
| 2-21-06 | 1-50 | clean surface, RT | | | 2-118 | 02-21-2006 | |
| | 51-60 | clean surface, 135 K | | | | | |
| 2-23-06 | 1-18 | clean surface, RT | | | 2-120 | 02-23-2006 | |
| | 19-30 | clean surface, < 135 K | | | | | |
| | 31-46 | clean surface, 135 K | | | | | |
| | 47-59 | after Ag deposition, flux = 310 nA, 90 sec, 135 K | < 0.1 | | | | |
| | 60 | after Ag deposition, 240 K | | | | | |
| 3-6-06 | all | clean surface, RT | | | 2-128 | 03-06-2006 | |
| 3-13-06 | all | clean surface, RT | | | 2-135 | 03-13-2006 | PRB 2007 |
| 3-15-06 | 1-14 | clean surface, RT | | | 2-137 | 03-15-2006 | |
| | 15-19 | during cooling | | | | | |
| | 20-21 | cooled to lowest temp., 124 K | | | | | |
| | 22-53 | heat back to 135 K | | | | | |
| | 54-75 | after Ag deposition, flux = 340 nA, 120 sec, 135 K | ~0.1 | | | | |
| 3-20-06 | 1-18 | clean surface, RT | | | 2-142 | 03-20-2006 | |
| | 19-22 | during cooling | | | | | |
| | 23-25 | clean surface, 135 K | | | | | |
| | 26 | heat back to 230 K | | | | | |
| | 27-37 | cool back | | | | | |
| | 38-48 | clean surface, 125 K | | | | | |
| | 49-74 | after Ag deposition, flux = 400 nA, 150 sec, 125 K | < 0.2 | | | | |
| | 75 | heat back to RT | | | | | |
| 3-22-06 | 1-9 | clean surface, RT, 500 points | | | 2-144 | 03-22-2006 | |
| | 10-304 | clean surface, RT, 250 points | | | | | |
| 3-23-06 | 1-14 | clean surface, RT | | | 2-145 | 03-23-2006 | |
| | 15-60 | clean surface, 130 K | | | | | |
| | 61-87 | after Ag deposition, flux = 360 nA, 10 min, 130 K | < 0.5 | | | | |
| 3-27-06 | 1-20 | clean surface, RT | | | 2-147 | 03-27-2006 | |
| | 21-66 | after cooling, 126 K | | | | | |
| | 67-95 | after Ag deposition, flux = 360 nA, 10 min, 126 K | < 0.5 | | | | |
| | 96-118 | heating up, 128-254 K | | | | | |
| 3-30-06 | 1-17 | clean surface, RT | | | 2-149 | 03-30-2006 | |
| | 18-55 | after cooling, 73 K | | | | | |
| | 56-120 | after Ag deposition, flux = 360 nA, 8 min, 73 K | < 0.4 | | | | |
| 4-4-06 | 1-17 | clean surface, RT | | | 2-153 | 04-04-2006 | |
| | 18-55 | after cooling, 73 K | | | | | |
| | 56-66 | heating up | | | | | |

Table 3

| Date | Image | What? | θAg/ML | θs/ML | Lab Nb Pg | File name | Note |
|---|---|---|---|---|---|---|---|
| 4-6-06 | 1-11 | clean surface, RT | | | 2-155 | 04-06-2006 | |
| | 12-32 | after cooling, ~ 75 K | | | | | |
| | 33-52 | after Ag deposition, flux = 400 nA, 8 min, 75 K | < 0.4 | | | | |
| | 53-60 | heat back to RT | | | | | |
| 4-13-06 | 1-5 | clean surface, RT | | | 4-5 | 04-13-2006 | |
| | 6-12 | after cooling, ~ 75 K | | | | | |
| | 13-144 | after Ag deposition, flux = 360 nA, 10 min, heating | < 0.5 | | | | |
| 5-30-06 | all | clean surface, RT | | | 4-22 | 05-30-2006 | |
| 5-31-06 | all | clean surface, RT | | | 4-22 | 05-31-2006 | |
| 6-7-06 | all | clean surface, RT | | | 4-26 | 06-07-2006 | |
| 6-8-06 | 1 | clean surface, during cooling | | | 4-27 | 06-08-2006 | |
| | 1-4 | heat back to flash sample | | | | | |
| | 5-10 | cooling again | | | | | |
| | 11-32 | after cooling to ~130 K | | | | | |
| 6-12-06 | 1-26 | clean surface, RT | | | 4-29 | 06-12-2006 | |
| | 27-128 | after cooling, 235 K | | | | | |
| 6-14-06 | 1-2 | clean surface, RT | | | 4-31 | 06-14-2006 | |
| | 3-12 | after cooling, 235 K | | | | | |
| | 13-38 | heat back to RT | | | | | |
| 6-15-06 | all | after O2 exposure at RT(2x10^-8 Torr for 1000sec, 20 L) | | | 4-31 | 06-15-2006 | |
| 7-12-06 | all | clean surface, RT | | | 4-38 | 07-12-2006 | |
| 7-13-06 | all | after O2 exposure at RT(2x10^-8 Torr for 1000sec, 20 L), first STM taken ~ 1 h after exposure | | | 4-38 | 07-13-2006 | |
| 7-18-06 | all | clean surface, RT | | | 4-41 | 07-18-2006 | |
| 7-20-06 | all | clean surface, RT | | | 4-42 | 07-20-2006 | |
| 7-24-06 | 1-10 | clean surface, RT | | | 4-44 | 07-24-2006 | |
| | 11-91 | during O2 exposure at RT(8x10^-10 Torr, 3 h 25 min, 9.84 L) | | | | | |
| 8-2-06 | all | clean surface, RT | | | 4-49 | 08-02-2006 | |
| 8-3-06 | all | during O2 exposure at RT(2x10^-9 Torr, 3 h, 21.6 L) | | | 4-50 | 08-03-2006 | |
| 8-9-06 | all | clean surface, RT | | | 4-53 | 08-09-2006 | |
| 8-10-06 | all | clean surface, RT | | | 4-56 | 08-10-2006 | |
| 9-6-06 | all | clean surface, RT | | | 4-59 | 09-06-2006 | |
| 9-20-06 | all | clean surface, RT | | | 4-69 | 09-20-2006 | |
| 9-22-06 | all | clean surface, RT | | | 4-70 | 09-22-2006 | |
| 9-25-06 | all | clean surface, RT | | | 4-72 | 09-25-2006 | |
| 9-27-06 | all | clean surface, RT | | | 4-73 | 09-27-2006 | |
| 10-1-06 | all | clean surface, RT | | | 4-75 | 10-01-2006 | |

Table 3 (continued)

| Date | Image | What? | θAg/ML | θs/ML | Lab Nb Pg | File name | Note |
|---|---|---|---|---|---|---|---|
| 10-3-06 | 1-7 | clean surface, RT | | | 4-77 | 10-03-2006 | |
| | 8 | after cooling, 135 K | | | | | |
| | 9-13 | after flashing, cooled back to 133 K | | | | | |
| | 14-59 | after Ag deposition, flux = 1000 nA, 2 min, 135 K | ~ 2.1 | | | | |
| 10-5-06 | 1-6 | clean surface, RT | | | 4-78 | 10-05-2006 | |
| | 7-11 | cool-heat-cool, 135 K | | | | | |
| | 12-55 | after Ag deposition, flux = 1100 nA, 30 sec, 135 K | ~ 0.6 | | | | |
| | 56-85 | during O2 exposure at 135 K(2x10^-9 Torr, 102 min, ) | | | | | |
| 10-10-06 | 1-3 | clean surface, RT | | | 4-81 | 10-10-2006 | |
| | 4-22 | after Ag deposition, flux = 1000 nA, 30 sec, RT | ~ 0.5 | | | | |
| 10-12-06 | 1-5 | clean surface, RT | | | 4-83 | 10-12-2006 | |
| | 6-10 | after cooling, 235 K | | | | | |
| | 11-35 | after Ag deposition, flux = 960 nA, 30 sec, 235 K | ~ 0.4 | | | | |
| | 36-75 | during O2 exposure at 235 K(2x10-9 Torr, 143 min 10 sec) | | | | | |
| | 76-122 | after O2 exposure, RT | | | | | |
| 10-18-06 | 1-5 | clean surface, RT | | | 4-87 | 10-18-2006 | |
| | 6-8 | after cooling, 155 K | | | | | |
| | 9-25 | after Ag deposition, flux = 960 nA, 120 sec, 155 K | ~ 1.2 | | | | |
| | 26 | heating up | | | | | |
| | 27-58 | after Ag deposition, 275 K | | | | | |
| | 59-65 | during O2 exposure at 275 K(2x10^-8 Torr, 20 L) | | | | | |
| | 66-135 | after O2 exposure, 275 K | | | | | |
| 10-24-06 | 1-5 | clean surface, 135 K | | | 4-91 | 10-24-2006 | |
| | 6-8 | after Ag deposition, flux = 1000 nA, 100 sec, 135 K | ~ 1.2 | | | | |
| | 9-111 | during and after O2 exposure at RT(5x10^-8 Torr, 20 L) | | | | | |
| 10-26-06 | all | clean surface, RT | | | 4-92 | 10-26-2006 | |
| 10-27-06 | 1-5 | After Ag deposition at 135 K, flux = 1000 nA, 100 sec | ~ 1.2 | | 4-93 | 10-27-2006 | |
| | 6-79 | heated back to RT | | | | | |
| 11-1-06 | 1-2 | After Ag deposition at 135 K, flux = 1000 nA, 100 sec | ~ 1.2 | | 4-095 | 11-01-2006 | |
| | 3-12 | heated back to RT | | | | | |
| 11-8-06 | 1-10 | clean surface, RT | | | 4-98 | 11-08-2006 | |
| | 11-38 | after Ag deposition, flux = 600 nA, 3 min, RT | ~ 0.8 | | | | |
| | 39-123 | during and after O2 exposure at RT(5x10^-8 Torr, 20 L) | | | | | |
| 12-5-06 | all | clean surface, RT | | | 4-125 | | |
| 12-7-06 | 1-8 | clean surface, RT | | | 4-126 | 12-07-2006 | |
| | 9-13 | after S deposition, trace S, RT | | | | | |
| | 14-26 | more S deposition, trace S, RT | | | | | |
| | 27-32 | more S deposition, trace S, RT | | | | | |
| | 33-34 | after AES, RT | | | | | |
| | 35-44 | after more S deposition, RT | | 0.884 | | | |

Table 3 (continued)

| Date | Image | What? | θAg/ML | θs/ML | Lab Nb Pg | File name | Note |
|---|---|---|---|---|---|---|---|
| 12-11-06 | 1-10 | clean surface, RT | | | 4-129 | 12-11-2006 | |
| | 11-23 | after S deposition, RT | | 0.341 | | | |
| | 24-25 | after AES | | | | | |
| | 26-50 | more S deposition, RT | | 0.462 | | | |
| 12-13-06 | 1-14 | clean surface, RT | | | 4-131 | 12-13-2006 | |
| | 15-25 | after S deposition, trace S, RT | | | | | |
| | 26 | more S deposition, RT | | 0.042 | | | |
| 12-14-06 | 1-3 | surface of 12-13-06, RT | | 0.097 | 4-132 | 12-14-2006 | |
| | 4 | after heating at ~ 200 °C for 1 h, RT | | | | | |
| 12-18-06 | 1-18 | clean surface, RT | | | 4-134 | 12-18-2006 | |
| | 19-25 | after Ag deposition, flux = 1000 nA, 30 sec, RT | ~ 0.4 | | | | |
| | 26-40 | after S deposition, RT | | 0.095 | | | |
| | 41-55 | after heating at ~ 200 °C for 35 min, RT | | | | | |
| 12-21-06 | 1-5 | clean surface, RT | | | 4-136 | 12-21-2006 | |
| | 6 | during cooling | | | | | |
| | 7-10 | after cooling, 150 K | | | | | |
| | 11-33 | after Ag deposition, flux = 950 nA, 15 sec, 150 K | ~ 0.1 | | | | |
| | 34-65 | after S deposition, 150 K | | 0.451 | | | |
| 12-28-06 | 1-5 | clean surface, RT | | | 4-139 | 12-28-2006 | |
| | 6-8 | after cooling, 225 K | | | | | |
| | 9-39 | after Ag deposition, flux =980 nA, 30 sec, 225 K | ~ 0.2 | | | | |
| | 40-82 | after S deposition, trace S, 225 K | | *< 0.005* | | | |
| 1-3-07 | 1-6 | clean surface, RT | | | 4-142 | 01-03-2007 | |
| | 7-9 | after cooling, 135 K | | | | | |
| | 10-17 | after Ag deposition, flux = 1000 nA, 1 min, 135 K | ~ 0.9 | | | | |
| | 18-59 | heat up to 225 K | | | | | |
| | 60-79 | after S deposition, 225 K | | 0.135 | | | |
| | 80-82 | heating up | | | | | |
| 1-8-07 | 1-5 | clean surface, 135 K | | | 4-144 | 01-08-2007 | SS2009 |
| | 6-10 | after cooling, 135 K | | | | | |
| | 11-15 | after Ag deposition, flux = 995 nA, 45 sec, 135K | ~ 0.6 | | | | |
| | 16-50 | heat up to 200 K | | | | | |
| | 51-75 | after S deposition, 200 K | | 0.117 | | | |
| | 76-83 | cooling down to 175 K | | | | | |
| | 84-93 | after cooling, 175 K | | | | | |

Table 3 (continued)

| Date | Image | What? | θAg/ML | θs/ML | Lab Nb Pg | File name | Note |
|---|---|---|---|---|---|---|---|
| 1-11-07 | 1-5 | clean surface, RT | | | 4-147 | 01-11-2007 | JPCC 2008 |
| | 6-8 | after cooling, 135 K | | | | | |
| | 9-20 | after S deposition, 135 K | | 0.094 | | | |
| | 21-40 | heating up to 195 K | | | | | |
| | 41-50 | after heating, 195 K | | | | | |
| | 51-60 | cool back to 135 K | | | | | |
| | 61-63 | heat up to RT | | | | | |
| | 64-79 | cool back to 200 K | | | | | |
| 1-17-07 | 1 | clean surface, RT | | | 4-149 | 01-17-2007 | |
| | 2-5 | after cooling, 135 K | | | | | |
| | 6-12 | after S deposition, 135 K | | 0.122 | | | |
| | 13-24 | heating up to 175 K | | | | | |
| | 24-43 | after heating, 175 K | | | | | |
| 1-22-07 | 1-4 | clean surface after cooling, 195 K | | | 4-152 | 01-22-2007 | |
| | 5-12 | after S deposition, 195 K | | 0.007 | | | |
| 1-25-07 | 1-5 | clean surface, RT | | | 4-154 | 01-25-2007 | |
| | 6-8 | clean surface after cooling, 195 K | | | | | |
| | 9-29 | after S deposition, 195 K | | 0.031 | | | |
| 1-29-07 | 1-2 | clean surface, RT | | | 4-156 | 01-29-2007 | |
| | 3-5 | clean surface after cooling, 195 K | | | | | |
| | 6-23 | after S deposition, 195 K | | 0.326 | | | |
| 2-1-07 | 1-2 | clean surface, RT | | | 5-3 | 02-01-2007 | |
| | 3-5 | clean surface after cooling, 195 K | | | | | |
| | 6-23 | after S deposition, 195 K | | 0.173 | | | |
| 2-5-07 | 1-2 | clean surface, RT | | | 5-5 | 02-05-2007 | |
| | 3-5 | clean surface after cooling, 195 K | | | | | |
| | 6-24 | after S deposition, 195 K | | 0.030 | | | |
| 2-8-07 | 1-2 | clean surface, RT | | | 5-7 | 02-08-2007 | |
| | 3-5 | clean surface after cooling, 195 K | | | | | |
| | 6-26 | after S deposition,195 K | | 0.406 | | | |
| 2-12-07 | 1-3 | clean surface, RT | | | 5-9 | 02-12-2007 | |
| | 4-6 | clean surface after cooling, 195 K | | | | | |
| | 7-34 | after S deposition, 195 K | | 0.141 | | | |
| 2-14-07 | 1-7 | clean surface, RT | | | 5-11 | 02-14-2007 | |
| | 8-13 | clean surface after cooling, 195 K | | | | | |
| | 14-17 | during S deposition, 195 K | | | | | |
| | 18-30 | after S deposition, 195 K | | 0.109 | | | |

Table 3 (continued)

| Date | Image | What? | θAg/ML | θs/ML | Lab Nb Pg | File name | Note |
|---|---|---|---|---|---|---|---|
| 2-19-07 | 1-3 | clean surface, RT | | | 5-13 | 02-19-2007 | |
| | 4-14 | clean surface after cooling, 195 K | | | | | |
| | 15-41 | during S deposition, 195 K | | | | | |
| | 42-46 | after S deposition, 195 K | | 0.043 | | | |
| 2-26-07 | 1-5 | clean surface after cooling, 195 K | | | 5-15 | 02-26-2007 | |
| | 6-26 | during S deposition, 195 K | | | | | |
| | 27-28 | after S deposition, 195 K | | 0.051 | | | |
| 3-5-07 | 1-5 | clean surface, RT | | | 5-18 | 03-05-2007 | JCP 2009 |
| | 6-8 | during S deposition, RT | | | | | |
| | 9-12 | after S deposition, trace S, RT | | *< 0.003* | | | |
| | 13-57 | after Ag deposition, flux = 1000 nA, 35 sec, RT | ~ 0.3 | | | | |
| 3-9-07 | 1-3 | clean surface, RT | | | 5-20 | 03-09-2007 | |
| | 4-62 | after Ag deposition, flux = 1000 nA, 35 sec, RT | | | | | |
| 3-14-07 | 1-7 | clean surface, RT | | | 5-22 | 03-14-2007 | |
| | 8-12 | during S deposition, RT | | | | | |
| | 13-16 | after S deposition, trace S, RT | | *< 0.003* | | | |
| | 17-72 | after Ag deposition, flux = 1000 nA, 35 sec, RT | ~ 0.3 | | | | |
| 4-10-07 | 1 | clean surface, RT | | | 5-31 | 04-10-2007 | |
| | 2-3 | clean surface, ~ 130 K | | | | | |
| | 4-7 | After Ag deposition, flux = 980 nA, 30 sec, ~ 130 K | ~ 0.2 | | | | |
| | 8-15 | during heating up to 200 K | | | | | |
| | 16-22 | after Ag deposition, 200 K | | | | | |
| | 23-37 | during S deposition, 200 K | | 0.085 | | | |
| 4-19-07 | 1-3 | clean surface, 200 K | | | 5-34 | 04-19-2007 | |
| | 4-10 | After Ag deposition, flux = 1000 nA, 45 sec, 200 K | ~ 0.5 | | | | |
| | 11-12 | during S deposition, 200 K | | 0.495 | | | |
| | 13-29 | after S deposition, 200 K | | | | | |
| 4-23-07 | 1-2 | clean surface, RT | | | 5-36 | 04-23-2007 | |
| | 3-5 | clean surface, 200 K | | | | | |
| | 6-13 | after Ag deposition, flux = 860 nA, 1 min, 200 K | ~ 0.7 | | | | |
| | 14-16 | during S deposition, 200 K | | | | | |
| | 17-21 | after S deposition, 200 K | | 0.280 | | | |
| | 22-28 | after S deposition, ~ 135 K(after heating to 280 K) | | | | | |
| | 29-38 | heat up to 200 K | | | | | |
| 4-26-07 | 1-5 | clean surface, RT | | | 5-38 | 04-26-2007 | |
| | 6-8 | clean surface, 200 K | | | | | |
| | 9-23 | after Ag deposition, flux = 800 nA, 45 sec, 200 K | ~ 0.6 | | | | |
| | 24-63 | during S deposition, total = 2.5 h, trace S, 200 K | | *< 0.005* | | | |
| | 64-72 | after S deposition, 200 K | | | | | |

Table 3 (continued)

| Date | Image | What? | θAg/ML | θs/ML | Lab Nb Pg | File name | Note |
|---|---|---|---|---|---|---|---|
| 4-30-07 | 1-6 | clean surface, RT, line mode | | | 5-41 | 04-30-2007 | |
| | 7-10 | clean surface, RT, frame mode | | | | | |
| | 11-18 | clean surface, 200 K, line mide | | | | | |
| | 19-20 | clean surface, 200 K, frame mode | | | | | |
| | 21-29 | after Ag deposition, flux = 800 nA, 30 sec, 200 K | ~ 0.4 | | | | |
| | 30-31 | during S deposition, 200 K | | | | | |
| | 32-40 | after S deposition, 200 K | | 0.353 | | | |
| | 37-39 | STS of dot structure, 200 K | | | | | |
| | 41-53 | after S deposition, RT | | | | | |
| | 43-44 | STS of S/Ag(111), RT | | | | | |
| | 45-53 | line mode of S/Ag(111), RT | | | | | |
| 5-7-07 | 1-3 | clean surface, RT | | | 5-44 | 05-07-2007 | |
| | 4-8 | STS of clean surface, RT | | | | | |
| | 9-10 | clean surface, 200 K | | | | | |
| | 11-13 | STS of clean surface, 200 K | | | | | |
| | 14-25 | after Ag deposition, flux = 810 nA, 40 sec, 200 K | ~ 0.4 | | | | |
| | 26-27 | during S deposition, 200 K | | | | | |
| | 28-33 | after S deposition, 200 K | | 0.735 | | | |
| | 34-36 | STS after S deposition, 200 K | | | | | |
| | 37-40 | after S deposition, 200 K | | | | | |
| 5-10-07 | 1-3 | clean surface, RT | | | 5-46 | 05-10-2007 | |
| | 4-7 | STS of clean surface, RT | | | | | |
| | 8-10 | clean surface, 135 K, frame mode | | | | | |
| | 11-14 | clean surface, 135 K, line mode | | | | | |
| | 15-16 | clean surface, 135 K, frame mode | | | | | |
| | 17-21 | during S deposition, 135 K | | <0.03 | | | |
| | 22-24 | after S deposition, 135 K | | | | | |
| | 25-40 | during heating up to 200 K | | | | | |
| | 41-45 | deposit more S, 200 K | | 0.048 | | | |
| | 46-52 | after second S deposition, cool down to 135 K | | | | | |
| | 53-60 | after second S deposition, heat up to 200 K | | | | | |
| | 61-72 | after second S deposition, cool down to 135 K again | | | | | |
| 5-14-07 | 1-2 | clean surface, RT | | | 5-48 | 05-14-2007 | |
| | 3-5 | clean surface, 200 K | | | | | |
| | 6-18 | after Ag deposition, flux = 800 nA, 40 sec, 200 K | ~ 0.4 | | | | |
| | 19-20 | during S deposition, 200 K | | | | | |
| | 21-34 | after S deposition, 200 K | | 0.143 | | | |

Table 3 (continued)

| Date | Image | What? | θAg/ML | θs/ML | Lab Nb Pg | File name | Note |
|---|---|---|---|---|---|---|---|
| 6-4-07 | 1-2 | clean surface, RT | | | 5-57 | 06-04-2007 | |
| | 3-5 | clean surface, 175 K | | | | | |
| | 6-14 | after Ag deposition, flux =830 nA, 35 sec, 175 K | ~ 0.3 | | | | |
| | 15-16 | during S deposition, 175 K | | | | | |
| | 17-37 | after S deposition, 175 K | | 0.417 | | | |
| 6-7-07 | 1-4 | clean surface, RT | | | 5-59 | 06-07-2007 | |
| | 5-9 | during S deposition, trace S, RT | | | | | |
| | 10-11 | after S deposition, RT | | *< 0.003* | | | |
| | 12-63 | after Ag deposition, flux = 1000 nA, 35 sec, RT | ~ 0.4 | | | | |
| 6-11-07 | 1-4 | clean surface, RT | | | 5-61 | 06-11-2007 | |
| | 5-7 | during S deposition, RT | | | | | |
| | 8-10 | after S deposition, RT | | 0.032 | | | |
| | 11-20 | after Ag deposition, flux = 1000 nA, 35 sec, RT | ~ 0.4 | | | | |
| 6-14-07 | 1-3 | clean surface, RT | | | 5-63 | 06-14-2007 | |
| | 4-8 | clean surface, 200 K | | | | | |
| | 9-10 | during S deposition, 200 K | | | | | |
| | 11-25 | after S deposition, 200 K | | 0.066 | | | |
| | 26-38 | after Ag deposition, flux = 810 nA, 40 sec, 200 K | ~ 0.3 | | | | |
| 6-25-07 | 1-5 | clean surface, RT | | | 5-65 | 06-25-2007 | |
| | 6-8 | during S deposition, RT | | | | | |
| | 9-10 | after S deposition, RT | | 0.057 | | | |
| | 11-16 | after S deposition, 250 K | | | | | |
| | 17-21 | line mode of S/Ag(111), 250 K | | | | | |
| | 22-30 | After Ag deposition, flux = 825 nA, 40 sec, 250 K | ~ 0.3 | | | | |
| 6-28-07 | 1-4 | clean surface, RT | | | 5-67 | 06-28-2007 | |
| | 5-10 | after Ag deposition, flux = 1000 nA, 35 sec, RT | ~ 0.4 | | | | |
| | 11-12 | during S deposition, RT | | | | | |
| | 12-18 | after S deposition, RT | | 0.024 | | | |
| 7-2-07 | 1-5 | clean surface, RT | | | 5-068 | 07-02-2007 | JCP 2009 |
| | 6-20 | after Ag deposition, flux = 1030 nA, 35 sec, RT | ~ 0.4 | | | | |
| | 21-22 | during S deposition, RT | | | | | |
| | 22-29 | after S deposition, RT | | 0.036 | | | |
| 7-5-07 | 1-5 | clean surface, RT | | | 5-70 | 07-05-2007 | JCP 2009 |
| | 6-28 | after Ag deposition, flux = 1050 nA, 35 sec, RT | ~ 0.4 | | | | |
| | 29 | during S deposition, RT | | | | | |
| | 30-149 | after S deposition, RT | | 0.007 | | | |
| 7-9-07 | 1-5 | clean surface, RT | | | 5-71 | 07-09-2007 | JCP 2009 |
| | 6-22 | after Ag deposition, flux = 1010 nA, 30 sec, RT | ~ 0.4 | | | | |
| | 23 | during S deposition, RT | | | | | |
| | 24-58 | after S deposition, RT | | 0.011 | | | |

Table 3 (continued)

| Date | Image | What? | θAg/ML | θs/ML | Lab Nb Pg | File name | Note |
|---|---|---|---|---|---|---|---|
| 7-19-07 | 1-5 | clean surface, RT | | | 5-74 | 07-19-2007 | |
| | 6-21 | after Ag deposition, flux = 1050 nA, 30 sec, RT | ~ 0.4 | | | | |
| | 22 | during S deposition, RT | | | | | |
| | 23-142 | after S deposition, RT | | <0.001 | | | |
| 7-26-07 | 1-6 | clean surface, RT | | | 5-77 | 07-26-2007 | |
| | 7-22 | after Ag deposition, flux = 1100 nA, 30 sec, RT | ~ 0.4 | | | | |
| | 23-112 | after S deposition, RT | | 0.021 | | | |
| 8-2-07 | 1-5 | clean surface, RT | | | 5-79 | 08-02-2007 | SS2009 |
| | 6-14 | after Ag deposition, flux = 1000 nA, 30 sec, RT | ~ 0.3 | | | | |
| | 15-24 | after S deposition, RT | | 0.020 | | | |
| 8-9-07 | 1-5 | clean surface, RT | | | 5-82 | 08-09-2007 | |
| | 6-22 | after Ag deposition, flux = 1000 nA, 30 sec, RT | ~ 0.3 | | | | |
| | 23-33 | after S deposition, RT | | 0.048 | | | |
| 8-16-07 | 1-6 | clean surface, RT | | | 5-84 | 08-16-2007 | |
| | 7-26 | After Ag deposition, flux = 980 nA, 30 sec, RT | ~ 0.3 | | | | |
| | 27-161 | after S deposition, RT | | 0.003 | | | |
| 8-20-07 | 1-5 | clean surface, RT, frame mode | | | 5-85 | 08-20-2007 | |
| | 6-19 | clean surface, RT, line mode | | | | | |
| | | deposit S, RT | | 0.002 | | | |
| | 20-22 | afetr 1st S deposition, frame mode, RT | | | | | |
| | 23-40 | afetr 1st S deposition, line mode, RT | | | | | |
| | | deposit more S, RT | | 0.004 | | | |
| | 41-45 | afetr 2nd S deposition, frame mode, RT | | | | | |
| | 46-59 | afetr 2nd S deposition, line mode, RT | | | | | |
| | | deposit more S, RT | | 0.013 | | | |
| | 60-64 | afetr 3rd S deposition, frame mode, RT | | | | | |
| | 65-83 | afetr 3rd S deposition, line mode, RT | | | | | |
| 9-4-07 | 1-2 | clean surface, frame mode, RT | | | 5-92 | 09-04-2007 | |
| | 3-20 | clean surface, line mode, RT | | | | | |
| | 21-22 | clean surface, frame mode, RT | | | | | |
| | 23-24 | after S deosition, frame mode, RT | | <0.001 | | | |
| | 25-42 | after S deposition, line mode, RT | | | | | |
| 9-6-07 | 1-4 | clean surface, frame mode, RT | | | 5-94 | 09-06-2007 | |
| | 5-13 | clean surface, line mode, RT | | | | | |
| | 14-15 | clean surface, frame mode, RT | | | | | |
| | 16 | after S deposition, frame mode, RT | | 0.002 | | | |
| | 17-25 | after S deposition, line mode, RT | | | | | |
| | 16-28 | after S deposition, frame mode, RT | | | | | |
| | 29-32 | after more S deposition, frame mode, RT | | | | | |
| | 33-45 | after more S deposition, line mode, RT | | | | | |

Table 3 (continued)

| Date | Image | What? | θAg/ML | θs/ML | Lab Nb Pg | File name | Note |
|---|---|---|---|---|---|---|---|
| 9-10-07 | 1-5 | clean surface, frame mode, RT | | | 5-96 | 09-10-2007 | |
| | 6-13 | clean surface, line mode, RT | | | | | |
| | 14-15 | clean surface, frame mode, RT | | | | | |
| | 23-24 | after S deposition, frame mode, RT | | 0.017 | | | |
| | 25-36 | after S deposition, line mode, RT | | | | | |
| | 37-40 | after S deposition, frame mode, RT | | | | | |
| 9-17-07 | 1-6 | clean surface, RT | | | 5-99 | 09-17-2007 | |
| | 7-15 | after Ag deposition, flux = 1010 nA, 30 sec, RT | ~ 0.4 | | | | |
| | 16-18 | during O2 exposure at RT (8 x 10^-7 Torr for 40 min, 2000 L) | | | | | |
| | 19-160 | after O2 exposure, RT | | | | | |
| 10-29-07 | 1-5 | clean surface, RT | | | 5-107 | 10-29-2007 | |
| | 6-10 | after Ag deposition, flux = 1000 nA, 30 sec, RT | ~ 0.3 | | | | |
| | 11-36 | during O2 exposure at RT (5 x 10^-7 Torr for 60 min, 2000 L) | | | | | |
| | 37-42 | after O2 exposure, frame mode, RT | | | | | |
| | 43-55 | after O2 exposure, line mode, RT | | | | | |
| | 56-75 | after O2 exposure, frame mode, RT | | | | | |
| 11-12-07 | 1-2 | clean surface, 135 K | | | 5-110 | 11-12-2007 | |
| | 3-4 | after Ag deposition, flux = 970 nA, 25 sec, 135 K | ~ 0.2 | | | | |
| | 5-16 | after O2 exposure at 135 K (8 x 10^-7 Torr for 40 min, 2000 L) | | | | | |
| | 17-43 | after O2 exposure, 200 K | | | | | |
| | 44-73 | after O2 exposure, 250 K | | | | | |
| | 74-105 | after O2 exposure, RT | | | | | |
| 11-15-07 | 1-2 | clean surface, 135 K | | | 5-111 | 11-15-2007 | |
| | 3-16 | after Ag deposition, flux = 970 nA, 25 sec, 135 K | ~ 0.2 | | | | |
| | 17-36 | after Ag deposition, 200 K | | | | | |
| | 37-50 | after Ag deposition, 250 K | | | | | |
| | 51-65 | after Ag deposition, 300 K | | | | | |
| 2-13-08 | 1-8 | clean surface, RT | | | 5-143 | 02-13-2008 | |
| | 9-18 | clean surface, 200 K | | | | | |
| | 19-20 | after Ag deposition, flux = 800 nA, 45 sec, 200 K | ~ 0.2 | | | | |
| | 21-31 | during S deposition, 200 K | | | | | |
| | 32-35 | after S deposition, 200 K | | 0.017 | | | |
| 2-18-08 | 1-5 | clean surface, RT | | | 5-145 | 02-18-2007 | |
| | 6-12 | after Ag deposition, flux = 840 nA, 45 sec, RT | ~ 0.2 | | | | |
| 2-19-08 | 1-10 | clean surface, RT | | | 5-146 | 02-19-2008 | |
| | 11-20 | clean surface, 200 K | | | | | |
| | 21-32 | after Ag deposition, flux = 840 nA, 1 min, 200 K | ~ 0.3 | | | | |
| | 33-40 | during S deposition, 200 K | | | | | |
| | 41-50 | after S deposition, 200 K | | 0.021 | | | |

Table 3 (continued)

| Date | Image | What? | θAg/ML | θs/ML | Lab Nb Pg | File name | Note |
|---|---|---|---|---|---|---|---|
| 2-26-08 | 1-5 | clean surface, RT | | | 5-147 | 02-26-2008 | |
| | 6-8 | clean surface, 200 K | | | | | |
| | 9-25 | after Ag deposition, flux = 600 nA, 90 sec, 200 K | ~ 0.4 | | | | |
| | 26-28 | during S deposition, 200 K | | | | | |
| | 29-88 | after S deposition, 200 K | | 0.009 | | | |
| 2-28-08 | 1-2 | clean surface, RT | | | 5-149 | 02-28-2008 | |
| | 3-5 | clean surface, 175 K | | | | | |
| | 6-29 | after Ag deposition, flux = 400 nA, 60 sec, 175 K | ~ 0.8 | | | | |
| 3-3-08 | 1-3 | clean surface, RT | | | 5-150 | 03-03-2008 | |
| | 4-6 | clean surface, 130 K | | | | | |
| | 7-10 | after Ag deposition, flux = 400 nA, 30 sec, 128 K | ~ 0.4 | | | | |
| | 11-16 | after Ag deposition, 200 K | | | | | |
| | 17-36 | after Ag depostion, RT | | | | | |
| 4-8-08 | all | clean surface, RT | | | 6-3 | 04-08-2008 | |
| 4-10-08 | 1-5 | clean surface, RT | | | 6-3 | 04-10-2008 | |
| | 6-10 | clean surface, 200 K | | | | | |
| | 11-32 | after Ag deposition, flux = 590 nA, 30 sec, 200 K | ~ 0.3 | | | | |
| | 33-41 | during S deposition, 200 K | | | | | |
| | 42-103 | after S deposition, 200 K | | 0.036 | | | |
| 4-17-08 | 1-2 | clean surface, RT | | | 6-6 | 04-17-2008 | |
| | 3-5 | clean surface, 200 K | | | | | |
| | 6-20 | after Ag deposition, flux = 610 nA, 30 sec | ~ 0.5 | | | | |
| | 21-35 | during S deposition, 200 K | | | | | |
| | 36-39 | after S deposition, 200 K | | 0.200 | | | |
| | 40-75 | after S deposition, 296 K | | | | | |
| 4-24-08 | 1-5 | clean surface, RT | | | 6-8 | 04-24-2008 | |
| | 6-9 | clean surface, 132 K | | | | | |
| | 10-14 | during S deposition, 132 K | | | | | |
| | 15-16 | after S deposition, 132 K | | | | | |
| | 17-25 | after more S deposition, 132 K | | 0.515 | | | |
| | 26-52 | after S deposition, 200 K | | | | | |
| | 53-70 | after S deposition, 132 K | | | | | |
| | 71-77 | after S deposition, 200 K | | | | | |
| | 78-100 | heating up to 265 K | | | | | |
| | 101-143 | after S deposition, 300 K | | | | | |
| | 144-158 | after S deposition, 200 K | | | | | |
| 5-1-08 | 1-4 | clean surface, RT | | | 6-11 | 05-01-2008 | |
| | 5-8 | clean surface, 130 K | | | | | |
| | 9-15 | after S deposition, 133 K | | 0.320 | | | |
| | 16-44 | after S deposition, 200 K | | | | | |
| | 45-55 | after S deposition, 133 K | | | | | |
| | 56-65 | after S deposition, 300 K | | | | | |
| | 66-79 | after S deposition, 200 K | | | | | |

Table 3 (continued)

| Date | experiment | $\Theta_{Ag}$/ML | $\Theta_S$/ML | STM image feature |
|---|---|---|---|---|
| 6/23/2008 | S deposition at 120 K , heat up to 160 K, 175 K, 240 K, and RT | | < 0.003 | S on terraces near edge; "S" like worms/blotches |
| 7/22/2008 | S deposition at 120 K, heat up to 170 K, 230 K, RT, and then cool back to 230 K, heat up again to RT | | 0.368 | Islands at 120 K, 170 K, and 230 K, two phases (dense and checkerboard) formed at RT and stayed after cooling and heating |
| 7/30/2008 | S deposition at 120 K, heat up to 170 K, 240 K, RT, and then cool back to 230 K | | 0.248 | Islands at 120 K, 170 K, and 230 K, two phases (dense and checkerboard) formed at RT and stayed after cooling and heating, more dense phase on the surface |
| 8/5/2008 | Ag deposition at RT | < 0.1 | | A few square islands on the surface |
| 8/18/2008 | Ag deposition at RT | > 1.2 | | Multilayer Ag islands |
| 9/16/2008 | Ag deposition at RT | ~ 0.3 | | Distorted Ag islands with pits |
| 9/18/2008 | Ag deposition at RT | ~ 0.7 | | Distorted Ag islands, wormy |
| 9/30/ 2008 | Ag deposition followed by S deposition at RT | ~ 0.2 | 0.235 | Less islands after S deposition, islands rotated |
| 10/15/2008 | Ag deposition at RT | ~ 1 | | Square islands, no more distortion |
| 12/1/2008 | Ag deposition followed by S deposition at RT | ~ 0.5 | 0.0087 | Islands perform Ostwald ripening after S deposition |
| 12/5/2008 | Ag deposition, observe for more than 3 h, followed by S deposition at RT | ~ 0.3 | 0.036 | SR for islands on clean Ag(100) surface, OR with S |
| 12/10/2008 | S deposition followed by Ag deposition at RT | ~ 0.3 | 0.046 | Islands perform Ostwald ripening with S |
| 12/15/2008 | Ag deposition followed by in situ S deposition | ~ 0.3 | 0.04 | Islands perform Ostwald ripening with S |
| 12/22/2008 | Ag deposition followed by S deposition at RT | ~ 0.3 | 0.034 | Islands perform Ostwald ripening with S |
| 12/30/2008 | Ag deposition followed by S deposition at RT | ~ 0.3 | 0.118 | OR, some islands changed orientation for 45º |
| 1/6/2009 | Ag deposition followed by S deposition at RT | ~ 0.3 | 0.21 | Fast OR, islands changed orientation for 45º |
| 1/13/2009 | Ag deposition followed by S deposition at RT | ~ 0.3 | 0.265 | Checkerbord and dense phase form, irregular shape islands |
| 1/21/2009 | Ag deposition followed by S deposition at RT | ~ 0.3 | 0.114 | OR, some islands changed orientation for 45º |
| 1/26/2009 | Ag deposition followed by S deposition at RT | ~ 0.3 | 0.083 | OR, islands turned round |
| 1/29/2009 | Ag deposition followed by S deposition at RT | ~ 0.3 | 0.094 | OR, islands turned round |
| 2/5/2009 | Ag deposition followed by S deposition at RT | ~ 0.3 | 0.081 | OR, islands turned round |
| 2/12/2009 | S deposition at RT | | 0.088 | Similar to clean Ag(100) surface |
| 2/16/2009 | Ag deposition followed by S deposition at RT | ~ 0.3 | 0.10 | OR, some islands changed orientation for 45º |
| 2/23/2009 | S deposition at 228 K | | 0.085 | No obvious difference from clean surface |
| 2/26/2009 | Ag deposition at 225 K and then heat up to RT | ~ 0.5 | | Wormy islands at 225 K, square at RT |
| 2/27/2009 | Ag deposition at RT | ~ 0.6 | | Wormy islands |
| 3/2/2009 | Ag deposition followed by S deposition at RT | ~ 0.3 | 0.153 | OR, most islands changed orientation for 45º |
| 3/9/2009 | S deposition at 120 K, heat up to 170 K, 230 K, RT | | 0.23 | Only dense phase structure, no checkerboard |

Table 4

| Ag(111) data list | | | | | | | |
|---|---|---|---|---|---|---|---|
| **Date** | **Image** | **What?** | **θAg/ML** | **θs/ML** | **Lab Nb Pg** | **File name** | **Note** |
| 5-19-08 | all | Clean surface after many cycles of cleaning, RT | | | | 05-19-2008 | |
| 05-27-08 | all | clean surface, RT | | | | 05-27-2008 | |
| 06-04-08 | all | clean surface, RT | | | | 06-04-2008 | |
| 06-18-08 | all | clean surface, RT | | | 6-14 | 06-18-2008 | |
| 06-23-08 | 1-6 | clean surface, RT | | | 6-16 | 06-23-2008 | |
| | 7-10 | clean surface, 120 K | | | | | |
| | 11-16 | after S deposition, 120 K | | < 0.003 | | | |
| | 17-19 | after heating, 160 K | | | | | |
| | 20-21 | after heating, 175 K | | | | | |
| | 22-23 | after heating, 240 K | | | | | |
| | 24-27 | after heating, RT | | | | | |
| 06-27-08 | all | clean surface, RT | | | 6-19 | 06-27-2008 | |
| 07-01-08 | all | clean surface, RT | | | 6-21 | 07-01-2008 | |
| 07-03-08 | all | clean surface, RT | | | 6-23 | 07-03-2008 | |
| 07-08-08 | all | clean surface, RT | | | 6-24 | 07-08-2008 | |
| 07-09-08 | all | clean surface, RT | | | 6-25 | 07-09-2008 | |
| 07-14-08 | all | clean surface, RT | | | 6-26 | 07-14-2008 | |
| 07-17-08 | all | clean surface, RT | | | 6-28 | 07-17-2008 | |
| 07-22-08 | 1-10 | clean surface, RT | | | 6-29 | 07-22-2008 | |
| | 11-18 | clean surface, 120 K | | | | | |
| | 19-31 | after S deposition, 120 K | 0.368 | | | | |
| | 32-41 | after heating, 170 K | | | | | |
| | 42-63 | after heating, 230 K | | | | | |
| | 64-104 | after heating, RT | | | | | |
| | 105-121 | after cooling, 230 K | | | | | |
| | 122-145 | after heating, RT | | | | | |
| 07-30-08 | 1-3 | clean surface, RT | | | 6-34 | 07-30-2008 | |
| | 4-10 | clean surface, 120 K | | | | | |
| | 11-27 | after S deposition, 120 K | 0.248 | | | | |
| | 28-35 | after heating, 170 K | | | | | |
| | 36-50 | after heating, 240 K | | | | | |
| | 51-91 | after heating, RT | | | | | |
| | 92-107 | after cooling, 230 K | | | | | |
| 08-05-08 | 1-7 | clean surface, RT | | | 6-38 | 08-05-2008 | |
| | 8-21 | after Ag deposition, flux = 660 nA, 25 sec, RT | < 0.1 | | | | |
| 08-07-08 | all | clean surface, RT | | | 6-39 | 08-07-2008 | |
| 08-12-08 | all | clean surface, RT | | | 6-40 | 08-12-2008 | |

Table 5

| Date | Image | What? | θAg/ML | θs/ML | Lab Nb Pg | File name | Note |
|---|---|---|---|---|---|---|---|
| 08-18-08 | 1-5 | clean surface, RT | | | 6-43 | 08-18-2008 | |
| | 6-60 | after Ag deposition, flux = 660 nA, 1 min, RT | > 1.2 | | | | |
| 08-21-08 | all | clean surface, RT | | | 6-44 | 08-21-2008 | |
| **New RHK controller** | | | | | | | |
| 08-27-08 | all | clean surface, RT | | | 6-46 | 2008-08-27 | |
| 08-28-08 | all | clean surface, RT | | | 6-46 | 2008-08-28 | |
| 09-03-08 | all | clean surface, RT | | | 6-47 | 2008-09-03 | |
| 09-04-08 | all | clean surface, RT | | | 6-48 | 2008-09-04 | |
| 09-05-08 | all | clean surface, RT | | | 6-48 | 2008-09-05 | |
| 09-09-08 | all | clean surface, RT | | | 6-50 | 2008-09-09 | |
| 09-11-08 | all | clean surface, RT | | | 6-51 | 2008-09-11 | |
| 09-15-08 | all | clean surface, RT | | | 6-52 | 2008-09-15 | |
| 09-16-08 | 1-16 | clean surface, RT | | | 6-53 | 2008-09-16 | |
| | 17-55 | after Ag deposition, flux = 670 nA, 30 sec, RT | ~ 0.3 | | | | |
| 09-17-08 | all | clean surface, RT | | | 6-53 | 2008-09-17 | |
| 09-18-08 | 1-20 | clean surface, RT | | | 6-53 | 2008-09-18 | |
| | 21-105 | after Ag deposition, flux = 490 nA, 33 sec, RT | ~ 0.7 | | | | |
| 09-23-08 | all | clean surface, RT | | | 6-55 | 2008-09-23 | |
| 09-30-08 | 1-14 | clean surface, RT | | | 6-56 | 2008-09-30 | |
| | 15-26 | after Ag deposition, flux = 460 nA, 35 sec, RT | ~ 0.2 | | | | |
| | 27-44 | after S deposition, RT | | 0.235 | | | |
| 10-15-08 | 1-23 | clean surface, RT | | | 6-63 | 2008-10-15 | |
| | 24-33 | after Ag deposition, flux = 400 nA, 100 sec, RT | ~ 1 | | | | |
| 10-21-08 | all | clean surface, RT | | | 6-65 | 2008-10-21 | |
| 10-27-08 | all | clean surface, RT | | | 6-68 | 2008-10-27 | |
| 11-18-08 | all | clean surface, RT | | | 6-78 | 2008-11-18 | |
| 11-20-08 | 1-4 | clean surface, RT | | | 6-80 | 2008-11-20 | |
| | 5-8 | after Ag deposition, flux = 2000 nA, 8 min, RT | > 10 | | | | |
| | 9-13 | after annealing, 1.20A for 30min | | | | | |
| 11-25-08 | all | clean surface, RT | | | 6-82 | 2008-11-25 | |
| 12-01-08 | 1-37 | clean surface, RT | | | 6-84 | 2008-12-01 | |
| | 38-73 | after Ag deposition, flux = 460 nA, 40 sec, RT | ~ 0.5 | | | | |
| | 74-123 | after S deposition, RT | | 0.0087 | | | |
| 12-05-08 | 1-36 | clean surface, RT | | | 6-88 | 2008-12-05 | |
| | 37-155 | after Ag deposition, flux = 490 nA, 20 sec, RT | ~ 0.3 | | | | |
| | 156-297 | after S deposition, RT | | 0.036 | | | |
| 12-10-08 | 1-20 | clean surface, RT | | | 6-92 | 2008-12-10 | |
| | 21-45 | after S deposition, RT | | 0.046 | | | |
| | 46-108 | after Ag deposition, flux = 495 nA, 20 sec, RT | ~ 0.3 | | | | |

Table 5 (continued)

| Date | Image | What? | θAg/ML | θs/ML | Lab Nb Pg | File name | Note |
|---|---|---|---|---|---|---|---|
| 12-15-08 | 1-22 | clean surface, RT | | | 6-95 | 2008-12-15 | |
| | 23-44.5 | after Ag deposition, flux = 485 nA, 20 sec, RT | ~ 0.3 | | | | |
| | 44.5-49 | during S deposition, RT | | | | | |
| | 50-111 | after S deposition, RT | | 0.040 | | | |
| 12-22-08 | 1-22 | clean surface, RT | | | | | |
| | 23-37 | after Ag deposition, flux = 505 nA, 18 sec, RT | ~ 0.3 | | 6-98 | 2008-12-22 | |
| Date | Image | What? | θAg/ML | θs/ML | Lab Nb Pg | File name | Note |
| 02-26-09 | 1-12 | clean surface, RT | | | 6-129 | 2009-02-26 | |
| | 13-20 | clean surface, 225 K | | | | | |
| | 21-44 | after Ag deposition, flux = 485 nA, 16 sec, 225 K | ~ 0.5 | | | | |
| | 45-56 | after heating, RT | | | | | |
| 02-27-09 | 1-18 | clean surface, RT | | | 6-100 | 2009-02-26 | |
| | 19-35 | after Ag deposition, flux = 485 nA, 18 sec, RT | ~ 0.3 | | | | |
| | 36-42 | after Ag deposition, flux = 308 nA, 1 min, RT | ~ 0.3 | 0.200 | | | |
| 03-02-09 | 1-17 | clean surface, RT | | | 6-131 | 2009-03-02 | |
| | 18-37 | after Ag deposition, flux = 470 nA, 16 sec, RT | ~ 0.3 | | | | |
| | 38-117 | after S deposition, RT | | 0.1534 | | | |
| 03-05-09 | 1-18 | after S deposition, RT | | 0.200 | | | |
| 03-21-09 | 1-38 | clean surface, RT | | | 6-134 | 2009-03-05 | |
| | 39-75 | clean surface, 120 K | | | | | |
| 03-09-09 | 1-14 | clean surface, RT | | | 6-110 | 2009-03-21 | |
| | 15-42 | clean surface, 120 K | | | | | |
| | 43-55 | after S deposition, 120 K | | 0.2323 | 6-136 | 2009-03-09 | |
| | 56-72 | after S deposition, 170 K | | | | | |
| | 73-95 | after S deposition, 228 K | | | | | |
| | 96-117 | after S deposition, RT | | | | | |
| 03-10-09 | 1-35 | after Ag deposition, flux = 472 nA, 13 sec, RT | ~ 0.3 | | 6-137 | 2009-03-10 | |
| | 1-17 | surface of last night, after heating to 300 K for 1 h | | 0.025 | | | |
| 04-06-09 | 1-22 | clean surface, RT | | | 7-1 | 2009-04-06 | |
| | 23-61 | clean surface, 120 K | | | | | |
| 04-09-09 | 1-12 | after Ag deposition, flux = 490 nA, 15 sec, RT | ~ 0.3 | | 7-3 | 2009-04-09 | |
| | 13-80 | after S deposition, RT | | 0.0811 | | | |
| 04-13-09 | all | clean surface, RT | | | 7-5 | 2009-04-13 | |
| | 82-101 | after S deposition, RT | | 0.0882 | | | |
| 02/16/09 | 1-20 | clean surface, RT | | | 6-124 | 2009-02-16 | |
| | 21-37 | after Ag depsosition, flux = 485 nA, 18 sec, RT | ~ 0.3 | | | | |
| | 38-140 | after S deposition, RT | | 0.1 | | | |
| 02-23-09 | 1-9 | clean surface, RT | | | 6-127 | 2009-02-23 | |
| | 10-33 | clean surface, 228 K | | | | | |
| | 34-97 | after S deposition, 228 K | | 0.0846 | | | |

Table 5 (continued)

# ACKNOWLEDGEMENTS

First I would like to thank Professor Pat Thiel and Professor Jim Evans for their support and guidance throughout these years with my graduate study in Iowa State University. Their enthusiasm in scientific research in different styles inspired me during my own research work. When I sometimes got frustrated with my experiments and wanted to quit, I told myself "they work harder than me". I truly appreciate their patience and willingness to let me keep trying my work at the very beginning without getting anything for months.

I have to thank all the Thiel group members, past and present. I would like to especially acknowledge the people I worked closest with including Dapeng Jing, Selena Russell, and Chad Yuen. We can always joke around when things are not working and still work hard to fix the problem.

I would like to express a special thanks to Dr. Cynthia Jenks for all her help and advice on equipment work and personal life over the years.

I want to thank everyone who played a part in my life here in Ames. Feili, for talking about raising kids and having more kids. Jia Tao, for staying around with me while I was in Ames alone by my own. Jim Anderegg, for giving advice on our chamber. Chun Lu and Aoshuang, for hanging around and visit to my dear Emma. … …

Last but not least, I want to thank my family for supporting my study here in USA. The support from my parents in my twenty-four years of study is greatly appreciated. The travelling from China of my husband Haiyang Zhu is also greatly appreciated.